Solution Processed Semiconducting Nanosheet Networks Towards Optoelectronic Applications

SHIXIN LIU

A THESIS SUBMITTED FOR THE DEGREE OF

DOCTOR OF PHILOSOPHY

UNDER THE SUPERVISION OF

PROFESSOR JONATHAN N. COLEMAN

SCHOOL OF PHYSICS

TRINITY COLLEGE DUBLIN

2024

Declaration

I declare that this thesis has not been submitted as an exercise for a degree at this or any other university and it is entirely my own work.

I agree to deposit this thesis in the University's open access institutional repository or allow the library to do so on my behalf, subject to Irish Copyright Legislation and Trinity College Library conditions of use and acknowledgement.

Elements of this work that have been carried out jointly with others or by collaborators have been duly acknowledged in the text wherever included.

Shixin Liu

Solution Processed Semiconducting Nanosheet Networks Towards Optoelectronic Applications

Abstract

Two-dimensional (2D) semiconducting transition metal chalcogenides (TMDs) are attractive materials owing to their superb electronic and optoelectronic properties. The great advancement of material exfoliation and thin film fabrication methods over the past years allows these 2D materials to be solution-processed into nanosheet networks, serving as basic electronic components. In this thesis, to fully reveal their potential, these 2D networks will be integrated with other low-dimensional materials, forming novel device structures towards optoelectronic applications.

The device structure determines their electrical behaviors. To test this, vertically metal-semiconductor-metal (MSM) devices were fabricated using liquid exfoliated semiconducting tungsten disulfide (WS_2) nanosheets and one-dimensional metallic nanomaterials as electrodes, such as single-walled carbon nanotubes (SWNTs). Electrical short-free vertical heterostructures, down to a WS_2 film thickness ~0.5 μm, were realized. By performing the electrical measurements, the obtained devices displayed bulk-limited conduction behaviors when SWNTs were dispersed in isopropanol. The out-of-plane conductivity and mobility were extracted to be ~1.63×10^{-4} S m^{-1} and ~5.36×10^{-3} cm^2 V^{-1} s^{-1}, respectively, which were around 1 order of magnitude lower than their in-plane values. When SWNTs were dispersed in a surfactant aqueous solution, the surfactant induced doping effect to the semiconducting nanosheet networks and resulted in electrode-limited Schottky behaviors at the SWNTs/ WS_2 interfaces. Furthermore, by increasing the WS_2 film thickness, a transition from electrode- to

bulk-limited electrical behavior was observed with a critical transition film thickness of ~2.6 μm.

The porous and rough nanosheet networks could also be covered with a thin film semiconductor to avoid the electrical shorts and form heterojunctions at this semiconductor-semiconductor interface. Using ZnO nanoparticles and PEDOT:PSS as carrier transport layers, vertically stacked heterojunctions were successfully fabricated with liquid exfoliated tungsten diselenide (WSe_2) nanosheets. Due to the improved energy band alignment at the interface, the heterojunctions exhibited a high rectification ratio ~10^4 at ±1 V, which is the highest among solution-processed heterojunctions using liquid exfoliated nanosheets without relying on the heavily doped silicon. The devices could be used as self-powered photodetectors in both photoconductor and photodiode modes under AM 1.5D illumination. The photoresponsivity at 1 V was ~1.5 A W^{-1} which is highest for photodetectors based on solution-processed WSe_2 nanosheets.

The interface properties play a vital role in the performance of heterojunction devices. Therefore, the interfacial behaviors of the liquid exfoliated WSe_2 nanosheet network were manipulated by sandwiching it between various types of transport layers, such as ZnO, TiO_2, and NiO, etc. The photovoltaic performances of these devices were tested under AM 1.5D illumination. The devices displayed distinctive electrical behaviors with short-circuit current densities ranging from 1.32×10^{-3} to 2.50 A m^{-2} and open circuit voltages from 4 to 242 mV, but a rather low fill factor around 20-27%. The highest efficiency was obtained to be 1.95×10^{-3} % when ZnO and NiO were used as transport layers. The low short circuit current density is identified to be the main limiting factor for the poor photovoltaic performance and further improvements will be required.

The van der Waals (vdW) heterojunction formed with two types of semiconducting TMDs nanosheets are expected to exhibit a better performance

where the interface is constructed with dangling bonds-free surfaces. Using electrochemically exfoliated (EE) nanosheets, conformal and lateral nanosheet alignment could be realized due to their atomic thin thicknesses and large aspect ratios. The vdW heterojunctions were successfully fabricated with EE WS_2 and niobium doped WSe_2. The electrical measurements showed that the vdW heterojunction could form a broken-gap type heterojunction that induces band-to-band tunneling behaviors. The device was further measured under 1000 W m^{-2} AM 1.5D illumination, and photoresponsivity of 0.13 and 0.14 A W^{-1} were obtained at -1 V and 1 V, respectively.

Publications

1. **Liu, S.,** Ding, E.X., Kelly, A.G., Doolan, L., Gabbett, C., Kaur, H., Munuera, J., Carey, T., Garcia, J. and Coleman, J.N., 2022. Solution processed, vertically stacked hetero-structured diodes based on liquid-exfoliated WS_2 nanosheets: from electrode-limited to bulk-limited behavior. *Nanoscale*, *14*(42), pp.15679-15690. (The basis of Chapter 6)
2. **Liu, S.**, Carey, T., Munuera, J., Synnatschke, K., Kaur, H., Coleman, E., Doolan, L., Coleman, J. N.*, Solution-processed heterojunction photodiodes based on WSe_2 nanosheet networks, *Small*, 2023, 2304735. (The basis of Chapter 7)
3. Gabbett, C., Doolan, L., Synnatschke, K., Gambini, L., Coleman, E., Kelly, A.G., **Liu, S.,** Caffrey, E., Munuera, J., Murphy, C. and Sanvito, S., 2023. 3D-imaging of printed nanostructured networks using high-resolution FIB-SEM nanotomography. *arXiv preprint arXiv:2301.11046*.
4. Carey, T., Cassidy, O., Synnatschke, K., Caffrey, E., Garcia, J., **Liu, S.,** Kaur, H., Kelly, A.G., Munuera, J., Gabbett, C. and O'Suilleabhain, D., 2023. High-mobility flexible transistors with low-temperature solution-processed tungsten dichalcogenides. *ACS nano*, *17*(3), pp.2912-2922.
5. Carey, T., Maughan, J., Doolan, L., Caffrey, E., Garcia, J., **Liu, S**., Kaur, H., Ilhan, C., Seyedin, S. and Coleman, J.N., 2023. Knot Architecture for Biocompatible and Semiconducting Two-Dimensional Electronic Fibre Transistors. arXiv preprint arXiv:2311.02545.
6. Gabbett, C., Kelly, A.G., Coleman, E., Doolan, L., Carey, T., Synnatschke, K., **Liu, S.**, Dawson, A., OSuilleabhain, D., Munuera, J. Caffrey, E., Coleman, N. J., 2023. Quantifying the contribution of material and junction resistances in nano-networks. arXiv preprint arXiv:2311.16740.

Acknowledgements

I would like to thank Johnny for giving me this great opportunity to conduct research in this group. I cannot remember how many times the meeting was filled with frustrating results but you can always find a possible solution. None of my work could be achieved without your patient guidance and supervision.

Specially thanks to Adam, aka the Bad Boy, I wondered about why whiskey could be used for LPE (with permission from Johnny), but after four years sitting next to you, I only feel it is such a pity that I missed this chance. To Erxiong, who we worked through the entire “limited lab access” period, I am confident to say that we could achieve better results together if all these equipment do not need to be moved from lab to lab every day! For someone like Cian who cannot resist a Harp is totally worth mentioning here as you always relentlessly show up for my stupid troubles. To Tian and Kev, really appreciate your generous help all the time. To Yash, JB and Aideen, you helped me overcome the awkward beginning stage.

To the rest of the group: Ruiyuan, Dan, Seb, Jose, Harneet, Bharathi, Joe, James, Dominik, Mark, Luke, Eoin, Jack, Emmet, Oran, Alina, Anthony, Yufan, and Yumei, it is my honor to work with you in this group and the memory in ~~pu~~labs with you is definitely unforgettable. I would also like to thank for all the support from Joe, Marie, Karl, Catherine and Pat in SoP, and Mike, Riley and David in CRANN. To my friends, Jingjing, Jing L, Meiying, Ji, Gaozhong, Haizhong, Lulin, Ke, Jing Q, and Fanqi, you accompanied me with the happiest moments.

To my parents, you encouraged me to take this path four years ago and told me I will not regret. With all your good wishes, I am nearly approaching the end of this journey. I would like to thank you for your constant encouragements and kindly supports.

It is great to have someone pay for your curiosity.

Contents

List of Figures

TO MY FAMILY AND FRIENDS,

The pursuit of science is a never-ending journey
into the unknown, fueled by curiosity and guided
by reason.

Neil Armstrong

Chapter 1 Introduction

The discovery and manipulation of materials paves the way for modern technologies. Since the first demonstration of transistor using bulk semiconductor Germanium in 1947, after decades of research and development, we are already standing on a point that the transistor can be miniaturized to a very small size that trillions of them could be accommodated on a fingernail sized chip. However, bulk semiconductor-based electronics approach to material's inherent limitations gradually and cannot meet the current requirements. Therefore, new generation nanomaterials, e.g., two-dimensional (2D) materials, are expected to be the solution and can lead to a new surge of novel applications. Since the first discovery of an atomic thick carbon layer (graphene) and its exotic properties in 2004, the "gold rush" of 2D materials have been lasted for a few decades and numerous materials have been identified. These novel materials exhibit a wide range of promising properties and can be used as basic building blocks for electronic and optoelectronic devices. Importantly, their dangling bonds free surfaces are expected to realize an ideal carrier transport if van der Waals (vdW) heterostructures are formed.

Although there are many successful demonstrations of single flake-based electronic devices, the poor scalability limits their practical applications. Solution-processing of these materials into networks is believed to be able to make them into realistic applications. However, there is a lack of reliable fabrication methods to realize the heterostructures based on nanosheet networks, and their electrical

behaviors are still not well understood. Therefore, the central question of this thesis is:

How to realize vdW heterostructures and manipulate their electrical behavior?

With this question in mind, the aim of this thesis is to realize heterostructures using 2D semiconducting nanosheet networks and to investigate their electronic properties. The outline of the thesis is given as follows.

The family of nanomaterial includes zero- to two-dimensional nanomaterials. These materials exhibit distinctive morphologies and properties, which can be integrated together to form novel device structures and used for various applications. In Chapter 2, the fundamental properties of 2D materials and other types of low dimensional nanomaterials will be introduced. Further, to meet the practical requirements of the real world, cheap and scalable methods to produce 2D materials will be desirable. Chapter 3 will introduce the exfoliation and stabilisation methods for 2D materials, which will allow 2D materials to be produced in liquids.

The obtained nanomaterials in liquids are suitable mediums which are compatible with current solution-processing techniques, such as spray coating and spin coating, etc. Thin films made from nanomaterial networks can function as basic electrical components. Chapter 4 will introduce film formation methods by solution-processing techniques. Moreover, the device structure and the operation mechanism of photo-sensitive devices will be explained, following by a literature review of the current research progress. The advanced material and thin film equipment and characterisation techniques adopted in this thesis will be introduced in Chapter 5.

Although the simplest electronic device can be fabricated with one semiconductor and two spatially separated electrodes, the current dominant device structure is

lateral ones for those photodetectors based on nanosheet networks, which will always be bulk-limited due to the low electrical conductivity of the semiconducting nanosheet network and the limited electrode geometries. Chapter 6 will demonstrate that such bulk-limited behaviors can be mitigated once the vertically stacked device structure with reduced channel length is adopted that the electrical rectifying behaviors arising from the metal-semiconductor interface can be observed.

Adopting vertical device structures, it is shown in Chapter 7 that nanosheet networks can form heterojunctions with zero-dimensional semiconducting nanoparticles, which could simultaneously avoid the electrical shorts problem during metal deposition on the top of the porous nanosheet network. Moreover, the electrical properties can be improved when transport layers are used to enhance the carrier transport at the interface.

Manipulating the interfacial properties of the nanosheet networks is crucial to improve the optoelectronic responses. Some semiconducting materials could be used as transport layers, providing a suitable energy band alignment at the interface to enable facile carrier transport or selectivity properties. Therefore, various types of transport layer materials are adopted and investigated regarding the photovoltaic performance of the heterojunctions based on nanosheet networks in Chapter 8.

The networks formed by liquid-exfoliated nanosheets are always limited by its inter-nanosheet junction resistance and a high porosity. It is expected that the large-sized and atomic thick nanosheets produced by electrochemical exfoliation can form conformal and well-aligned networks that will exhibit much enhanced electrical properties and an ultra-low porosity. Importantly, the dangling bonds free interface could provide ideal carrier transport through the vdW junction. In

Chapter 9, vdW heterojunction using electrochemically exfoliated nanosheets will be fabricated and characterised.

The conclusion will be presented in the end along with possible solutions to the problems that encountered in this thesis. It is hoped that the thesis presented here will provide reliable methods and device structures to guide further investigations on the electrical properties of 2D nanosheet networks.

Imagination is more important than knowledge.

Albert Einstein

Chapter 2 Low-Dimensional Nanomaterials

Low-dimensional materials (LDMs) are these that have at least one dimension on the order of nanometers, usually less than 100 nm. The fundamental properties of bulk materials are inherently determined by their structure and compositions. Therefore, by simply reducing the dimensions, the physiochemical properties of these nanomaterials could be greatly altered due to spatially confined carriers and exotic behaviors could arise which are absent in their bulk form. Depending on the number of dimensions that on the order of nanometers, LDMs can be classified into zero-dimensional (0D), one-dimensional (1D) and two-dimensional (2D) materials. When at least one dimension of LDMs is comparable with the characteristic length scale of carriers (the De Broglie wavelength: $\lambda_{DB} = \frac{h}{m^* v}$, where h is the Planck's constant, m^* is the effective mass of carriers, and v is the velocity) of its bulk material, the energy spectrum becomes quantized along this reduced dimension. This leads to changes in the electronic band structure and density of states (DOS) due to the reduction of dimensions to nanometers, which is referred to as the quantum confinement effect. For bulk materials, their DOS in an energy band is proportional to the square root of the energy E ($DOS_{3D} \propto \sqrt{E}$) and the DOS is continuous through energy levels, as shown in **Figure 2.1A**. For 2D materials (2DMs) with one dimension that is comparable with its De Broglie wavelength, its DOS is proportional to the energy E to the exponent of 0 ($DOS_{2D} \propto E^0$), so its DOS exhibits step-like profiles (**Figure 2.1B**). When more than one dimension of the material is reduced below or comparable with the De

Broglie wavelength (0D & 1D), the permitted energy levels for 0D structures are discrete ($DOS_{0D} \propto \delta(E)$), while the energy levels tend to spread out between the quantized levels for 1D structures ($DOS_{1D} \propto E^{-1/2}$) , as shown in **Figure 2.1C-D**. These fascinating properties are not accessible in bulk materials and are believed to be crucial to develop the next generation electronic and optoelectronic devices.

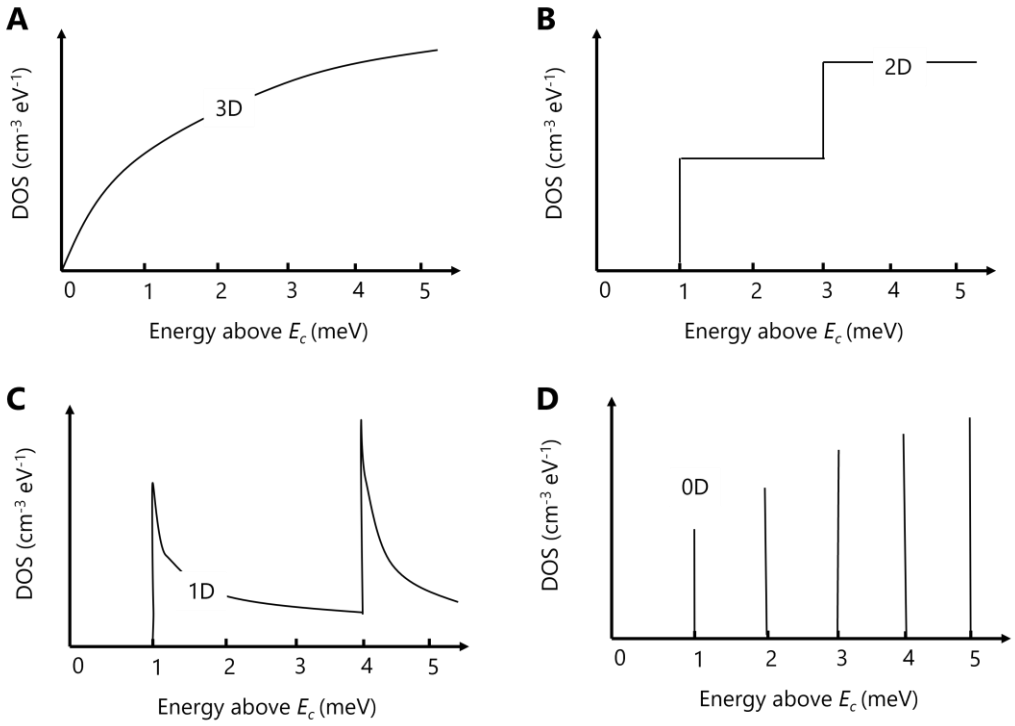

Figure 2.1 Density of states of materials. Density of states above the conduction band for bulk material (A) and low-dimensional nanomaterials (B-C). Adapted from Ref. [1].

2.1 Two-dimensional materials

Two-dimensional materials are a class of nanomaterial with one dimension being orders of magnitude smaller than the other two. This unique structure would only allow carriers to move along the horizontal plane but to be confined within the smallest dimension, bringing them with interesting properties that are absent in their bulk counterparts.

2.1.1 Introduction to 2D materials

The most representative 2D material is graphite in the monolayer form: graphene. As early as 1859, an English Chemist Benjamin Collins Brodie reported that reduced graphite oxide exhibits naturally layered structure.[2] PR Wallace predicted in 1947 the semi-metallic properties of graphite in monolayer.[3] With the advancement of characterisation techniques, H. P. Boehm successfully identified few-layer graphite flakes using transmission electron microscopy and X-ray diffraction in 1962.[4] He and his colleagues were the first to name such down to few-layered graphite as graphene. However, the existence of atomic-thick monolayer was doubted over a long time as it was generally regarded that thermal fluctuation would easily tear the material apart.[5]

While there were more researchers attempting to prepare and study graphene, the recognized work was done by Andre Geim and Konstantin Novoselov in 2004.[6] In their work, a high-quality atomic thick monolayer graphite was isolated simply by using a tape repeatedly peeling off a graphite crystal until there was one monolayer left on the substrate. This could be done due to that the adjacent layers in graphite are hold together by van der Waals (vdW) force rather than by covalent bonds, and less energy is required to peel off layers rather than to break the covalent bonds on the basal plane, which is one of the most important features for other 2DMs. This monolayer was characterised to be only around 0.35 nm thick by atomic force microscopy, as shown in **Figure 2.2A**. Their work proved the existence of free-standing monolayers. It was later found that graphene monolayers can be thermodynamically stabilised by the formation of ripples up to 1 nm that could decouple the bending and stretching modes in such atomic thin structure.[7, 8] Importantly, this facile tape-exfoliation method can be applied on other crystals so long as it is naturally layered structure that adjacent layers are governed by vdW forces, which is still adopted to achieve high-quality nanosheets

nowadays.

Graphene has a simple honeycomb structure where carbon atoms are arranged in a hexagonal lattice. For each monolayer, every carbon atom is bonded in sp^2 hybridization with fully occupied *2s*, *2px*, and *2py* atomic orbitals. This leads to a formation of σ bond between adjacent carbon atoms with a spacing of 1.42 Å, which contributes to the in-plane bonding strength. The remaining *2pz* atomic orbitals that are perpendicular to the basal plane of graphene will bind with neighbouring atoms, forming a filled π band as the valence band and an empty band as the conduction band.[9] As there is no covalent bonding between adjacent layers, the out-of-plane (OoP) properties of few-layered graphene vary significantly compared with these along the in-plane (IP) directions due to tunnelling barriers in these vdW gaps[10], and such OoP to IP anisotropy is one of the common features for 2DMs.

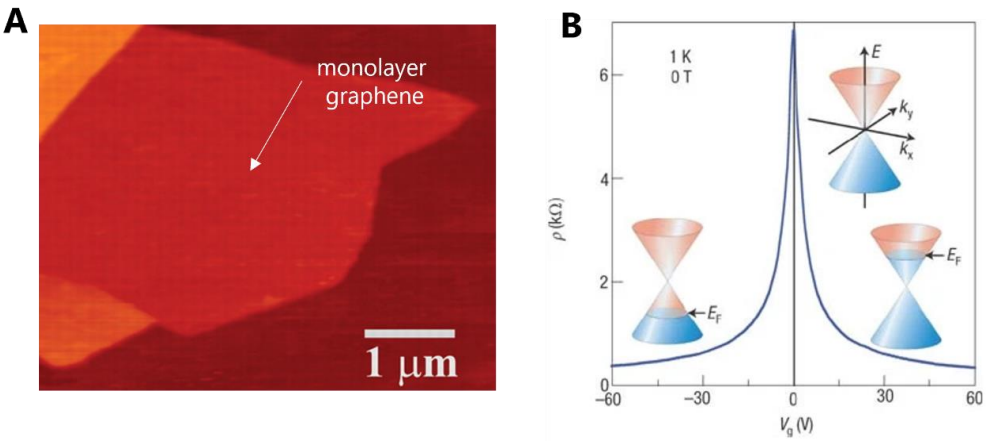

Figure 2.2 The structure and electronic properties of graphene. (A) The AFM image of a single layer graphene on SiO_2/Si by Scotch tape method (Adapted from Ref. *6*). (B) Ambipolar electric field effect in a single-layer graphene. The insets show the change of Fermi energy with respect of the gate voltage.

The unique structure of graphene brings itself unusual properties. The charge carriers in single-layer graphene can be better described by the Dirac equation, unlike those in most of other materials that are usually described by the

Schrödinger equation.[11] It exhibits semi-metallic properties due to its half-filled energy band that the valence band is filled with electrons while the conduction band remains empty. The energy depends on the wave vector linearly, resulting in a linear band dispersion. The type of charge carrier in this structure can be tuned by the external gate voltage from electron to hole continuously: an ambipolar field effect, as shown in **Figure 2.2B**. In fact, these charged carriers are massless Dirac fermions[12, 13], and can move along the basal plane up to thousands of interatomic distances without any scattering, which is known as the ballistic transport.[6] Therefore, graphene exhibits carrier mobility up to 15,000 $cm^2 V^{-1} s^{-1}$ at room temperature[14], which shows great potential for next generation electronics. The optical properties of graphene are also attractive. The single-layer graphene could absorb 2.3% of a broadband light with a high absorption coefficient (~6.8×10^5 cm^{-1}).[15] For pristine graphene, only inter-band transition between conduction band and valence band is possible. However, graphene can be doped by chemicals and both inter-band and intra-band (within an energy band) transitions exist in the doped graphene owing to that its Fermi level can induce Pauli blocking of inter-band transitions.[16] When the incident light has an energy less than twice that of the Fermi level energy ($2\times E_f$), the optical conductivity is dominated by the intra-band transition, while for incident light with an energy larger than that, the optical conductivity is almost independent of wavelength, that is dominated by the inter-band transition.[16] Other than these peculiar optical and electronic properties, graphene also exhibits extremely high mechanical strengths (a tensile strength of 130 GPa and a Young's modulus of 1 TPa)[11, 17] and thermal conductivity of ~5×10^6 $W K^{-1}$.[18]

So, where is the boundary between 2D and 3D? For graphene, it was found that its electronic structures vary upon changing the layer numbers, appearing like that of the bulk counterparts at 10 layers.[6, 19, 20] For example, when two monolayer

graphene are stacked together to form a bilayer, based on calculations by the tight-binding Hamiltonian method, it was found that the bilayer graphene shows parabolic band structures.[9] Such a bilayer is metallic without any external bias but a gap between the conduction band and the valence band could be formed depending on the external bias.[9] Generally, it is only graphite with a layer number less than 10 can be regarded as graphene. This rule is also similar for other 2DMs but not strictly at 10 layers and will be further introduced in the next section.

"*There's Plenty of Room at the Bottom*"[21] - Richard Feynman, 1959

The successful demonstration of free-standing graphene and its fascinating properties soon led a gold rush into other materials in 2D forms. Numerous types of 2DMs have been identified since 2004. In fact, although the early investigations focused on naturally layered inorganic crystals such as graphite[22], it was found that many other materials including organics could be synthesized or assembled in 2D forms by using specially designed methods.[23, 24] Therefore, the subject of 2DMs is too broad and complicated to be fully covered here. Nevertheless, this thesis will mostly focus on naturally layered inorganic materials and they can be classified by different categories, e.g., elemental composition and electronic properties, etc.

If we view these materials from the perspective of composition, they can be made from single element, two elements, and multiple elements. Single elemental 2D materials are from the group III, IV, V, and VI and are usually named with a suffix "ene" to indicate its 2D structure, e.g., borophene (B), antimonene (Sb), silicene (Si). Unlike graphene with its flat structure due to sp^2 hybridization, most of them form ordered buckling surfaces due to sp^2-sp^3 or sp^3 hybridization that may exhibit an exceptional stability and an increased flexibility compared with those for graphene.[25] Their electronic properties are not only limited to metallic

(borophene, gallenene, and indiene) or semi-metallic (graphene, silicene, and germanene), but also semiconducting with a bandgap (phosphorene, arsenene, and bismuthene).[25-27]

2D materials made from two elements are very common, with representative examples being hexagonal boron nitride (*h*-BN), transition metal dichalcogenides (TMDs), and transition metal oxides (TMOs), etc. *h*-BN is one of the early investigated 2D materials with the same honeycomb structure as graphene where the carbon atoms are replaced by alternatively arranged boron and nitrogen atoms.[28, 29] *h*-BN exhibits a large bandgap of ~6 eV, making it as a well-known 2D insulator that can be used as dielectric layers for electronics.[30-33] Importantly, if other 2DMs are sandwiched between *h*-BN layers, this defect-free and atomically flat dielectric surface can screen external scattering sources and allows the intrinsic properties of these 2DMs to be investigated.[9, 34, 35] Another promising 2DMs are TMDs family. Its properties are versatile ranging from metallic to insulating and will be introduced in the following section.

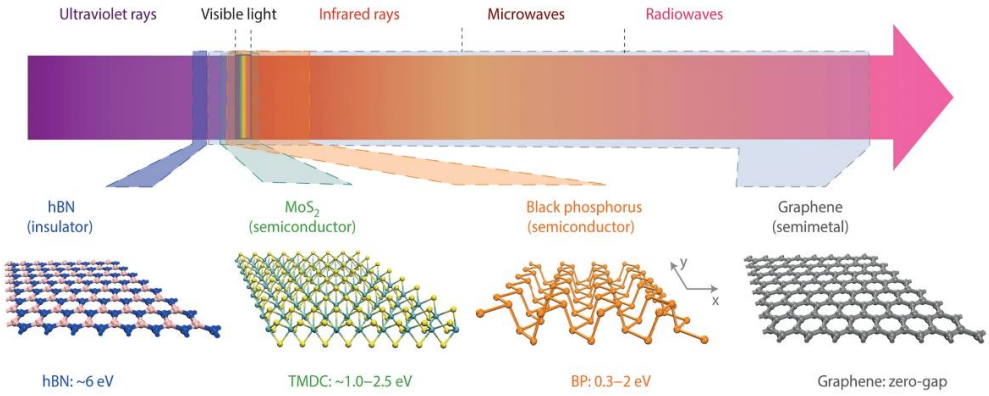

Figure 2.3 2D material family. 2D materials with various bandgaps could be used as basic electronic components for various applications. Adapted from Ref. 36.

2DMs can be composed of more than two elements, with examples such as MXenes[37], 2D perovskite[38], and alloys[39]. One important feature of these materials is their compositions and properties can be varied continuously.[40, 41] This enables

the properties of 2DMs to be tuned prior to exfoliation and specifically to certain applications, and not necessarily rely on post processing and treatments.

The diverse electronic properties of 2DMs ensure that there will always be suitable for any desired applications, as shown in **Figure 2.3**. One could conceive that these 2DMs could be used to fabricated mixed-dimensional junctions with other low-dimensional nanomaterials. Interesting phenomena could happen at such interfaces[42], which could not just compete with current electronics that is dominated by bulk semiconductors, but also for opening a new era of electronics driven by new physics mechanisms behind it.

2.1.2 Transition metal dichalcogenides

Transition metal dichalcogenides (TMDs) are a class of materials with a general chemical formula MX_2, where M represents transition metal atoms in the group IV-X and X stands for chalcogenide atoms, i.e., S, Se, and Te (**Figure 2.4A**). It is worth noting that only TMDs with transition metals in group IV-VII that are predominately layered structure, while those in group VIII-X are usually non-layered.[43] The layered nature of this material family was recognized back in 1920[44], and monolayer TMDs was already exfoliated by tape-assisted method in 1966[45] and also by chemical exfoliation in 1986[46]. It was the discovery of graphene leading to the resurgence of research interests in these materials in 2005.[28]

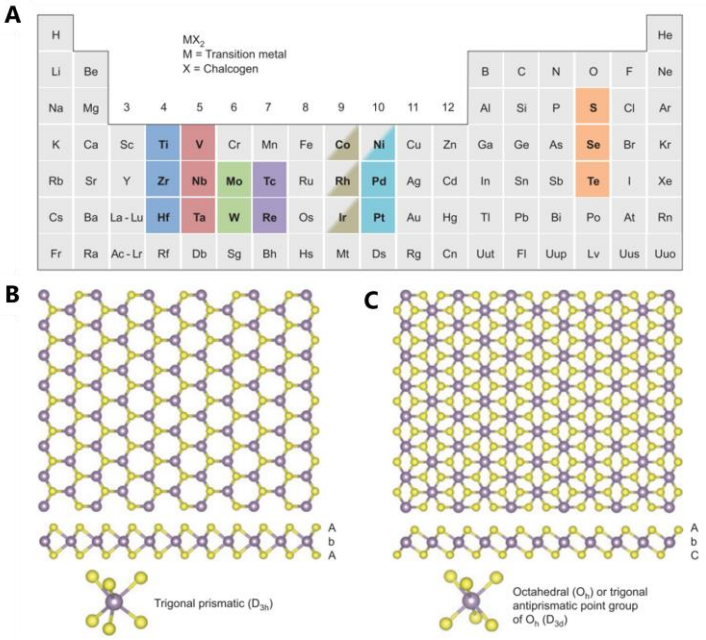

Figure 2.4 The chemical composition and crystal structures of TMDs. (A) An elemental table highlighting the transition metal and chalcogen elements. Schematic illustrations of the top-view and cross section-view of monolayer TMDs with trigonal (B) and octahedral (C) coordination, respectively. Adapted from Ref. 43.

TMDs exhibit different polymorphs and stacking polytypes.[47] The monolayer consists of one layer of metal atoms sandwiched by two layers of chalcogen atoms. The chalcogen layer terminates the surface and no dangling bonds exist on the surface, with the interaction between monolayers being vdW force. TMDs have three different polymorphs: 1T, 2H, and 3R. The letter represents trigonal, hexagonal, and rhombohedral, respectively. The number stands for the number of monolayers in the stacking sequence. Monolayer TMDs only show two polymorphs, which are trigonal prismatic (2H) and octahedral (1T) phases, as shown in **Figure 2.4B-C.** Each TMD would be in any of these polymorphs and polytypes depending on its initial formation, which would lead to diverse properties regarding crystalline phases.

The electronic structures of TMDs are largely affected by the metal's coordination environment and its number of *d*-electrons. The non-bonding *d* bands of TMDs

are located within the bonding and antibonding bands of M-X bonds. *d* orbitals in trigonal prismatic coordinated TMDs split into 3 groups: d_{z^2}, $d_{x^2-y^2,\ xy}$, and $d_{xz,\ yz}$, giving an appreciable bandgap between the first two orbitals. *d* orbitals in octahedral coordinated TMDs form degenerate $d_{z^2,\ x^2-y^2}$ and $d_{yz,xz,xy}$ orbitals to accommodate TMDs' electrons. As a result, the electronic properties of TMDs arise from the filling of the non-bonding *d* bands from transition metals. TMDs exhibit metallic or semiconducting properties if the orbitals are partially or fully filled, respectively.[43] For example, V, Nb, and Ta based TMDs are semi-metals, and Mo and W based sulphides and selenides are semiconductors, while Pd and Pt based tellurides are metals. The chalcogen atoms have a lesser impact in tuning the electronic properties than the transition metals, although the general trend is that the increase of chalcogen atomic number would result in a decrease in bandgaps due to broadening of the *d* bands. Moreover, phase transformation could happen in TMDs when alkali metals are introduced between the layers. Lithium intercalation could transform 2H-MoS_2 into 1T phase, and its electronic properties vary from semiconducting to metallic due to the phase change as well as alkali induced doping effects.[48, 49]

One important feature of TMDs is its layer number dependent properties. When decreasing their layers, the change in interlayer coupling and quantum confinement will cause a significant transformation in their electronic structures. The energy versus wavevector *K* of bulk to monolayer MoS_2 obtained by density functional theory (DFT) calculation are shown in **Figure 2.5A.** [50] The blue and red solid lines represent valence band and conduction band edges, respectively. The lowest energy transition is shown in solid arrows. The valence band maximum (VBM) of bulk MoS_2 is located at the *Γ* point and its conduction band minimum (CBM) is located roughly at the midpoint on the *K*-*Γ* line. In this case,

to allow recombination events to occur in such material, that electron jumps from the CBM into the VBM to recombine with holes, it requires an appropriate momentum to be transferred to electrons, usually achieved through collisions with phonons to supply momentums to the electron.[1] Such a process is referred as the indirect transition with no photon emission, corresponding to the non-radiative recombination.[1] In contrast, as both VBM and CBM are located at the *K* point in the case of monolayer MoS_2, electrons recombine with holes and release the energy in the form of photons that equals to the bandgap energy of the semiconductor, and such transition is a direct one and is called the band-to-band recombination, corresponding to the radiative recombination.[50] However, there could be permitted energy levels introduced by impurites, contaminants or defects within the energy band of the semiconductor, acting as recombination centers. These recombination centers allow electrons to recombine with holes at different *K* points, producing photoluminescence with the photon energy usually less than the bandgap energy of the semiconductor, and this phenomennon could happen in both direct and indirect bandgap semiconductors. The change in electronic structure leads to a dramatic change in its properties. The photoluminescence from monolayer MoS_2 is much higher than it from its bulk conterpart[50], and the former's quantum yield is up to 10^4 higher than that of the latter[51]. Furthermore, bandgaps of monolayer TMDs are also larger than those in their bulk due to contributions from the excitonic energies.[52]

The optical properties of TMDs are also attractive for any optical and optoelectronic applications.[53, 54] The optical absorption spectra of semiconducting TMDs usually exhibit two main characteristic peaks as called A and B exciton peaks.[47] The position of two peaks correspond to the energy required to fulfil the band transition at the K point, and the band splitting is due to the spin-orbit coupling[55]. The excitonic binding energy for monolayer TMDs is quite large (up

to hundreds of meV), while it will decrease with relatively thicker samples and is almost negligible for its bulk.[56] Such behavior is originated from a reduced dielectric screening and enhanced 2D confinement with less layers, leading to strong light-matter interactions.[53, 57] Looking at the spectra in **Figure 2.5B**, it can be found that TMDs cover a wide range over the sunlight spectrum. Given their large absorption coefficients (~10^5 cm^{-1}) in the sunlight range, only 15 nm GaAs or 50 nm of Si could compete with a monolayer MoS_2 with a sub-nanometer thick monolayer that remains transparent (less than 10% light absorption), but is able to effectively interact with sunlight.[58] Such monolayers are desired as it could realize an extremely high power density given the almost negligible mass of a monolayer.

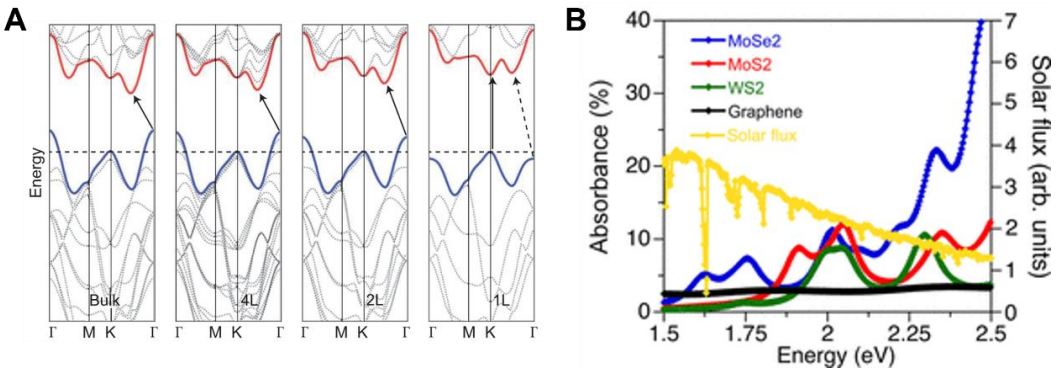

Figure 2.5 The electronic and optical properties of TMDs. (A) Energy dispersions of MoS_2 predicted by DFT calculation. Adapted from Ref. 50. (B) Absorbance of TMDs and graphene monolayers comparing with AM1.5G solar flux. Adapted from Ref. 58.

The mechanical flexibility and strength of TMDs are also one of their appealing properties. The Young's modulus of MoS_2 monolayer is comparable with that of the steel and can deformed up to 11%.[59] This is promising for any devices or composites that require high level degrees of flexibility. In comparison, Si and other conventional bulk semiconductors tend to be rigid and are difficult to meet the requirements for flexible and bendable devices.

The difference in the band structure for monolayer and bulk TMDs implies that they can find their suitable positions in various applications. For example,

monolayers are suitable for light-emitting layers where radiative recombination of electrons and holes are more effective in a direct bandgap semiconductor, while multi-layered indirect bandgap TMDs are more suitable for photovoltaic devices, so that more photons can be absorbed and converted into photocarriers to be collected by electrodes. Nevertheless, monolayer or few-layer TMDs are capable to fabricate transparent, low-weight, and ultra-high powder density electronic and optoelectronic devices. Overall, TMDs exhibit promising electronic and optical properties that are required for optoelectronic applications. Therefore, TMDs materials will be mainly focused on this thesis and will be solution-processed into networks and are used as semiconducting and light-absorbing layers in the devices through all experimental chapters.

2.2 Other low-dimensional materials

Other than 2DMs, other low-dimensional materials such as 0D nanoparticles, 1D nanotubes, and 1D nanowires are also attractive for their exotic properties and the potential to be integrated together and form mixed-dimensional junctions that could utilize their advantages from each of them.

2.2.1 Metal oxide nanoparticles

Metal oxides (MOs) are among one of the most abundant materials on earth. This type of material was proposed for electronics in competing with silicon and other III-V group semiconductors. MOs exhibit excellent carrier mobilities, a good compatibility with other active materials, and high optical transparency in visible regime due to its wide bandgap (>3 eV).[60] The first thin film transistor based on MOs was fabricated with SnO_2 in 1964[61] and it was discovery of In-Ga-Zn oxide (IGZO) in 2004 that bring world-wide attentions to these types of materials.[62] So far, MOs have shown their capability in various electronic applications, such as transistors[63], carrier selective layers[64], and transparent electrodes[65], etc.

The electronic structure of MOs differs from that of silicon. In silicon, the conduction and valence band depend on the hybridized sp^3 σ-bonding and sp^3 σ^*-anti-bonding states, respectively, while CB and VB for MOs are related to the un-occupied *ns* metal bonding states and the occupied *2p* oxygen anti-bonding states, respectively. Its CBM is extended spatially and is spherically symmetric, resulting in small electron effective masses.[62] Smaller electron effect mass would bring higher degree of CBM and VBM hybridization and higher electron mobilities. Therefore, electron conduction in MOs is highly efficient even in amorphous states, which greatly reduce the relying on single crystalline material.[60] However, such electronic structure causes a limited hole conduction due to its localized O *2p* orbitals and the deep VBM.[66] There are relatively less MOs that show p-type conduction.[67] MOs such as ZnO, TiO_2, and NiO, are widely used for carrier injection or transport layers in light emitting diodes[68] and solar cells[69].

High quality metal oxide thin films can be fabricated by sputtering, thermal evaporation, and chemical vapor deposition techniques.[70] Thin film transistors with a field mobility up to ~80 $cm^2\ V^{-1}\ s^{-1}$ could be realized with sputtered IGZO.[71] However, these methods are high-cost and not efficient to coat large area substrates. In contrast, solution-based fabrication methods such as sol-gel, spray pyrolysis, chemical bath deposition, and printing based methods, are more cost-friendly and are compatible with large-area substrates.[68] Ink-jet printed IGZO thin film transistors exhibited a mobility of 10.5 $cm^2\ V^{-1}\ s^{-1}$ [72], which is only a few times lower than that from the sputtered ones. However, these methods also have major limitations for its high processing temperature and its incompatibility with other sensitive active materials. Typically, the precursor solution is coated on the desired substrate and metal oxide films are formed under thermal annealing. To form crystalline film, the annealing temperature is generally around hundreds of degree Celsius. The high annealing temperature would degrade the active

materials and limit the choice of substrates.

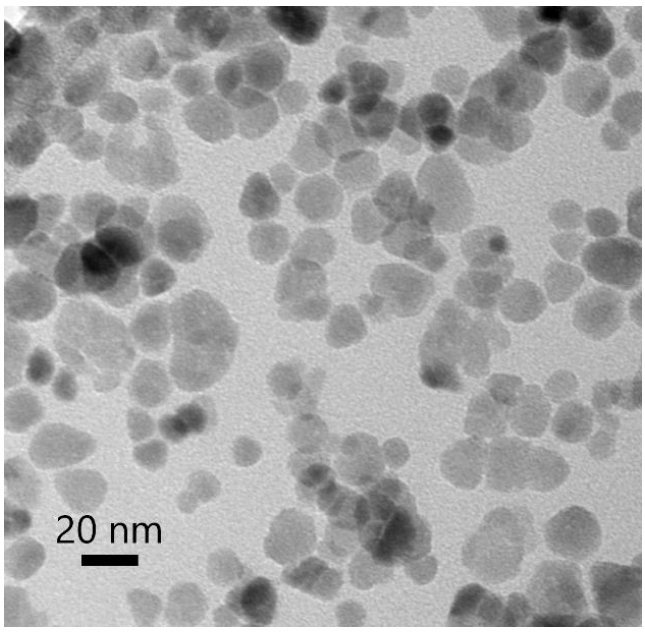

Figure 2.6 Metal oxide nanoparticles. A transmission electron microscopy image of commercially available zinc oxide nanoparticles.

The above problems could be mitigated by using nanoparticles. The metal oxide nanoparticles can be synthesized by various methods, such as sol-gel, hydrolysis, and hydrothermal, etc.[68] The resulting nanoparticles can be dispersed in liquids with suitable ligands, which can be easily coated onto various substrates. A transmission electron microscopy image of the commercially available ZnO nanoparticles is shown in **Figure 2.6**. These nanoparticles are relatively uniform in the size and have sphere-like shapes. The nanoparticle-based method enables the crystallization and film formation to be independent, so that high temperature annealing process can be avoided. Nanoparticles could be integrated with other active materials at low temperature, and new types of device structures could be therefore realized. Secondly, the conventional precursor-based film formation may produce by-products that alter the electronic properties of oxides[73], while this issue can be avoided in nanoparticle-based methods if purification steps are introduced during the nanoparticle synthesis. Thirdly, the electronic properties of

nanoparticles can be altered by their size, shape, composition, and surface ligands, providing great versatility towards various applications beyond electronics.[64, 74-76] Compared with organic semiconductors or semiconducting nanoparticles such as CdS quantum dots, MOs nanoparticles are more stable in ambient and can be processed without relying on the inert environment. Due to their superb electronic properties and good air stabilities, the MOs nanoparticles will be used in Chapter 7-9 to fabricate heterojunctions with TMDs nanosheet networks in ambient to explore their functionalities in manipulating the carrier transport behaviors across the nanosheet network interfaces.

2.2.2 Carbon nanotubes

Carbon nanotubes (CNTs) are one of the most well-known one-dimensional materials, discovered by Iijima et al. in 1991.[77] They display diameters of a few nanometers, with lengths in the range of a few microns. CNTs show hollow cylindrical structures with layers of hexagonally arranged carbon atoms with sp^2 hybridizations. It was later confirmed by NEC and IBM corporations they are comprised of one or several layers of graphene rolled up.[78, 79] If only one layer of graphene is used to form such structure, it is called single-walled carbon nanotubes (SWNTs, **Figure 2.7A**) with a diameter around 1-2 nm, and will be called multi-walled carbon nanotubes (MWNTs, **Figure 2.7B**) if there are more than one layer of graphene forming such cylindrical structures. For MWNTs, they can form two types of structures with one called Russian doll, that graphene sheets are arranged in concentric cylinders, and the other one called Parchment mode that one single graphene sheet wraps around itself many times to form a cylinder.

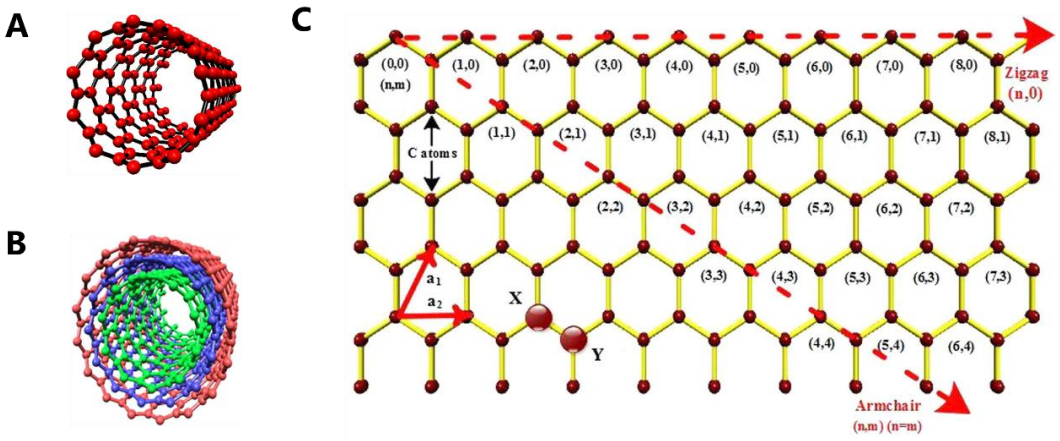

Figure 2.7 Carbon nanotubes. Schematic illustrations of structures of SWNTs (A) and MWNTs (B). (C) A graphene sheet to demonstrate the chirality (n, m) of CNTs. Adapted from Ref. 80.

Unlike graphene which is a semi-metal, CNTs exhibit rich electronic properties depending on their chirality. CNTs are nothing more than rolled-up graphene sheets, and graphene is formed with two basis vectors $\boldsymbol{a_1}$ and $\boldsymbol{a_2}$, as shown in **Figure 2.7C**, where $\boldsymbol{a_1}=\boldsymbol{a}(\sqrt{3}, 0)$ and $\boldsymbol{a_2}=\boldsymbol{a}(\sqrt{3/2}, 3/2)$, that $\boldsymbol{a}$ is the bonding length of C-C bonds. The chiral vector of CNTs is represented by $\boldsymbol{C}=n\boldsymbol{a_1}+m\boldsymbol{a_2}$, where n and m are two integers. If the graphene is rolled in the case that m=0, so that the structure is zigzag, and it would be armchair if n=m. The electronic properties of CNTs would change with (n, m) indices, they exhibit metallic properties if (n-m)/3 is an integer and will be semiconducting otherwise.[81, 82] This indicates that all CNTs with armchair structures are metallic and the others are semiconducting. The difference in electronic properties originates from how the one-dimensional band of CNTs are cut from a two-dimensional band structure of graphene. Depending on their chirality and the number of cutting lines, the cutting line can either cross the K-point in the two-dimensional first Brillouin zone of graphene or not. CNTs are metallic if it is the former case and semiconducting for the latter one.[83] The bandgap for semiconducting CNTs inversely depends on their diameter. The bandgap arises from the distance between π and π^* bands at the

same *K* point. The separation of one-dimensional bands is inversely proportional to the diameter, so that larger diameter CNTs make the allowed state be closer to the *K*-point and therefore induces a smaller gap between bands.[84]

CNTs exhibit various exotic properties due to their unique structures. Metallic CNTs exhibit high electrical conductivity up to 10^7 S m^{-1} [85] and semiconducting species show high field-effect mobility (79000 cm^2 V^{-1} S^{-1}) with a theoretically estimated intrinsic mobility up to 10^6 cm^2 V^{-1} S^{-1}[86], that both types are promising materials towards electronics. Especially, sub-1 nm channel transistors could be realized with a single nanotube[87], which could provide a solution to overcome the short-channel effect. Moreover, CNTs show superior mechanical properties and are regarded as the strongest materials so far given its tensile strength of 11-63 GPa and an elastic modulus of 270-950 GPa.[88] Meanwhile, CNTs and their networks remain flexible due to their large aspect ratios. Large quantity and high quality CNTs could be synthesised by electric arc discharge, laser ablation, and chemical vapor deposition, etc.[80, 89] Therefore, metallic CNTs have been used as a novel conductive additive for various applications providing its mechanical and electrical advantages, such as transparent flexible electrodes[90], energy storage[91], EMI shielding[92], etc.

Commercial CNTs can be easily obtained nowadays, and they can be processed in suitable liquids to be de-bundled and yield nanotube dispersions. Such dispersions can be used to deposit electrically conductive thin films onto other materials or substrates, serving as electrodes and forming mixed-dimensional junctions. For the current study, SWNTs with metallic properties are chosen and are used to fabricate solution-processable electrodes that will be integrated on top of the semiconducting nanosheet networks. The details will be further discussed in Chapter 6.

2.2.3 Silver nanowires

Silver nanowires (AgNWs) are a class of attractive materials with large aspect ratios due to one-dimensional morphology and high electrical conductivity inherited from silver. AgNWs can be synthesized by hydrothermal method, microwave-assisted process, electrochemical technique, and wet chemical method.[93] To obtain such large aspect ratio nanowire, the synthesis of AgNWs by the wet chemical method usually has three steps: nucleation, evolution of nuclei into seeds and growth of seeds into nanocrystals. The growth of nanowire replies on several parameters, such as temperature, reaction time, injection rate, and so on. As an example, one important parameter is the molar ratio of $AgNO_3$ and polyvinylpyrrolidone (PVP), where the former provides the source of silver atoms and the latter can passivate specific crystal facets allowing nanocrystals only growing on both ends. AgNWs with 300 μm long and less than 150 nm diameter could be obtained with careful adjusting of the synthesis parameters.[94] The aspect ratio of AgNWs has a significant influence on their electrical properties. AgNWs networks consist of long and small diameter nanowires usually possess higher electrical conductivity than that from the ones with shorter and larger diameter nanowires, as less nanowires are required to form a continuous network and the number of junctions between adjacent nanowires are much reduced.[95]

One of the important applications of AgNWs is transparent conductive electrodes (TCEs). Early investigation on TCEs mainly focused on conductive metal oxides fabricated by high-temperature and vacuum processes. The well-known one is indium tin oxide (ITO) glass, which has been widely used in industrial and academic fields. However, due to the scarcity of indium on earth and its increasing cost, alternative materials with a high electrical conductivity and an optical transmission are pursued, and new functions such as flexibility, low cost, and facile fabrication are also desired to meet requirements for next generation

electronics.[96] Under this background, several new materials were investigated, e.g., graphene, carbon nanotubes, metal nanowires, and conductive polymers, etc. These materials could be easily processed in solutions with reduced fabrication cost and form interconnected and percolated conductive networks. A scanning electron microscopy image of AgNWs networks is shown in **Figure 2.8A.**

One of the key Figure of Merits to evaluate TCE is the ratio of the optical transmittance at 550 nm to the sheet resistance of the network. The network transparency can be obtained with a relatively thinner film while the sheet resistance will increase due to less available conductive paths in a thinner network. Therefore, the trade-off between these two main parameters must be considered. The opto-electronic properties of some representative metallic nanomaterial networks are shown in **Figure 2.8B**. Metal nanowires-based networks show superior performance than the others given their low sheet resistances and high transmittances, and AgNWs perform the best among them. For such networks formed by nanomaterials with considerable amounts of junctions, the conductivity is usually limited by intra-junction resistances between adjacent nanomaterials, such as in the case of graphene and CNTs, even though some post-treatments (high temperature annealing and acid-treatment, etc) could lower the junction resistance.[97] For AgNWs networks, these junctions could be fused together by thermal annealing so that these networks are no longer limited by the junction resistance, therefore high conductivity could be achieved at high transmittances.[98]

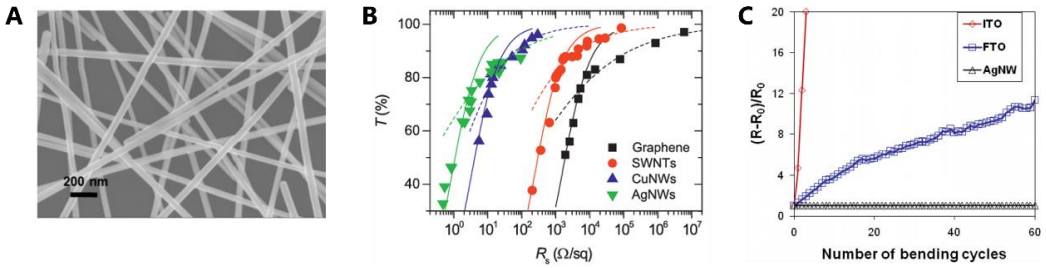

Figure 2.8 Silver nanowires. (A) A scanning electron microscopy image of the silver nanowire network. Adapted from Ref. 93, (B) Transmittance measured at 550 nm as a function of sheet resistance of graphene, SWNTs, CuNWs, and AgNWs networks. Adapted from Ref. 99, and (C) The resistance change of ITO, FTO, and AgNWs upon mechanical bending. Adapted from Ref. 93.

Another key feature of AgNWs is their superior mechanical properties. Traditional TCEs such as ITO and FTO are extremely brittle and cannot be bent or stretched. Their resistance increases significantly after only a few bending cycles, as shown in **Figure 2.8C**. In contrast, the resistance of AgNWs networks barely changes upon bending, showing a high degree of flexibility.[100] AgNWs are not just useful on their sole networks but can also be used as conductive additive with other functional organics, polymers, and nanomaterials, which can be applied into solar cells, light emitting diodes, touch panels, flexible transparent circuit, etc. [101]

In Chapter 6, 1D high-aspect ratio SWNTs and AgNWs with metallic properties will be used to form conducting networks by solution-processing techniques and it will be shown that such networks are advantageous to reliably construct vertical heterostructures based on semiconducting nanosheet networks to avoid electrical shorts issues.

Scientists have become the bearers of the torch of discovery in our quest for knowledge.

Stephen Hawking

Chapter 3 Two-Dimensional Material Synthesis

The isolation of monolayer graphene was achieved by using mechanical exfoliation of graphite crystal repeatedly using the Scotch tape.[6] This method utilizes the fact that adjacent layers of covalently bound atoms in naturally layered crystals are held by comparatively weak vdW forces, which allows to delaminate individual layers. Micromechanical exfoliation provides a facile way to study nanosheets from all kinds of 2D materials (2DMs), at high quality, while pristine 2D flakes are achieved. However, while micromechanical exfoliation provides high quality nanomaterials, the method is overall tedious and time consuming, which leads to the development of additional methods for the exfoliation of layered crystals. These can be classified into two types: bottom-up and top-down methods. As indicated by the naming, bottom-up approaches focus on growing nanostructures from smaller precursors, such as gas-phase reactions of elements and small molecules. In contrast, top-down methods focus on exfoliation of nanomaterials from a layered bulk crystal (see **Figure 3.1**). In further detail, bottom-up methods require precursor molecules with the target chemical composition forming 2DMs under controlled growth conditions. Typical examples are chemical vapor deposition[102], molecular beam epitaxy[103], and wet chemical methods[104], to name a few. The obtained 2D flakes or thin films facilitating bottom-up methods are often of low-yield and are challenging for large-scale applications. Due to harsh experimental conditions (high temperature or pressure), the fabrication cost is relatively high. Moreover, these methods show significant

challenges for integrating the fabricated 2DMs in combination with other materials or substrates due to restrictions on compatible substrates.

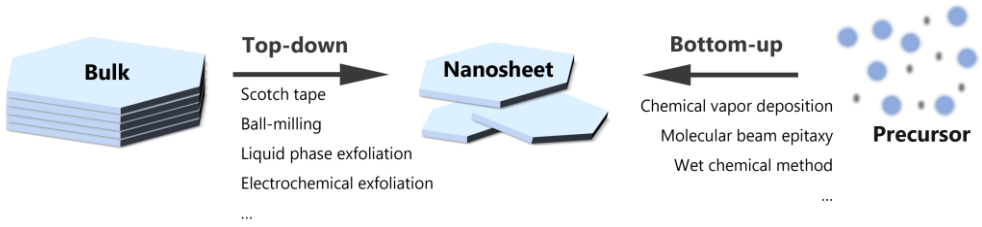

Figure 3.1 Synthesis of 2D nanomaterials. A schematic illustration of top-down and bottom-up methods.

While bottom-up approaches require harsh conditions for the targeted growth of thin layers of 2D crystals, Top-down methods require extenal stimulii to overcome the vdW forces between adjacent layers of crystals to achieve the exfoliation into 2D nanosheets. Other than the micromechanical exfoliation method which was already mentioned above, many other techniques have been reported in the past few years, including ball-milling[105], liquid phase exfoliation (LPE)[106], and electrochemical exfoliation (EE)[107]. Some of these methods are suitable for large-scale production of nanosheets using commercially available and cheap powders. These nanosheets can be dispersed into appropriate solvents or surfactant solutions to form nanosheet dispersions. Moreover, such dispersions after proper modifications are compatible with solution-processing techniques to form active films on arbirary substrates.

3.1 Solution-based exfoliation methods

In this section, exfoliation methods in liquid mediums, such as LPE and EE will be introduced. The focus will be on their general working principle, advantages and disadvantages. However, for preparation of nanomaterial dispersions, a general protocol has to be followed, which includes finding suitable conditions for the material exfoliation, the colloidal stabilisation of the nanomaterial dispersion, and the facilitation of size-selection protocols to remove unexfoliated materials

from the nanosheets. However, this section will mainly focus on the first step, the material exfoliation.

3.1.1 Liquid phase exfoliation

Liquid phase exfoliation refers to the exfoliation of bulk crystals of naturally layered materials into nanosheets in suitable liquids through either ultrasonication[108] or high-shear mixing[109]. The first successful demonstration was done by Hernandez et al. in 2008, where the exfoliation of mono- and few-layered graphene was demonstrated in different solvents.[106] LPE requires the mixing of a bulk powder with solvents or surfactant solution, which is subjected to either of the two above mentioned methods to overcome the vdW forces between layers to yield colloidally stable nanosheets.

Ultrasonication is widely used in the field of nanoscience to form homogeneous dispersions of nanoparticles or for general surface cleaning purposes.[110, 111] For example, ultrasonication has been employed to de-bundle aggregates of CNTs in liquids, yielding stable CNT dispersions.[112] When ultrasonication is applied to the immersed powder, high frequency and high-power ultrasonic waves propagate through the liquid medium. In turn, high-pressure and low-pressure cycles are generated, which form small vacuum voids (cavitation). These will continue to grow by constantly absorbing energy, and will eventually implode, releasing local high energy. The size and released energy of bubbles depend inversely on the ultrasonic frequency, and higher frequency will result in a greater number of bubbles imploding.[113] The energy released upon collapse of cavitation bubbles is high enough to overcome the vdW forces, and thus to exfoliate fractions of the initial crystallites, eventually yielding in nanosheets.[114] A typical workflow facilitating probe sonication for liquid phase exfoliation is illustrated in **Figure 3.2A**. Alternatively, high-shear mixing can be used to scale up the production as

long as the applied shear rate is above ~10^4 s^{-1}.[109, 115]

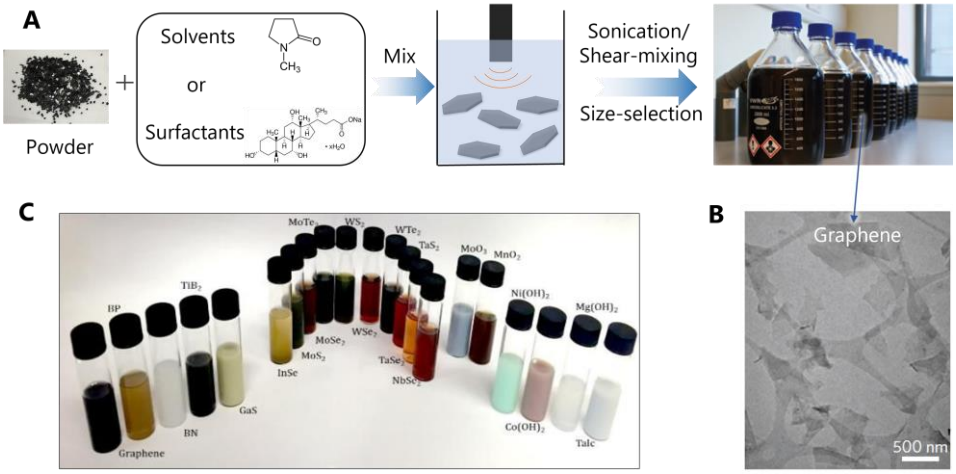

Figure 3.2 Liquid phase exfoliation. (A) An illustration of liquid phase exfoliation procedures. (B) Transmission electron microscopy image of liquid-exfoliated graphene. Adapted from Ref. 109. (C) A photograph of glass vials containing various types of liquid-exfoliated nanosheets (unpublished results and used with permission).

Notably, liquid exfoliation protocols can be performed in an ambient environment[116], and can readily be made compatible with inert exfoliation protocols to prevent sensitive nanosheets from oxidation.[117, 118] Inert exfoliation can be realized by constant exchange of the atmosphere inside the exfoliation vessel with an inert gas (i.e., nitrogen or argon). The inert exfoliation is employed in Chapter 7 & 8. Depending on the exfoliation and processing parameters, large quantities of nanosheets can be obtained (shown in **Figure 3.2A**) and the yield of mono- and few-layered graphene is up to around 1 wt% during early-stage investigations.[109] A transmission electron microscopy image of a representative exfoliated graphene sample is shown in **Figure 3.2B**. Unexfoliated material can be collected and recycled for a subsequent exfoliation so that material waste is minimized.[119] Hence, LPE can be considered as an efficient process and its production rate can be as high as 5.3 g h^{-1} using high-shear mixer.[109]

Due to the simplicity and versatile use of LPE as demonstrated by the fabrication of nanomaterials from various van der Waals materials and beyond, it is widely

employed in research laboratories to obtain nanomaterial dispersions. [108, 115, 120, 121] A photograph of dispersions containing different nanomaterials after their exfoliation and size-selection is shown in **Figure 3.2C**. Dispersions with semi-metallic graphene, semiconducting TMDs, metal hydroxides, insulating transition metal oxides, *h*-BN, and superconducting TiB_2 can be obtained. Due to differences in their electronic structure, different materials display distinct appearances. The resulting nanosheets exhibit pristine material properties with few defects.[106, 122]

However, even though LPE is such a facile method, it possesses some drawbacks. The resulting nanosheet dispersion after exfoliation typically consists of a broad distribution of different sizes and thicknesses.[123] This broad size and thickness distribution is based on the exfoliation mechanism facilitating forces based on collapsing cavitation bubbles, which do not only exfoliate nanosheets from the bulk material, but also tear delaminated sheets into smaller fragments. It was found that the energy equipartition holds between nanosheet tearing and exfoliating.[124] The morphology of resultant nanosheets will only depend on materials' own mechanical properties, particularly on the in-plane to out-of-plane binding energy. As a result, the statistical length and thickness aspect ratio of nanosheets exfoliated from LPE are coupled. While the fundamental aspects are partially understood, enriching dispersions with mono- and few-layered nanosheets of large lateral dimensions facilitating sonication, or sheer exfoliation still remains as a challenge.

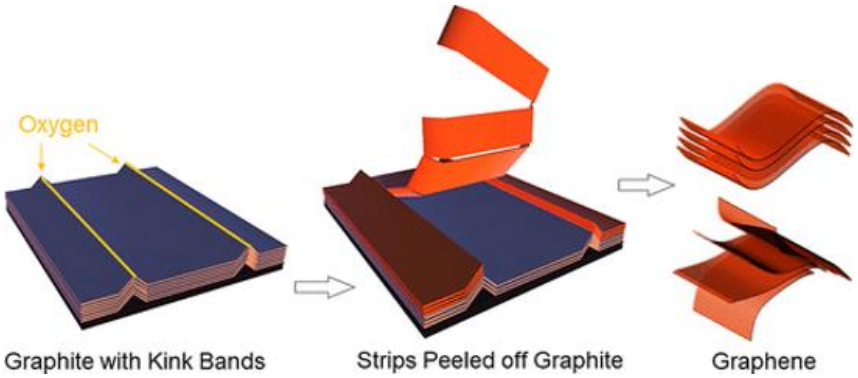

Figure 3.3 Liquid phase exfoliation mechanism. An illustration of fragmentation and exfoliation processes of graphite during LPE. Adapted from Ref. 114.

The mechanism associated with the processes occurring during LPE have long been hypothesized but the experimental evidence has only recently been reported employing a single graphite crystal for LPE in an isopropanol (IPA)/H_2O mixture.[114] The experiment suggests that the exfoliation includes three steps: kink band formation, peeling of graphite strips, and delamination of peeled off fragments. All three steps are illustrated in **Figure 3.3**. First, ultrasonic waves travel through the liquid medium to the liquid/solid interface, where they are converted into surface acoustic waves, which show an exponential decay of their amplitude with the penetration depth. Hence, only waves propagating along the surface contribute to the material fragmentation and exfoliation, which induce an elliptical vibration of the atoms on the material surface. Consequently, large flakes rupture and kink band striations form along already existing defects on the crystal surface. Further, intercalation of solvent molecules and chemical reactions with surface defects induced by the localized cavitation energy occurs along with the aforementioned kink band formation, which eventually leads to strips of graphite peeling off the larger crystallite. Note that at this stage of the process, almost no material is exfoliated into nanomaterial as the material delamination predominantly occurs on thinner fragments of the graphite crystal. However, with an increasing population of peeled off graphite strips, more material starts to be

exfoliated into nanosheets. This is because the kink band formation and stripe peeling are not favored over the exfoliation when the layer number of the graphite fragments is lower than 30. This implies that prolonged sonication would lead to a larger yield of smaller and thinner nanosheets based on the materials' intrinsic properties, as suggested by Backes et al.[124] Hence, due to competing events of layer scission and delamination, nanosheets of a material-characteristic length/thickness aspect ratio will be produced using predominantly mechanical exfoliation techniques. However, it is possible to overcome this limitation if the interlayer attraction can be decreased.

3.1.2 Electrochemical exfoliation

While 2DMs typically exhibit a strong covalent in-plane bonding along the 2D lattice within each layer, and comparatively weak out-of-plane vdW interactions between adjacent layers, it may be possible to insert ions or molecules in between layer spaces. Consequently, the vdW interactions would further be weakened. Such insertion process is usually referred as intercalation. To this end, different additives and solvents can be tested for an intercalation in between individual layers of the starting material, followed by a gentle exfoliation process, such as mild sonication, shaking or stirring. Following this protocol ideally yields exfoliated nanosheets of an increased length/thickness aspect ratio. The method dates back to 1960s: several kinds of ions were intercalated into vermiculite clay, TaS_2, and NbS_2. [125-127] In 1986, monolayer MoS_2 was successfully exfoliated using intercalation of *n*-Butyllithium providing Li^+ into vdW gaps.[46]

A different approach facilitating a decrease of the vdW interactions is to intercalate ions by applying a potential difference between the 2DM and a counter electrode. Around the same time as LPE was reported to produce graphene in dispersion in 2008, intercalation-based methods demonstrated their capability to

exfoliate graphite into nanosheets.[128] Consequently, electrochemical exfoliation received a growing attention in the field. Unlike nanosheets produced by LPE, where the nanomaterial size and thickness are coupled, intercalation-based exfoliation methods can realize atomically thin nanosheets with sizes ranging from a few to hundreds of microns.[129, 130] Further, novel properties may arise from intercalated crystals.[131] For example, superconductivity was observed in intercalated graphite, which is not the case for pristine graphite.[132] Bulk-like multilayered TMDs with intercalated molecules can exhibit monolayer characteristics due to greatly reduced vdW interactions.[133]

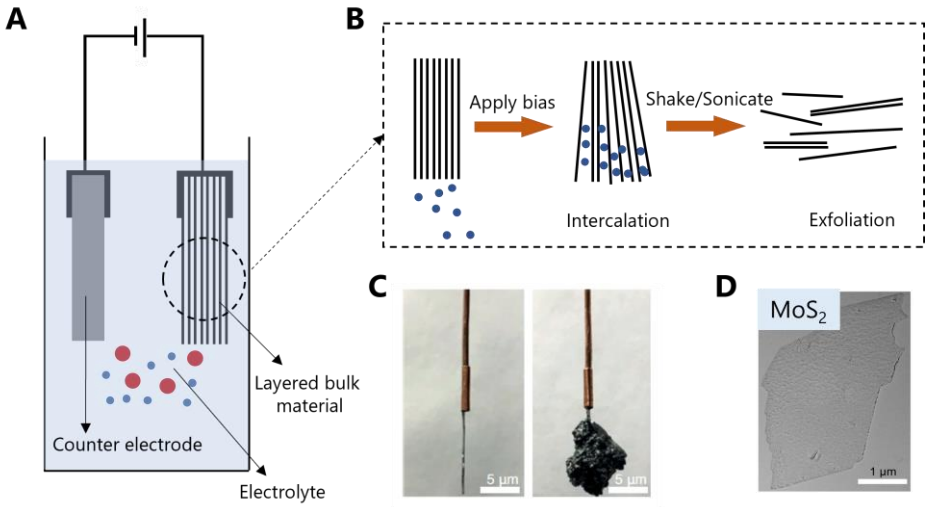

Figure 3.4 Electrochemical exfoliation. (A) An illustration of a typical setup of electrochemical exfoliation. (B) Illustration of the intercalation and subsequent exfoliation process. (C) The photo taken on the crystal before (left) and after intercalation (right). Adapted from Ref. 134. (D) A TEM image of electrochemically exfoliated MoS_2 from powder. Adapted from Ref. 135.

Early attempts mostly adopted Li^+ based chemicals as the intercalant, such as *n*-butyllithium[136], lithium borohydride[137], and naphthalenide lithium[138], owing to its small ionic radius. 2D crystals can be simply stirred in Li^+ containing solutions in an inert environment for days to allow a spontaneous ion intercalation. After the full intercalation, the compound will be immersed into water to let Li^+ ions

undergo hydration reaction that the produced hydrogen gas will expand the layers to realize exfoliation. Despite its difficulty in handling chemicals in glovebox and the safety concern over the chemical and the preparation process, this method usually results in a phase transition and a change of the material's electronic properties. Further, for some 2DMs, including TMDs, the nanomaterial undergoes a phase transition into a different polymorph (e.g., 2H to 1T/1T' for MoS_2, $MoSe_2$, WS_2 and WSe_2).[139] This is because Li^+ provides extra electrons to the *d*-orbitals of metal atoms. Once this electron doping exceeds a certain threshold, it causes the aforementioned phase change [130, 140], which limits its application potential as the phase-change leads to significant changes of the material's electronic structure. So far, several intercalation-based exfoliation methods have been developed, represented *i.a.*, by wet chemical intercalation, electrochemical exfoliation, and ion-exchange intercalation. Further, different types of intercalants have successfully been employed, based on alkali metal-ions, tetraalkylammonium-ions, small molecules, etc. Production of nanosheets have been obtained from various intercalated layered crystals ranging from metals to insulators, which include graphite, TMDs, *h*-BN, and black phosphorus, etc.[129-131, 141]

Electrochemical exfoliation is a popular intercalation-based exfoliation method.[107, 135, 142] The intercalants for this method are usually charged ions or molecules and an external bias is required to provide the driving force for the intercalants into vdW gaps. A schematic illustration of an experimental setup is shown in **Figure 3.4A.** 2D crystals and a counter electrode are both connected to the external power supply and are immersed into the electrolyte solution. The exfoliation process is schematically illustrated in **Figure 3.4B**. After applying direct current potential, the intercalants will go in between the vdW gap between the layers of the crystal and cause a significant expansion of the crystal due to an increase of the interlayer spacing (**Figure 3.4C**). Similar to the other intercalation

methods, gentle shaking or mild sonication would exfoliate the crystal into nanosheets. A representative TEM image of the ultra-thin and large-sized MoS_2 nanosheet as obtained by EE is shown in **Figure 3.4D**. As the driving force for the intercalation is provided by an external voltage, the choice of the intercalant can be greatly expanded. New functionalities can be introduced for the material if the introduced molecules provide novel properties.[129] Moreover, precise control and monitor of the exfoliation stages can be realized by varying the exfoliation parameters, such as the applied voltage, size of the intercalant (*i.e.*, the side groups, the choice of the solvent, and swelling time, etc.).[143] However, electrochemical exfoliation is limited to metals and semiconductors, as the process requires a reasonable material conductivity.[130] Moreover, EE currently relies on using comparatively expensive crystals as the starting material. It was only recently demonstrated that semiconducting TMDs nanosheets can be obtained by EE using compressed and sintered powder pellets.[135] While this may realize low-cost EE, further optimization of the process is required as the obtained nanosheets by EE tend to exhibit basal-plane defects, which are usually absent in LPE nanosheets. Further, intercalants may bring inevitable doping effects that alters materials' electronic properties. While the latter may present a mean to tailor the material's electronic structure, (e.g., it's emission properties), it is problematic in case pristine properties are required.

There are several important factors regarding the exfoliation quality and efficiency. The properties of the starting crystal will affect the lateral size of the nanosheets. For example, the size of MoS_2 nanosheets is usually ~1 μm if the starting crystal has the 2H phase while it will be tens of micrometers in the case of 1T' crystals.[144] The composition of the crystal has a similar effect: small sized nanosheets are usually found in crystals that have larger lattice difference compared with the exfoliated ones, at least in the case when Li^+ is intercalated.[145]

The intercalant and the solvents are also indubitably important factors. For example, when using Li^+ as intercalant, a transition change from 2H into 1T occurs for some TMDs materials,[146] while 2H TMDs can be obtained using R_4N^+ based intercalants for the same examples (MoS_2/WS_2/$MoSe_2$/WSe_2),[134] where the representative cations are tetramethylammonium[147], tetraethylammonium[148], and tetrapropylammonium[149]. The solvent will affect the behavior of intercalants mainly arising from its polarity, surface energy, and Brønsted–Lowry acidity.[130] Exfoliation of black phosphorous using alkylammonium cations can only be observed in polar solvents due to the effects of dissolution and solvation process of the intercalants.[150] The magnitude and time of the applied voltage will determine the magnitude and efficiency of the intercalation process.[143, 151] Careful control over a certain voltage range and magnitude could improve the yield of the monolayers.[143] At last, exfoliation methods, such as shaking or sonication of the fully intercalated samples, could yield nanosheets with different morphologies,[145] as sonication may lead to the fragmentation of the nanosheets and decrease their average size.

3.2 Stabilisation

The exfoliated nanosheets can easily aggregate if the interactions between the solvent, or additives to the solution are not suitable. Therefore, appropriate liquids are required to form colloidally stable dispersions. To this end, two strategies have shown successful nanomaterial stabilisation in liquid mediums: 1) using solvents and solvent blends which have matching solubility parameters with the solute, and 2) using (typically aqueous) surfactant solutions for the nanomaterial stabilisation.

3.2.1 Solvent stabilisation

Solvent stabilisation is a facile method to obtain stable nanosheet dispersions using suitable solvents or solvent blends. The stabilisation process can be

understood by the solubility theory.[106] The energy required for mixing nanosheets and solvents, or so-called Gibb's free energy ΔG_{mix} of mixing which describes molecular interactions, is given by

$$\Delta G_{mix} = \Delta H_{mix} - T\Delta S_{mix} \tag{3.1}$$

where ΔH_{mix} is the enthalpy of mixing, T is temperature, and ΔS_{mix} is the entropy of mixing. ΔG_{mix} should be negative to guarantee a spontaneous mixing process. The entropy to mix nanosheets is almost negligible due to that nanosheets are considerably larger and more rigid than molecules.[152] Therefore, it is the enthalpy of mixing that dominates the stabilization process. The term ΔH_{mix} is closely related to the surface energy of nanosheets and solvents. An approximation was made regarding dispersing graphene, which can be expressed by the following relation:[106]

$$\frac{\Delta H_{mix}}{V} \approx \frac{2}{t_{NS}}(\delta_{Gra} - \delta_{Sol})^2 \phi_{Gra} \tag{3.2}$$

Here, V is the volume, t_{NS} is the thickness of nanosheets, δ_{Gra} and δ_{Sol} are the surface tension of graphene and the solvent, respectively, which are the square root of their corresponding surface energy, and ϕ_{Gra} represents the volume fraction of graphene in the solvent. Based on this relation, solvents with a surface tension close to that of graphene will greatly minimize the enthalpy energy of mixing, which is favorable for the colloidal stabilization. As shown in **Figure 3.5**, the concentration of graphene in different solvents (after centrifugation to remove unexfoliated material) roughly follows a bell-shape curve with a peak around 40 mJ m^{-2} if they are plotted as a function of the solvent's surface tension.[106]

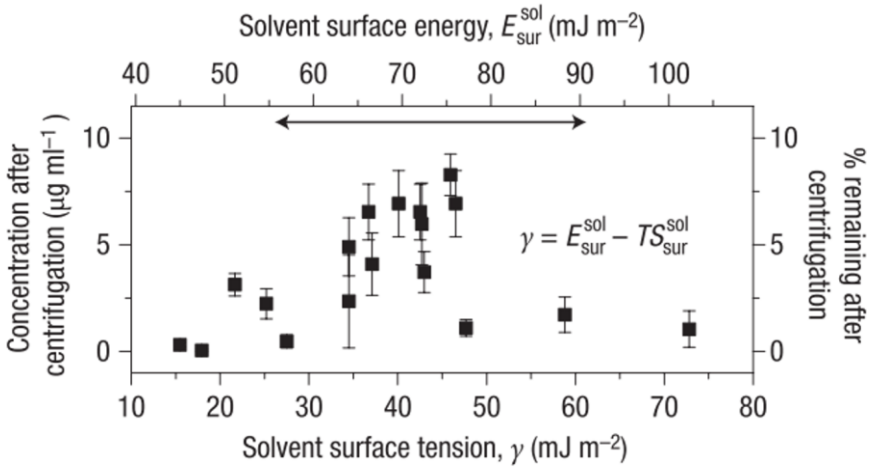

Figure 3.5 Solvent stabilization. The concentration of graphene after centrifugation in various solvents versus their surface tensions. Adapted from Ref. 106.

However, using the surface tension does not fully describe the solubility of nanosheets in solvents. The mixing process can be further understood if the enthalpy of mixing term is divided into terms describing the solvent-solvent, solute-solvent, and solute-solute interactions, individually. The well-known Hildebrand solubility parameter δ_T can be utilized.[153] Therefore, the enthalpy of mixing can be expressed as[108]

$$\frac{\Delta H_{mix}}{V} \approx (\delta_{T,NS} - \delta_{T,Sol})^2 \phi_{NS} (1 - \phi_{NS}) \tag{3.3}$$

where subscript NS denotes nanosheets. This indicates that a stable dispersion is formed if the solubility parameters of solvents and nanosheets match. The Hildebrand solubility parameter of the material is the square root of its cohesive energy density $\delta_T = \sqrt{E_{C,T} / V}$. To understand the nanosheet-solvent interactions, several factors need to be considered, such as dispersion, polar and H-bonding parameters.[153]

$$\delta_T^2 = \delta_D^2 + \delta_P^2 + \delta_H^2 \tag{3.4}$$

where the subscripts *D*, *P* and *H* correspond to dispersive, polar and H-bonding. Therefore, the enthalpy of mixing can be written as[108]

$$\frac{\Delta H_{mix}}{V} = \phi_{NS}(1-\phi_{NS})\sum_{i}(\delta_{i,NS} - \delta_{i,Sol})^2 \quad (3.5)$$

where *i* represents *D*, *P* and *H* as denoted above. This means that the energy cost for mixing can be minimized if all three parameters are minimized simultaneously. According to the above-described theoretical frame, a series of experiments has been performed on nanosheets from different materials, as well as solvents.[108] Well-defined peaks can be found if the concentration of the nanosheets is plotted against the solubility parameters of solvents and it was found for hBN and TMDs materials that the influence of polar and H-bonding is more significant than the effect of dispersive in practice.[108]

As a result, some solvents have been identified to generally disperse nanosheets reasonably well, such as N-Methyl-2-pyrrolidone (NMP), cyclohexyl-pyrrolidinone (CHP), N-vinyl-Pyrrolidinone (NVP), etc.[106, 108, 120] However, the aforementioned solvents are toxic and are difficult to be removed from the nanomaterial after exfoliation. Further, polymerization can occur for pyrrolidone-based solvents during high power probe-sonication, or upon light exposure.[154] Therefore, an alternative, non-toxic, and environment friendly solvent blends was identified, such as water and isopropanol.[155] By mixing, the solvent blend's Hildebrand parameters can be tuned to match with the nanomaterial.

3.2.2 Surfactant stabilisation

Aqueous surfactant solutions have shown to be effective to stabilise nanosheets in dispersions.[122, 123, 156] Unlike the solvent stabilisation, where a limited number of options are available to stabilise the required nanosheets, various surfactants can be used, and are suitable to be universally applied to nanomaterials, due to the

possibility of chemically tailoring the surfactant's properties to the surface characteristics of the nanomaterial.

Surfactants can be classified as anionic, cationic, zwitterionic, and non-ionic. Ionic surfactants, typically containing hydrophobic groups on one side and hydrophilic groups on the other side. This allows the hydrophobic groups to non-covalently interact, i.e., physiosorbed on the nanosheet's surface leaving the hydrophilic groups towards outside (**Figure 3.6**). The nature of these interactions can be described through London interactions. However, the hydrophilic groups pointing away from the nanomaterial enables a stable solvation shell to form around the nanosheets in water. Such a layer of surfactant molecules around the nanosheet surface forms an electrical double layer (EDL). The electrostatic repulsion force between each EDL surrounded nanosheet as well as the steric hindrance effect that will be introduced below will together prevent the nanomaterial from aggregation. This phenomenon can be explained by the so-called DLVO theory, proposed by Derjaguin, Landau, Verwey and Overbeek.[157, 158] In more details, it describes the potential energy U of two spherical particles interacting in liquid media, which is the sum of the electrostatic repulsion energy, and vdW attractive energy. The theory can further be adjusted given that nanosheets exhibit a plate-like morphology. The potential energy U per nanosheet area between nanosheets can be approximated by the following relation,[159, 160]

$$\frac{U}{A_{NS}} \approx 4\varepsilon_0\varepsilon_r r_p \kappa\zeta^2 e^{-\kappa D} - \frac{\pi\rho_{NS}^2 C}{2D^4} \tag{3.6}$$

where A_{NS} is the nanosheet area, ε_0 and ε_r are dielectric constants in vacuum and in the liquid medium, respectively. r_p is the particle radius, κ is the Boltzmann constant, ζ is the zeta potential of the dispersion, κ^{-1} is the Debye screening length, D is the inter-nanosheet distance, ρ_{NS} is the number of atoms per unit area

in nanosheets, and C is a constant regarding the vdW attractive force. Here, the zeta potential will indicate the stability of the dispersion. Larger absolute values of the zeta potential means that nanosheets in the dispersion are electrostatically repelled, and a stable dispersion is formed. Further, the concentration of the surfactant matters, and stable dispersions can only be formed below a certain concentration of surfactant, known as critical micelle concentration (CMC).[161, 162] Above this concentration, the formation of micelles starts due to higher surfactant concentration, and will lead to a low dispersibility of nanosheets.

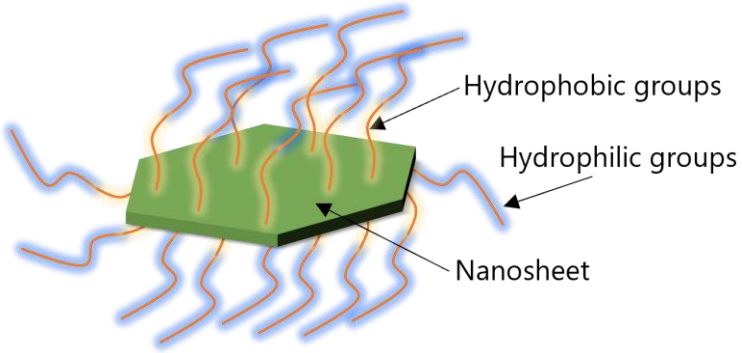

Figure 3.6 Surfactant stabilisation. A schematic illustration of a nanosheet with physically absorbed surfactant molecules.

For the non-ionic surfactants, such as polymers, the stabilization of the nanosheets is rationalized by the steric hindrance effect.[163] Once polymeric surfactants are absorbed on the nanosheet surface, the tails of the adsorbed polymers extrude towards the liquid. When two nanosheets come in a close proximity, these tails may attempt to occupy the same space, resulting in an increase of overall free energy and providing the repulsive forces between nanosheets.[31, 164, 165] Overall, surfactant stabilization may enable nanosheets to be dispersed in environment friendly and non-toxic aqueous solutions. However, to date, the chemical characteristics of polymers facilitated for nanomaterial stabilization are still to be optimized. In many cases, where the efficient stabilization of the nanomaterial in dispersion is achieved, the polymer can only be removed using harsh treatments,

which likely damage the nanomaterial.[163] Novel chemicals, such as ionic liquids[166] and proteins[167] have recently been utilized to obtain both dispersibility and additional functionalities of nanosheets.

3.3 Size selection

The top-down exfoliation of nanosheets through either LPE or EE has established a reliable way to produce nanosheets in liquids. However, the resultant dispersions typically contain a polydisperse size- and thickness distribution of nanosheets. Considering the 2DM's strong dependence on their lateral size and layer number, as produced nanosheet dispersions are not suitable to be directly used for many applications. As an example, large nanosheets are suitable for electronic applications due to the excellent carrier transport along their large basal planes, while small nanosheets are more useful for catalysis, due to the catalytic properties of nanosheet edges for water splitting applications.[123] Moreover, the liquid medium used for the nanomaterial exfoliation may not be suitable for further processing steps as residual solvent or surfactant on the nanomaterial surface may induce doping effects, which alters the electronic properties of the nanosheet network.[168, 169] Therefore, it is crucial to develop suitable size-selection, and solvent transfer protocols.

To this end, ultracentrifugation methods have widely been adjusted to fit requirements for sorting nanosheets by size and thickness. A popular approach is density gradient based ultracentrifugation (DGU), and sedimentation-based ultracentrifugation methods.[163, 170] DGU is a nanosheet thickness sensitive approach and works based on the buoyant density of nanosheets and their solvation shell.[171] However, this approach requires the use of bulky surfactants or polymers in a density gradient medium of high density to match the density of the gradient medium to the buoyant density of the nanosheets. If this is achieved, the

nanomaterial will travel through the gradient medium to the isopycnic point (i.e., where the nanosheet's buoyant density matches the density of the liquid medium in the density gradient).[172] As the buoyancy density strongly depends on the nanosheet thickness and little on their lateral size[173], DGU enables to select specific layer numbers from the distribution. However, this method can be easily affected by several parameters, such as material type, the type and concentration of surfactant[174], and pH[175], and many more, and requires careful adjustment, and experience. While the size selection of exfoliated graphite,[176] and *h*-BN[31] has been demonstrated facilitating DGU, the same strategy does not work on TMDs with higher densities, and requires careful, and tedious adjustment.[174] Further, it is challenging to remove residues of the gradient medium and surfactant, required for the method to work, from the nanomaterial surface.

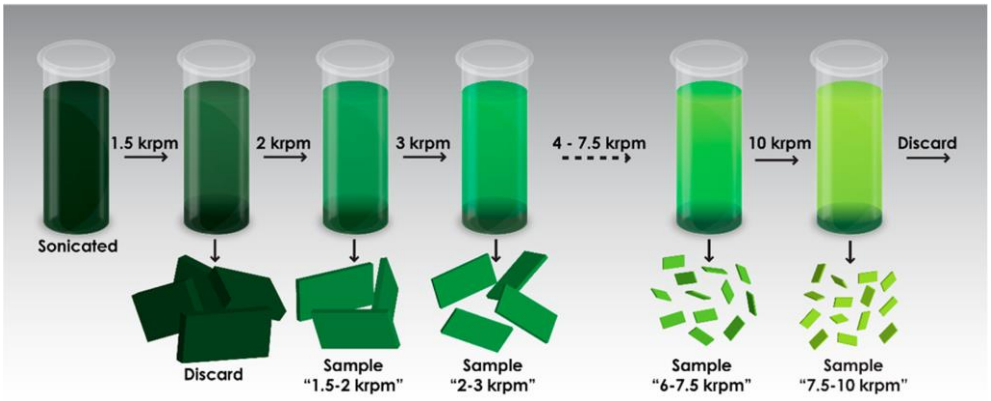

Figure 3.7 Size selection. A schematic illustration of liquid cascade centrifugation for nanomaterial size selection. Image taken from Ref. 123.

In contrast, sedimentation-based size selection is simpler, but allows less control over the size and thickness distribution compared to DGU. Employing this method allows to sort nanosheets depending on their sedimentation rate upon centrifugation, which depends on the material's buoyant density, but also on different parameters, such as the nanosheet's drag coefficient, and the viscosity, and density of the solvent.[163, 177] However, the sedimentation coefficient *s*, which

represents the time required for a particle to sediment, can be described by the Svedberg equation as follows:[178]

$$s = m(1-\rho v) / f \tag{3.7}$$

where m and ρ_{Sol} are the mass of the nanosheet and the density of the solvent, respectively. v is the volume of nanoparticle occupied per mass unit, f is the frictional coefficient. From this equation, it can be found that the sedimentation of nanosheets depends on the mass of the nanosheet and the frictional coefficient. The frictional coefficient for nanosheets with high aspect ratio is larger due to its two-dimensional geometry, when compared to a spherical particle.[178] Large and thick nanosheets, which exhibit higher mass consequently sediment faster compared to small and thin nanosheets. As a result, nanosheets with smaller masses and relatively larger aspect ratios would remain in the supernatant after centrifugation. However, it is important to note that not all particles have the same travel distance to the bottom of the centrifuge tube. Hence, small and thin particles with a smaller sedimentation velocity compared to larger and thicker particles may be found in the sediment as well. While this depends on the centrifugation speed, time, and the filling height of the centrifuge tube, this effect can be considered as inherent limitation of the precision of this approach.

However, following this strategy, a centrifugation cascade can be designed including multiple centrifugation steps at subsequently increasing centrifugation speeds. Based on this procedure of having multiple centrifugation steps, the technique is commonly referred to as liquid cascade centrifugation (LCC).[122, 123, 179] Typically, the resulting dispersion after exfoliation is subjected to a low-speed centrifugation step first, where the supernatant after centrifugation can be subjected to the next centrifugation step at higher centrifugation speed. The sediment of this first step typically contains residual unexfoliated material, which

can be collected, and recycled for the next exfoliation. While in the following steps, the supernatant is subjected to steps of increasing centrifugal acceleration, the sediments will contain smaller and thinner nanosheets after each step, which can be collected and redispersed in fresh solvent.[123] A schematic illustration of the LCC process is presented in **Figure 3.7**. Note that this sedimentation-based method does not require additives to tailor the properties of nanosheets and liquids. Further, the sediment can be collected in other solvents to exchange the solvent after exfoliation. LCC is adopted throughout the work presented in this thesis for size-selection and solvent-exchange purposes.

The pursuit of science is a never-ending journey of curiosity, perseverance, and wonder, and its rewards are immeasurable.

Carolyn R. Bertozzi

Chapter 4 Solution-Processed Nanosheet Networks For Optoelectronics

The superlative optical and electrical properties of semiconducting TMDs nanosheets are attractive for optoelectronic applications. Semiconducting nanosheets produced in liquids can be processed into thin films by various solution-processing techniques. The resultant nanosheet networks could be used as active components in optoelectronic devices. However, the device structure plays a vital role in their optoelectronic responses. In this chapter, the solution processing techniques are introduced, and the device structure and working mechanisms are compared. Representative applications such as photodetectors and solar cells are introduced, and the current research progress using TMDs nanosheet networks is discussed.

4.1 Solution-deposition techniques

Solution-processing techniques are regarded as a highly scalable and low-cost route to fabricate electronic devices. To form thin functional films from nanoparticle dispersions, one has to consider several parameters, such as the nanomaterial morphology, the rheology and the concentration of the dispersion, the property of the solvent, the substrate type, the processing equipment and temperature. The thin film quality will only be satisfied if all parameters are strictly adjusted. First of all, the properties of the dispersions should be considered. Nanosheets produced by either LPE or EE are stabilized in solvents or

surfactant aqueous solutions, that may not be suitable to be directly used as inks for the thin film formation due to their high boiling points, toxicity, and surfactant residuals.[173] Here, ink is referred to the dispersion that could be used to form thin films rather than a dispersion that its function is solely to form a stable colloidal solution. An ink for thin film formation requires additives sometimes to tune the rheology and surface tension of the dispersion.[173] Adding additives can be useful for some techniques such ink-jet printing or screen printing to prevent the satellite droplets for the former or avoid sedimentation of nanomaterials in a paste for the latter. [180-183] Moreover, it can improve the wettability of the ink on the substrate, which will be beneficial for forming thin films.[184] However, some additives are difficult to be removed out from the thin films and may bring an inevitably doping effect to the nanosheets, altering their electrical properties.[169]

The quality of solution-processed thin films can be affected by the spreading behaviors after the ink is coated onto the substrate. The wettability of the ink on the substrate can be explained by Young's equation:[185]

$$\gamma_{s-v} = \gamma_{s-i} + \gamma_{i-v}\cos\theta \tag{4.1}$$

where γ is the interfacial tension and the subscript s, i, and v represent solid (substrate), ink, and vapor, respectively. θ is the contact angle and a smaller contact angle indicates a good wettability of the ink on the substrate surface, that the ink can spread over the entire substrate spontaneously. Such spreading behavior is highly desired to ensure a uniform and pinhole-free feature. It is generally required that the surface tension of the ink is lower than that of the substrate to ensure a good wettability.[173] For example, the widely used substrates for solution-processed thin films have relatively low surface tensions, such as glass and Si/SiO_2 (3.6×10^{-2} N m^{-1}), polyimide (4×10^{-2} N m^{-1}), and Kapton (5×10^{-2} N m^{-1}).[173] When the nanomaterials are dispersed in aqueous solutions, a poor

wettability is usually observed due to the large surface tension of water (7.2×10^{-2} N m^{-1}). In this case, the substrate can be treated under an oxygen plasma or UV-Ozone to remove the surface organic residuals and generate hydroxyl functional groups on the substrate surface that can increase its surface tension[186], to match with the surface tension of the aqueous solution. Alternatively, the solvent-exchange step is introduced in this thesis during nanosheet preparation steps to exchange the nanosheets from undesirable solvents such as the surfactant aqueous solution into low boiling point solvents, e.g., isopropanol. Isopropanol was used for all the nanosheet containing dispersions in this thesis due to its low boiling point ~80 °C and a suitable surface tension ~2.3×10^{-2} N m^{-1} [173], which not only allow to form a stable nanosheet dispersion but also enable a facile coating of nanosheets by spray and spin coating methods onto various types of substrates without a much-elevated processing temperature. Additives are not used to maintain the intrinsic properties of the nanosheets. Nevertheless, it is reported that some solvent combinations, such as water and ethanol mixtures, could achieve a tiled nanosheet alignment, that is believed to play a vital role in their electronic properties.[173, 187-189] Therefore, further optimization on the dispersion composition is expected to be done in the future, but is beyond the scope of this thesis.

4.1.1 Spin coating

Spin coating is a technique widely adopted for thin film formations, including polymers, precursor solutions, and nanoparticles. The spin coating process involves applying a dispersion onto a static or rotating substrate. The rotating substrate provides centrifugal forces that spread liquids from the center towards the edge of the substrate. The rotation will further spread out the excessive liquids and forms a thin liquid layer on the substrate. Subsequently, the evaporating of the solvent, either by high-speed rotation or additional annealing steps, will result in the formation of a thin film. The spin coating process is illustrated in **Figure 4.1**.

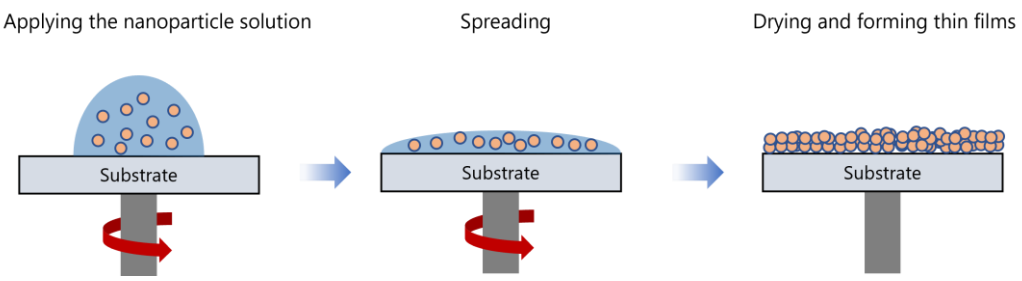

Figure 4.1 Spin coating. A schematic illustration of the spin coating process.

Spin coating could achieve reproducible films with controllable film thicknesses by adjusting several parameters such as rotation speeds, time, and the rheology and concentration of the dispersion.[190] The angular velocity ω of the rotation is an important parameter to determine the film thickness t_{film} for a given dispersion, which can be described by $t_{film} = C\omega^{\beta}$, where C and β are empirical constants. For low viscosity dispersions, which are absent of shear thinning effect, the exponent would be around -0.5[191], implying that higher rotation speed (angular velocity) will result in a thinner film. For 2D elongated objects with high aspect ratios, the rheology of the dispersion will vary due to non-negligible nanosheet/nanosheet interactions, which will depend on nanosheet morphology and its surface properties, concentration, and solvent/additives.[192-194] Therefore, the exponent β for nanosheet dispersions is expected to be somewhat different. Due to the centrifugal force generated by the rotation, nanosheets tend to align horizontally and form tiled nanosheet networks if the properties of dispersions and coating parameters are tuned carefully[195, 196], and this horizontal alignment is believed to be important for improving the conduction across nanosheet junctions.[189]

However, one of the drawbacks of spin coating is that it cannot realize patterning. Additional steps have to be adopted, such as photolithography.[197] As spin coating is usually performed on relatively small, flat and rigid substrates, it shows limitations on substrates which have large, curved and rough surfaces. Moreover, as most dispersion is spun off the substrate, the wastage of the dispersion is also a

problem. As a result, this coating technique is more suitable to be used as proof-of-concept experiments in research labs.

4.1.2 Spray coating

Spray coating is a well-established film formation method in industry. For a typical spray coating setup, it consists of an airbrush and a movable platform with a heating plate, as shown in **Figure 4.2A**. The dispersion is fed into the airbrush, and a compressed nitrogen gas is supplied to the airbrush. When the trigger is activated, it would retract the needle and release the dispersion, which would otherwise block the dispersion flowing in the nozzle if un-triggered. The cross-section of the nozzle is illustrated in **Figure 4.2B**. Due to the shear force supplied by the compressed gas, the dispersion will turn into micron-sized droplets and form aerosols, which will be transported to the substrate along with the gas flowing.

Spray coating usually requires the dispersion in low boiling point solvents, and adding additives for tuning dispersion viscosity is not so necessary. Isopropanol with a boiling point of ~80 °C can be used for nanosheet dispersions. The size of the nanomaterials in the dispersion should be smaller than the diameter of the nozzle (~40 μm) to prevent the clogging issue. Other than the size of the nanomaterial, the concentration of the dispersion should be relatively low to form a stable dispersion and to avoid the clogging in the nozzle due to the large size of the aggregated clusters. The film thickness can be easily adjusted by varying the volume and concentration of the dispersion or simply spraying more numbers of passes. However, due to the relatively complex setup, there will be several tuning parameters to obtain continuous pinhole-free and smooth films. The stand-off distance between the nozzle and the substrate is a key parameter. A long stand-off distance will result in poor film coverage, while a small distance will be

detrimental to the film formation due to the high pressure of the compressed gas which is~3-4 bar. Other than the stand-off distance, the line speed of the spraying, the spray rate of the dispersion, the compressed nitrogen pressure, the hotplate temperature and the nozzle diameter will all affect the droplet sizes and their evaporation rates on the substrate as well as the film morphology.[198]

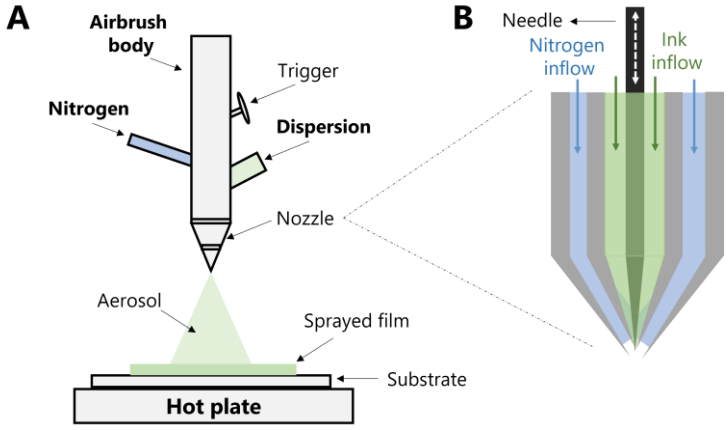

Figure 4.2 Spray coating. Schematic illustrations of the spray coating setup (A) and the cross-section of the nozzle (B).

Spray coating can be used for large-area deposition purposes. If a shadow mask is placed on top of the substrate, a certain level of simple patterning can be realized[168], however, the size of the feature and its resolution may not be as good as the one done by digital patterning processes such as inkjet printing.[182, 199] Compared with spin coating, the majority of the ink can be used for film formations with less material wastes. The substrate may not necessarily be flat or smooth, therefore spray coating can be used to deposit on non-conformal substartes.[200]

4.2 Photosensitive devices: structures and working principles

Photosensitive devices refer to the device that could respond to the incident light by changing their electronic properties, and this process is mainly realized by the semiconductor or the interfaces. The device types can be divided into

photoconductors and photodiodes, which both consist of metal contacts and semiconductors but work based on different mechanisms. Photosensitive devices are especially useful for applications such as photodetectors and solar cells, etc.

4.2.1 Device structures

The structure of electronic devices usually consists of at least two metals and one or several layers of semiconductors and is known as metal-semiconductor-metal (MSM) device structure. The semiconducting layers can be referred as active layers. These devices can be fabricated laterally or vertically as shown in **Figure 4.3**. The widely adopted structure is the lateral one, where active layers can be fabricated onto pre-patterned metal electrodes (**Figure 4.3A**), or metals can be fabricated onto active layers. The geometry of the device can be characterised by the active layer film thickness t_{film}, the channel length L defined as the distance between metal electrodes, and the channel width W defined as the length of the electrodes. Such device structure is relatively simple to be fabricated and can be used as photodetectors by directly shining light on top of the active layers. The resistance of the device R_{device} would come from the electrode resistance R_e, contact resistance R_c from the metal/active layer interfaces, the series resistance R_s from the active layer, and a negligible resistance from the external contact probes and wires.

$$R_{device} = R_s + R_c + R_e \tag{4.2}$$

If R_e is small enough, the device resistance will be dominated by R_s and R_c. The contact resistance will not only depend on the contact quality but also the energy band properties of the metal and semiconductors. For example, Schottky contact could arise if there is an energy level mismatch between the metal and semiconductor and causes the device to be mostly dominated by the contact resistance which will be introduced in the following section. Ohmic contact that

exhibits a smaller contact resistance is preferred in some applications, e.g., thin film transistors[201], to boost their device performance. However, devices such as Schottky diodes would require such energetically mismatched interfaces to operate, i.e., R_c is preferably larger than R_s to develop the electrical rectifying behaviors, implying that R_s should be minimized.

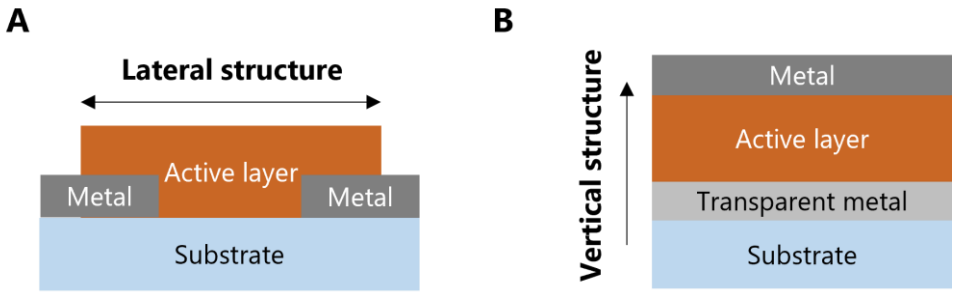

Figure 4.3 Device structures. Schematic illustrations of devices consisted of two metals and active layers in a lateral structure (A) and a vertical structure (B).

The series resistance R_s of the active layer refers to the in-plane (IP) carrier transport between electrodes and can be calculated by

$$R_s = \frac{L}{t_{film} W \sigma_{IP}} \tag{4.3}$$

where σ_{IP} is the IP conductivity of the active layer. For thin films that their thicknesses are usually on the orders of nanometers to micrometers, the common strategy to minimize the R_s is to decrease the ratio of L to W for electrodes. However, it is challenging to achieve low L/W without photolithography methods, not even mention that solution-processed electrodes usually suffer from their poor spatial resolutions and large L/W ratios. For semiconducting nanosheet networks, their IP conductivities are around 10^{-9} to 10^{-1} S m^{-1}.[189] The low network conductivity, thin nanosheet networks as well as relatively large L/W ratios make these IP devices usually exhibit linear current-voltage characteristics due to R_s is much larger than R_c, regardless of the metal used for contacting. Therefore, IP

devices based on nanosheet networks are always limited by the active layer resistance and exhibit Ohmic behaviors that are bulk-limited. It is challenging to observe any rectifying behaviors from the metal-semiconductor interface.

To observe metal-semiconductor contact electrical behaviors, the device structure can be changed to a vertical one, which is shown in **Figure 4.3B**. The vertical structure can be fabricated layer by layer and forms a sandwiched structure. To be used as optoelectronic devices, one of the metals has to be transparent to allow light to interact with the active layer. For vertically structured devices, carrier transport is along the OoP direction, and R_s of the active layer can be calculated by

$$R_s = \frac{t_{film}}{A\sigma_{OoP}} \tag{4.4}$$

where σ_{OoP} is the OoP conductivity of the active layer, and A is the device area defined by the overlapping area between electrodes. It can be found that R_s for a vertically structured device can be easily minimized by using a small film thickness and a larger device area without relying on the lithography to lower the ratio of *L/W*. Solution-processed electrodes could also be adopted as their spatial resolutions would not matter that much. With such vertically stacked devices, it is possible to minimize the series resistance coming from the semiconducting layer that could be comparable or even lower than the contact resistance originating from the semiconductor/metal interfaces, so we could observe electrical behaviors coming from the interfaces.

Moreover, it is expected that the OoP and IP electrical transport behaviors of the nanosheet network would be different due to the morphology of the nanosheet and the network, which is of interest to be investigated. Therefore, vertically structured devices are preferred and adopted throughout the thesis. The influence

of the device structure and the channel length will be further discussed in Chapter 6.

4.2.2 Photoconductor

Photoconductor refers to the type of photosensitive devices that its photoresponses arise from the conductivity change upon illumination. It involves three steps: absorption of light, generation of photocarriers, and collection of photocarriers. In order to let photodetectors operate, the properties of the semiconductor should be at least affected by the incident light. When light impinges on the semiconductor, only the photon energy hv above E_g, which is the bandgap energy of the semiconductor, could be able to scatter an electron from the conduction band to the valence band and create electron-hole pairs. This process is known as the absorption of photons. Upon illumination, the light intensity F will decay exponentially with the depth in semiconductors, which will depend on the absorption coefficient of the semiconductor $\alpha(\lambda)$ and also its thickness t_{film}. A schematic illustration of the light absorption through a semiconductor ignoring reflection or other effects is shown in **Figure 4.4A**. The light intensity $F(x)$ at a depth of x from its illuminated surface with a light intensity of F_0 can be obtained by $F(x) = F_0 \exp(-\alpha x)$. The rate of the generated electron-hole pairs can be calculated by $G(x) = \frac{\alpha(\lambda)F(x)}{hv}$, h is the Planck constant, v is the frequency of the light.[202] For high-performance photosensitive devices, a high absorption coefficient at the working wavelength is highly desirable. The thickness should be adjusted to the inverse of the absorption coefficient ($1/\alpha(\lambda)$) at this given wavelength to guarantee that all the incident light can be absorbed. If a broadband light is employed, the semiconductor with a smaller bandgap is preferred to cover the spectrum as broadly as possible. Other than the above effects, the radiative

recombination of carriers in the semiconductor will result in an emission of light and this emitted light could be re-absorbed by the semiconductor and further generate photocarriers.[203, 204] This could lead to an enhanced photocurrent that improve the photoresponses. However, this re-absorption phenomenon is more pronounced in the direct bandgap semiconductors with high quantum efficiencies in which the emission of light is significant that could be re-absorbed by the semiconductor and the re-absorption effect cannot be ignored in this case.[1] For the current study, the used semiconducting materials are few- to multi-layered TMDs nanosheets that have indirect bandgaps, and their photoluminescence properties are orders of magnitudes lower than their monolayer versions with direct bandgaps, so the effect of re-absorption is small.

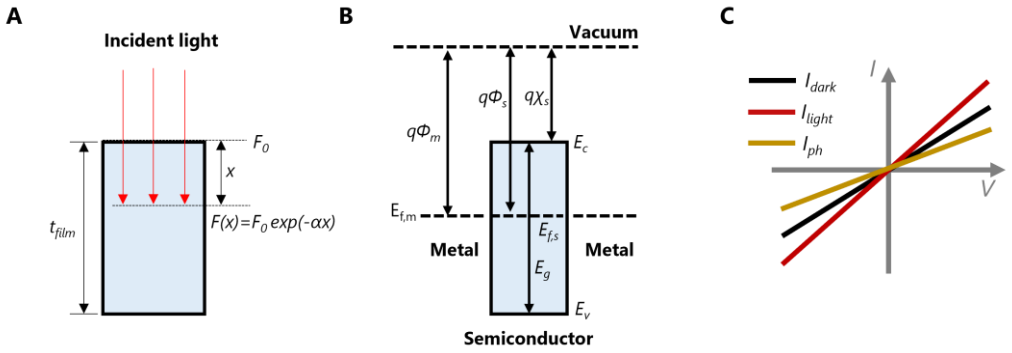

Figure 4.4 Photoconductor. (A) An illustration of light absorption process. (B) An energy band diagram of the semiconductor and metals. (C) An illustration of *I-V* characteristics for photoconductor in the dark and under illumination.

The electron-hole pairs will recombine immediately after generation in the absence of an external electric field. Therefore, a voltage must be supplied to the device to collect these photocarriers, and an Ohmic contact with a lower contact resistance would be preferred to minimize the carrier loss at the metal/semiconductor interfaces. The energy band diagram of materials to realize Ohmic contact is shown in **Figure 4.4B**. The photoelectric effect defines that the incident light with a critical energy is required to extract an electron from the

surface of a metal and can eject it into vacuum. This critical energy must be equal to the "work function" of the metal $q\phi_m$, which corresponds to its Fermi level $E_{f,m}$. Similarly, the Fermi level for semiconductors $E_{f,s}$ can be defined in the same way as $q\phi_s$. For semiconductors, there will be some electrons that exist in the conduction band and have an energy equal to E_c and the energy required to extract an electron from the conduction band edge is called "electron affinity", noted as $q\chi_s$. The semiconductors exhibit a forbidden gap with an energy of E_g, so that the position of the valance band edge, referred to as the ionization energy, corresponds to the sum of the bandgap and the electron affinity and is noted as E_v. Taking an example of an intrinsic semiconductor, its Fermi level will be in the mid of the bandgap. If a metal with a $E_{f,m}$~$E_{f,s}$ contacts the semiconductor, there will be virtually no potential barriers formed at the semiconductor/metal interfaces. A thermodynamic equilibrium will establish, and the Fermi level will align throughout these materials. Ohmic contact will allow carriers to flow freely across the contacts, and the contact resistance can be greatly reduced. The voltage drop at the interface is negligible so that the applied electric field on the semiconductor can be maximized to extract more photocarriers. The current-voltage (I-V) characteristics of such contacts obey Ohm's Law ($I \propto V^1$) and exhibit linear behaviors, as shown in **Figure 4.4C**.

However, Ohmic conduction only holds at relatively small voltages, and processes such as space-charge-limited conduction (SCLC) could dominate at higher voltages.[205] At small applied voltages, the number of the injected carriers is less than that of the free carriers in the semiconductor and will redistribute themselves to maintain the charge neutrality of the device, of which the process is known as the dielectric relaxation.[205] As the dielectric relaxation time is almost independent on the applied voltage in low injection levels, while the transition time for the injected carriers will decrease with increasing voltage (electric field). [205] As a

result, the injected carriers have little chance across the semiconductor as the transit time is longer than the dielectric relaxation time, resulting in an Ohmic conduction.

At higher applied voltages (a stronger injection level), the number of injected carriers will exceed that of free carriers in the semiconductor. The voltage will increase to a point that the Fermi level in the semiconductor reaches to the band edge and electrons as an example will be free to travel through the conduction band of the semiconductor, which is manifested by an obvious increase of current at certain voltages. Moreover, the high voltage will consequently lead to a shorter transit time compared with the relaxation time. The injected carriers will accumulate near the electrode and build up a space charge region. The current will be dominated by this space charge and limits further injection of carriers into the semiconductor.

The SCLC device should fulfil a few requirements.[205] First, the semiconductor should be intrinsic and trap-free. Second, the device should be Ohmic contacted and only allows one type of carrier to flow. This can be realized by using low-work function metals to contact the semiconductor, where the work function of the metal should be above or close to the conduction band minimum of the semiconductor, resulting in the device being fully governed by the electron transport, termed the electron-only device. Similarly, hole-only devices can be realized with deep-work function metals. Therefore, the current for such types of devices can be described by the Mott-Gurney Law[206] as

$$I_{SCLC} = \frac{9}{8} \mu \varepsilon_0 \varepsilon_r \frac{V^2}{L^3} \tag{4.5}$$

where μ is the mobility of the semiconductor. From the equation, it can be found that the current will be affected by the channel length L and the voltage for a

given semiconductor. If the above requirements are realized, one should be able to observe a transition behavior from Ohmic to SCLC in the *I-V* curves. The transition would happen due to these two conduction mechanisms are dominated by physically separated and independent paths in the semiconductor, and the applied voltage will cause a potential distribution change on these two conductions.[207] SCLC will appear at higher voltages due to its square law dependence. The critical voltage V_c for the transition can be expressed as[208]

$$V_c = \frac{\sigma L^2}{\varepsilon_0 \varepsilon_r \mu} \tag{4.6}$$

Therefore, to observe the transition from Ohmic conduction to SCLC, the applied voltage should be larger, and L should be reduced, which again highlights the importance of vertical structures where its channel length can be greatly reduced.

The photogenerated carriers will result in a conductivity change in the semiconductor. The photoconductivity σ_{ph} can be obtained by

$$\sigma_{ph} = \sigma_L - \sigma_D \tag{4.7}$$

where σ_L and σ_D are conductivity under illumination and in the dark, respectively.

$$\sigma_D = q(n_0\mu_{n0} + p_0\mu_{p0}) \tag{4.8}$$

$$\sigma_L = q(\Delta n\mu_n + \Delta p\mu_p) \tag{4.9}$$

where q is the elementary charge. n and p refer to densities for electron and hole, respectively. The subscript *0*, *n*, and *p* refer to intrinsic, electron, and hole, respectively. Δn and Δp are photogenerated electron and hole densities, respectively. The change in the photoconductivity may arise from the change in carrier density, mobility or a combination of both. For photosensitive devices, a lower dark conductivity is desired to improve the photoresponses. Overall, to

operate photoconductor type devices, an external voltage should be supplied to drive the photocarriers generated in the semiconductor towards electrode to be collected that will normally enhance the current corresponding to a positive photoconductivity.[203] A novel design has been developed recently that a graphene monolayer is placed underneath the light-absorbing material and connected with two electrodes. Such design enables the generated photocarriers in the semiconductor to be efficiently collected by the semi-metallic graphene layer first and are then driven to the electrode by the applied voltage, which can greatly enhance the photoconductor performance.[203, 209]

It is worth noting that the above description is based on ideal semiconductors without defects and impurities. All photocarriers will contribute to photoconductivity. However, for real-world devices, semiconductors may exhibit chemical impurities or structural defects. These defects will act as traps for photocarriers, inducing additional trap-filling processes that limit the device's response time, mobility and photosensitivity For nanosheet networks, nanosheet junctions could be an additional factor. These junctions could bring interface states that add a potential barrier between adjacent nanosheets. Therefore, the photoconductivity in such a network with considerable numbers of junctions could complicate the photoresponse behaviors. For example, Alzakia et al. found that photoconductors made from small and thin WS_2 nanosheets exhibit a longer response time than that made from relatively larger nanosheets, which was attributed to the nanosheet edges acting as trap sites for photocarriers.[210] After all, the limiting factor for photoconductors is mainly the quality of the semiconductor, and appropriate metals should be used as contacts to minimize the photocarrier loss at the metal/semiconductor interfaces.

4.2.3 Photodiode

Photodiodes are devices mainly employing the interface properties, such as Schottky junctions and heterojunctions. The former is based on non-Ohmic contacted metal/semiconductor interfaces, and the latter is based on interfaces between two semiconductors.

Schottky junction

Schottky contact could be realized when the Fermi level of the metal is different from that of the semiconductor, which is illustrated in **Figure 4.5A**. From the energy band diagram shown in **Figure 4.5B**, one of the metals exhibits $E_{f,m}$ that is deeper than $E_{f,s}$ that makes a Schottky contact, while the $E_{f,m}$ for the other one is close to $E_{f,s}$, realizing an Ohmic contact. However, it is possible that two metals with deeper or shallower $E_{f,m}$ that both make Schottky contacts to the semiconductor, which is usually called back-to-back (B2B) Schottky diodes.[211, 212]

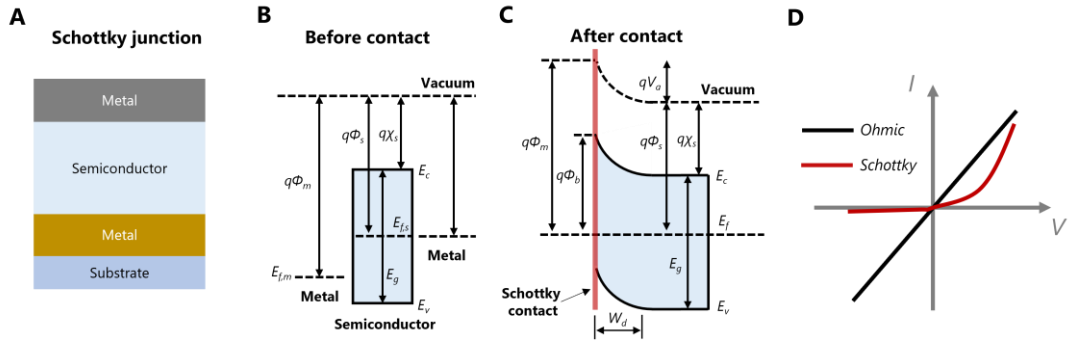

Figure 4.5 Schottky junction. (A) Device structure with different metals is shown in different colors. (B) The energy band diagram of Schottky junction before contact (C) and after contact. (D) Illustration of *I-V* curves for Ohmic and Schottky devices.

For the simplest case with only one Schottky contact, the Fermi level will align after contact under the thermodynamic equilibrium, as shown in **Figure 4.5C**. The alignment is realized by transferring electrons from the conduction band of the semiconductor to the metal and will leave positively charged donor atoms in the

semiconductor. An electron-depleted or so-called space-charge region with a width W_d is formed near the interface extending to the semiconductor side. An ultra-thin charge sheet is formed at the metal side near the interface, as the metal has orders of magnitude higher carrier density than that of the semiconductor and the width of the space-charge region W in the metal is roughly inversely proportional to the square root of the metal's carrier density N_m ($W \propto N_m^{-0.5}$). Due to the depletion region and the thin charge sheet, the energy band of the semiconductor will bend. For the electron in the metal, it will experience a potential barrier $q\phi_b$, that prevents electrons flowing from the metal to the semiconductor.

$$q\phi_b = q(\phi_m - \chi_s) \tag{4.10}$$

At room temperature T, the potential barrier is significantly larger than the kT/q, and only a limited number of electrons could overcome the barrier. The current for electrons flowing from the semiconductor to the metal can be expressed as $I_{m\to s}$.[1]

$$I_{m\to s} = AR^*T^2 \exp\left[-\frac{q(\phi_b - V_a)}{kT}\right] \tag{4.11}$$

The notation $m \to s$ is that electron carries negative charges, and its flow corresponds to a positive current flow from the metal into the semiconductor. R^* is the Richardson constant ($R^* = \frac{4\pi m_e q k^2}{h^3}$), where m_e is the effective electron/hole mass, and V_a is the applied voltage. The mechanism for electron overcoming the potential barrier is usually governed by thermionic emission that electrons are activated by the thermal energy. Similarly, the current flowing from semiconductor to metal can be expressed as $I_{s\to m}$, and $I_{m\to s} = -I_{s\to m}$ holds under the zero-bias condition.[1]

$$I_{s\to m} = -AR^{*}T^{2}\exp\left[-\frac{q\phi_b}{kT}\right] \tag{4.12}$$

Therefore, the total current for the Schottky device can be obtained by combining these two currents as follows,[1]

$$I = AR^{*}T^{2}\exp\left(-\frac{q\phi_b}{kT}\right)\left[\exp(\frac{qV_a}{nkT})-1\right] \tag{4.13}$$

where n is the ideality factor ($1 \le n \le 2$). The current will be dominated by the diffusion mechanism if n=1, and by the generation and recombination mechanism if n=2. Under reverse biases, the potential barrier ($\phi_b - V_a$) will be increased, and the current flow from the semiconductor to the metal will be reduced while the current flow for the other direction remains unchanged. Under forward biases, the potential barrier will be reduced which results in an exponential increase in the number of electrons flowing from the semiconductor to the metal. As a result, asymmetrical and non-linear *I-V* behaviors can be observed for Schottky diodes, as shown in **Figure 4.5D**. An *I-V* curve for an Ohmic device is also plotted in the figure. At a reasonably large positive bias, there will be literally no potential barrier at the interface. Therefore, the Schottky device will behave as an Ohmic one in this case, and their *I-V* curves will overlap on each other following the Ohmic conduction mechanism. Series resistance can be included in the equation to account for the voltage drop on it.

$$I = I_s\left[\exp(\frac{q(V_a - IR_s)}{nkT})-1\right] \tag{4.14}$$

where I_s is the saturation current.

The quality of the Schottky contact, such as the potential barrier, may be affected by several parameters. First, the potential barrier height is not strictly constant and

will be slightly affected by the applied voltage. This is caused by the mirror charge in the metal produced by the electrons in the semiconductor due to electrostatic attractions, which is known as the Schottky effect.[1] Secondly, the interfacial states on the surface of the semiconductor arising from defects or impurities will develop permitted states in the bandgap of the semiconductor. As a result, the alignment of the Fermi level will happen between the interfacial states and the metal, which is known as the Fermi level pinning effect.[1] Moreover, the above mathematical model is developed on perfectly smooth surfaces, where layers are planarly stacked. The roughness of the interface, in reality, will introduce spatial barrier height variations that will also affect the contact quality.[213]

Heterojunction

Electrical rectifying behaviors can also be realized by the interface formed between two semiconductors, e.g., a p-type and a n-type, being called p-n junctions. If these two materials are the same type but with different doping types, the junction is termed a homojunction, and it will be named a heterojunction when they are different types of materials, even with the same doping type. Here, it is the heterojunction that will be focused throughout this thesis. To obtain the heterojunction, the semiconductors can be fabricated layer by layer, forming a planar heterojunction, as shown in **Figure 4.6A**. The metal should provide a suitable Fermi level towards the contacted semiconductor to serve as an Ohmic contact. The heterojunction can also be formed if two semiconductors with different doping types (e.g., p- and n-doped) are physically mixed and are called a bulk heterojunction as shown in **Figure 4.6B**. This structure is favored for some optoelectronic materials with short carrier diffusion lengths (e.g., organic and polymeric semiconductors) to maximize the junction interface and facilitate the electron-hole pair separation.

The material used for the junction formation may not necessarily be a p-type or a n-type. Any material with different energy bands and Fermi-level positions can form such interfaces. Therefore, there will be three types of heterojunctions, and their energy bands before contacts are illustrated in **Figure 4.6C-E**. If the energy band of one of the semiconductors is completely contained in the bandgap of the other, forming a straddling gap, which is termed the Type-I heterojunction. There will be energy offsets ΔE_c and ΔE_v due to their relative CB and VB positions, respectively. If there is a certain level of overlap between the energy bands of two semiconductors, the heterojunction is called as a Type-II heterojunction with a staggered gap. Furthermore, it will be called as a Type-III heterojunction if the energy band of one semiconductor shows no overlapping with that of the other, forming a broken gap, which is a pronounced situation of the type-II.

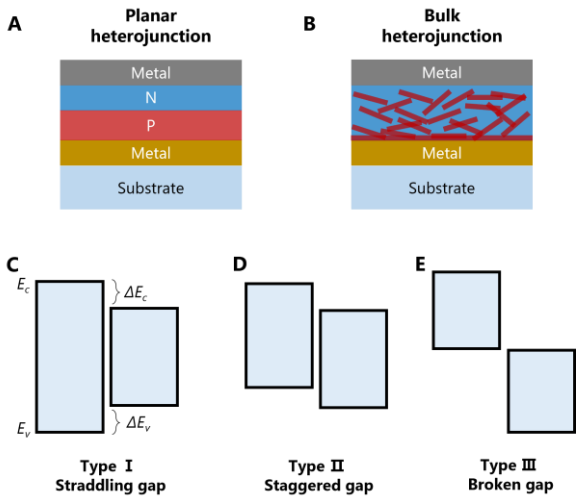

Figure 4.6 Heterojunction. Schematic illustrations of a planar heterojunction structure (A) and a bulk heterojunction structure (B). (C-E) The energy bands for different heterojunction types.

The type-II heterojunction with a staggered gap is more of interest to the current study. If we assume that there are one p-type semiconductor and one n-type semiconductor with energy bands shown in **Figure 4.7A**. Upon contacting and under thermal equilibrium conditions, the Fermi level will align by electrons

diffusing from the n-type semiconductor to the p-type semiconductor, and some of the electrons will recombine with majority carrier holes, and holes diffusing towards the opposite direction. The average distance that the minority carriers can reach is called as the diffusion length (e.g., electron diffusion distance in the p-type semiconductor). As a result of the charge displacement, the energy band near the interface will bend, and an internal built-in potential Φ_b is formed, which equals the Fermi energy difference between these two semiconductors. Focusing on electrons, its diffusing leaves positively charged ions in the n-type semiconductor, forming a depleted region extending from the interface towards the n-type semiconductor, and its width can be calculated by[1]

$$W_n = \sqrt{\frac{2\varepsilon_r\varepsilon_0}{q}\frac{(\Phi_b - V_a)N_a}{N_d(N_a + N_d)}} \tag{4.15}$$

where N_a and N_d are the acceptor concentration in p-type semiconductors and the donor concentration in n-type semiconductors, respectively. Similarly, the depletion width due to hole diffusing can be found by[1]

$$W_p = \sqrt{\frac{2\varepsilon_r\varepsilon_0}{q}\frac{(\Phi_b - V_a)N_d}{N_a(N_a + N_d)}} \tag{4.16}$$

Without external biases, the drift current generated by the internal built-in potential is exactly balanced by the diffusion current due to the carrier concentration gradient. The Fermi level potential difference acts as a barrier to prevent further carrier diffusion. It is worth noting that the alignment of Fermi level creates both conduction band and valence band energy offsets but takes opposite signs. This means that the photocarriers generated under illumination can be driven by the internal built-in potential towards opposite directions, which are spatially separated (**Figure 4.7B**). This feature would be preferred for solar cells and photodetectors, where photocurrent originates from the spatial separation of

electron-hole pairs. In contrast, type-I heterojunctions with offsets exhibiting the same signs will result in those electrons and holes being transferred into the relatively small bandgap semiconductor. This type of heterojunction will be beneficial for applications such as light emitting diodes, where carrier recombination only happening in the specific semiconductor is desired.[214]

Under forward biases (positive on the p-side), the built-in potential as well as band offsets, would be reduced, allowing more carriers to diffuse. The forward bias will also reduce the depletion width. Under reverse biases, the increase of the potential barrier and band offsets would limit the diffusion current. Therefore, the heterojunction also exhibits non-linear and rectifying electrical behaviors that current can only flow along one direction, as shown in **Figure 4.7C**. The current for the heterojunction can also be described by the Shockley equation, however, the saturation current should be modified as[1]

$$I_s = qA(\frac{D_n n_{p0}}{L_n} + \frac{D_p p_{n0}}{L_p}) \tag{4.17}$$

where D, n_0, and L refer to diffusion coefficient, equilibrium carrier concentration and diffusion length, respectively. n_{p0} and p_{n0} refer to equilibrium electron concentration in the p-type semiconductor and equilibrium hole concentration in the n-type semiconductor, respectively.

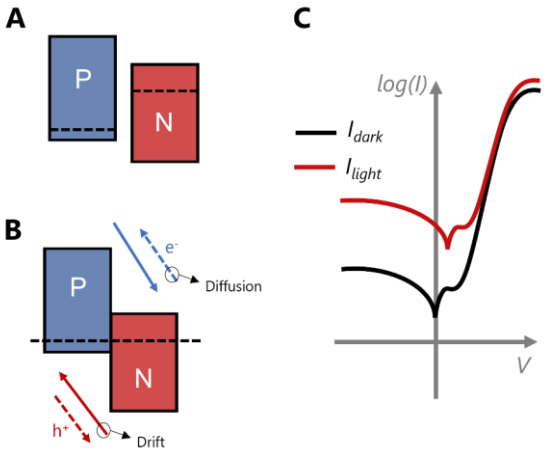

Figure 4.7 Type-2 heterojunction. The energy band diagram of type-2 heterojunctions before contact (A) and after contact (B). (C) Illustration of *I-V* curves for photodiodes in the dark and under illumination.

The conduction of carriers in heterojunctions is governed by the minority carrier diffusion, e.g., electron diffusion in the p-type semiconductor, which is different from the case for Schottky diodes in that its conduction is dominated by the majority carrier type. Similar to Schottky diodes, the forward bias will eventually lead to zero built-in potential and band offsets that the device is equivalent to an Ohmic contacted semiconductor, which corresponds to the linear *I-V* region.

For both hetero- and Schottky junction-type photodiodes and under illumination conditions, photocarriers generated in the depletion regions will be driven by the internal built-in potential and transport towards electrodes and create a photocurrent with an opposite sign of the dark current. An illustration of *I-V* curve under illumination is shown in **Figure 4.7**C. An obvious feature can be found that there is a photocurrent at the zero bias, which means that the device can be self-powered owing to the built-in potential. The self-powering ability is not possible to be realized for photoconductor type devices. If the device is reverse-biased, the depletion width will be extended, and this allows more photons to be absorbed and contributed to the photoresponses. Further, under enough high forward biases, there will be no built-in potential involved, and the device will behave as a

photoconductor that the photoresponses come from the photoconductivity change in the semiconductors. After all, the photoresponse for the photodiode can be affected by both the semiconductor/semiconductor interface and the semiconductor properties and displays voltage-dependent photoresponse behaviors. Comparing with photoconductors, photodiodes exhibit a self-powered ability and the dark current (e.g., at zero and reverse biases) can be greatly reduced with the assistance of the potential barriers at the interface so that the photocurrent (I_{light}-I_{dark}) can be enhanced.

4.3 Optoelectronic applications

4.3.1 Photodetector

The electronic properties of photodetectors will change upon illumination. The performance of a photodetector can be evaluated by a few parameters.[215-217]

(1) Photoresponsivity

The external photoresponsivity (R_{ph}) is the photocurrent density $J_{ph} = (I_{light} - I_{dark}) / A$ of the photodetector collected by the external circuit divided by the incident light density F at a given wavelength in the case of no other optical loss.

$$R_{ph} = \frac{J_{ph}}{F} \tag{4.18}$$

The photoresponsivity can also be defined regarding its internal photon-to-carrier conversion as the ratio of the number of photo-generated carriers to the number of absorbed photons at the given wavelength.[203]

(2) External Quantum Efficiency

External quantum efficiency (EQE) is the ratio of the number of charge carriers collected at the electrodes per second to the number of photons with a given energy incident on the photodetector per second.

$$EQE = \frac{electrons/\sec}{photons/\sec} = \frac{R_{ph} hv}{q} \tag{4.19}$$

(3) Detectivity

Detectivity D^* is a normalized measure of the minimum detectable light intensity of a photodetector. Noise from the dark current gives a fundamental limit on the detectivity.

$$D^* = \frac{\sqrt{A\Delta f}}{NEP} \tag{4.20}$$

where Δf is the bandwidth, NEP is the noise equivalent power in Watts. The NEP can be expressed as function of the responsivity R_{ph} and the noise spectral density $S_n = R_{ph} \times NEP$ of the dark current.

(4) Photogain

The photogain of the photodetector G_{ph} is defined as the number of photogenerated carriers collected by the electrodes per number of photogenerated electron-hole pairs. G_{ph} can be quantified by the ratio of the lifetime of carriers τ_{life} over the drift transition time τ_{trans} as:

$$G_{ph} = \frac{\tau_{life}}{\tau_{trans}} \tag{4.21}$$

The transition time can be found by $\tau_{trans} = \frac{L^2}{\mu V}$, which depends on the carrier mobility and the applied voltage.

(5) Response time

The photodetector response time τ is the time required for the photodetector to rise or fall from 10% to 90% of the maximum photocurrent or vice versa (**Figure 4.8**). The response speed of the photodetector can either be limited by the transit time between the opposite electrodes for the photoconductor type devices or by the recombination time of the photogenerated carriers for the photodiode type

devices.

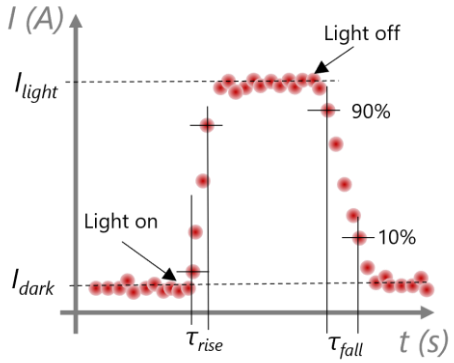

Figure 4.8 Photodetector. The temporal current responses under illumination.

4.3.2 Solar cell

Solar cells are an important type of energy conversion devices that can convert photon energy into electricity with the help of Schottky or heterojunctions. The performance of the solar cell is usually evaluated by collecting the *I-V* curve of the device under illumination, which is illustrated in **Figure 4.9**. The photocarriers absorbed in the depletion region will be driven by the internal built-in potential towards opposite electrodes, and the photocurrent will take an opposite sign compared with that of the dark current. Therefore, the photocurrent at 0 V can be found to be negative values and is known as the short-circuit current I_{sc}. $I_{sc,}$ in the case of the p-n junction, can be calculated by using the generation rate, the diffusion length and the depletion width.

$$I_{sc} = qA\left[G_p(L_p + W_p) + G_n(L_n + W_n)\right] \tag{4.22}$$

where subscripts *p* and *n* refer to the material type in the p-n junction. Therefore, the current for the solar cell under illumination can be expressed by

$$I = I_{ph} - I_s\left[\exp(\frac{qV}{nkT}) - 1\right] \tag{4.23}$$

where I_{ph} equals to I_{sc} when the series resistance of the solar cell is relatively

small. The voltage when the current is zero is referred as the open-circuit voltage V_{oc}. V_{oc} is a factor depending on the photocurrent and saturation current.

$$V_{oc} = \frac{nkT}{q} \ln(1 + \frac{I_{ph}}{I_s}) \tag{4.24}$$

The maximum output power P_{max} can be found by $P_{max} = I_{mp} V_{mp}$, where I_{mp} and V_{mp} refer to the current and voltage at the maximum power point, respectively. The *I-V* curve at the fourth quadrant will form a square with the x and y-axis. P_{max} can be increased if this *I-V* curve in the fourth quadrant shown in the figure is close to a square, as I_{mp} and V_{mp} will be close to I_{sc} and V_{oc}, respectively. The squareness can be evaluated by the fill factor (*FF*), which can be obtained by $FF = \frac{I_{mp} V_{mp}}{I_{sc} V_{oc}}$. The fill factor can be improved by increasing the shunt resistance or decreasing the series resistance. Therefore, the photo-to-electricity conversion efficiency η can be obtained by

$$\eta = \frac{P_{\max}}{F} = FF \frac{I_{sc} V_{oc}}{F} \tag{4.25}$$

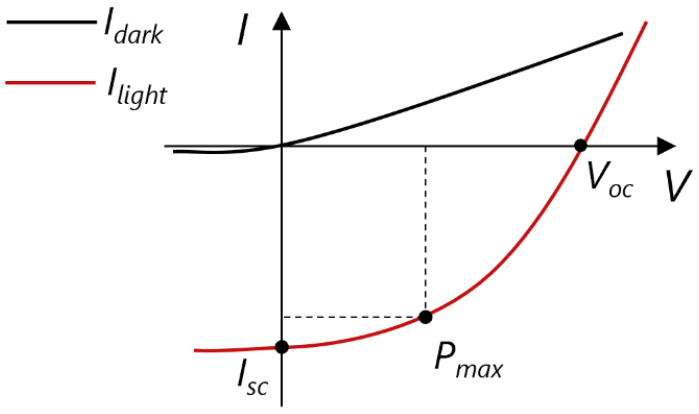

Figure 4.9 Solar cell. The typical *I-V* curves for solar cells operated in the dark and under illumination.

4.4 Optoelectronic devices based on solution-processed networks

4.4.1 Solution-processed networks

Solution-processed optoelectronics has long been dominated by the network formed by organic or polymeric semiconductors. However, organic based optoelectronics suffered from low stabilities in ambient, strict handling environments and high cost and low yield of the material. Therefore, the research interest has shifted to the inorganic material based semiconducting networks which can be classified regarding their material dimensions, such as 0D quantum dots, 1D nanowires or nanotubes and 2D nanosheets. Quantum dots possess nanoscale dimensions (< 10 nm) with rich numbers of surface dangling bonds. The assembled network comprised of quantum dots would contain a large number of grain boundaries (~10^5 μm^{-2}).[218] The chemical defects and lattice mismatch from these boundaries will act as potential barriers and is detrimental for carrier transports, as shown in **Figure 4.10A**. Surface passivation with organic ligands is usually required to terminate the surface defects. However, the passivation itself will also introduce additional potential barriers due to the insulating nature of the ligands. For 1D networks, due to the 1D elongated material morphology, the percolated network can be relatively easy to form and would exhibit fewer numbers of grain boundaries than that of the 0D networks. However, it is challenging to obtain a complete surface coverage as the 1D network alone will be inherently highly porous and is not compatible with a vertically structured device.

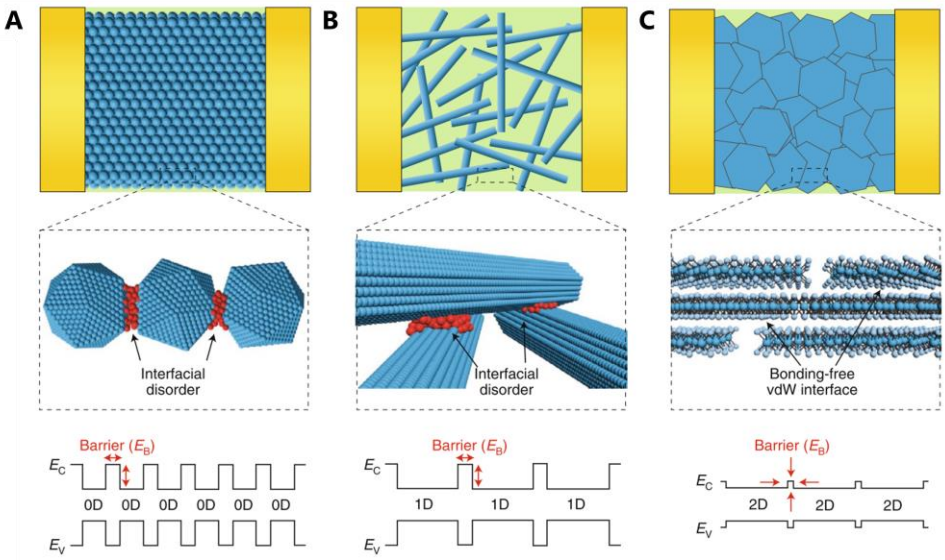

Figure 4.10 Nanomaterial networks. Schematic illustrations of networks comprised of 0D (A), 1D (B), and 2D nanomaterials (C) with their corresponding potential barrier variations. Adapted from Ref. 218.

2D nanosheets exhibit distinct features of atomic thicknesses and large lateral dimensions. Some of them, such as TMDs, graphene, and *h*-BN are free of surface dangling bonds. However, nanosheets obtained by different top-down exfoliation methods could display different morphology, which is mainly reflected by their aspect ratios defined as the ratio of the nanosheet length to the thickness. Nanosheets produced by the direct liquid exfoliation will have relatively lower aspect ratios compared with ones by electrochemical exfoliation.[219] Therefore, LPE nanosheets tend to be rigid due to their relatively larger thicknesses, while atomically thin EE nanosheets display a higher degree of flexibility. As a result, it is mostly EE nanosheets that could realize the conformal alignment of the nanosheets as they are able to bend across the edge of the nanosheet, providing large-area basal plane contacts, which ensures highly compact and fully covered films. EE nanosheets could tile on each other to form atomically clean vdW interfaces that will be similar to the natural vdW interfaces in the bulk layered crystals. As a result, the interface quality is expected to be superior to that formed by 0D or 1D counterparts, which will enable near-ideal carrier transport behaviors

with almost negligible junction resistances. Moreover, the vdW forces between neighboring nanosheets will provide stronger mechanical properties, which will result in a robust and flexible network. In contrast, LPE nanosheets usually stack on each other randomly due to nanosheets' rigidity, and the network displays a certain level of porosity depending on the size of nanosheets but is around 50% for LPE nanosheet networks in general.[168, 199] The high porosity of such a network will cause potential device fabrication problems. LPE nanosheets usually form point-like contacts or edge-to-plane contacts rather than vdW contacts. The electrical properties of the LPE nanosheet based networks are mostly limited by the junction resistance, which could be as high as Gigaohm for semiconducting nanosheets.[220] LPE nanosheet based networks are also known to display poor mechanical properties and is not suitable for any flexible device.[221] Here, the literature review in the following sections will be mainly focus on optoelectronic devices using semiconducting TMDs nanosheet networks.

4.4.2 Photodetectors

The first solution-processed photodetector using liquid exfoliated TMDs was fabricated in 2013 by Cunningham et al.[222] The liquid exfoliated MoS_2 was coated on ITO glasses using Langmuir-Blodgett method. Gold top electrodes were evaporated onto the MoS_2 film and the final device was ITO/MoS_2/Au, as a vertical metal-semiconductor-metal (MSM) structure. To avoid the electrical shorts between Au and ITO, the thickness of the MoS_2 film was deliberately increased to ~6 μm by several coatings. By electrical measurements under the simulated solar light, it was found that the photocurrent would increase sublinearly, indicating the presence of traps that limits the transport of photocarriers. The obtained photodetector exhibited a R_{ph} of ~10^{-4} A W^{-1} at 15 V. Later, in 2015, a systematic study was performed by Cunningham et al.[223] on six semiconducting type TMDs: MoS_2, $MoSe_2$, $MoTe_2$, WS_2, WSe_2 and WTe_2. Using

the same film formation method as above, TMDs films with a thickness of ~1 μm were fabricated onto pre-patterned gold electrodes on SiO_2/Si substrates. The obtained lateral two-terminal devices exhibited material dependent photoresponses. Sulfide based TMDs with lower dark conductivities would be more suitable for photodetector aiming for higher photoresponses, while tungsten based TMDs are more suitable for solar cell applications due to their relatively high conductivities and small bandgaps. Finn et al.[224] fabricated all-printed lateral two-terminal devices with graphene as electrodes and MoS_2 as the active material on PET substrates. The current increased around 10-fold under 640 mW cm^{-2} laser illumination. McManus et al.[225] also fabricated all-printed photodetectors and used WS_2 as the active material and graphene as the electrodes. However, the device structure was changed to a vertical one and achieved a R_{ph} of 10^{-3} A W^{-1} at 1 V. A systematic photocurrent study was performed by the same group on various TMDs but using a lateral two-terminal device structure that electrodes are made from graphene. The obtained R_{ph} ranged from 10^{-8} to 10^{-5} A W^{-1}.[226] There are several other reports on LPE TMDs photodetectors taking MSM device structures. However, the obtained R_{ph} was usually on the order of 10^{-8}-10^{1} A W^{-1}.[155, 210, 222-230] The highest R_{ph} of 16 A W^{-1} was achieved under 1064 nm illumination for a composite made from LPE TMDs and amine-terminated polymers.[230] The results so far clearly indicate the potential of solution-processed photodetectors using LPE TMDs nanosheets. However, it can be found that the obtained R_{ph} so far scatters over such a wide range, and this is probably due to the differences in material preparation, thin film formation, device geometries and measurement conditions. With the development of the electrochemical exfoliation technique in recent years, EE TMDs nanosheets are integrated into photodetectors and are expected to display better performances due to their tiled nanosheet networks. The MSM structured photodetectors using EE MoS_2 nanosheets had achieved R_{ph} on

the order of 10^3-10^5 A W^{-1}.[231-234] The obtained values are significantly better than those based on LPE TMDs, highlighting the importance of the network morphology.

So far, most devices are fabricated in MSM structures, and the devices are operated as photoconductors so the involvement of the interface is neglected. The only solution-processed photodetector employing Schottky junction, i.e., the metal-semiconductor interface, was fabricated with LPE black phosphorene (BP) by Farbod et al. in 2021.[235] The Schottky diode with a structure of FTO/BP/Al displayed a rectification ratio of 44 at ±1 V and a R_{ph} of 1.08×10^{-2} A W^{-1} under simulated solar light. For heterojunction type photodetectors, the current research is mostly focusing on integrating LPE TMDs nanosheets with 3D bulk semiconductors to form heterojunctions, such as heavily doped silicon.[236-245] The obtained photodetectors not only showed improved performances regarding R_{ph} but also exhibited self-powered abilities due to the presence of the built-in potential at the TMDs/Si interfaces. For example, a heterojunction formed by WSe_2 network and silicon can be operated at zero bias and showed a R_{ph} of 8.61×10^{-2} A W^{-1} using LED light source.[245] However, as silicon itself is already a matured semiconductor for optoelectronic applications, the role of TMDs nanosheet network, especially the interface properties, is not well-understood yet.

4.4.3 Solar cells

Solar cells are devices based on photodiodes, and there could be several layers of materials providing different functionalities. For example, other than metal and light absorbing layers, interfacial layers between metal and light absorbing layers may be required to balance the photocarrier extraction/injection and adjust the energy band alignment to minimize the energy offsets.[246, 247] These interfacial layers are usually called electron/hole transport, injection and blocking layers,

represented by organic and polymers[248, 249], inorganic nanoparticles[250] and inorganic films formed from the precursor solutions[251]. For simplicity, such layers will be referred as transport layers in this thesis. Semiconducting TMDs nanosheets displaying various energy band properties can easily find their application in interfacial layers.[252-254] For instance, organic solar cells using LPE MoS_2 or WS_2 nanosheets as hole transport layers exhibited slightly increased efficiency compared with cells with PEDOT:PSS layers,[255] indicating TMD nanosheets could be candidates to replace organic based hole transport layers.

However, what is more exciting is to use TMDs nanosheet networks as the light-absorbing layers. Theoretical calculations have shown that the conversion efficiency could approach 40% for TMDs based solar cells due to their excellent optical and electrical properties.[256-258] Moreover, hot-carrier type solar cells made from vdW junctions could overcome the Shockley-Quiesser limit and are no longer restricted by the thermodynamic limit of the power conversion efficiency.[259-263] Fortin et al. demonstrated Schottky type solar cells based on bulk crystals in 1982 with a device structure of Cu/MoS_2/In, which could realize 1% efficiency under white-light illumination at ~120 K.[264] In 1994, heterojunctions based on polycrystalline TMDs films showed an open-circuit voltage of 550 mV and a short-circuit current density of 1 mA cm^{-2} under 1.5G illumination.[265] Early investigations on bulk TMDs crystals have proven their capability in solar cell applications. For solution processable TMDs nanosheets, they have been investigated as photoactive dopants and light-absorbing layers. Photoactive dopants mean that a small amount of nanosheets is physically mixed with other photoactive materials[266], such as semiconducting organic materials. The mixture is used as a light absorbing layer, corresponding to the bulk heterojunction device structure. For example, organic solar cells incorporating LPE WSe_2 nanosheets in the active layer could lead to an increase of ~15% for the efficiency.[267] Another

organic solar cell with MoS_2 nanosheets as photoactive dopants have realized efficiency, increasing by ~32%.[268] In general, the enhanced efficiency was ascribed to the broader absorption spectrum and an improved charge transfer, etc. However, as there is only a small amount of the nanosheets in the bulk heterojunction, their potential for photovoltaic applications cannot be fully displayed.

Nanosheets in liquids can be solution-processed into networks, which can be used as light absorbing layers themselves. Similar to photodiodes for photodetection applications, the diodes are mainly fabricated by integrating TMDs networks with bulk silicon, forming 2D/3D heterojunctions.[236-238, 243, 245, 269-271] For example, Lee et al. [269] fabricated the In/Si/MoS_2/Au solar cell by spray coating MoS_2 nanosheets onto Si. The obtained solar cell exhibited an efficiency of 1.01% under 100 mW cm^{-2} illumination. Pataniya et al.[245] obtained Ag/Si/WSe_2/Ag heterojunctions by drop-casting WSe_2 nanosheets onto Si substrates. The device showed an efficiency of 2.91% under 15 mW cm^{-2} illumination.

Despite the low efficiency of the obtained 2D/3D heterojunctions, the electrical behavior of the nanosheet networks in junction with other semiconductors are not systematically investigated and understood yet. In particular, there is no report on TMDs nanosheet networks in junction with commonly used transport layer materials, such as ZnO, PEDOT:PSS, and NiO, etc. The introduction of transport layers is important to manipulate the interface properties as well as the electrical behaviors, which will ultimately affect the photovoltaic performances. Moreover, vdW heterojunctions formed by 2D/2D interfaces that are free of dangling bonds could exhibit better performances than other types of interfaces. A planar 2D/2D homojunction was fabricated in 2015 with a device structure of ITO/n-MoS_2/p-MoS_2/Ag[272], where MoS_2 was liquid exfoliated and n-doped by sodium chloride and p-doped by thermally annealing in air, and its layer was formed by spin-

coating. The obtained homojunction barely rectified but displayed a V_{oc} of ~450 mV and a J_{sc} of ~11 nA cm^{-2}.

Overall, semiconducting TMDs nanosheet networks are promising for next-generation optoelectronic devices, however, are still in the infancy stage. Firstly, as the building block of the film is such high aspect ratio nanosheets showing asymmetric electrical properties, the morphology of the network would be critical to determine the electrical properties. This has led the research interest to move from LPE rigid nanosheets to EE flexible nanosheets to achieve tiled and conform nanosheet alignment. Secondly, the device structure is crucial to investigate any interface-related electrical behaviors, and the vertical one is clearly demonstrating its advantages. This enables the device can be slightly more complicated if multilayers of thin film semiconductors are within the device, and the interfaces could be the dominating factor for the electrical behaviors. As a result, the obtained optoelectronic devices will not be limited to only photoconductor types, and more advanced device structure photodiodes such as Schottky and heterojunction type diodes could be realized.

The value of an idea lies in the using of it.

Thomas Edison

Chapter 5 Experimental Methods

5.1 Material and ink preparation

5.1.1 Liquid phase exfoliation

Liquid phase exfoliation processes are conducted both in ambient and under protection of inert gases. For the ambient exfoliation, a Sonics Vibra-cell VCX-750 horn tip sonicator equipped with a solid head probe is used. The schematic of the setup is shown in **Figure 5.1A**. The transducer will drive the probe to vibrate at high frequencies and transmit the ultrasonic waves into the dispersion. The metal beaker containing the dispersion is placed under a water-cooling bath which is set at ~10 °C during sonication to avoid heating of the dispersion. The amplitude is set at 40% and a pulse of 6 seconds on and 2 seconds off.

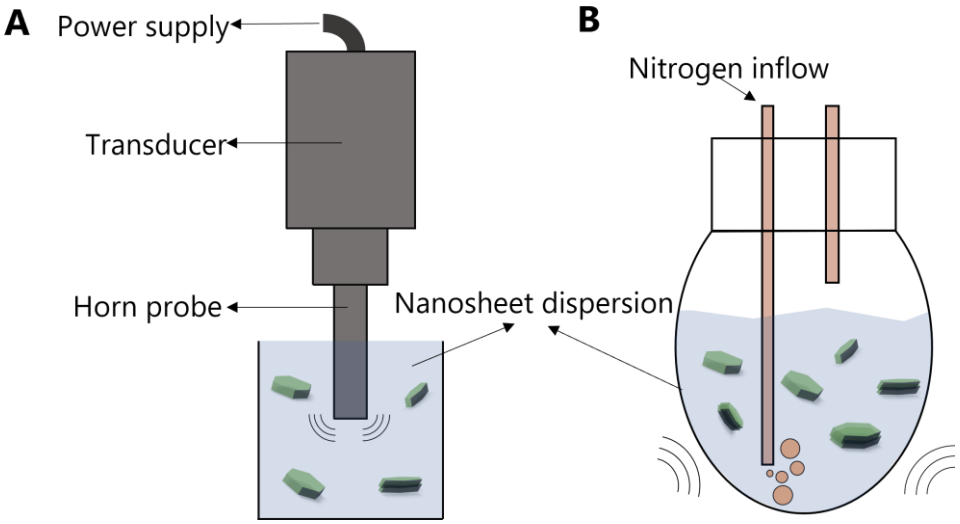

Figure 5.1 Liquid phase exfoliation set-ups. Schematic illustrations of the probe sonication process in ambient (A) and the inert exfoliation by bath sonicator (B).

For the inert exfoliation, a 100 mL flask is used and sealed by the rubber cap, as shown in **Figure 5.1B**. Two syringe needles are inserted into the cap with one of them submerged in the dispersion to allow the nitrogen gas into the dispersion, while the other is placed above the dispersion to let nitrogen flow out the flask. The flask is placed in a sonic bath filled with ice-cooled water, which is replaced every one-two hour. The protocol and set-up are proposed by Dr. Kevin Synnatschke and permission has been obtained before use.

For a general exfoliation process, the bulk powder is mixed with solvents and the mixture is subjected to a short-time exfoliation (~1 h) and centrifugation to remove any impurities from the powder. This step is found to be important to improve the yield of the nanosheets.[273] The sediment after centrifugation will be collected and re-dispersed in solvents for exfoliation that will usually take 6-10 hours.

Tip ultrasonication process is also applied to disperse carbon nanotubes in liquids. The probe is changed to a tapered one and the amplitude is adjusted to 30% with a pulse of 3 seconds on and 3 seconds off.

5.1.2 Electrochemical exfoliation

An electrochemical cell with two electrodes is used to intercalate TMDs crystals. The crystal is used as the cathode and a platinum foil is used as the anode. Copper crocodile clips are used to hold the electrodes in place. The electrolyte is formed by mixing tetrapropylammonium (TPA) bromide with propylene carbonate. A voltage is applied between the electrodes to intercalate the crystal with TPA^+ cations. An obvious volume expansion can be observed after intercalation, which confirms the successful intercalation of cations into crystal layers. The intercalated crystal is immersed in isopropanol overnight to dissolve and remove any residual bromide ions (Br^-). The dispersion is then subjected to the bath-

sonication to delaminate the intercalated crystals.

5.1.3 Size selection and solvent exchange

The obtained nanosheet dispersion either by LPE or EE contains un-exfoliated bulky nanosheets as well as ultra-small nanosheets. A size selection step is adopted after exfoliation by liquid cascade centrifugation.[122, 274, 275] The centrifugation is performed with 50 mL centrifuge tubes or 1.5 mL Eppendorf tubes by a Hettich Mikro 220R refrigerated centrifuge. The temperature during centrifugation is kept at 10 °C. The relative centrifugal force (RCF) can be found by

$$RCF = \frac{\omega^2 r}{g} = 106.4 f^2 \tag{5.1}$$

where ω is the angular speed, r is the rotor radius (90 mm), g is the gravitational force constant and f is the rotation rate in revolutions per minute (rpm). The rotation rate is referred to throughout the thesis for consistency.

To transfer the exfoliated nanosheets into a solvent that is suitable for the film formation, e.g., isopropanol, the dispersion is subjected to 6 krpm for 30 min. The sediment is collected and redispersed in fresh isopropanol using the sonic bath. This step is conducted twice to fully transfer the nanosheets to isopropanol.

5.2 Thin film fabrication

5.2.1 Spin coating

Spin coating is performed with WS-400A-8NPP/LITE and WS650 spin coaters in ambient. The spin coating speed is typically in the range of 500-4000 rpm and the coating time is set at 40 seconds. Two different coating methods are used: dynamic dispense and static dispense. For the dynamic dispense process, the ink is dispensed on top of the substrate ~2-3 cm after the spin speed reaches the set

value. The static dispense refers to the process that ink is drop-casted over the entire substrate evenly before spinning. The static dispense is especially useful for inks showing less wettability on the substrate surface. The film thickness is controlled by either multiple coatings or changing the spin speed.

5.2.2 Spray coating

A Harder and Steenbeck Infinity airbrush was attached to a Janome JR2300N mobile gantry to spray the dispersion over a programmed area at a line speed of 5 mm s^{-1} in ambient. The distance between the airbrush and the substrate is around 10 cm. The mobile gantry is supported by a compressed air supply and a compressed nitrogen gas with a pressure of ~3 bar is used as the carrier gas for the ink. The spray pattern was set by a controller by determining the start and end of the line dispense coordinates. The spray length is usually slightly larger than the desired length to guarantee the full substrate coverage. The pattern is usually in a square and the airbrush will move following a serpentine manner which is shown in **Figure 5.2**. The distance between adjacent dispensing lines is 2 mm. A heated platen is used evaporate excess solvent during spraying. Due to the effective cooling of the nitrogen gas flow, the temperature of the substrate during spraying is usually lower than the set temperature on the hotplate and never exceeds 100 °C, at least for the hotplate temperature set below 250 °C. The spray rate is adjusted according to the ink types. For example, a lower spray rate is used for water-based inks to guarantee a better solvent evaporation. The annealing step is performed in an argon-filled glovebox ([O_2]~1 ppm and [H_2O]~1-20 ppm) to remove the residual solvent trapped in the network.

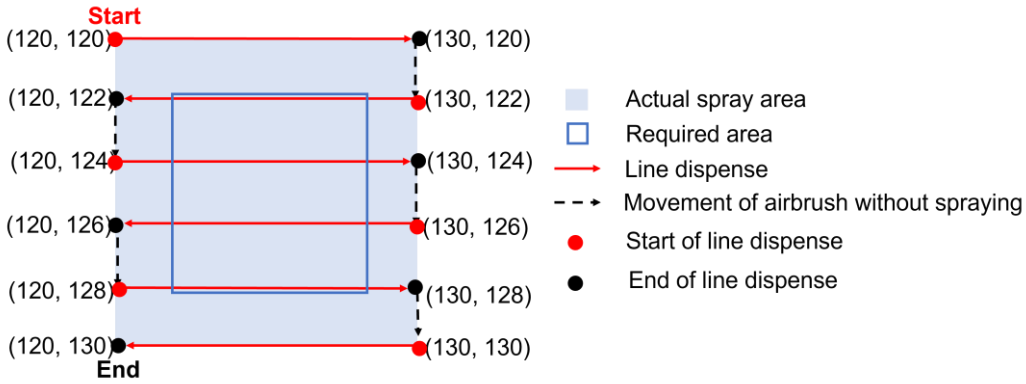

Figure 5.2 Spray pattern. A schematic illustration of the spray pattern following a serpentine movement.

5.2.3 E-beam evaporation

E-beam evaporation refers to a physical vapor deposition process that materials are vaporized upon a high energy electron beam scanning their surfaces. The formed vapor can condense onto the substrate and forms thin films. E-beam evaporation of metals is conducted with a Temescal with the model FC2000. A shadow mask is used to cover the substrate and determine the area of the device. The evaporation of aluminum, silver and gold is done under vacuum < 10^{-6} mbar, with evaporation rates of 2 Å s^{-1}, 1.5 Å s^{-1} and 1.5 Å s^{-1}, respectively. The metal deposition procedures are provided by the CRANN cleanroom technical officer. The device after the metal evaporation will be placed into glovebox for a further brief annealing at 80 °C to improve the contact quality.

5.3 Characterisations

5.3.1 Spectroscopic characterisations

UV-Vis-NIR spectroscopy

UV-Vis-NIR spectroscopy is a simple analytic technique for measurements of the attenuation of the electromagnetic radiation by certain substances.[276] The measurement can be done in the ultraviolet (UV), visible (Vis) and near-infrared

(NIR) regimes and will yield the optical spectra that contains information about optical properties and electronic structures of the material. Metallic, semiconducting, and insulating materials have distinct features in their spectra due to their different band structures. For example, an insulating material with a large bandgap will display a characteristic peak around UV regimes, while semiconductors with relatively smaller bandgaps will show an absorption edge at higher wavelengths. The spectra of metals will exhibit non-zero absorption intensity at any wavelength, which are illustrated in **Figure 5.3A**.

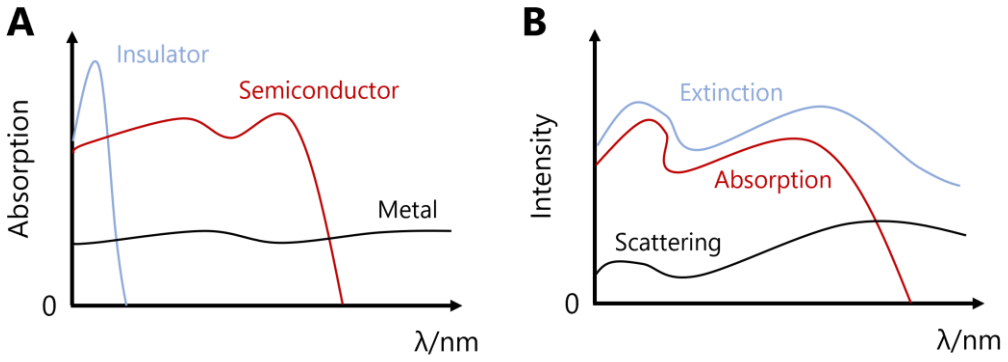

Figure 5.3 UV-Vis-NIR spectroscopy. (A) Illustration of absorption spectra of materials with different energy band structures, including a metal, a semiconductor and an insulator. (B) Extinction, absorption and scattering spectra of a semiconducting nanosheet dispersion.

UV-Vis-NIR spectroscopy can be used as a quantitative technique to determine the concentration of the molecules or nanomaterials in liquids or the thickness of the film on a substrate if the absorption coefficient at a certain wavelength is known. The quantitative analysis can be realized as the measured absorption intensity, i.e., optical absorbance $A_{opt}(\lambda) = -\log T(\lambda)$, follows a linear relationship with the concentration of the dispersed material in the liquid, which is known as the Beer-Lambert Law[277]:

$$A_{opt}(\lambda) = \alpha(\lambda) C_{NMs} l_{light} \tag{5.2}$$

where $\alpha_{opt}(\lambda)$ and C_{NMs} are absorption coefficient and nanomaterial concentration

in the liquid. l_{light} is the light path length and refers to the cuvette length for a dispersion or the film thickness for a solid-state sample. However, for nanosheet containing dispersions, material sizes can range from tens of nanometers to a few microns. This will introduce scattering processes that will depend on the size of the nanosheet and the wavelength.[122, 123] The commonly collected spectrum is usually referred to as an extinction spectrum and contains information on both absorption and scattering $Ext(\lambda) = Abs(\lambda) + Scat(\lambda)$, which is shown in **Figure 5.3B**. As a result, the spectra can be used to derive empirical metrics regarding the dimensions of nanosheets.[122, 123] The average size and thickness of nanosheets in size-selected dispersions can be obtained by the UV-Vis-NIR spectroscopy. This provides a quick and facile method better than time-consuming counting methods based on the electron microscopy.

In this study, a UV-Vis-NIR spectrometer Cary 1050 is used to collect the extinction and absorption spectra of dispersions and another spectrometer Cary 50 is used to collect the transmission spectra of the thin films on glass substrates. Prior to the sample measurement, the baseline is auto-corrected and the transmission without a sample is automatically adjusted to 100%. For dispersions, the solvent and nanomaterial dispersions are both contained in 1 cm optical length quartz cuvette and are measured to obtain the extinction and absorption spectra. The absorption spectrum is obtained by using an integrating sphere to collect the scattered light. The nanomaterial dispersions contain information from both solvents and nanomaterials. Therefore, the directly measured extinction and absorption spectra of nanomaterial dispersions will need to be corrected by the corresponding spectra of solvents. For thin films on glass substrates, the transmission spectra are collected and are converted into absorbance spectra. The absorbance spectrum of the thin film can be obtained after removing the absorbance of the glasses.

Raman spectroscopy

In 1928, a physicist Chandrasekhara Venkata Raman discovered a phenomenon that the scattered light from a molecule upon a monochromatic light illumination will show a shift in its wavelength compared with that from the incident light, which is known as the Raman effect.[278] The wavelength change of the scattered light will depend on the chemical composition and structure of the material. Therefore, Raman spectroscopy is developed based on this phenomenon that each material will have its unique response which can be regarded as a fingerprint, allowing identification of chemicals.

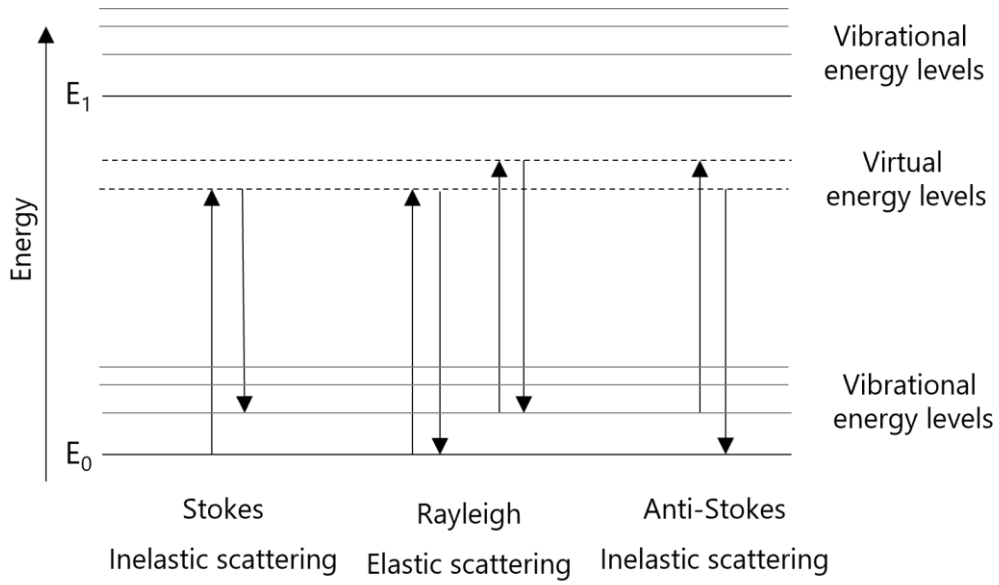

Figure 5.4 Raman spectroscopy. An energy diagram for Raman scattering processes. Adapted from Ref. 279.

Upon illumination of a monochromatic light, there will be two light scattering processes: elastic and inelastic[279, 280], which are illustrated in **Figure 5.4**. The elastic process refers to the case that the net exchange of the energy between the material and the incident light is zero, that frequency of the scattered light will be identical to that of the incident light, which is known as Rayleigh scattering. For the inelastic processes, there will be two cases. In the first case, the material loses vibrational energy upon illumination and the net exchange of the energy for the

scattered light is positive, causing a shift to higher frequencies, which is known as anti-Stokes Raman scattering. Conversely, Stokes Raman scattering refers to the case that the material gains energy from the incident light and the frequency of the scattered light will be lower. The frequency shift Δν can be found by

$$\Delta\nu = \frac{1}{\lambda_i} - \frac{1}{\lambda_s} \tag{5.3}$$

where λ_i and λ_s are the wavelengths of the incident light and the scattered light, respectively. For 2D nanosheets, Raman spectroscopy can be used to study the layer number dependent properties[281], defects[106], doping levels[282], and chemical compositions[283].

The Raman spectra are acquired using the Renishaw inVia Raman microscope. A laser with wavelengths of 532 nm or 632 nm is used to excite the sample using a 100× objective. A grating of 1800 grooves/mm is used to disperse the signal onto the detector. The sample for the Raman spectroscopy is prepared by drop-casting the dispersion on pre-heated silicon wafers coated with 300 nm of silicon dioxide. The Raman spectroscopy measurements are conducted by Dr. Tian Carey.

5.3.2 Morphological characterisations

Atomic force microscopy

Atomic force microscopy (AFM) was firstly developed by Binnig, Quate and Gerber in 1986[284], which was proven to be able to image the topographic information of a material surface on atomic levels. A typical AFM setup is shown in **Figure 5.5**. A laser beam is focused on the cantilever with a tip. When the tip experiences an external force, the cantilever will bend towards the opposite directions as to the experienced force direction. The bending behavior will be manifested by the reflected beam change that will be captured by the photodetectors, which are position sensitive. The optical signal will be fed into a

controller to tune the bending of the cantilever through a piezo actuator. By scanning the surface, the surface height at each point can be recorded and eventually can be integrated together with spatial ordinates to create a three-dimensional image of the surface.

For nanomaterials, especially nanosheets, acquired AFM images can be used to find the statistical information of the size and thickness distributions. The statistical results can be obtained by manually counting the thickness and lateral size of all nanosheets in an AFM image. The required counting number of nanosheets is at least 100 to guarantee the accuracy. However, the measured nanosheet thickness may sometimes be over-estimated, at least for LPE nanosheets. The measured thickness from AFM could be a sum of the nanosheet thickness and the residual surfactants on the surface or beneath the nanosheet. As the measurement is performed in ambient conditions, there will be an ultra-thin layer of water on the surface, which will also contribute the measured thickness due to the capillary force between the water surface and the tip.[285] The solvent or the used chemicals for exfoliation may intercalate into layers and also increase the thickness.[286] The measurement itself will also introduce some errors due to the dangling bonds on the silicon-based tips or tip-sample interactions.[285] For example, the monolayer thickness for TMDs is 0.65 nm[287], however, the measured thickness for LPE TMDs monolayers is 1.9 nm.[122, 123] Increased monolayer thickness from measurements is also observed for LPE graphene[288] and others.[160, 289] Therefore, to obtain the number of layers for LPE nanosheets, the measured monolayer thickness should be used rather than the theoretical one.

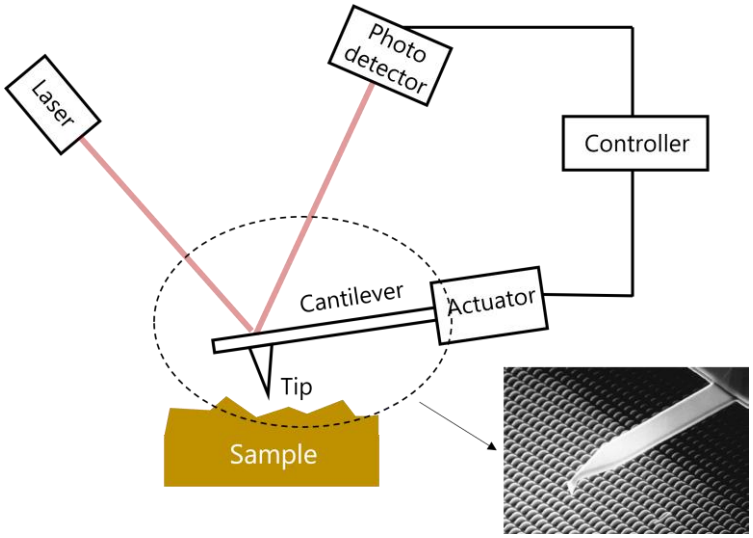

Figure 5.5 Atomic force microscopy. Schematic illustration of the AFM setup and an image of the cantilever and the tip. Adapted from Ref. 290 and Ref. 285.

AFM is performed using a Bruker Multimode 8 microscope to determine the dimensions of 1D and 2D nano-objects. Materials after dilution and bath-sonication are drop-cast onto Si/SiO_2 and are annealed to remove residual solvents. The samples are scanned using OLTESPA R3 cantilevers in ScanAsyst mode. Gwyddion software is used to process the raw image. AFM images and statistical results are acquired by Dr. Jose Munuera and Dr. Tian Carey.

Electron microscopy

As the conventional optical microscope relies on the visible light radiation, its resolution is proportional to the wavelength (400-700 nm). Therefore, this technique is insufficient to distinguish any material less than hundreds of nanometers.[291, 292] In the field of nanomaterials, the morphology of a material and its networks clearly require higher-resolution microscopy techniques to reveal their features. The standard technique for this is the electron microscopy. Employing a high energy electron beam, the resolution is inversely proportional to the square root of the accelerating voltage.[293] Therefore, the resolution could approach sub-Angstrom theoretically[291], although the resolution in reality will be

affected by other factors. The obtained resolution for the electron microscopy is orders of magnitude smaller for the optical microscopy. The magnification range can be varied from 10 to millions, which enables characterisations of features with different length scales. Importantly, electron microscopy uses electrons to interact with samples. The interactions with different elemental atoms are unique and will produce distinctive signals, which could provide both chemical and structural information of the sample.[291]

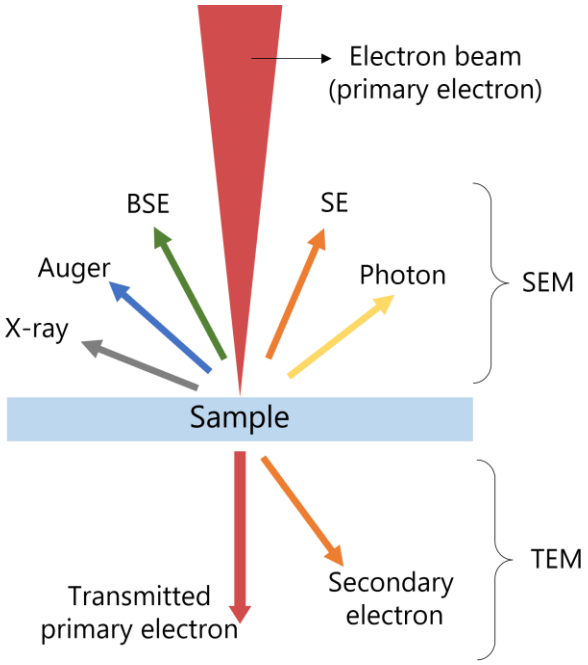

Figure 5.6 Electron microscopy. A schematic illustration of the interactions between the electron beam and the sample. Adapted from Ref. 291.

There are mainly two types of electron microscopy: scanning electron microscopy (SEM) and transmission electron microscopy (TEM), both utilizing a highly focused electron beam (primary electrons) onto samples under high vacuum conditions. SEM is used for examining the material surfaces, which the electron beam will scan sequentially across the surface. The signal generated at each point, including secondary electrons (SEs), backscattered primary electrons and X-rays, will be collected by the photodetector and combined into an image with the

known location of each signal.[291] A schematic illustration of the electron beam and sample interaction is shown in **Figure 5.6**. The SEM images were collected by a Zeiss Ultra Plus at accelerating voltages of 2 kV. SEM images were collected by Dr. James Garcia, Eoin Caffrey, and Emmet Coleman.

For TEM, the electron beam is incident onto a specific area of the sample, and the transmitted electrons through the sample will be collected by a photodetector to form an image. The required electron energy for TEM (8-300 keV) is much higher than that for SEM (1-30 keV) to allow the electron to penetrate through the sample. For TEM imaging, a JEOL 2100 microscope operated at an accelerating voltage of 200 kV was used. The grids were prepared by drop-casting 10 µl of dispersion on Holey carbon grids (400 mesh). The grids were dried in a vacuum oven at 70 °C overnight prior to the TEM observation.

Focused ion beam microscopy

The focused ion beam (FIB) technique was developed back in 1970[294] and was later widely used in combination with SEM in the field of electronics. This technology could realize milling and deposition of materials in local areas with a high precision, and can be therefore used for device fabrication, mask repair, and failure analysis, etc.[295] The FIB ion column is similar to a SEM electron beam column, while the difference is that the former uses gallium ions (Ga^+) instead of the electron beam. The ion beam can be generated by applying a strong electric field and positively charged ions will emit under this field from a liquid gallium cone. The energy of the ion beam is usually around 10-50 keV with the beam current varying from 1 pA to 10 nA.[295]

FIB-SEM is adopted in this thesis to acquire cross-sectional images of the devices. Before milling, a layer of organometallic precursor molecules is introduced on top of the sample surface and the molecules will dissociate under

the ion beam, where volatile organic components will be removed from the sample and a metallic layer will be left on the surface. The metallic layer could smooth the sample surface and protect the sample from destructive milling processes. The ion beam is then applied onto the surface that will allow displacement and sputtering of the atoms, i.e., the milling process. In this way, the cross-section of the device can be revealed and observed by a standard SEM setup. The cross-sectional images of devices were obtained by a Zeiss Auriga dual-beam FIB-SEM microscope. The accelerating voltage was 30 kV. The FIB-SEM characterisation was performed by Dr. Cian Gabbett and Luke Doolan.

5.4 Electrical measurements

Current-voltage characteristics

The current-voltage (*I-V*) characteristics of the devices are measured by Keithley 2612A and 2400. To find the optoelectronic response of the device, a solar simulator Newport 96000 equipped with an AM1.5D filter is used. The light intensity F of the solar simulator is calibrated to 1000 W m^{-2} by a reference silicon solar cell (RQS3677) with an active area of 2 cm × 2 cm from Prof. David McCloskey group. The illumination is applied to the entire substrate without additional masks to define the illumination area. To vary the light intensity, several neutral density filters (O.D.: 0.1, 0.3, 0.5 and 1) are used, which correspond to transmittances of 79%, 32%, 50%, and 10%, respectively. To record the temporal photo-responses, a metal foil was used as a shutter and was manually placed and removed on top of the device to simulate light “on” and “off” states.

There is nothing permanent except change.

Heraclitus

Chapter 6 Vertical Heterostructures: From Electrode- To Bulk-Limited Electrical Behaviors

6.1 Introduction

Solution-processed semiconducting nanosheet networks could be used for various electronic applications. The simplest electronic device structure is the metal-semiconductor-metal (MSM) structure, where metal electrodes can be fabricated onto the surface of semiconductor to allow the carrier transport along the in-plane direction of the semiconductor. Such type of devices is referred as lateral or in-plane (IP) devices. However, IP devices based on LPE semiconducting nanosheet networks usually exhibit a large series resistance R_s owing to low network conductivities and large channel lengths. Such devices are regarded as bulk-limited as the contact resistance R_c of the metal-semiconductor interface is much less significant than the series resistance from the nanosheet network itself ($R_s >> R_c$). As a result, IP devices will show linear *I-V* characteristics and it is challenging to observe any electrical rectifying behaviors (e.g., Schottky contact) from the metal-semiconductor interface.

In contrast with IP devices, vertical (or out-of-plane, OoP) devices that the semiconductor layer is vertically sandwiched between two metal electrodes could significantly reduce the channel length and decrease the series resistance from the channel. Therefore, OoP devices could potentially display electrical behaviors arising from the metal/semiconductor interfaces, i.e., Schottky contacts that are known to be limited by the electrode, when R_s is comparable with R_c.

However, the difficulties to fabricate OoP devices may be under-estimated so far. First of all, solution-processed thin films fabricated from either precursor solutions or nanoparticle dispersions may leave pinholes on the surface. These pinholes may be induced by the surface impurities, the dispersion or the fabrication process. Second, the resultant nanosheets from LPE usually exhibit irregular shapes and are rigid in nature due to their relatively low aspect ratios. The solution-processed nanosheet networks will display porous structures. The pinhole and porosity problems could together cause issues during fabricating the top electrode. For example, evaporation of the metal contacts is widely adopted and the metal vapors would diffuse into the pores and form electrical shorts with the bottom electrodes. Moreover, if the top electrode is also solution-processed from metal nanoparticle dispersions, these nanoparticles could re-disperse with the nanosheet networks, which may also cause electrical shorts or decrease the actually semiconducting layer thickness. Apparently, the electrical shorts can be overcome by increasing the thickness of the nanosheet network. However, as most optoelectronic applications in fact require only tens of to hundreds of nanometers thick semiconductor films[296-298], it is critical to fabricate MSM devices with a thinner semiconducting layer. Previous attempts have shown that solution-processed capacitors with a vertical graphene/insulating nanosheets/graphene structure requires the dielectric layer to be above ~1.6 μm to avoid the electrical shorts.[299, 300] Bessonov et al. achieved vertical MSM heterostructure with liquid-liquid interface assembled thin films of TMDs nanosheets and silver nanomaterials as top and bottom electrodes. The minimum thickness without shorts is down to ~50 nm but such assembly method is not scalable and limited to small-area devices.[301] There may be solutions such as mixing the nanosheets with polymers to fill the pores.[225, 302] However, this may result in a change of the electronic properties of the nanosheet network and is not adopted here.

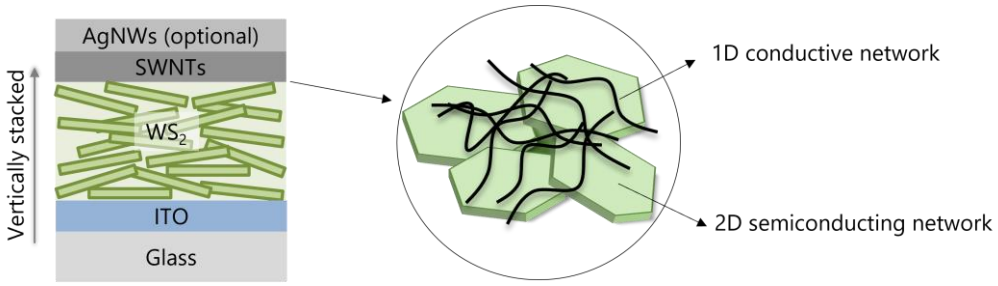

Figure 6.1 Vertically stacked devices. The schematic demonstration of the proposed device structure.

In this chapter, to fabricate vertically stacked MSM devices, a novel method is proposed to use 1D metallic nanomaterials, such as nanotubes and nanowires as the solution-processable top electrode. These 1D metallic nanomaterials can be dispersed in liquids and form processable inks for thin film fabrications. Importantly, due to their high aspect ratios and flexibility, they could stand over the nanosheet pores as illustrated in **Figure 6.1**, forming a bridge to avoid the electrical shorts problem. Meanwhile, they could form a conductive network to be used as electrodes. Here, as shown in the figure, commercially available transparent ITO glass is used as the bottom electrodes and LPE WS_2 is fabricated into thin films as the semiconducting layer, and the top electrode is made of single-walled carbon nanotubes and silver nanowires, which complete the MSM device structure. The electrical behaviors of OoP devices are investigated and compared with those from IP ones by performing a WS_2 film thickness study. It is also found that the electronic behavior of the device will also depend on the ink composition of the top electrodes, which is ascribed to the doping effects from the surfactants.

6.2 Experimental procedure

6.2.1 Material preparation

WS_2 dispersion was prepared by probe sonicating the powder (Alfa Aesar, 99.9%) in IPA (HPLC grade). The powder was mixed with IPA with a concentration of 30

mg mL^{-1} in a metal beaker and being sonicated by a replaceable head tip for 1 h at 40% amplitude with a pulse of 6 s on and 2 s off. The dispersion was centrifuged at 2 krpm for 1 h and the supernatant was discarded. The sediment was re-dispersed with IPA and being sonicated for 8 h at 40% amplitude with a pulse of 6 s on and 2 s off. The metal beaker was kept in water bath cooling during sonication. The size-selection of nanosheets was done by liquid cascade centrifugation method. First, the dispersion was subjected to 2 krpm centrifugation for 2 h and the supernatant was collected. Then, the supernatant was further centrifuged at 6 krpm for 2 h and the sediment after centrifugation was collected and re-dispersed with IPA as the WS_2 ink for further characterisations and device fabrication.

SWNTs aqueous dispersion was prepared by sonicating P3-SWNTs (Carbon Solutions) in an aqueous surfactant solution. 20 mg SWNTs powder was dispersed in 40 mL deionized water containing 200 mg sodium dodecyl benzene sulfonate (SDBS, Sigma-Aldrich, technical grade). The dispersion was sonicated by a tapered tip for 0.5 h at 30% amplitude with a pulse of 3 s on and 3 s off. The dispersion was then centrifuged for 2 h at 6 krpm. The supernatant was collected for device fabrication.

SWNTs IPA dispersion was obtained by probe-sonicating 2 mg P3-SWNTs powder in 40 mL IPA for 4 h at 30% amplitude with a pulse of 3 s on and 3 s off. The final dispersion was used without centrifugation. A low concentration and longer sonication time ensure that the dispersion can be stable at least for a few hours, which is required for spray coating.

AgNWs IPA dispersion (Sigma-Aldrich, 5 mg mL^{-1} in IPA, diameter 40 nm and length 35 μm) was diluted in IPA with a concentration of about 0.5 mg mL^{-1}.

6.2.2 Device fabrication

Indium tin oxide (ITO) coated glass substrate (Ossila, 20 Ω sq^{-1}) was used as bottom electrode. To pattern it, Kapton tape was used to cover the ITO surface. ITO was immersed in diluted hydrochloride acid (Sigma-Aldrich, ACS reagent, 37%) aqueous solution at 80 °C for 5 min to create one long 25 mm × 6 mm ITO strip in the middle of the glass and four ITO patches on each corner of the slide (**Figure 6.2**). The distance between the strip and each patch is 1-2 mm. The etched ITO glasses were cleaned with Hellmanex aqueous solution, water, and IPA sequentially in sonic bath for 10 min each. The substrates were blow dried by a stream of nitrogen gas. The glass substrates were cleaned in the same way.

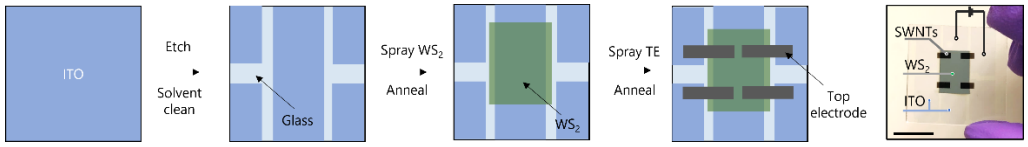

Figure 6.2 Device fabrication by spray coating. Schematic demonstration of the device fabrication process. A photograph of the obtained device is shown.

For spray coating, the dispersion (except AgNWs) was sonicated in sonic bath for 10-20 min before spraying. The AgNWs dispersion was briefly sonicated and shaken before spraying. The WS_2 film was obtained by spraying ~1 mg mL^{-1} WS_2 dispersion on solvent-cleaned ITO at 100 °C with a spray rate of ~0.5 mL min^{-1}. The spray pattern is set to be a square with a size of 15 mm×15 mm to make sure that the edge of ITO is covered with nanosheets. The films were annealed at 200 °C in glovebox ($[O_2]/[H_2O]$< 0.8 ppm) for 30 min and were allowed to cool down naturally before depositing top electrodes. A laser-cut shadow mask was used to deposit top electrode. It was placed on the substrate and its position was fixed by attaching Kapton tape around the mask onto the substrate. The hotplate was set to 150 °C for SWNTs and AgNWs IPA dispersion and 250 °C for SWNTs aqueous dispersion. 2 mL 0.05 mg mL^{-1} SWNTs IPA dispersion was sprayed at a

rate of ~0.1 mL min^{-1}, while 0.5 mL 0.5 mg mL^{-1} aqueous dispersion was sprayed at a rate of ~0.015 mL min^{-1}. The final devices were annealed at 80 °C for 30 min in glovebox and left overnight to remove residual solvents and stabilise the performance. Devices with AgNWs were further annealed at 120 °C for 15 min to fuse the junctions. No additional surface treatment was conducted except annealing. The device area was defined as the overlapping region between ITO, WS_2, and top electrodes, which is about 2-4 mm^2. The device fabrication process and a photo of the obtained device are shown in **Figure 6.2**.

6.2.3 Characterisations

Electrical

The *I-V* characteristics were collected in ambient environment under dark conditions by using the Suss probe station connected with Keithley 2612A from -3 to 3 V (the first sweep) and from 3 to -3 V (the second sweep). There was no pause between these two sweeps.

AFM

Height and length profiles across 50 I-SWNT and S-SWNT were extracted to determine their diameters and lengths. The length and thickness of WS_2 were extracted with more than 100 nanosheets.

Scanner

The sprayed WS_2 film on glass was optically scanned by an Epson Perfection V700 photo flatbed scanner. The spatial resolution is 6400 dpi and spectral resolution is 48 bits. The point resolution of the image is about 4 μm.

Profilometry

The thickness and average roughness of films were measured by a Bruker Dektak

profilometer. The line profile was taken with 2000 μm length and a resolution of ~100 nm/sample. More than 4 profiles were taken for each sample. For each measurement, we can read the measured height versus the profile distance on the software. The region corresponding to the thin film was chosen and a function in the software can be used to auto-calculate the mean thickness and average roughness over this region. The obtained thickness and roughness were further averaged to find their mean values.

6.3 Results and discussion

6.3.1 Material characterisations

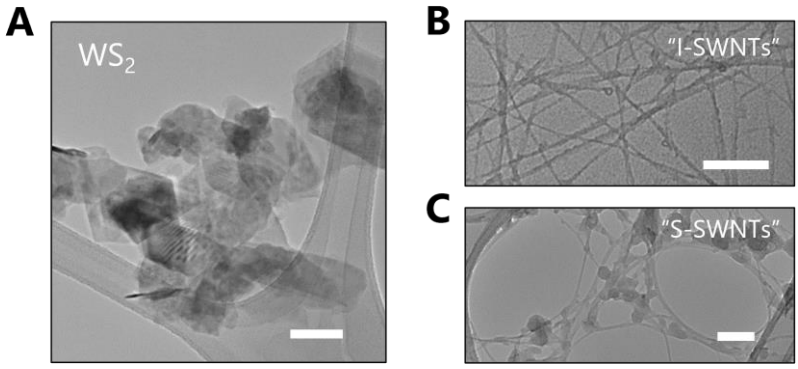

Figure 6.3 TEM images of materials. (A) Liquid exfoliated and size selected WS_2 nanosheets, (B) and (C) are SWNTs dispersed in IPA and SDBS/H_2O, respectively. Scale bar: 200 nm.

The WS_2 nanosheet dispersion was prepared by LPE in IPA. Using IPA allows the formation of a reasonably stable dispersion with a relatively high yield of nanosheets and, because of its low boiling point, facilitates further device fabrication without solvent exchange. As is typical for LPE, immediately after exfoliation the dispersion contained poly-disperse nanosheets with a wide distribution of lateral size and thickness[124]. Thus, a two-step liquid cascade centrifugation (LCC) procedure was used to narrow the distribution[123, 275]. Since large and thick nanosheets tend to be rigid,[189] and so may lead to a nanosheet network with high porosity and large pores, they were discarded by centrifuging

the dispersion after exfoliation at 2 krpm for 2 h. Meanwhile, to avoid few-layered WS_2 with thickness-varying bandgaps[303, 304], small and thin nanosheets were also discarded by a 6 krpm centrifugation. The transmission electron microscopy (TEM) image of exfoliated nanosheets obtained after LCC is shown in **Figure 6.3A**. Many nanosheets were seen, all similar in size, confirming our successful exfoliation and size-selection.

Two types of SWNTs dispersion were obtained by probe sonicating P3-SWNTs in IPA and SDBS aqueous solution (SDBS/H_2O), which are termed as I-SWNTs and S-SWNTs, respectively. **Figure 6.3B-C** show the morphology of SWNTs in IPA and SDBS/H_2O, respectively. Narrow and straight bundles were found in TEM images, indicating the SWNTs were well-dispersed in both media. The I-SWNTs present clean surfaces while polymeric residuals were visible on the surface of S-SWNTs possibly due to SDBS, which is notoriously difficult to be removed.

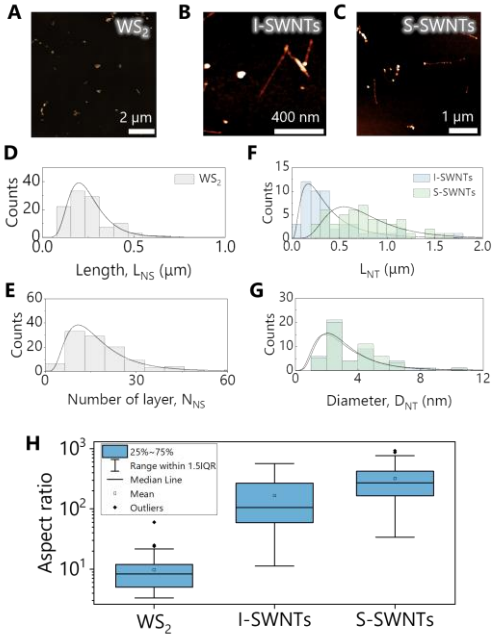

Figure 6.4 AFM characterisations of materials. AFM images of WS_2, I-SWNTs, and S-SWNTs are given in (A-C), respectively. Statistical results from AFM for WS_2 and SWNTs are shown in (D-E) and (F-G), respectively. The aspect ratios for all three materials are shown in (H).

To determine the size and thickness distribution of nanosheets, the WS_2 and SWNTs dispersions were characterised by AFM. Their typical AFM images are shown in **Figure 6.4A-C**. For WS_2, the statistical results were obtained by counting the size and thickness of more than 100 individual nanosheets and are shown in **Figure 6.4D-E**. Most of the nanosheets are shorter than 500 nm with a mean length $\langle L_{NS} \rangle$ of 250 nm, which is in good agreement with the TEM images. The number of layers, N_{NS}, was obtained by dividing the nanosheet thickness by the apparent monolayer thickness (1.9 nm).[305] The mean layer number is $\langle N_{NS} \rangle$ =17.5. The AFM result indicates the obtained WS_2 nanosheets are mostly multi-layered with a relatively medium size compared to its bulk counterpart, consistent with the requirements as mentioned above. The SWNTs were also characterised with AFM and the statistical results are shown in **Figure 6.4F-G**. The mean length $\langle L_{NT} \rangle$ of S-SWNT is 771 nm, while that for I-SWNTs is 405 nm. The shorter nanotubes are caused by a long-time sonication in IPA. The mean diameter of nanotube bundles $\langle D_{NT} \rangle$ is around 3.2 nm for both I-SWNTs and S-SWNTs. The statistic results of aspect ratios (AR) for nanosheets (L_{NS}/t_{NS}) and for nanotubes (L_{NT}/D_{NT}) are shown in **Figure 6.4H**. The average AR for nanosheet is ~10. This AR value is relatively small compared to values of 20-40 reported previously for aqueous TMD dispersions,[124] probably due to the use of IPA in this study. The mean AR for S-SWNTs and I-SWNTs are ~166 and ~322 respectively, which are both much larger than that of WS_2. The aspect ratio for silver nanowire is largest and is 875 according to the specification sheet from the supplier.

UV-Vis-NIR absorption spectra of WS_2, I-SWNTs and S-SWNTs dispersions were collected in the integrating sphere to remove the influence of the scattering and the obtained spectra normalized, which are shown in **Figure 6.5A**. The characteristic A-exciton peak for WS_2 can be found at 637 nm. The absorption

peaks for I-SWNTs and S-SWNTs can be observed at around 700 nm and 1022 nm, corresponding to M_{11} metallic and S_{22} semiconducting characteristic peaks[306] respectively, with no obvious dependence on dispersing medium.

The WS_2 and SWNTs films drop-casted on Si/SiO_2 substrates were characterised by Raman spectroscopy, which are shown in **Figure 6.5B**. The WS_2 characteristic modes at 349.5 and 418.5 cm^{-1} are found and correspond to its in-plane E^1_{2g} and out-of-plane A_{1g} modes. For both SWNTs, characteristic peaks such as the radial breathing mode (RBM) at 170 cm^{-1}, disorder D band at 1345 cm^{-1}, and graphite (G) band at 1593 cm^{-1} can be seen.[307] There is very little difference in G band position for I-SWNTs and S-SWNTs, implying minimal doping by SDBS relative to IPA. Overall, the optical characterisations of nanosheets and nanotubes show consistent results with previous reports.

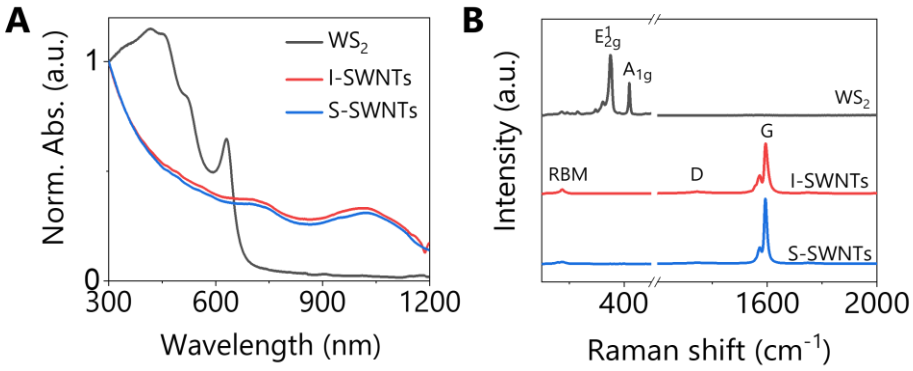

Figure 6.5 Optical characterisations. UV-Vis-NIR absorption spectra (A) and Raman spectra (B) of WS_2, I-SWNTs and S-SWNTs.

6.3.2 Morphological characterisations

As this project mainly focuses on devices in stacked geometries where current flow is out-of-plane. To this end, vertically stacked, sandwich structure-type devices were sequential spray coated. These devices consist of a patterned ITO bottom electrode, then a network of semiconducting WS_2 nanosheets, followed by a top electrode. A network of carbon nanotubes was used as the top electrode,

followed in some cases by a network of silver nanowires (AgNWs) as a current collector. To make it clearer, other than the case of the single-layer SWNTs top electrode, there will be double-layer structured top electrodes with a structure of SWNTs/AgNWs. The function of these electrodes will be further discussed below. A schematic of the device structure is shown in **Figure 6.1** with a device structure ITO/WS_2/SWNTs/AgNWs (optional).

A common problem during sequential liquid-based depositions is the redispersion of the previously deposited layer during the deposition of the next layer before the deposited solvent has dried. This effect probably limits the minimum thickness of the semiconducting layer (i.e. the channel length) that can be achieved without shorts appearing between ITO and SWNT layers, as well as device reproducibility. It is believed that the likelihood of the formation of vertical shorts is highest when the top electrode is deposited by evaporation or sputtering. Metal atoms can diffuse through the porous interior of the network, perhaps at locally thin regions, leading to the formation of metallic filaments which can short the device. To avoid electrical shorts as well as achieving low semiconducting layer thickness, it is proposed that this problem may be mitigated by using networks of high-aspect ratio conducting nanomaterials, such as nanotubes or nanowires, as the top electrode. Such extended structures could sit on top of the semiconducting nanosheet network without penetrating the pores of the network, bridging any locally thin regions and so avoiding the formation of vertical shorts.

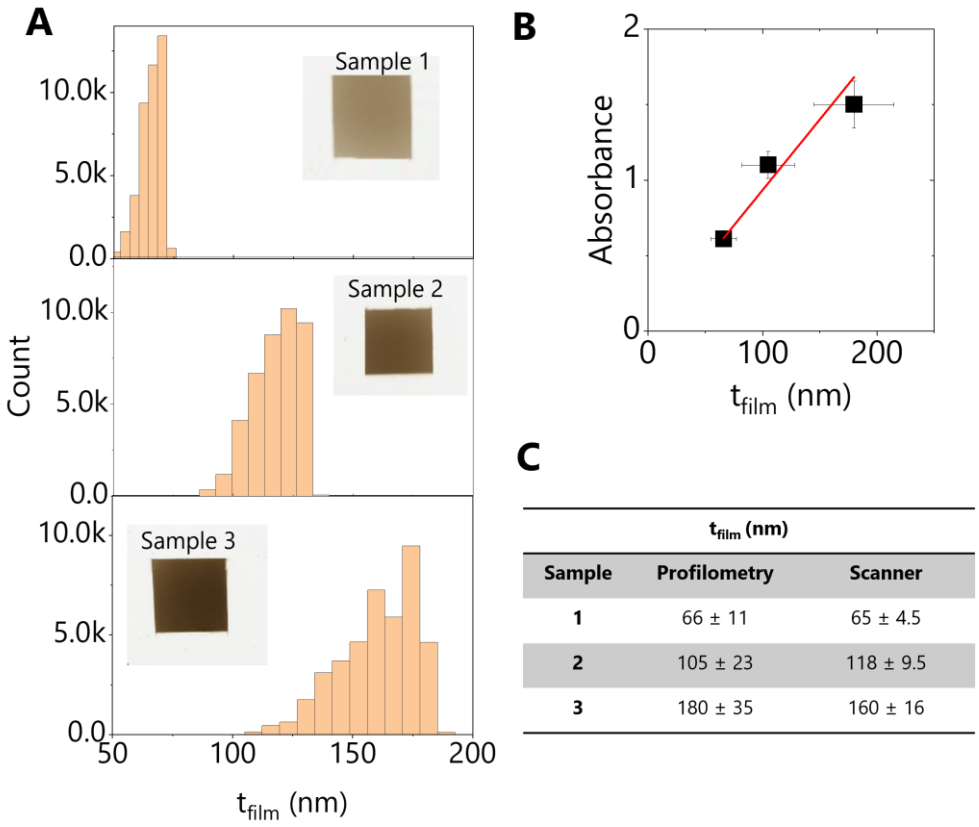

	t_{film} (nm)	
Sample	**Profilometry**	**Scanner**
1	66 ± 11	65 ± 4.5
2	105 ± 23	118 ± 9.5
3	180 ± 35	160 ± 16

Figure 6.6 Optical characterisations on sprayed WS_2 films. (A) Histogram plots of three sprayed WS_2 films with different thicknesses on glasses. The optically scanned image of the film is given in each plot. (B) The extracted absorbance is plotted against the film thickness. (C) A comparison of measured thicknesses by profilometer and converted thicknesses from scanned images.

The morphology of a thin WS_2 nanosheet network on glass slides was investigated by a flatbed optical transmission scanner. The optical signal was converted on a pixel-by-pixel basis into film thickness and searched for localized regions of negligible thickness. The obtained images (**Figure 6.6A** insets) were uploaded into Image J and split into 3 channels: red, green, and blue. The blue image was kept and used further as it allows minimum interference fringes with glass. The image was then opened by Origin and converted into data matrix. There were ~2000 columns of data obtained after conversion and 20 columns for every 100 columns were picked. These columns were combined into one column. These optical signal values were converted into transmittance using the following

equation:

$$T = -0.01622 + (4.2922 \times 10^{-6} S) + (1.6598 \times 10^{-10} S^2) \quad (6.1)$$

where S is the optical signal and T is the transmittance. The transmittance of glass substrate was obtained following the above step and the mean transmittance of the glass substrate $\langle T_{glass} \rangle$ is obtained to be 88.91%. The transmittance of WS_2 film T_{WS_2} is obtained by $T_{WS_2+glass}/T_{glass}$, which is further converted into absorbance. The mean absorbance for three films with different thicknesses t_{film} are obtained and plotted against t measured by profilometry in **Figure 6.6B**. As A should scale linearly with t, it allows us to find the following equation:

$$t = \frac{A}{9.34 \times 10^{-2}} \quad (6.2)$$

The absorbance for each sample was converted into t_{film} by using equation 6.2. The histogram plots of 3 samples are shown in **Figure 6.6A**.

In this way, it can be found that there are no locally thin regions (pinholes) of size larger than the resolution of the scanner (~10 μm), even when probing a relatively large area ~1 cm^2 for film thicknesses as low as 66 nm. This supports the assessment that continuous and uniform nanosheet networks were obtained by spray coating. The mean film thicknesses $\langle t_{film} \rangle$ determined by profilometry and optical scanner are shown in **Figure 6.6C**. The thickness for each sample is close measured by these two methods.

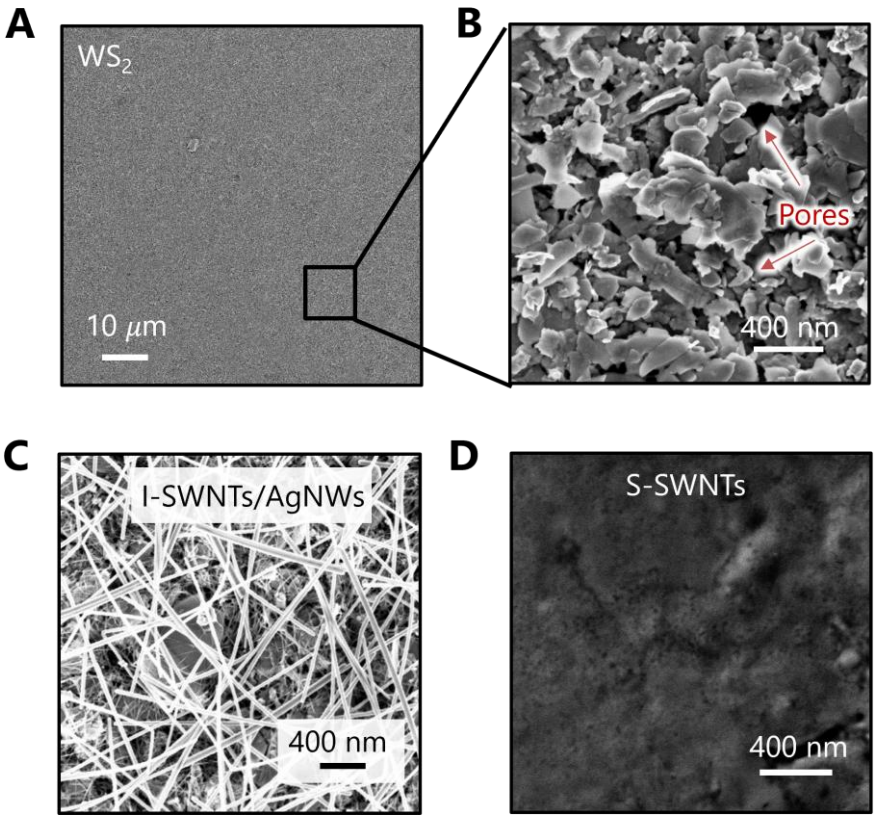

Figure 6.7 SEM characterisation. (A) The top-view SEM image of WS_2 nanosheet networks, and its magnified image is given in (B). (C) and (D) are top-view SEM image of I-SWNTs/AgNWs and S-SWNTs on top of the nanosheet networks, respectively.

The morphology of the sprayed nanosheet networks and devices was further investigated by SEM. Top-view SEM images of WS_2 nanosheet networks are shown in **Figure 6.7A-B**. The low-magnification image shows that nanosheets are uniformly deposited over a large area and form networks that appear to be pinhole-free. The zoomed-in SEM image shows that nanosheets are randomly stacked together, forming a porous, disordered network. The top-view SEM images of obtained devices with I-SWNTs/AgNWs and S-SWNTs top electrodes are shown in **Figure 6.7C-D.** The I-SWNTs/AgNWs are uniformly distributed on the surface of the WS_2 film and form an open, porous structure. WS_2 nanosheets are still visible through this double-layered electrode. In contrast, S-SWNTs are densely packed on the top of WS_2 films due to the presence of surfactants.

The thickness and morphology of these top electrodes were also characterised by profilometry. To do this, I-SWNTs, S-SWNTs and I-SWNTs/AgNWs films were sprayed directly onto pre-cleaned glass slides. More than four line profiles were conducted at different locations of the thin films from the edge to the interior. The thickness and average roughness of the thin film is recorded for each measurement over the film. The obtained thickness and averaged roughness are further used to find the average values. The It is found that the mean film thickness $\langle t_{film} \rangle$ of the I-SWNTs film is 79±23 nm but it shows a high average roughness $\langle Ra \rangle$ of about 58±31 nm. Such large $\langle Ra \rangle$ may indicate that aggregates formed during spraying due to instability of SWNTs in IPA. The thickness of the S-SWNTs film is 647±34 nm and has a $\langle Ra \rangle$ of about 49±24 nm, consistent with good network uniformity. The $\langle t_{film} \rangle$ of I-SWNTs/AgNWs film is 257±21 nm with a $\langle Ra \rangle$ of 57±34 nm. It should be possible to further optimize the roughness in the future. However, for now it is good enough to be used as the top electrode.

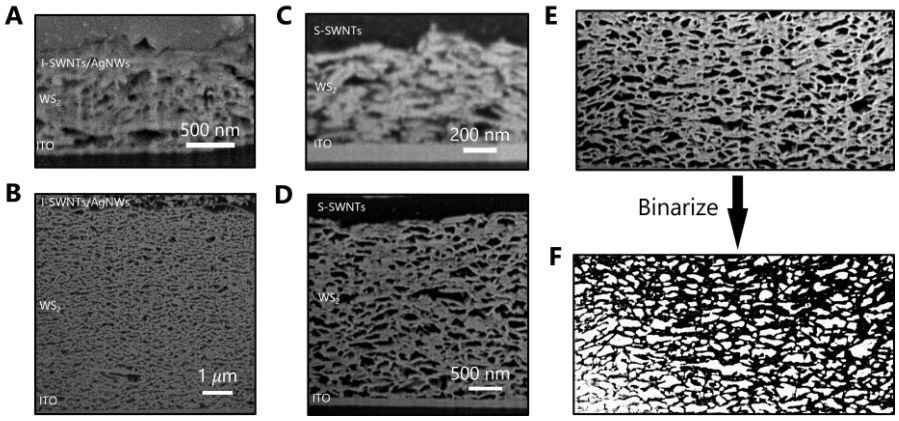

Figure 6.8 FIB-SEM characterisations on hetero-stacks. (A) and (B) are cross-sectional SEM images of two ITO/WS_2/I-SWNTs/AgNWs devices with different WS_2 film thicknesses, respectively. (C) and (D) are cross-sectional SEM images of two ITO/WS_2/S-SWNTs devices with different WS_2 film thicknesses, respectively. (E) A region of the cross-sectional SEM of the WS_2 film. (F) The binarized image of (E) using software Image J.

To confirm the device structure, cross-sectional images of the fabricated devices using I-SWNT/AgNWs and S-SWNT were obtained using focused ion beam milling followed by SEM, as shown in **Figure 6.8A-D**. It can be seen that the WS_2 nanosheet networks are sandwiched between the solution-processed top electrodes and ITO bottom electrodes. The thicknesses of WS_2 networks used to produce these images are about 700 nm, 6.4 μm, 580 nm and 2.6 μm from A-D, respectively, which are consistent with those found by profilometry (680 nm, 6 μm, 544 nm and 2.5 μm). In these cross sections, the top electrode, made from either I-SWNTs/AgNWs or S-SWNTs, sits on top of the WS_2 network, and no visible nanowire/nanotubes are diffusing into the network. This confirms our expectation that 1D nanomaterials could form a network on top of nanosheet network without solvent-driven inter-layer mixing. This is an important result as it shows that a clean interface can be formed during sequential spray deposition. However, the interface quality is largely affected by the roughness of the underlying layer. The smooth ITO surface forms a sharp interface with WS_2, while the SWNT top electrodes form a locally clean interface with the WS_2, over longer horizontal length scales, the interface does display some peak-and-valley character due to spatial variations in the thickness of the WS_2 network (i.e. roughness). Depending on the mean thickness of the WS_2 network, the thickness difference between the peak and valley could be hundreds of nanometers. Moreover, the highly porous structure of WS_2 networks is observed which is further shown in **Figure 6.8E.** This image was imported into ImageJ. The brightness/contrast of the image was automatically adjusted and is shown in **Figure 6.8F**. Then, the image was converted into binary image where white area represents pores and black area represents nanosheets. Using measure function, the percentage of white area was obtained to be 56%, which could be regarded as

an estimation of porosity. Such porosity is close to the value of ~ 50% estimated by the film density method for thick films.[199]

6.3.3 Electrical measurements

On the effect of the electrode resistance

Before measuring the *I-V* characteristics of devices, we start by measuring the IP electrical properties of the electrodes. The I-SWNTs, I-SWNTs/AgNWs and S-SWNTs were separately sprayed on glass substrates. Their electrical resistances were measured by a two-probe measurement using silver paste as contacts. The IP conductivities σ_{IP} of I-SWNTs and S-SWNTs films were found to be relatively low: 1.8×10^3 and 6.8×10^3 S m^{-1}, respectively. This means that the IP resistance of the top electrodes may not be negligible compared to the OoP resistance of WS_2. This is significant as, in these devices, current flows first through the top electrode in the in-plane direction before flowing through the WS_2 in the OoP direction. Then, if the IP SWNT resistance, is non-trivial compared to the OoP WS_2 resistance, the voltage drop across the device will not be the same as the applied voltage, leading to an incorrect calculation of WS_2 network properties. This effect is shown schematically in **Appendix A1**. Thus, two different strategies were used to remove the influence of the electrode. In the first case, AgNWs was sprayed on top of I-SWNTs to reduce the IP resistance. This led to a conductivity of the I-SWNTs/AgNWs film of $\sim5\times10^5$ S m^{-1} (which may still be underestimated due to the effect of contact resistance coming from the two-probe measurement). It was also found that AgNWs did not alter the shape of *I-V* characteristic curves of devices, indicating that they do not change the nature of charge injection, which will be shown later. In the second case, for S-SWNTs based devices, AgNWs were not used to increase the electrode conductivity, as it is found that AgNWs will be in contact with WS_2 at the edge of electrodes due to spray coating through the

shadow mask, which will eliminate the diode behavior. Instead, we used the conductivity determined from the SWNTs film on the glass coupled with the electrode dimensions, to estimate the electrode resistance and remove its effect from the *I-V* curves. The second strategy is used for S-SWNTs electrode-based devices.

In-plane bulk-limited devices

The electrical response of thin semiconductor films can be limited by either the properties of the semiconductor itself or the properties of the metal-semiconductor interface.[205] In the former case, the conduction is termed as bulk-limited while in the latter case, it is electrode-limited. Bulk-limited devices are those where the resistance of the semiconductor itself is much greater than that associated with the interface (i.e. the contact resistance) while electrode-limited devices are those where the resistance of the semiconductor can be neglected. In some cases, the bulk resistance can be similar to that of the interface. Then the device can display bulk- or electrode-limited regimes depending on the applied voltage.

The basic electrical characterisation on the WS_2 networks is performed by measuring the IP conductivity of these networks as this is the most common reported measurement method.[189] IP measurements on networks are usually performed with a long channel length which generally yields bulk-limited conduction. However, ideally, Ohmic contacts should also be used to minimize contact resistance. In a p-type[199] material such as WS_2, Ohmic contact can be realized when the work function of the electrode material lies between the Fermi energy (E_f) and the valence band edge of the semiconductor. In this case, when the metal contacts WS_2, its bands only bend slightly in a way that leads to minimal built-in voltage, allowing carriers to flow freely across the contact. The Fermi energy of bulk-like WS_2 nanosheets produced by LPE has been reported to be -4.8

eV[270] (for completeness the conduction band minimum (CBM) is reported to be -4.2 eV[270] while, taking the bandgap of ~1.2 eV, the valence band maximum (VBM) is then around -5.4 eV). However, the doping state and hence Fermi energy of TMDs will depend on processing conditions (e.g. via residual solvent, etc), meaning we might expect E_f vary to somewhat from this value. The widely cited WF for ITO is -4.7 eV.[255] It is conceivable that, for our WS_2, E_f is close to -4.7 eV that the developed potential barrier is small (possibly less than 0.1 eV), leading to Ohmic contact at the ITO/WS_2 interface.

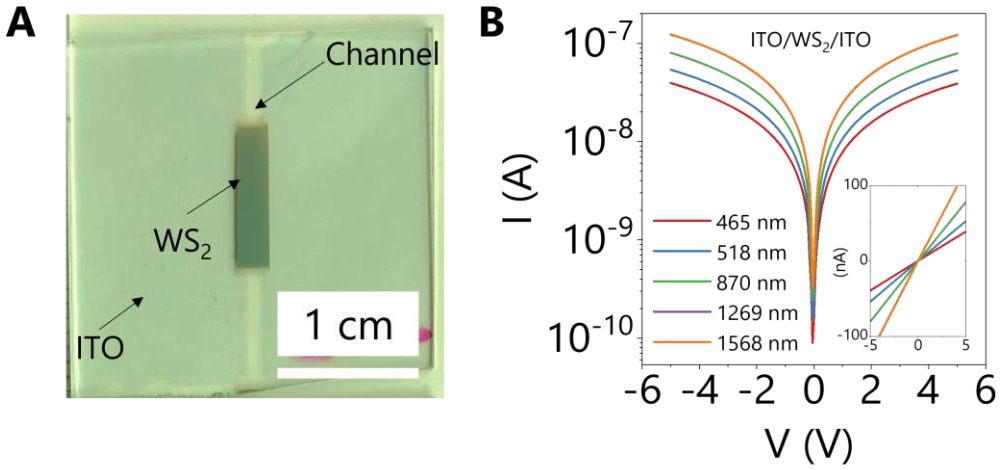

Figure 6.9 In-plane devices characterisations. (A) A photograph of IP device ITO/WS_2/ITO. (B) The semi-log *I-V* characteristics of IP devices with various WS_2 film thicknesses. The inset in (B) is its linear *I-V* curves.

Thus, to measure WS_2 conductivity in the IP direction, ITO/WS_2/ITO devices were fabricated. A pre-patterned gap was etched onto ITO-coated glass, leading to two separate ITO electrodes. The gap between ITO pads led to a channel length L of ~1 mm and a channel width W of ~10 mm. A WS_2 IPA dispersion was sprayed onto ITO-coated glass leading to networks covering both gap and electrodes (**Figure 6.9A**). Multiple networks were made with thicknesses varying from 465 nm to 1568 nm. The semi-log and linear *I-V* curves of these devices measured from -5 to 5 V are shown in **Figure 6.9B** and its inset, with the equivalent linear plots shown in its inset. The curves are linear and symmetric and exhibit

thickness-dependent properties with current increasing with increasing film thickness, exactly as expected for bulk limited devices. These curves yielded very similar conductivities for all thicknesses with a mean of ~2.01×10^{-3} S m^{-1}. This is considerably higher than previous reports on liquid-exfoliated WS_2[223], but similar to that reported for dry-deposited WS_2 networks.[308]

Out-of-plane bulk-limited devices

While IP conductivity measurements on nanosheet networks are widely reported,[189] OoP measurements are much less common because of problems with shorting in thin sandwich-structure devices.[189] Here we measure the vertical current flowing through the WS_2 in the OoP direction for the devices with I-SWNTs/AgNWs as the top electrodes. The *I-V* characteristics of the devices were measured in the range of -3 to 3 V. The current density *J* was obtained by dividing *I* by the measured device area *A*. **Figure 6.10A** shows one typical *J-V* curve of ITO/~1.2 μm WS_2/I-SWNTs/AgNWs device. The curve is symmetrical and shows a linear behavior at low biases which is consistent with Ohmic conduction as described by $J = \sigma_{OoP}E$, where σ_{OoP} is the OoP electrical conductivity. The electric field *E* can be estimated by dividing the voltage drop across WS_2 by its mean thickness t_{film}.

These results above imply that this device to be Ohmic contacted. It is already argued that the ITO/WS_2 interface can be Ohmic depending on the doping state of the WS_2. However, the nature of the WS_2/I-SWNTs interface should also be considered. The WF of SWNTs film after acid-treatment is reported to be -5 eV[309], slightly greater than the pristine value of -4.8 eV[310]. Thus, so long as the E_f of WS_2 is not deeper than -5 eV, we expect Ohmic contact at this top interface. The energy band diagram of each material is presented in the inset of **Figure 6.10A**.

It should be noted that because the coverage of I-SWNTs on top of the WS_2 film is not 100% as seen from SEM, it is possible that AgNWs may be in contact with WS_2. The electrical properties of the device with and without AgNWs were compared and identical *J-V* behaviors were observed for these two types of devices. However, using I-SWNTs/AgNWs double-layered electrodes gives the advantage that the resistance of this type of electrode is negligible compared to that of the WS_2, significantly simplifying data analysis.

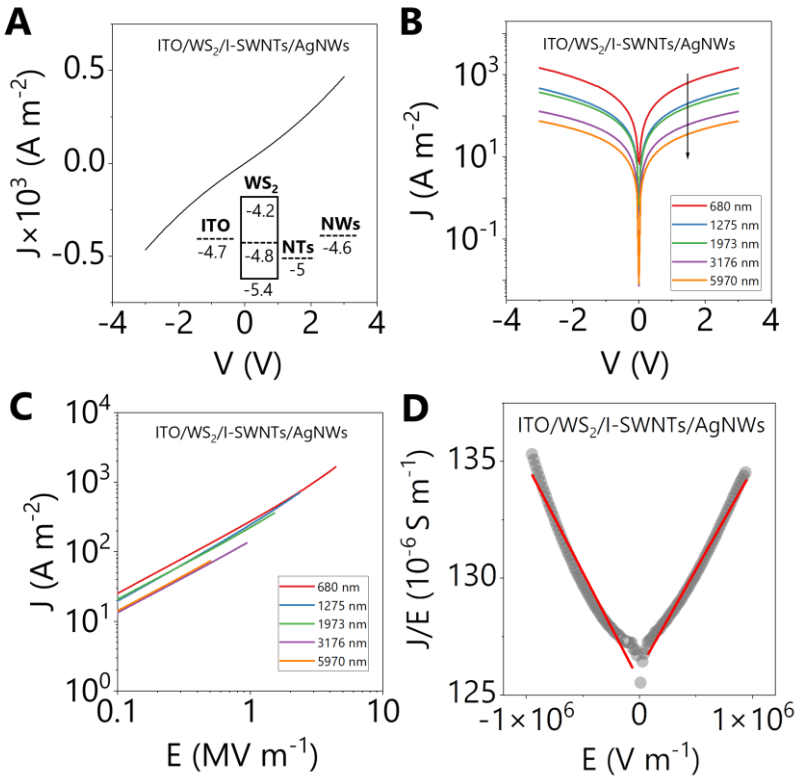

Figure 6.10 Electrical characterisations on out-of-plane devices with I-SWNTs/AgNWs electrodes. (A) A typical *J-V* curve of ITO/WS_2/I-SWNTs/AgNWs device with WS_2 film thickness of ~1.2 µm. The inset gives energy bands of each material before contacting. (B) Semi-log *J-V* curves of Ohmic OoP devices with various WS_2 film thicknesses. (C) *J-E* curves of these devices, where E is calculated by voltage drop only on the WS_2 layer. (D) *J/E* versus *E* plots for fitting purposes, where fitting lines are shown in solid red.

The discussion above implies the devices using I-SWNTs as the top electrode have Ohmic contacts on both top and bottom and so are bulk-limited. This can be

confirmed by examining *J-V* curves for devices with different WS_2 thicknesses. Purely electrode-limited devices should show no dependence on semiconductor thickness. Several devices with various WS_2 film thicknesses, using I-SWNTs/AgNWs as top electrodes were fabricated, and their typical *J-V* curves are shown in **Figure 6.10B** and all curves are shown in **Figure 6.11**. It is found that all *J-V* curves to be symmetric, and exhibit thickness-dependent properties with *J* falling with increasing film thickness, exactly as expected for bulk-limited devices. As the voltage drop on the I-SWNT/AgNW electrodes is negligible, *E* can be estimated by directly dividing the bias voltage *V* by t_{film}. The *J-E* curves are plotted in **Figure 6.10C** and almost perfectly overlap with each other. This is what we would expect for a bulk-limited devices with the current flow controlled by WS_2 conductivity and electrode dimensions.

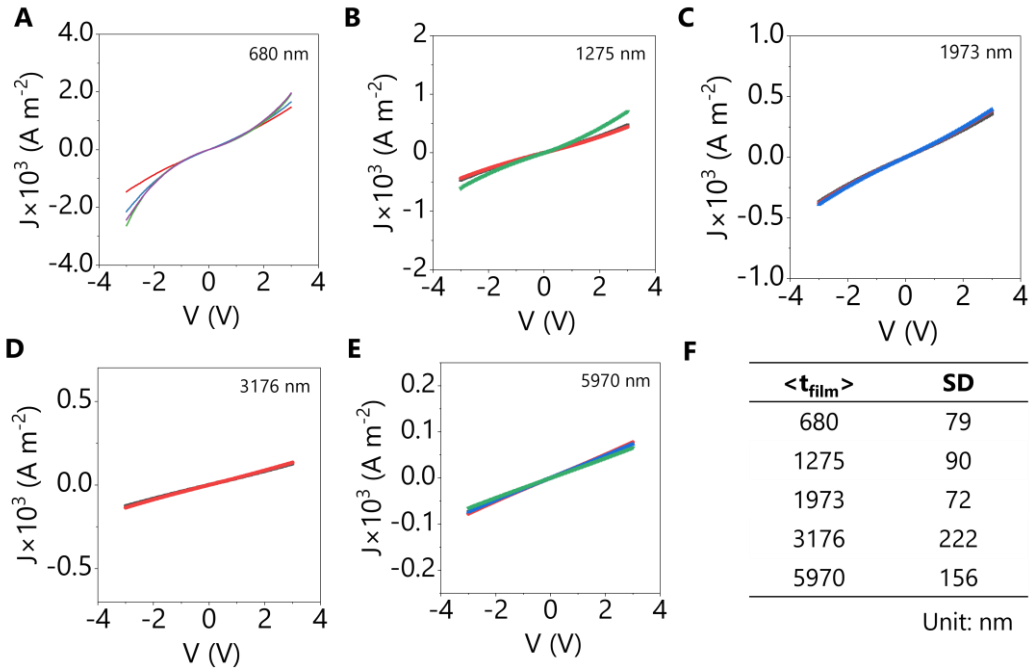

Figure 6.11 Electrical results of ITO/WS_2/I-SWNTs/AgNWs devices. *J-V* curves of these devices with various WS_2 film thicknesses are shown in (A-E). (F) The WS_2 film thicknesses and their corresponding standard deviations.

While one may expect Ohmic contacts at both top and bottom electrodes to result in purely linear *J-V* curves, slight curvature appears at higher biases in the *J-V*

curve (**Figure 6.10(A)**). This nonlinearity of *J* does not mean we have electrode-limited conduction as might be found in a Schottky diode. There are a number of bulk conduction mechanisms that can lead to such non-linearities.[205] One common mechanism that becomes visible at higher biases is space charge limited conduction (SCLC) which leads to a contribution to the current density as described by the Mott-Gurney law[311], which is usually adopted to describe symmetric, Ohmic-contacted, single carrier devices.[312] In this case, ITO and I-SWNTs both have deep work functions and display reasonable Ohmic behaviors. Considering LPE WS_2 is a p-type material[199], it is expected that the hole current to dominate in our devices. Thus, it is expected that these conditions to apply reasonably well here. It is worth noting that Yu et al.[302] reported electron-only SCLC in stacked ITO/TiO_2/MoS_2/Al devices although the presence of the TiO_2 hole-blocking layer does mean some deviation from the conditions listed above.

Mott-Gurney equation allows OoP electrical properties of MoS_2 can be extracted using such device structure. Usually, SCLC analysis is done by identifying a high-voltage regime where the current scales as voltage squared and fitting using equation 1. However, the curvature appearing in *J-V* curves is very weak indicating that SCLC is not dominant in the voltage range under study.

To analyze the current-voltage data for the ITO/WS_2/I-SWNTs/AgNWs devices, it is assumed that Ohmic and space charge limited currents flow in parallel, physically separated paths.[207] When two types of conductions take up the same physical volume, the transition from one to another will be likely due to the voltage distribution for these two are different. A competition between these two conductions is expected to establish the appropriate voltage distribution. It is expected that the conduction mechanism that could introduce a large amount of the carriers will dominate the conduction behavior.[207] Although this is not perfectly accurate, it is known to be a very good approximation.[313] Then, the total

current density is given by an addition of both types of currents:

$$J = \sigma E + \frac{9}{8}\varepsilon_0 \varepsilon_r \mu \frac{E^2}{L} \tag{6.3}$$

This equation can be re-arranged to give equation 6.4.

$$J / E = \sigma_{OoP} + \frac{9}{8}\varepsilon_0 \varepsilon_r \mu_{OoP} \frac{E}{L} \tag{6.4}$$

where the subscript OoP is to signify that we use this equation to analyze out-of-plane conduction. This equation predicts a linear relationship between *J/E* and *E* with the intercept and the slope controlled by the OoP conductivity, σ_{OoP}, and mobility, μ_{OoP}, respectively (using the theoretical WS_2 OoP dielectric constant of 6.4[314]). A typical fitting curve is shown in **Figure 6.10D** and all ITO/WS_2/I-SWNTs/AgNWs data sets give good linear curves when plotted in this way (**Figure 6.12**). However, it is worth noting that assuming current addition leads to extracted electrical parameters that may be slightly under-estimated although the error is typically <10%.[313]

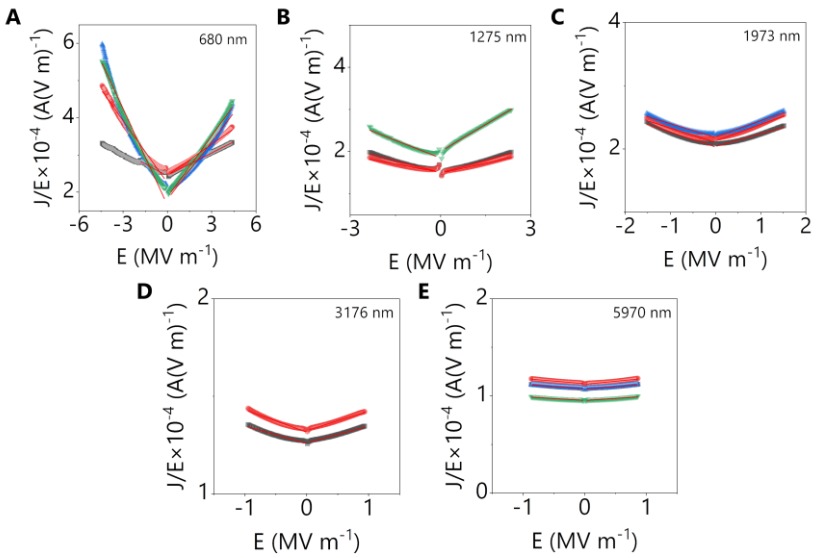

Figure 6.12 Fitting results of ITO/WS_2/I-SWNTs/AgNWs devices. (A-E) *J/E* versus *E* curves with Ohmic OoP devices with various WS_2 film thicknesses, which are shown in top right.

The OoP conductivity of these Ohmic devices is extracted and is plotted versus WS_2 network thickness in **Figure 6.13A**. It is found that σ_{OoP} is almost constant as expected, with a mean value of 1.63×10^{-4} S m^{-1}. In addition, the in-plane conductivity, σ_{IP}, extracted from ITO/WS_2/ITO devices is included for comparison, highlighting the thickness independence of σ_{OoP}. Using this data, the ratio of $\langle\sigma_{IP}\rangle/\langle\sigma_{OoP}\rangle$ to be 12.3, corresponding to the electrical anisotropy of the semiconducting nanosheet network. This ratio is low compared to vacuum filtered graphene nanosheet networks which have reported values of $\langle\sigma_{IP}\rangle/\langle\sigma_{OoP}\rangle$ between 20 and 1000, depending on porosity.[315] Barwich et al.[315] showed that the conductivity anisotropy also depends on the dimensions of the nanosheets. The maximum conductivity anisotropy (assuming perfect alignment) in a network is related to the mean length $\langle L_{NS}\rangle$ and mean thickness $\langle t_{NS}\rangle$ of the nanosheets via:

$$\langle\sigma_{IP}\rangle/\langle\sigma_{OoP}\rangle=\left(\langle L_{NS}\rangle/\langle t_{NS}\rangle\right)^2 \tag{6.5}$$

In this case, the upper limit of the conductivity ratio can be found to be ~100. We expect the reduced conductivity anisotropy observed here is due to the open nature of the sprayed network and the relatively low nanosheet alignment.

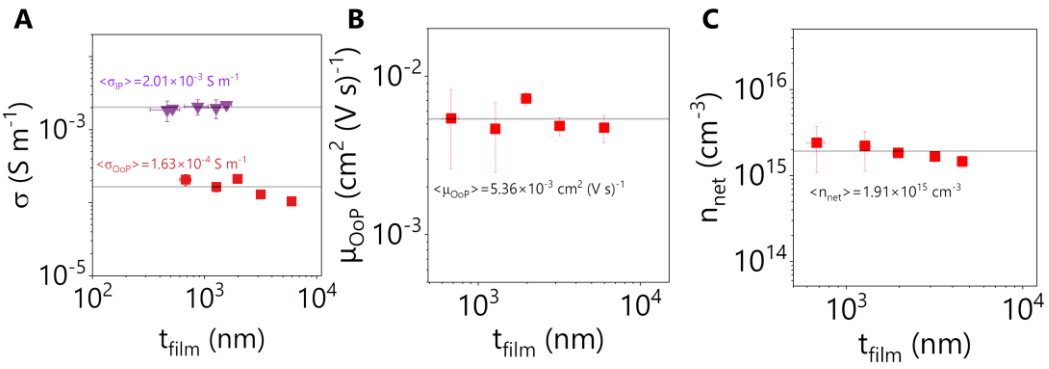

Figure 6.13 The extracted electrical parameters for ITO/WS_2/I-SWNTs/AgNWs devices. The obtained parameters conductivity σ, mobility μ and network carrier density n_{net} are plotted against WS_2 film thicknesses in (A), (B) and (C), respectively.

The obtained values of μ_{OoP} are shown in **Figure 6.13B** and are constant with thickness with a mean value of $\langle \mu_{OoP} \rangle$=5.36×10^{-3} cm^2 V^{-1} s^{-1}. Because the carrier density is the same regardless of conduction direction, we expect $\sigma_{OoP} / \sigma_{IP} = \mu_{OoP} / \mu_{IP}$. Then, taking $\langle \sigma_{IP} \rangle / \langle \sigma_{OoP} \rangle$=12.3, we find $\langle \mu_{IP} \rangle$=6.5×10^{-2} cm^2 V^{-1} s^{-1}. This is consistent with the IP values of ~0.01 cm^2 V^{-1} s^{-1}, ~0.1 cm^2 V^{-1} s^{-1} and ~0.2 cm^2 V^{-1} s^{-1}for liquid exfoliated WS_2 obtained by Higgins et al.,[316] O'Suilleabhain et al.[317] and Kelly et al.[199], respectively.

The network carrier density, n_{net}, can be calculated by using $n_{net} = \sigma_{OoP} / q\mu_{OoP}$ and is plotted in **Figure 6.13C** as a function of WS_2 thickness. This curve shows a slight decrease with increasing thickness possibly due to substrate doping effect associated with charge transfer from one of the electrodes to the WS_2. The mean carrier density is 1.91×10^{15} cm^{-3}, which is close to the previously reported value of 5.8×10^{15} cm^{-3}.[318] The carrier density is lower than the individual multi-layered flake value (~10^{17} cm^{-3})[319],which could be due to the residual doping effect during solution processing.[189]

Out-of-plane electrode-limited devices

Having shown that the ITO/WS_2/I-SWNTs devices are Ohmic, we move on to a slightly different device, where isopropanol-dispersed SWNTs is replaced with surfactant-suspended SWNTs (S-SWNTs): ITO/WS_2/S-SWNTs. For these devices, AgNWs were not used on top of SWNTs to increase conductivity as it was found that rectifying behaviors could be lost due to undesired AgNWs/WS_2 contacts at the electrode edge caused during spray coating. Thus, all *I-V* curves with S-SWNTs as the top electrode are corrected by subtracting the voltage drop on the S-SWNTs top electrode.

A set of ITO/WS_2/S-SWNTs devices with different WS_2 thicknesses were

prepared and their *I-V* curves were measured from -3 to 3 V and then from 3 to -3 V, denoting these the first and the second sweeps, respectively. A typical *J-V* curve for the device of ITO/1.5 μm WS_2/S-SWNTs is shown in **Figure 6.14A** and all curves (original and corrected ones) are shown in **Figure 6.15** and their insets. This curve is clearly very different from these for Ohmic devices as it shows an obvious rectifying behavior with a noticeable hysteresis. The hysteresis is most obvious for the 1.5 μm and 2.5 μm WS_2 thick devices, and it may be caused by interfacial trap states in our devices at WS_2/S-SWNTs interfaces.[320] Similar behaviors were observed in solution-processed amorphous indium gallium zinc oxide (a-IGZO) Schottky devices with a device structure of Pt/IGZO/Cu[320]. The hysteresis was ascribed to the interfacial trap states due to ionized oxygen vacancies. Although the origin of the surface traps is still unknown in our case, it could be induced by the sulfur vacancies on the nanosheets[321]. The sulfur vacancies could bring significant deep-level traps to trap holes with a very long transient time constant of 2800 s.[321] The electrical hysteresis could be caused by the filling and releasing charges in these traps by the external voltages.[321] The surfactant used for dispersing nanomaterials could also introduce trap states and cause electrical hysteresis depending on the dipole structure of the surfactant and its interactions with the material.[322] The surface trap is likely gradually filled under the first sweep from -3 to 3 V, which causes the barrier height to be changed. For the second sweep, the trap states are neutralized already, and the barrier height is close to its real value regardless of other effects. The hysteresis was also found in chemical-vapor-deposited monolayer WS_2 and it was found that charge trapping accounts for the hysteresis effect[324]. Given the complexity of solution-processed devices, there could be several factors that affect the quality of the interface. The presence of interfacial traps will affect the electronic parameters that will be extracted later. As it is found later that the extracted parameters from

the second sweep give better agreement with those from Ohmic devices, *J-V* curves from the second sweep will be mainly focused for the following analysis.

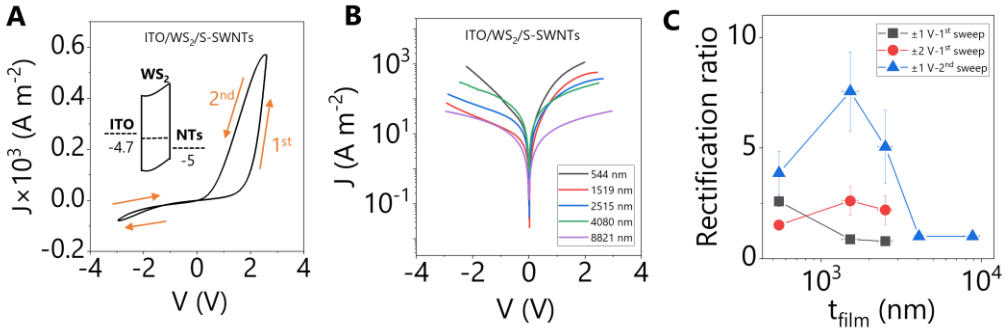

Figure 6.14 Electrical characterisations on out-of-plane devices with S-SWNTs electrodes. (A) A representative *J-V* curve of ITO/WS_2/S-SWNTs. The inset gives energy band of each material before contact. (B) Semi-log *J-V* curves of Schottky OoP devices with various WS_2 film thicknesses. (C) The extracted rectification ratios from both sweeps at ±1 V and ±2 V are plotted against WS_2 film thicknesses.

From the results of the ITO/WS_2/I-SWNTs/AgNWs devices, it is known that Ohmic contact is realized at ITO/WS_2 interface. Thus, the rectifying behavior is likely due to a potential barrier at the WS_2/S-SWNTs interface yielding Schottky diodes rather than Ohmic devices. To create such potential barrier, the E_f of either WS_2 or S-SWNTs has to be different from the values described above. However, SDBS is not an effective dopant for SWNTs and there is no evidence from the UV-Vis-NIR absorption and Raman spectra of the S-SWNT that their electronic structure is altered by SDBS. Alternatively, Biccai et al. [169] found that poly(ethylene oxide) could dope MoS_2 nanosheets, leading to at least one order of magnitude increase in network conductivity. Thus, it is more likely that SDBS dopes the interfacial WS_2 in some way, shifting its E_f, leading to the formation of a potential barrier at the WS_2/S-SWNTs interface. Given that the cathode is on the S-SWNTs side, the anode is on the ITO side, and the rectification appears on the positive applied voltage, this implies that positive applied voltage should lower the potential barrier. Thus, the E_f of doped WS_2 should be deeper than its pristine

value. The possible energy band diagram is illustrated in **Figure 6.14A**.

Second sweep *J-V* curves for ITO/WS_2/S-SWNTs devices with different WS_2 thicknesses are shown in **Figure 6.14B**. As WS_2 thickness increases, the *J-V* curves appear to exhibit a range of behaviors. For the thinnest films, *J* increases rapidly with *V* for both negative and positive polarities. However, as the thickness is increased, the curves become more diode-like with much reduced currents at negative voltages. However, for the thickest films, the curves become much more symmetric. This behavior can be interpreted as a transition from back-to-back (B2B) Schottky-type behavior[211] to normal (single) Schottky diode behavior, and finally to Ohmic behavior as WS_2 network thickness is increased.

The device with the thinnest WS_2 layer (ITO/544 nm WS_2/S-SWNTs) shows roughly exponential increases of *J* for both polarities above transition voltages of about 0.5 and -1 V. This strong super-linear behavior is much more pronounced than the slight curvature seen in the Ohmic devices in **Figure 6.11** (for a comparable WS_2 thickness). It is believed that this behavior implies Schottky barriers at both electrodes which is due to shifts in the WS_2 E_f throughout the thin film. The nanosheet networks are highly porous as observed in SEM images so residual SDBS could easily diffuse into the network from the top electrode during spraying. Thus, for this very thin film (544 nm), it is likely that SDBS has diffused throughout the entire network, even reaching the ITO/WS_2 interface. This leads to enough doping to shift the Fermi level everywhere, resulting in band bending and potential barriers at both top and bottom electrodes.

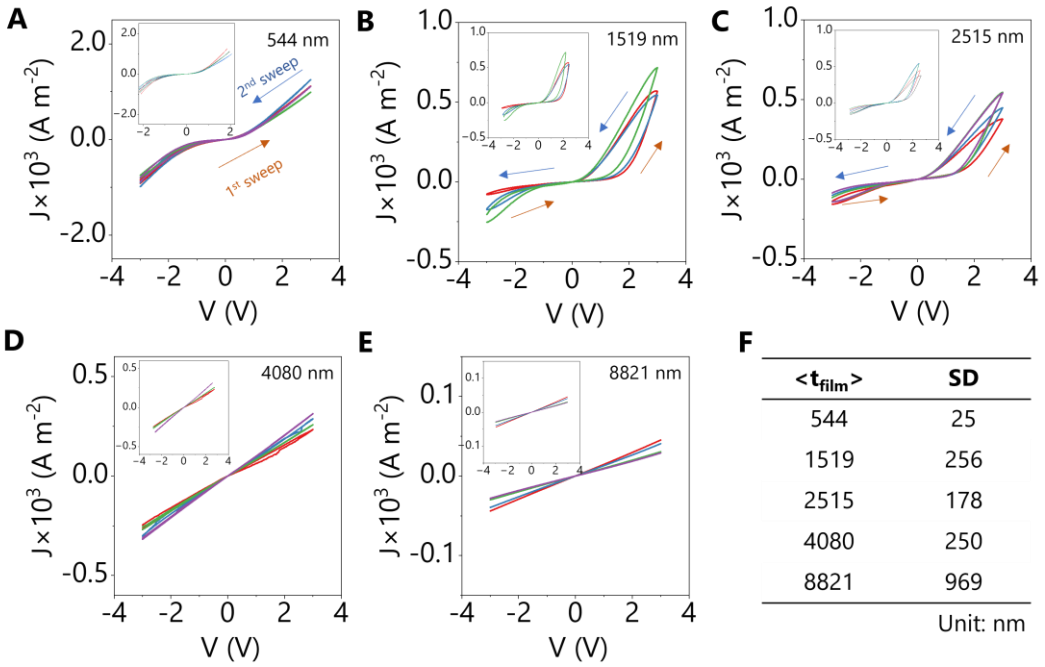

Figure 6.15 Electrical results of ITO/WS_2/S-SWNTs devices. Original *J-V* curves of these devices with various WS_2 film thicknesses are shown in (A-E). The inset in each figure is the *J-V* curve after removing electrode resistance accordingly. (F) The WS_2 film thicknesses and their corresponding standard deviations. The arrows in figures indicate the sweep directions.

For the medium WS_2 thicknesses (1.5-2.5 μm), clear rectifications are observed, consistent with single Schottky diode behavior. In this case, SDBS has probably only diffused slightly into the WS_2 network, leading to doping only in the vicinity of the top electrode, leaving the ITO/WS_2 interface un-changed. For the thicker films (>4 μm), symmetric, Ohmic-like behavior is observed. This is possible when the high WS_2 thickness leads to the WS_2 network acting as a large series resistance. Once this series resistance becomes larger than the Schottky contact resistance, the thick film devices become bulk limited.

To visualize this thickness-induced transition, the rectification ratios (RR) of these devices, measured at ±1 V and ±2 V, versus film thickness for the first and the second sweeps in **Figure 6.14C**. RR is defined as the ratio of *J* at the same applied voltage with opposite polarity and manifests the ability of the diode to

rectify current. For the first sweep at ±1 V, the thinnest device has a RR of ~2.5, while 1.5 and 2.5 μm WS_2 thick devices have RR of ~1. At ±2 V, RR increases and approaches 3 for the latter two devices. Such behavior comes from the hysteresis of the device and results in a higher turn on voltage for the first sweep. Thus, we could barely observe rectification at lower biases. The rectifying behavior is more pronounced for the second sweep. The RR for the three thinner devices is ~3-10, falling to 1 for the two thickest devices, behavior which is consistent with the hypothesis given above. The RR from the thinner devices are lower than previously reported Schottky diodes based on LPE nanosheet mixed in a polymer matrix with a vertical MSM structure[326], which were around 40-110 at ≤ ±2 V. It may be caused by several factors, such as a large leakage current[326], a high series resistance[326] or a poor interface quality[327]. The RR reaches to 1 show that the transition to bulk-limited behavior is complete by a WS_2 thickness of ~4 μm.

The forward bias (positive polarity) parts of the *J-V* characteristics for different WS_2 thicknesses are plotted as *J* versus electric field, *E* (where $E=V/t_{film}$), on a log-log basis in **Figure 6.16A**. For Schottky diodes with thin WS_2 films (e.g., 544 nm), at lower electrical fields, holes have insufficient energy to overcome the potential barrier leading to low currents which scale roughly linearly with *E*. Such devices are thus electrode-limited at low voltage. As the voltage is increased, the potential barrier is lowered resulting in an exponential increase of *J*. However, at relatively higher electrical field, when the potential barrier is greatly reduced, the voltage drop across the interface becomes less than the series resistance of the WS_2, and the device becomes bulk-limited. At this point the device should carry the same current as the equivalent Ohmic device. This is exactly what is observed in the figure with curves shifting upwards and to the left as the WS_2 thickness (and so series resistance) is increased. The black dash line in **Figure 6.16A** is a

plot of a *J-E* curve representing an Ohmic device with a conductivity of 4×10^{-4} S m^{-1}. The thicker ITO/~4 μm WS_2/S-SWNTs device, which is expected to be bulk limited, matches this curve very well. The thinner devices, appear to approach this Ohmic line at high applied voltage, in line with their expected transition to being bulk limited. Indeed, the current densities for devices with rectifying behavior are all below this line, confirming they are all electrode-limited at lower *E*.

When MSM systems are modelled as Schottky diodes, it is usually assumed that there is a Schottky barrier at one electrode, but Ohmic contact at the other. In addition, the resistance associated with the semiconductor should be included. Then, the current density *J* is given by equation,[328]

$$J = J_s\left[\exp(q(V - JR_sA)/nkT) - 1\right] \tag{6.6}$$

where R_s is the series resistance of WS_2. In order to model our *J-V* curves, the contribution of the series resistance of WS_2 has to be considered. The thickness and field dependent transition from electrode-limited to bulk-limited can be visualized by rewriting equation 6.6 to represent electric field:

$$E = \frac{nkT}{qt}\ln\left(\frac{J\exp(q\phi_b/kT)}{A^*T^2} + 1\right) + \frac{J}{\sigma} \tag{6.7}$$

This equation is used to calculate *E* as a function of *J* using reasonable values for each parameter and for a range of thicknesses. These data sets are then plotted as *J* versus *E* in **Figure 6.16B**. It is found that the simulated data matches well with our experimental results in **Figure 6.16A**. This implies that the ITO/WS_2/S-SWNTs devices are limited by both the Schottky barrier at the WS_2/S-SWNT interface and the series resistance associated with the WS_2 network with the balance of these relative contributions controlled by the relative values of contact resistance and series resistance. It is worth noting that the value of the Schottky

barrier (and so the contact resistance) is controlled by the doping level of the WS_2 and so the ink formulation, while the series resistance is controlled by the WS_2 network thickness. That both these parameters can be controlled allows the Schottky/Ohmic properties of these devices to be tuned.

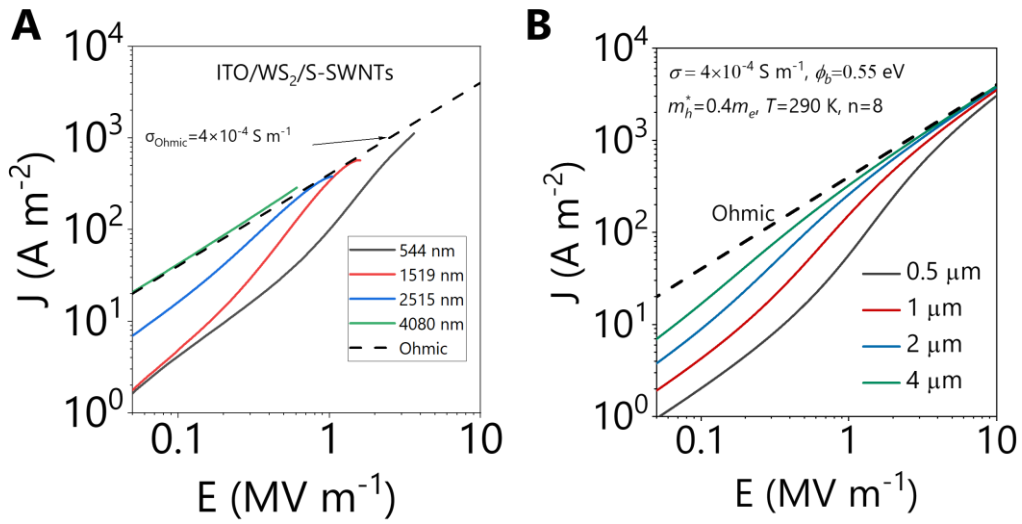

Figure 6.16 *J-E* curves of ITO/WS_2/S-SWNTs devices. (A) Experimental *J-E* curves of Schottky OoP devices and (B) is the simulated *J-E* curves with reasonable parameters to match with the trend in (A).

The equation to describe J for Schottky devices assumes that the conduction is dominated by thermionic emission (TE), that the carrier conduction through the potential barrier is governed by the thermal activation processes.[205] To verify if carriers in our Schottky devices follow TE, J is plotted against $V^{0.5}$,[329] which are shown in **Figure 6.17A-C** insets. The straight line indicates the voltage range that the obtained Schottky device follows TE. It can be observed that this linear dependence from roughly 0 to 1 V for the first sweep and from 0 V to the maximum bias V_{max} for the second sweep. The curve for the first sweep from 1 V to V_{max} is obviously deviated from TE conduction. The fitting was conducted above thermal voltage $3kT/q$=25 mV in all cases. As the hysteresis for the 544 nm thick WS_2 device was weak and almost entirely followed TE at ~25 mV-V_{max}, its

J-V curves were fitted to the entire range. For the ~1.5 and ~2.5 μm thick devices, their curves were fitted from ~25 mV to 1 V for the first sweep and were fitted from ~25 mV to V_{max} for the second sweep. Thus, equation 6.7 is used to fit *log(V)-J* curves in their corresponding range to extract J_s, R_s and n. The fittings can be successfully done and are presented in **Figure 6.17A-C**. The two devices with the thickest WS_2 networks are completely bulk limited and so must be fitted using equation 6.4 to yield μ_{OoP} and n_{net} (after subtraction of the top electrode resistance), which are shown in **Figure 6.17D-E**.

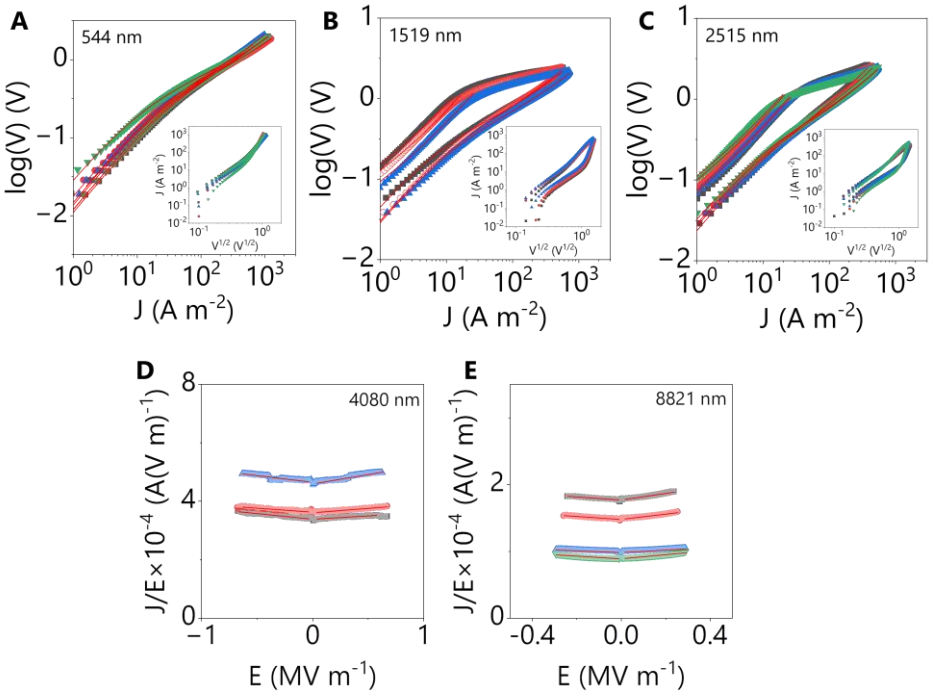

Figure 6.17 Fitting results of ITO/WS_2/S-SWNTs devices. (A-C) log(V) versus J curves of Schottky OoP devices with various WS_2 film thicknesses. The fitting lines are shown in solid red. The inset in each figure is J-$V^{0.5}$ curves to verify the transport mechanism. (D-E) J/E versus E curves of S-SWNTs electrodes-based devices but showing Ohmic behaviors.

The obtained values of R_s are converted into conductivity σ_{OoP} and are shown in **Figure 6.18A**. For the second sweep, the Schottky device with the thinnest WS_2 film gives σ_{OoP} about 1 order of magnitude higher than the one extracted from the Ohmic device at a comparable WS_2 thickness. σ_{OoP} decreases with t_{film} but is

always higher than σ_{OoP} from Ohmic devices. The device with 8.8 μm thick WS_2 exhibits a conductivity very similar to the Ohmic ones. Such trend may be evidence of slight doping caused by SDBS. The thinnest film is affected by SDBS most while the thickest one is the least affected. For the first sweep, the conductivity is lower than OoP Ohmic values, which is induced by the additional resistive effects from the interfacial traps.

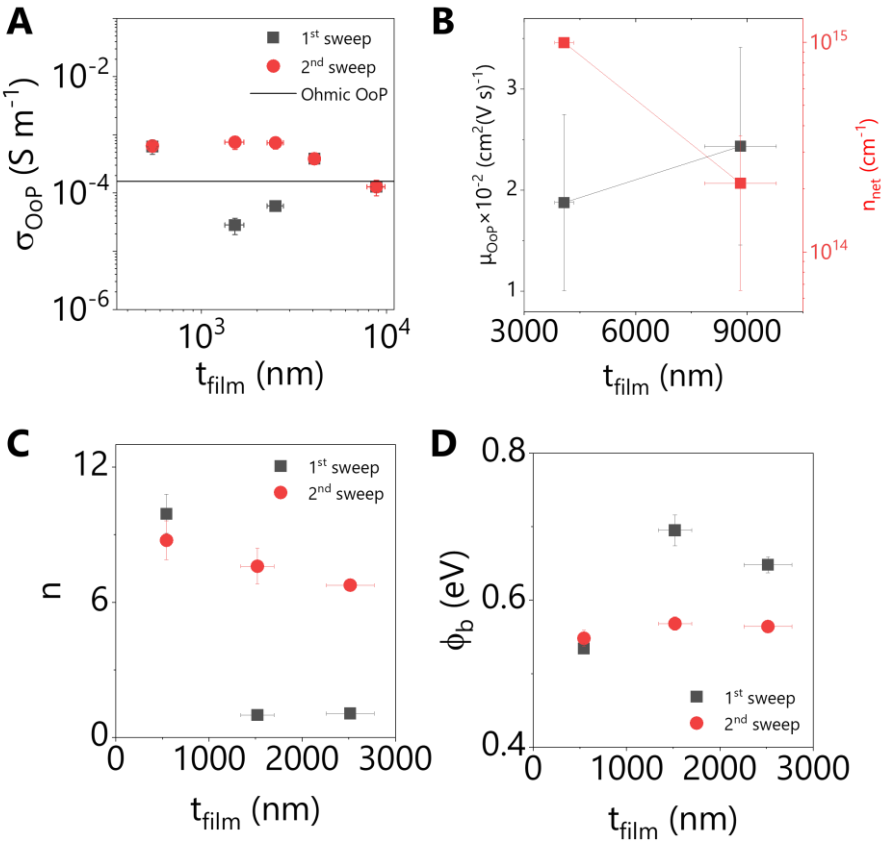

Figure 6.18 The extracted electrical parameters for ITO/WS_2/S-SWNTs devices. The obtained parameters σ, μ and n_{net}, n, and ϕ_b are plotted against WS_2 film thicknesses in (A), (B), (C) and (D), respectively.

Values of μ_{OoP} and n_{net} extracted from the two thickest devices were included in **Figure 6.18B**, respectively. μ_{OoP} is roughly 5 times larger than the device with I-SWNTs as top electrodes, but the carrier density seems lower than the latter. The reason is still not clear and requires further investigation. However, it is worth

noting that I-SWNTs/AgNWs based vertical devices and ITO/WS_2/ITO lateral devices would allow WS_2 network to interact with the ambient environment, i.e., oxygen and water, which could act as p-type dopants.[330] In contrast, less interaction with ambient in S-SWNTs based devices is expected due to the visible full coverage of S-SWNTs on WS_2. There could be several times difference in electrical properties between these two types of devices.[331, 332] The extracted carrier density for ~4 um WS_2 device is close to the value extracted from OoP Ohmic devices. However, a reduction in the carrier density is observed for the 8.8 μm thick WS_2 device.

The ideality factor n is found to be around 7.7 for the second sweep, and slightly decreases with t_{film} (**Figure 6.18C**). Ideally, n should be in the range of 1-2 for a perfect Schottky diode although larger n values >2 have been widely reported in other solution processed Schottky diodes.[333, 334] The electrical properties of the Schottky diode can be easily affected by the quality of the interface. It is known that surface roughness can greatly affect the quality of interfaces.[335] From the profilometer measurements on all WS_2 films, it is found that the average surface roughness R_a can be around 0.017 of the film thickness obtained by a linear fit. This could lead to spatial barrier height inhomogeneity which could be one of the causes of high ideality factor. It is also likely the edge of nanosheets are oxidized in ambient conditions and forms WO_x[336], which could also cause local barrier height variation.

Using effective hole mass $m_h^*=0.4m_e$[337] for WS_2 and T=290 K, ϕ_b can be calculated from the extracted J_s using $J_s = R^*T^2 \exp\left(-\frac{q\phi_b}{kT}\right)$ and is about 0.56 eV for the second sweep (**Figure 6.18D**). The barrier height from the first sweep is obviously higher than that from the second sweep owing to the interfacial traps. However, the obtained ϕ_b is slightly larger than the expected difference between

the VBM of WS_2 and the WF of SWNTs of 0.4 eV.

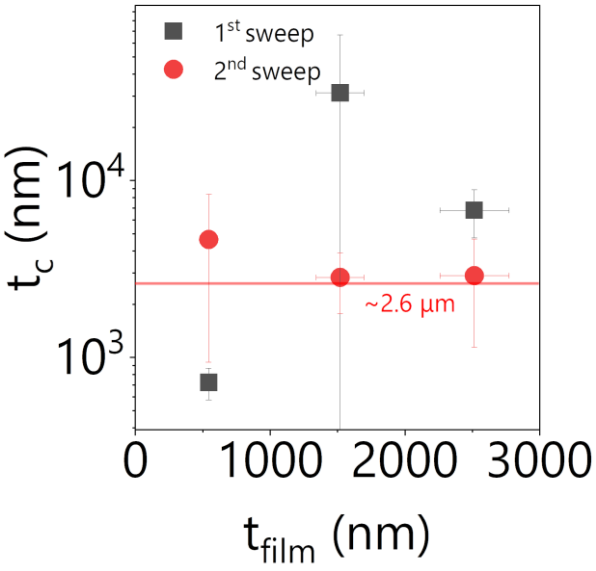

Figure 6.19 The critical film thickness for electrode- to bulk-limited transitions. The critical film thicknesses t_c for both sweeps are plotted against WS_2 film thicknesses.

It is worth noting that the contact resistance R_c associated with the Schottky barrier is given by $AR_c = dV_c / dJ$ in the limit of low voltage. Applying this to equation 6.6 yields $R_c = kT / AqJ_s$.[338] Thus, in order to find the electrode-limited to bulk-limited critical transition film thickness t_c, we should first find R_c=R_s so that devices above t_c will has a larger R_s than R_c and thus to be bulk-limited. As R_s is given by $R_s = t_{film} / (\sigma_{OoP} A)$, we can obtain $t_c = \sigma_{OoP} kT / (qJ_s)$. Using the extracted conductivity and J_s values, we can find that t_c for the second sweep is more consistent due to the negligible involvement of the interfacial traps which is filled during the first sweep and the averaged t_c is ~2.6 μm (**Figure 6.19**). This is consistent with our results that bulk-limited behaviors are observed in devices with WS_2 thickness of ~4 μm.

6.4 Conclusion

Vertical heterostructured MSM devices based on liquid exfoliated semiconducting

WS_2 nanosheets and conducting SWNTs were fabricated by spray coating. Carefully adjusted spraying parameters leading to pinhole-free WS_2 nanosheet networks enable these vertical heterostructures to be realized. It was found that devices could exhibit Ohmic or Schottky behaviors depending on the composition of SWNTs dispersion. WS_2 network thickness-dependent electrical properties of devices were investigated. From Ohmic devices, we extracted values of the OoP conductivity and mobility to be in the range 1-2×10^{-4} S m^{-1} and 4-8×10^{-3} cm^2 V^{-1} s^{-1} respectively, which were roughly one order of magnitude lower than their in-plane values. The low anisotropic electrical properties along their IP and OoP directions were attributed to the porous networks formed by the random alignment of nanosheets and low aspect ratio of the nanosheet. On the other hand, the Schottky behavior may be caused by SDBS doping WS_2 nanosheet and resulted in a potential barrier at WS_2/SWNTs interface.

One produced Two.

Two produced Three.

Three produced All things.

Laozi

Chapter 7 Heterojunction Type Photodiodes

7.1 Introduction

In the last chapter, it is demonstrated that the metal diffusion problem in the porous LPE nanosheet networks can be overcome by using high aspect ratio 1D metallic nanomaterial networks as the top electrodes. Here, in this chapter, another possible solution is attempted by constructing semiconductor-semiconductor vertical hetero-stacks. As aforementioned, the porous structures and rough surfaces for LPE nanosheet networks are mainly caused by the irregular shape of nanosheets, their relatively high aspect ratios and rigidity. Therefore, if a layer of semiconductor is coated on top of the nanosheet network and forms a pinhole-free film, there will be literally no metal diffusing problems, regardless of the methods or materials used to realize the top electrode. The semiconductor on top of the network may diffuse into the nanosheet network, forming a semiconductor/semiconductor interface (either a hetero- or homo-junction), however, this will not lead to electrical shorts (i.e., metal/metal contacts). It would only lead to a slight deviation from a planar heterojunction structure to a bulk one (a mixture of semiconductors), or a structure in between of them. The area of the semiconductor/semiconductor interface will be enhanced as these two semiconductors are partially mixed compared with the perfect planar interface, which will actually improve the carrier diffusion and extraction as observed in bulk heterojunctions.[339]

The semiconductor on top of the LPE nanosheet network have quite a few options regarding the material types and deposition methods. Here, we mainly focus on the solution-based materials and methods. There will be some candidates such as organic and polymeric semiconductors, semiconducting inorganic quantum dots and nanoparticles. The organic and polymeric semiconductors are known to be sensitive to the ambient environment and have to be processed and measured in glovebox, which brings complexities in handling them. Inorganic semiconducting nanomaterials are more stable in air, especially, the metal oxides (MOs), which have been proven their capabilities in optoelectronic applications for the past decades.[340, 341] For the current project, their sizes and shapes are also important. Preferably, nanoparticles should be as small as possible and a regular shape is more desirable. The network formed by this kind of nanoparticles can be pinhole-free and exhibits an almost seamless morphology with only nanometer-sized pores[342, 343], although the film formation will also have an influence on the morphology. This hypothesized morphology will fulfill our requirements to allow ideal top electrode deposition on top of the semiconducting networks. As a proof of concept, commercially available zinc oxide nanoparticles with an average size of ~12 nm and a near-spherical shape is chosen, which are dispersed in solvents and can be solution-processed into thin films. Therefore, the device will be a 0D/2D heterojunction type as the junction is formed by two different kinds of semiconductors.

Moreover, it is worth mentioning that manipulating the interface properties using transport layers is a common strategy in optoelectronic applications.[255, 344] Materials like metal oxides can be used to modify the interfacial energy potential barriers at the metal/2D interface and facilitate the carrier injection or extraction.[68] However, so far, this interfacial layer strategy has not been applied to the LPE semiconducting networks yet. Therefore, in this project, the interfacial properties

of the metal/2D interface will be modified by introducing transport layers in-between. The proposed heterojunction-type device structure is cathode/hole transport layer (HTL)/light absorbing layer/electron transport layer (ETL)/anode, where the semiconducting nanosheet network serves as the light absorbing layer. The electrical behaviors of heterojunctions will be studied in the dark and under illumination. The photodetection performance of the obtained heterojunctions will be explored.

7.2 Experimental procedure

7.2.1 Material preparation

The WSe_2 nanosheet dispersion is obtained by liquid phase exfoliation in an inert atmosphere. WSe_2 powder (Alfa Aesar, metal basis) is mixed in 2 mg mL^{-1} sodium cholate hydrate (Sigma-Aldrich, ≥99%) aqueous (SC/H_2O) solution at a concentration of 30 mg mL^{-1}. The powder dispersion was contained in a glass flask with a rubber cap. Nitrogen was injected into the dispersion continuously through a needle to maintain the inert atmosphere. As a pre-treatment step to remove any impurities in the powder, the dispersion was bath-sonicated for 1 h and was centrifuged at 6 krpm for 1 h. The sediment was kept and re-dispersed in a fresh 6 mg mL^{-1} SC/H_2O solution. This dispersion was again under bath sonication for another 8 h with a continuous nitrogen flow. The water in the sonic bath was replaced with ice-cooled water every hour to avoid over-heating.

The obtained dispersion from the last step contains poly-dispersed nanosheet with a broad distribution of size and thickness. Thus, a size-selection step is introduced by liquid cascade centrifugation (LCC). The dispersion was centrifuged at 2 krpm for 2 h and the supernatant was collected so that the large and thick partially-exfoliated nanosheet was removed. The supernatant was centrifuged again at 6 krpm and the sediment was collected to remove the ultra-small and thin

nanosheets.

As water is problematic for device fabrication due to its high boiling point, the obtained sediment was dispersed and washed in isopropanol (IPA, Sigma Aldrich, HPLC grade) by centrifuging and decanting twice. The WSe_2 IPA dispersion was finally obtained and used for further characterisation and device fabrication.

7.2.2 Device fabrication

Substrate treatment

Indium tin oxide (ITO) coated glass slides (Ossila, 100 nm thick, 20 Ω sq^{-1}) were used as bottom electrodes. The ITO glass was cut into 2.5 cm×2.5 cm and Kapton tape was used to cover each substrate with an area of 2.5 cm×1.3 cm. The covered ITO glass was immersed into 2 M hydrochloric solution at 80 °C for 5 min to etch the exposed ITO area. The obtained ITO glass was cleaned in ~5 vol% Hellmanex/H_2O solution, H_2O, and IPA in sequence for 10 min each. Then, ITO glass was blow-dried by a compressed nitrogen flow and was under oxygen plasma treatment for 5 min at a power of 100 W.

Heterojunction devices

For heterojunction devices, ITO glasses were used as bottom electrodes as well as the substrates. All the solution processes were done in ambient. Poly(3,4-ethylenedioxythiophene) polystyrene sulfonate (PEDOT:PSS) aqueous solution (Ossila, Al4083) was filtered through 0.45 μm PTFE filters to remove aggregates. The filtered PEDOT:PSS was spin-coated onto ITO at a speed of 3000 rpm for 40 s using a spin coater (Model: WS-400A-8NPP/LITE). The ITO/PEDOT:PSS was annealed at 140 °C for 20 min. The mean thickness of PEDOT:PSS layer was 50 ± 3 nm. WSe_2 IPA dispersion was then sprayed on ITO/PEDOT:PSS and annealed in glovebox at 100 °C for 30 min with a mean thickness of 20 ± 8 nm. ZnO

nanoparticles in IPA and propylene glycol (Sigma-Aldrich, N-11-Jet, particle size: 8-16 nm, 2.5 wt%) was diluted in IPA at a volume ratio of 1:1 and was bath-sonicated for 10 min before use. It was spun onto ITO/PEDOT:PSS/WSe_2 at a speed of 2000 rpm twice and annealed in ambient at 80 °C for 10 min. The mean thickness of ZnO layer was 55±11 nm. A precision cotton swab (Ossila) wet by acetone was used to wipe off the coated layers to expose ITO in the middle as shown in the figure. Subsequently, the top electrode aluminum (100 nm) was deposited by Temescal FC-2000 through a shadow mask at a rate of 0.2 nm per second and the final device structure was ITO/PEDOT:PSS/WSe_2/ZnO/Al. A bar of Al electrode was evaporated onto the exposed ITO region to evenly collect current from each device. The silver paste was then applied to each Al electrode and ITO for the purpose of electrical contacts. The completed devices were annealed in glovebox for 1 h at 80 °C to improve the contact. For ITO/PEDOT:PSS/WSe_2/Al and ITO/WSe_2/ZnO/Al, they were fabricated in the same way. The device area was defined as the overlapping area between top and bottom electrodes, which is around 6.5 mm^2.

Encapsulation

We noticed that the electrical behaviors of heterojunctions could change significantly in ambient within a few hours. Given the measurement were performed in ambient, we deliberately left devices in air overnight to give stabilised performance. The “aged” devices were encapsulated by drop-casting a transparent varnish (Sally Hansen). The devices were again left in air overnight to allow the varnish to dry completely before measurements.

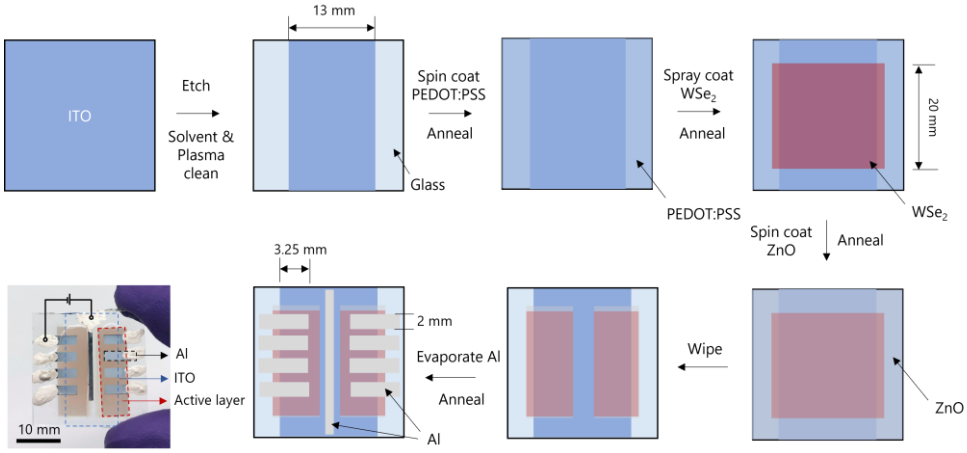

Figure 7.1 The heterojunction fabrication process. A schematic illustration of the fabrication process and a photograph of the obtained device is shown.

7.2.3 Characterisations

UV-Vis absorption spectroscopy

The transmittance spectra of the WSe_2 film on a glass slide and a glass slide alone were recorded by Cary 50 spectrophotometer in the range of 300-900 nm. The transmittance T was converted into absorbance A using formula $A = -\log_{10}(T)$. The absorbance of WSe_2 was obtained by $A_{WSe_2} = A_{Total} - A_{Glass}$. The absorption coefficient α was calculated by $\alpha = 2.303A / t_{film}$, where t_{film} is the film thickness.

Raman spectroscopy

WSe_2 ink were drop-casted onto Si/SiO_2 substrate and the obtained film was annealed at 120°C. The Raman spectrum of the film was acquired with a 20× objective at a laser wavelength of 633 nm. The final spectrum is an average of 10 accumulations.

Profilometry

The thicknesses of films were measured by a Bruker Dektak profilometer. The line profile was taken with 1000 μm length and a resolution of ~50 nm/sample.

More than 4 profiles were taken for each sample. The stylus force was set to 1 mg. The thickness of each layer was determined on another identical film fabricated in the same way on pre-cleaned glass substrates.

7.3 Results and discussion

7.3.1 Basic characterisations

WSe_2 nanosheets were prepared by liquid phase exfoliation of the powder in SC aqueous solution in an ultrasonic bath under the protection of nitrogen gas. The dispersion was purged with the high purity nitrogen during exfoliation to remove excess oxygen and prevent nanosheet oxidation. The size selection of nanosheets were performed by liquid cascade centrifugation[123] to remove un-exfoliated material as well as ultra-small species. As water is problematic for film formation due to its high surface tension and boiling point[200], the SC/H_2O dispersion was solvent-exchanged to isopropanol (IPA, Sigma Aldrich, HPLC grade) by repeat centrifugation and re-dispersing. The experimental details are presented in supporting information S1. The final obtained WSe_2/IPA dispersion with a concentration of around 3 mg mL^{-1} (**Figure 7.2A** inset).

The exfoliated nanosheets were characterised by TEM, and a typical TEM image of nanosheets is shown in **Figure 7.2**. Plate-like morphology can be observed, and their sizes range from around 100 to 200 nm. To find the length and the thickness distribution of these nanosheets, AFM was performed with nanosheets deposited on Si/SiO_2 substrates by drop-casting. More than 100 nanosheets were counted and the statistical results are given in **Figure 7.2B-C**, respectively. The mean length $\langle L \rangle$ and number of layers $\langle N \rangle$ for nanosheets are 174 nm and 10, respectively, corresponding to a length to thickness aspect ratio of ~27, which agrees with previous reported LPE TMDs nanosheets exfoliated in water/surfactant.[122, 123]

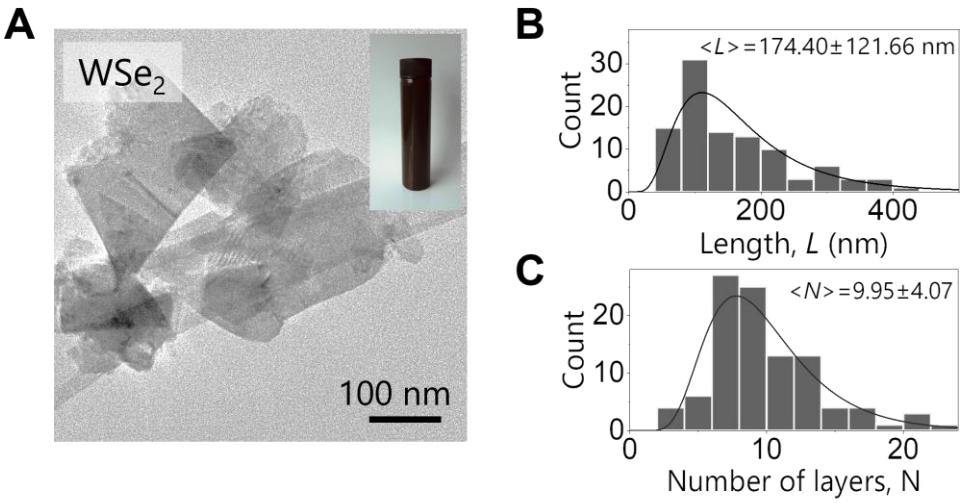

Figure 7.2 Nanosheet morphology. (A) TEM images of liquid-exfoliated WSe_2 nanosheets. The inset is a photograph of the obtained nanosheet dispersion in IPA. Statistical results of nanosheets length (B) and number of layers (C) from AFM.

The WSe_2 dispersion was spray-coated onto a glass slide to yield a network of thickness around 20 nm, which was then characterised by UV-Vis spectroscopy. The absorption coefficient α spectrum is plotted in **Figure 7.3**. The mean absorption coefficient of WSe_2 in the visible regime (400 to 700 nm) is around 2.14×10^7 m^{-1} (characteristic absorption length, $1/\alpha$~50 nm) which is appropriate for optoelectronic applications. The characteristic excitonic absorption peaks A and B for WSe_2 can be found at around 760 nm and 590 nm, respectively. The ZnO dispersion was spin-coated onto glass slides to form a film with a thickness of ~55 nm and its absorption coefficient spectrum is also included in the figure. The absorption coefficient of ZnO is much smaller than WSe_2 in visible regime as expected. The optical bandgap E_g can be obtained using $(\alpha h\nu)^{1/r} = C(h\nu - E_g)$ [345], where r=0.5 and 2 for the direct allowed transition and indirect allowed transition, respectively, and C is a constant.[346] The intercept by extrapolating the linear portion of the plot of $(\alpha h\nu)^2$ and $(\alpha h\nu)^{1/2}$ versus $h\nu$ to the x axis corresponds to the E_g of ZnO, which is known as the Tauc plot and is shown in **Figure 7.3B** and

its inset. A cutoff to the absorption edge gives an indirect and direct E_g of around 3.1 and 3.25 eV, respectively. Although ZnO is widely reported to be a direct bandgap semiconductor, there are also reported cases that the indirect bandgap is actually smaller than the direct one[347-349], possibly due to a phase transition from the wurtzite structure to a hexagonal one.[348] Here, the indirect bandgap is used for the following analysis. The bandgap of WSe_2 was not obtained in this way as the excitonic binding energy is unknown and is likely involved and contributes to the actual bandgap. The dispersion was drop-casted on a Si/SiO_2 substrate and the film was characterised by Raman spectroscopy (**Figure 7.3C**). The Raman spectrum shows two distinct peaks corresponding to E^1_{2G} and A_{1G} modes. Overall, the optical properties of the exfoliated WSe_2 are consistent with previously reported results. [303, 350]

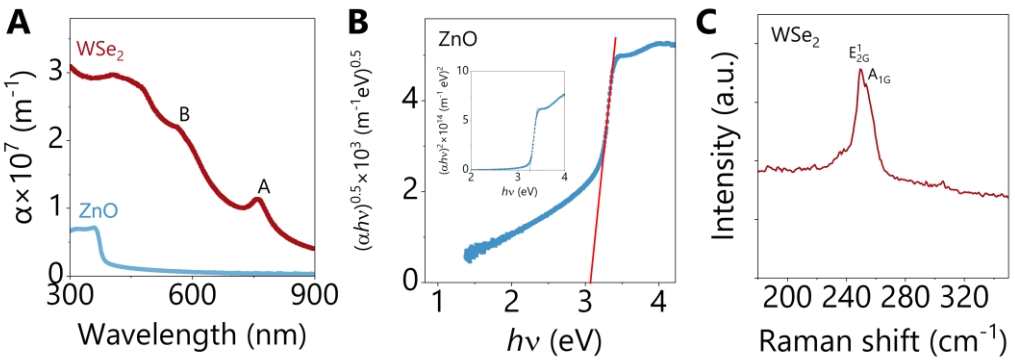

Figure 7.3 Optical characterisations of WSe_2 and ZnO. (A) UV-Vis absorption coefficient spectra of WSe_2 and ZnO thin films. (B) Tauc plots of the ZnO film. (C) The Raman spectrum of WSe_2 thin films on the Si/SiO_2 substrate.

The obtained average absorption coefficient of WSe_2 in the visible regime is around 2.14×10^7 m^{-1}, corresponding to a characteristic absorption length of around 50 nm. We used ~20 nm thick WSe_2 thin film as the light absorbing layer to investigate its optoelectronic responses. Because it is recently found that the electrical properties of these LPE semiconducting nanosheet networks are greatly limited by the point-contact between nanosheets.[189] For example, the mobility is

usually low (in-plane: 10^{-2} to 10 $cm^2 V^{-1} s^{-1}$) and this will cause the factor, such as the photocarrier diffusion length $L \propto \mu^{0.5}$, to be limited. For the current study, the devices are all fabricated in a vertical fashion that it is expected the out-of-plane mobility will be 1-2 order of magnitude lower than the mobility along the in-plane direction, which will further decrease the diffusion length. Therefore, as the first attempt, we used such thin WSe_2 nanosheet networks to allow the photocarriers to be able to diffuse through the network. Moreover, the series resistance of the WSe_2 layer should also be considered. We have observed that increasing the thickness of the nanosheet network will increase the series resistance and the electrical behavior from the interface will be less significant (Chapter 6). Therefore, restricting the thickness of the WSe_2 layer to only ~20 nm can allow us to easily observe the electrical behavior coming from the WSe_2/ZnO heterojunction interfaces.

Following the successful preparation of nanosheet dispersions, we now move on to heterojunction. We aim to realize a conventional diode structure e.g., cathode/ HTL/light absorbing layer/ETL/anode. Here, ITO glasses are used as the bottom transparent electrodes, and PEDOT:PSS and ZnO nanoparticles as transport layers, respectively. The final device structure is ITO/PEDOT:PSS/WSe_2/ZnO/Al as depicted in **Figure 7.4A**. The TEM image of the as-received ZnO nanoparticles is shown in **Figure 7.4B**. The position of the CBM for ZnO is reported to be around -4 to -4.5 eV[351], which will be further verified below. The position of its Fermi level is close to its conduction band minimum due to n-doping by the oxygen vacancies. The shallow work function and CBM of ZnO imply that it can be used to facilitate electron transport. Moreover, ZnO is a wide bandgap semiconductor (E_g=3.1 eV obtained from UV-Vis characterisations) that can provide a hole-blocking function and impose negligible light absorption in the visible regime. Therefore, ZnO is used here as the electron transport and hole

blocking layer. PEDOT:PSS is a polymer that incorporates conductive PEDOT with positive charges into insulating PSS with negative charges. The chemical structure is shown in **Figure 7.4C**. It possesses high transparency in the visible regime, a relatively high and adjustable electrical conductivity and exhibits a deep work function of around -5.1 eV (from supplier). PEDOT:PSS aqueous solution can be solution-processed into thin films, which will be able to provide desirable Ohmic contacts for p-type semiconductors due to its deep WF. Overall, both PEDOT:PSS and ZnO are established transport layer materials for various optoelectronic applications[352, 353] and can be simply solution-processed into thin films. They have distinct energetic properties and low absorption coefficients in the visible regime compared with WSe_2, allowing us to investigate the role of WSe_2 nanosheet networks as the light absorbing layer in such hetero-structured devices. In addition, assuming ZnO nanoparticles can realize full coverage on top of the porous nanosheet network they will help avoid metal diffusion into networks.

The morphology of the fabricated devices was characterised by SEM. A representative top-view SEM image is shown in **Figure 7.4D**. ZnO nanoparticles are uniformly coated on the WSe_2 layer with the absence of pinholes, and distinct edge between the Al electrode and ZnO film can be observed. The heterojunction ITO/PEDOT:PSS/WSe_2/ZnO/Al was fractured after frozen by liquid nitrogen to expose the cross section, which is further imaged by SEM as shown in **Figure 7.4E**. There is no visible metal filament formed between Al and ITO, which confirms the successful fabrication of the proposed device structure.

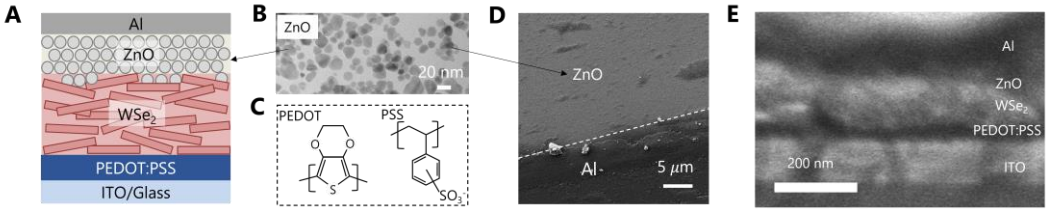

Figure 7.4 Heterojunction device structure and characterisation. (A) A schematic illustration of the device structure. (B) A TEM image of the as-received ZnO nanoparticle. (C) The chemical structure of PEDOT and PSS. (D) A SEM image of the obtained heterojunction. (E) Cross-sectional image of the full-stack heterojunction.

7.3.2 Electrical measurements

The energy band of each material determines the electrical behaviors of the heterojunctions. First, ITO/PEDOT:PSS/ZnO/Al Schottky type diodes were fabricated following the same fabrication procedures as the ones with WSe_2 to examine the energetic position of ZnO. The electrical properties of devices were investigated by collecting current-voltage (*I-V)* characteristics from -1 to 1 V in ambient and dark conditions. The current was then converted into current density J by dividing the device area A. The obtained *J-V* curves are shown in **Figure 7.5A**, and the semi-log plots are shown in the inset. The Schottky devices show rectifying behaviors with a rectification ratio (RR) at ±1 V around 100 (**Figure 7.5A**). The electrical properties were extracted using the Shockley equation with a resistor in series:

$$J = J_s \exp\left[\frac{q(V - JR_sA)}{nkT}\right] \tag{7.1}$$

where J_s is the saturation current density $J_s = A^*T^2 \exp(-\frac{q\phi_b}{kT})$ and n is the ideality factor, q is the elementary charge, k is the Boltzmann constant, and T is the temperature. ϕ_b is the potential barrier height at the PEDOT:PSS/ZnO interface, which corresponds to the difference between the CBM of ZnO and WF of

PEDOT:PSS. A^* is the Richardson constant. The fittings were conducted in the range of 0-1 V and are shown in **Figure 7.5B**. The obtained ideality factor n is 2.81±0.33, series resistance R_s is 92.71±14.85 Ohm, and ϕ_b is 0.65±0.03 eV taking the effective electron mass m^* in ZnO is $0.3m_0$. Therefore, it can be found that the CBM for ZnO is around -4.5 eV, given the WF of PEDOT:PSS is -5.1 ± 0.1 eV from the supplier.[354] The energy band diagram for the Schottky diode is illustrated in **Figure 7.5C.**

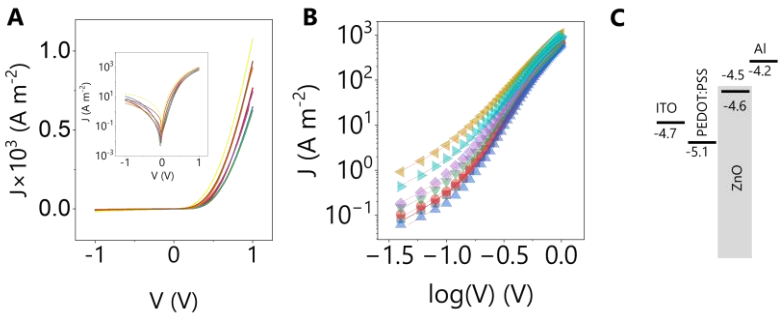

Figure 7.5 Electrical characterisation on ZnO based Schottky diodes. (A) The *J-V* curves of ITO/PEDOT:PSS/ZnO/Al. The inset is the semi-log *J-V* curves. (B) The fitting curves of the Schottky devices. (C) The energy band diagram before contact. The *J-V* curves are obtained by the electrical measurements on 8 identical fabricated devices on one ITO substrate.

The energy bands of each material used for the device are depicted in **Figure 7.6A**. The WF of ITO is -4.7 eV.[355] PEDOT:PSS can only weakly block electron transport due to the metallic nature of PEDOT.[356] The reported conduction band minimum (CBM) of WSe_2 ranges from -3.5 to -4 eV for few- and multi-layered nanosheets.[267, 304, 357] We estimate -3.8 eV as its CBM, taking 1.4 eV as the bandgap,[358] the valence band maximum (VBM) will be -5.2 eV. The Fermi level E_f for WSe_2 is unknown and will likely be affected by processing details. However, it was previously reported to exhibit p-type behavior.[199] It is found in the following electrical characterisation section that there could be a potential barrier at the ITO/WSe_2 interface for hole transport, indicating E_f for WSe_2 is probably deeper than -4.7 eV. As ZnO is a naturally n-doped material due to

oxygen vacancies, its E_f will be very close to its CBM and is estimated to be -4.6 eV.[359] Using optical bandgap E_g~3.1 eV, the VBM will be around -7.6 eV. The top electrode is Al which has a WF of -4.2 eV and so can make Ohmic contact with ZnO.

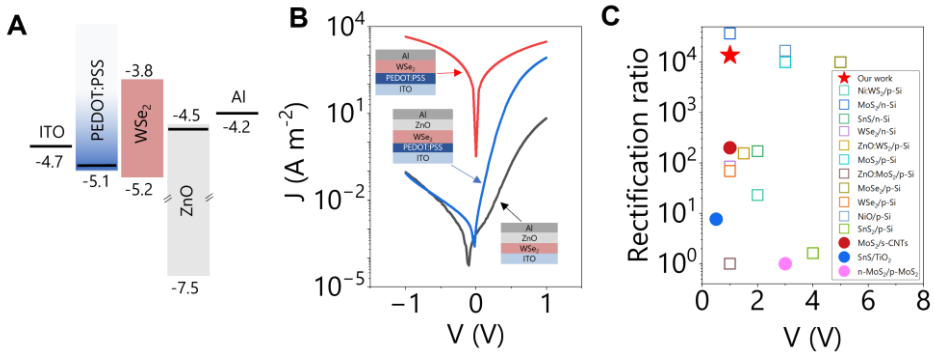

Figure 7.6 Electrical characterisations on heterojunctions. (A) Energy bands of each material in the heterojunction. (B) Semi-log representative *J-V* curves for different heterojunctions. The device structure is schematically illustrated in the insets. (C) Rectification ratios at various biases extracted from literatures.

To understand the role of each layer in the primary 3-layer device (ITO/PEDOT:PSS/WSe_2/ZnO/Al), we also characterised heterojunctions with structure: ITO/WSe_2/ZnO/Al, and ITO/PEDOT:PSS/WSe_2/Al. The thicknesses for each layer type in these devices were kept constant from device to device using identical coating parameters. Their representative *J-V* curves are given in **Figure 7.6B**. The ITO/PEDOT:PSS/WSe_2/Al device shows an almost symmetric *J-V* curve with *J* much larger than the other devices. However, these results may be misleading since Al metal atoms probably diffuse into pores or pinholes of WSe_2 nanosheet networks and are likely in contact with metallic PEDOT:PSS during evaporating top electrode process.[168, 360] This highlights the difficulty in working with porous nanosheet networks. Such electrical shorts can be avoided by coating ZnO nanoparticles on top of WSe_2. For example, a clear rectifying behavior can be observed for ITO/WSe_2/ZnO/Al with a RR at ±1 V of about 73 (Full *J-V*

curves are in **Figure 7.7A**). When both PEDOT:PSS and ZnO are used in the full device stack (ITO/PEDOT:PSS/WSe_2/ZnO/Al), *J* at forward bias is significantly larger than that from ITO/WSe_2/ZnO/Al devices. A stronger rectification was observed with a RR of ~10^4 (Full *J-V* curves are in **Figure 7.7B)**. During the forward bias measurement, there were no visible light emission which could be due to the few-layered WSe_2 nanosheets are indirect bandgap semiconductors that the radiative recombination is a less likely event.

To understand their electrical behaviors, the WSe_2/ZnO interface is assumed to act as a type-2 heterojunction. Without external biases, once WSe_2 and ZnO are in contact and form an interface with an internal built-in potential Φ_b, the Fermi level will be constant throughout WSe_2 and ZnO under thermal equilibrium. Therefore, electrons diffuse from ZnO into WSe_2 and holes diffuse in the opposite direction, forming depletion regions extending from the interface into both semiconductors up to certain thicknesses defined by their doping densities. As a result, we expect a CBM offset ΔCBM of ~0.7 eV and a VBM offset ΔVBM of ~2.4 eV formed at the WSe_2/ZnO interface.

Here, only devices with ZnO ETLs are discussed. Under small forward biases, electrons have insufficient energy to overcome ΔCBM from ZnO to WSe_2. With increasing of forward bias, the reduction of ΔCBM greatly improves electron injection, resulting in an exponential increase of *J*. Under higher forward biases, ΔCBM is compensated by the bias, and *J* becomes linear as the device becomes limited by its series resistance. From the *J-V* curves in **Figure 7.6B**, the forward-bias *J* from the device without PEDOT:PSS is much lower than the one with PEDOT:PSS. This is due to a Schottky barrier formed at the ITO/WSe_2 interface that blocks hole transport from WSe_2 to ITO. Introducing PEDOT:PSS at this interface can reduce or even remove the potential barrier and allows facile hole injection, eventually yielding a higher *J* at forward biases. Under reverse biases,

both heterojunction devices gave similar small *J*. The small reverse current density could be attributed to the prohibited hole transport from WSe_2 to ZnO due to the large ΔVBM formed at this interface. Therefore, this analysis indicates that rectifying behavior would mainly come from the WSe_2/ZnO interface.

The presence of the p-n junction and the electron- and hole-injecting electrodes means the ITO/PEDOT:PSS/WSe_2/ZnO/Al heterojunction device works effectively as a diode with much higher forward than reverse bias as mentioned above. We quantify this via the RR at ±1 V, of which our best device displayed RR=1.4×10^4 which is among the highest reported for such devices. We summarize the reported solution-processed diodes incorporating LPE TMDs nanosheets in **Appendix A2** and plot their RR against various biases in **Figure 7.6C**. The open symbols represent RR from diodes using nanosheets deposited on heavily doped silicon, and closed symbols represent diodes with all-solution-processed active layers. The RR from our device is shown in red star and is higher than all but one TMDs/Si device.

The current density of a heterojunction formed at the WSe_2/ZnO interface can also be described by equation 7.1.[1] To extract the electrical parameters of the fabricated devices, the *J-V* data was fitted using this equation.[168] This procedure gave good fits, yielding the diode parameters n, J_s and R_s, which are shown in **Figure 7.7C-D**. The obtained fitting parameters are summarized in **Table 7.1**. Generally, the ideality factor is usually in the range of 1-2, where n=1 accounts for diffusion current dominated conduction and n=2 stands for generation/recombination dominated conduction mechanism.[1] The obtained n for ITO/PEDOT:PSS/WSe_2/ZnO/Al is around 2, indicating these devices are dominated by generation/recombination. n for ITO/WSe_2/ZnO/Al is larger than that from the ITO/PEDOT:PSS/WSe_2/ZnO/Al. This phenomenon is likely associated with imperfect Ohmic contact at the ITO/WSe_2 interface.

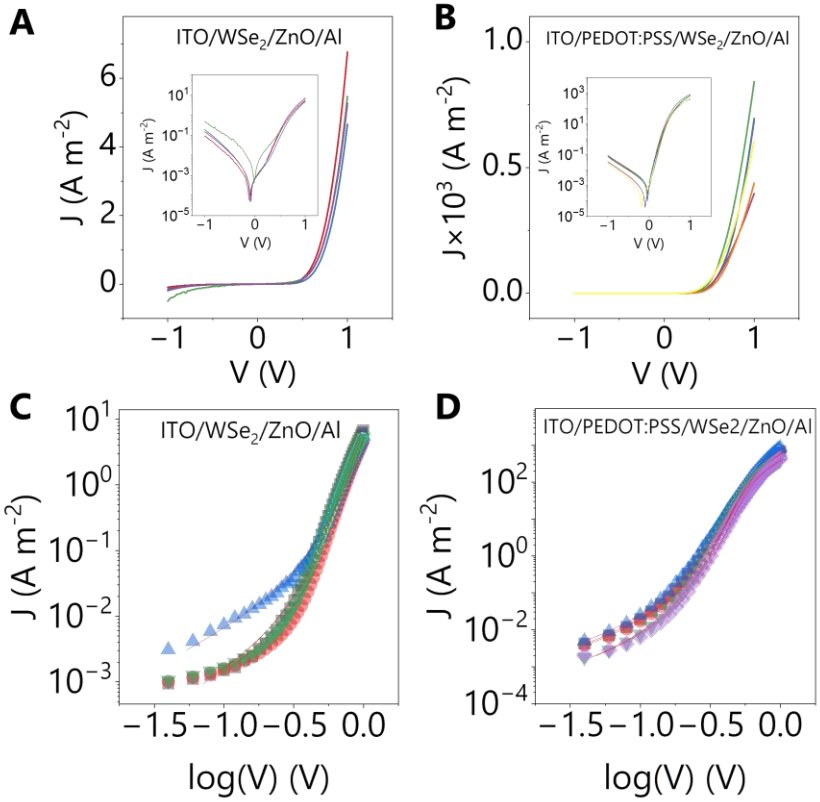

Figure 7.7 Electrical and fitting results of heterojunctions. (A-B) *J-V* curves of ITO/WSe_2/ZnO/Al and ITO/PEDOT:PSS/WSe_2/ZnO/Al, respectively. (C-D) Fitting curves of corresponding heterojunctions, respectively. The *I-V* characterisations were performed on all the devices fabricated on the same substrate. The *I-V* curves from the same type of devices on one substrate are included in one figure and are shown in different colours.

Table 7.1 The extracted electrical parameters from fittings.

Device	Extracted parameters		
	n	***J_s* (mA m^{-2})**	***R_s* (Ohm)**
ITO/PEDOT:PSS/ZnO/Al	2.81 ± 0.33	0.43 ± 0.57	92.71 ± 14.85
ITO/WSe_2/ZnO/Al	4.78 ± 0.92	2.57 ± 3.11	1205 ± 331
ITO/PEDOT:PSS/WSe_2/ZnO/Al	2.02 ± 0.11	2.64 ± 1.40	133 ± 22

Lower J_s values imply a lower recombination current, leading to a better performance for applications such as solar cell. The extracted J_s for both types of heterojunctions are comparable, which is around 2.6 mA m^{-2}. The obtained J_s value is orders of magnitude larger than state-of-the-art solution-processed solar cells, fabricated from organics[361], quantum dots[362] and perovskites[363]. Therefore, the obtained heterojunctions suffer from significant recombination associated with either the heterojunction interface or the nanosheet network.

The obtained R_s for ITO/PEDOT:PSS/WSe_2/ZnO/Al is 133±22 Ohm, which includes the resistance of WSe_2 network along the OoP direction as well as that of the other materials. The OoP resistance of WSe_2 is obtained by subtracting the series resistance of the ITO/PEDOT:PSS/ZnO/Al device (~ 93 Ohm) from that of the full 3-layer device. The resultant resistance yields an OoP conductivity of WSe_2: $\sigma_{OoP,WSe_2} = 7.55\times10^{-5}$ S m^{-1}. This value is roughly one order of magnitude lower than its IP value which tends to be in the range 10^{-4} to 10^{-3} S m^{-1}.[199, 364] This low electrical anisotropy (IP to OoP) is consistent with our previous study on LPE semiconducting nanosheet networks in a random stacking arrangement.[168] The value of R_s for ITO/WSe_2/ZnO/Al is significantly larger than that from the one with PEDOT:PSS. A potential barrier is formed and thus induces higher contact resistance as well as the poor diode behaviors.

7.3.3 Optoelectronic responses

Given the observed diode behavior of these devices, optoelectronic responses of all three types of devices are measured under AM1.5D illumination (the measurement details are given in Chapter 5). We randomly chose one device for each type of device structures for the measurement. The light intensity F was tuned using a shutter and neutral density filters, varying from dark to 1000 W m^{-2}. The temporal behavior of photocurrent I_{ph} under illumination was recorded

without any external bias. A shutter was manually placed and removed on top of the device to simulate the light "on" and "off" states. The obtained photocurrent was then divided by device area A to obtain photocurrent density J_{ph}. The temporal J_{ph} responses from ITO/PEDOT:PSS/WSe_2/ZnO/Al at various light intensities are shown in **Figure 7.8A**. The device exhibited obvious photoresponses with rise and decay time both less than a second (limited by the equipment resolution ~450 ms). Further improvement on the measurement equipment will be required. Because no bias was applied, the background current is purely noise from the Keithley (the noise current density fluctuated from around -2×10^{-3} to 6×10^{-4} A m^{-2}) and the measured current density is exactly J_{ph} that doesn't need to subtract the background current. J_{ph} can also be regarded as the short-circuit current density J_{sc}. No smoothing of photocurrent signal was conducted. This means that the device can be operated as a self-powered photodetector. For completeness, the photoresponses for the other two types of devices were also measured. Under the same measurement conditions, there was no measurable photocurrent. This phenomenon verifies that the WSe_2/ZnO interface indeed forms a built-in potential and a depletion region that could separate photo-carriers. Moreover, the PEDOT:PSS layer can remarkably reduce the recombination at the ITO/WSe_2 interface and therefore enhance the photocurrent.

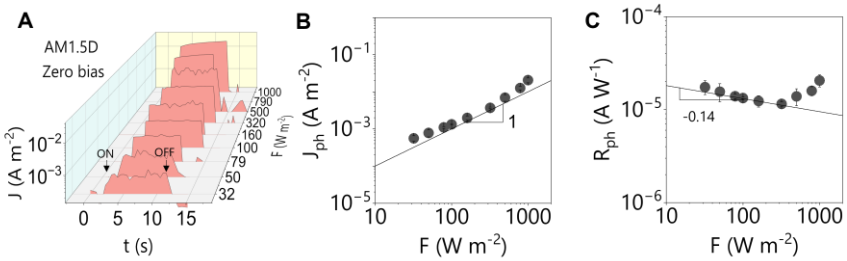

Figure 7.8 Photoresponses of ITO/PEDOT:PSS/WSe_2/ZnO/Al under illumination. (A) Temporal photocurrent density J_{ph} under AM 1.5D illumination with various light intensities F at 0 V. (B) The F-dependent photocurrent density J_{ph}. (C) The F-dependent photoresponsivity R_{ph}.

The F-dependent J_{ph} is extracted from **Figure 7.8A** and is shown in **Figure 7.8B**. J_{ph} increases with F with an exponent very close to unity, consistent with the presence of only very shallow traps.[223] One important parameter to evaluate the photodetector performance is the photo-responsivity, R_{ph}, which is defined as $R_{ph} = J_{ph} / F$. Thus, using averaged data in **Figure 7.8B**, the F-dependent R_{ph} can be obtained and is given in **Figure 7.8C**. R_{ph} decreases very weakly with F with an exponent of around -0.14 at relatively low F. A slight increase of R_{ph} is observed at higher F probably due to the increased number of carriers generated under higher light intensities owing to thermal effects. Under optical excitation, the WSe_2 (the main light absorbing material) will absorb the incident light and generate photocarriers. Its temperature will increase due to the defect-related non-radiative recombination. The increased temperature will in turn change the optical/electrical properties of semiconducting layers and the interfacial electrical behavior associated with both semiconductors. For example, the mobility of the semiconductor is usually higher at elevated temperatures as a greater number of carriers can be thermally activated. The mobility μ is related to the diffusion length L by $D=kT\mu/q$ and $L=(D\tau)^{0.5}$. In the case of no applied voltage, $J_{ph}=qG(L+W)$. Therefore, we can find the factor L can be increased at higher temperatures and an overall increase of J_{ph} could be observed. However, as both optical and electrical properties of materials will change with temperature and illumination, the mechanism behind the observed phenomenon is complicated and it requires further careful measurement to identify the dominant factors regarding the J_{ph} behavior.

As WSe_2 is the main light absorbing material due to its large coefficients and the small indirect bandgap in such devices (ITO/PEDOT:PSS/WSe_2/ZnO/Al), it is expected that photocarriers generated in the WSe_2 layer may suffer from the non-radiative recombination process that the energy is released in the form of

phonons, i.e., heat. However, it is difficult to directly measure the temperature of the WSe_2 layer as it is sandwiched by the other materials in the vertical devices. Alternatively, the device could be measured in an *I-V* test system integrated with the solar simulator that is capable to controllably vary temperature on the device. The device performance can be investigated over a wide temperature range to study the influence of the thermal effect on the device performance.

The *J-V* curves under various *F* were also collected with 1 mV steps and are shown in **Figure 7.9A**. The semi-logarithmic plot is given in its inset. The linear *J-V* curves show obvious photoresponses at forward biases, while the semi-logarithmic curve shows that photoresponses can also be observed at reverse biases. This indicates that the fabricated photodetector can not only work in photodiode mode (at zero and reverse biases), but also in photoconductor mode (at enough high forward biases).

The short-circuit current (at V=0 V) and open circuit voltage (at J=0 A m^{-2}) were not so obvious but were small but detectable (**Figure 7.9B**). J_{sc} increases with F while V_{oc} only increases with F at F <100 W m^{-2}. This indicates that thermal effect due to higher light intensity would increase J_s and leads to smaller V_{oc}, which is widely observed in other type of solar cells.[365, 366] The extracted V_{oc} is plotted against J_{sc} in **Figure 7.9C**. V_{oc} is described by the following equation.[367]

$$V_{oc} = \frac{nkT}{q} \ln(1 + \frac{J_{sc}}{J_s}) \tag{7.2}$$

Taking n=2, several plots with various J_s values can be made in the figure. The increase of J_s with F can be clearly visualized.

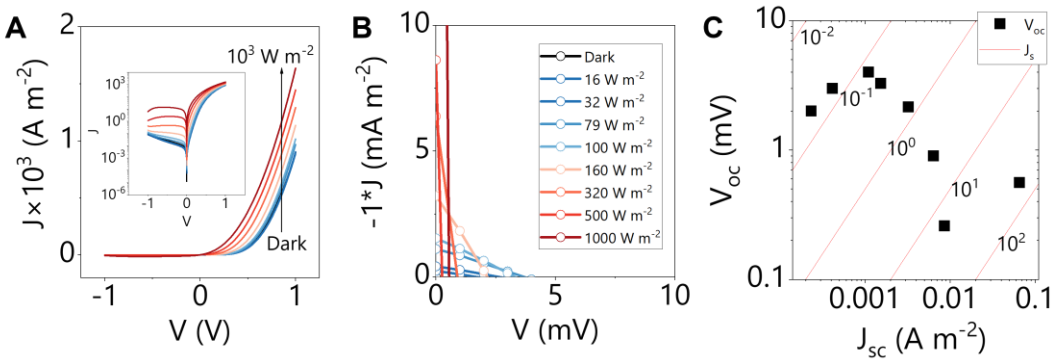

Figure 7.9 Electrical characterisation on ITO/PEDOT:PSS/WSe_2/ZnO/Al under illumination. (A) *J-V* curves of the device under illumination with various *F*. The inset is the semi-log *J-V* curves. (B) The *J-V* curves around origin is shown, which give V_{oc} and J_{sc}. (C) The obtained V_{oc} is plotted versus J_{sc}.

J_{ph} values were extracted from the *J-V* curves at -1, 0 and 1 V and converted into R_{ph}, which is plotted against *F* in **Figure 7.10A**. This plot directly compares the photodetector performance operated in photodiode and photoconductor modes. R_{ph} at 0 V is consistent with the result from temporal J_{ph} measurement (**Figure 7.8**), which is low, around 10^{-5}-10^{-4} A W^{-1}. It is worth noting that when there is no external bias, only photons absorbed in or within a diffusion length from the depletion region in either WSe_2 or ZnO will be converted into photocarriers that can contribute to J_{ph}. When the device is reverse biased (-1 V), the depletion width will be extended, and it allows more photons being absorbed in the depletion region. This is consistent with our observation that R_{ph} at -1 V is at least 1 order of magnitude higher than that at 0 V. Interestingly, R_{ph} at 1 V is more than 4 orders of magnitude higher than it at 0 V, indicating that the photoconductor mode is superior to the photodiode mode. Moreover, R_{ph} at -1 and 0 V increase at *F* above ~100 W m^{-2}, indicating the presence of thermal effects.

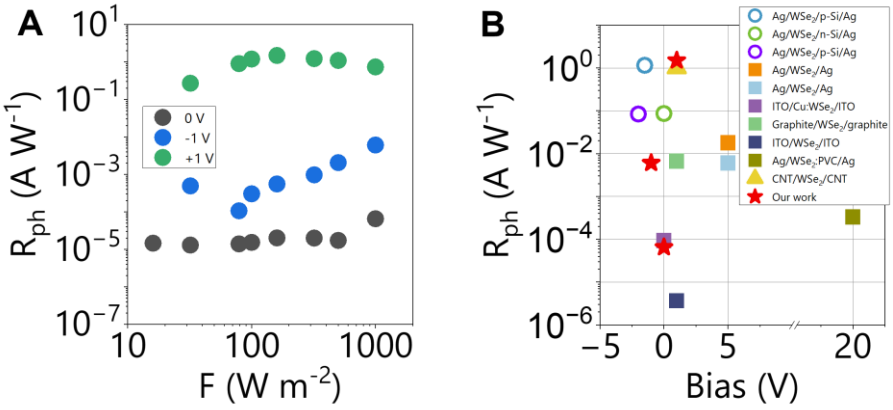

Figure 7.10 Photoresponsivity of the heterojunction. (A) *F*-dependent R_{ph} at -1, 0 and 1 V. (B) Comparison of R_{ph} at various biases, which are extracted from literatures.

The fact that R_{ph} is higher at -1 V than 0 V, implies that the depletion width is smaller than its film thickness such that the reverse bias can further widen the depletion width. This means that even though the WSe_2 layer is thin (~20 nm), it likely contains two regions, a normal region and a depleted region in contact with ZnO. This depleted region enables the device to work as a photodiode at zero and further at reverse biases. The photo-carriers generated in this region will be driven by the built-in potential and diffuse towards opposite electrodes. In the normal region, illumination will decrease its resistance via standard photoconductivity processes[222] so that the device can be operated as a photoconductor at positive biases.

For simplicity, the obtained heterojunction can be modelled as a p-n junction, where WSe_2 serves as a p-type material and ZnO serves as a n-type material. The built-in potential Φ_b for the heterojunction can be estimated by the E_f difference between two semiconductors. As the E_f of WSe_2 is close to -5.1 eV (PEDOT:PSS) according to the experimental observations, we estimate an E_f value of around -5.1 eV. ZnO is a highly doped semiconductor and its E_f will be very close to its CBM. Taking E_f of -4.6 eV for ZnO, Φ_b should be around 0.5 eV.

The depletion width for a p-n junction is given by:

$$W_p = \sqrt{\frac{2\varepsilon_0\varepsilon_r}{q}\frac{\Phi_b N_d}{N_a(N_a+N_d)}} \tag{7.3}$$

$$W_n = \sqrt{\frac{2\varepsilon_0\varepsilon_r}{q}\frac{\Phi_b N_a}{N_d(N_a+N_d)}} \tag{7.4}$$

where W_p and W_n are the depletion width on p-side and n-side semiconductors, respectively. N_d and N_a refer to donor concentration in ZnO and acceptor concentration in WSe_2, respectively. The relative permittivity ϵ_r for WSe_2 is 7.7.[368] As WSe_2 is not deliberately doped, the donor concentration in ZnO arising from its oxygen vacancies will be much larger than the acceptor concentration in WSe_2 ($N_d >> N_a$). This results in a small value of W_n. Moreover, $N_d/(N_a + N_d)$ will be approximately 1. Taking previously reported intrinsic carrier density as the acceptor concentration of WSe_2 that $N_a \sim 10^{13}$ cm^{-3},[199] we can find W_p to be around 6.53 μm. The depletion width is much larger than the thickness t of WSe_2 ~20 nm in this study. Thus, we can assume the WSe_2 layer is fully depleted.

J_{ph} at 0 V (J_{sc}) depends on the absorption of the material, diffusion length and the depletion width, which is described by equation.

$$J_{ph} = q\left[G_p(L_p + W_p) + G_n(L_n + W_n)\right] \tag{7.5}$$

G is the optical generation rate of the material. $L = \sqrt{D\tau}$ is the diffusion length of the minority carriers in the corresponding material, where $D = \frac{kT}{q}\mu$ is the diffusion coefficient and μ is mobility, and τ is the photocarrier lifetime. The photocarrier lifetime should be further determined by time-resolved photoluminescence techniques. Considering the small absorption coefficient of ZnO in visible regime (small G_n), the ZnO related terms can be therefore

neglected and will not be used for further calculation. This allows equation 7.5 to be re-written as:

$$J_{ph} = qG_p(L_p + W_p) \tag{7.6}$$

The light intensity at the WSe_2/ZnO interface is $Fe^{-\alpha t_{film}}$ if the optical loss from ITO and PEDOT:PSS is ignored. Therefore, we can obtain $G_p = \frac{\alpha F}{h\nu} e^{-\alpha t_{film}}$. G_p can be averaged in visible regime (400-700 nm) to be 5.84×10^{28} m^{-3} s^{-1}. The carrier lifetime and mobility are unknown. However, even though L_p is small, the sum of L_p and W_p should be at least larger than 20 nm (thickness of WSe_2). We can calculate the expected J_{ph} at 0 V (J_{sc}) should be at least 116.8 A m^{-2} at 1000 W m^{-2}.

The theoretical value of J_{sc} (116.8 A m^{-2}) is order of magnitudes higher than the experimental value (6.5×10^{-2} A m^{-2}). This implies that either G_p or the sum of L_p and W_p to be small. As is known that the optical generation of TMDs is superior from above calculation, the reason can only be the latter. The device is limited by both short diffusion length and narrow depletion width on the WSe_2 side.

The observed phenomena may be associated with various factors. First, as the device was illuminated on the ITO side, the un-depleted, normal region experienced light first. This may also favor the photo-conductor mode rather than the photo-diode mode. Second, as these nanosheets are mostly few-layered, energy band variation across the network could trap the photocarriers and limit the diffusion length. Lastly, although no dopant was added to the dispersion on purpose and the surfactant was removed before film formation, some dopants from either trace amount of residual surfactants[168] or O_2 and H_2O in the air[369] are inevitable. This un-intentional doping effects could make the depletion width on the WSe_2 side narrower than expected.

To compare our photodetector performance, the literature R_{ph} values from LPE WSe_2 based devices were summarized in **Appendix A2** and are plotted against various biases to distinguish different photodetector operation modes in **Figure 7.10B**. The open circle symbols represent the devices using heavily doped silicon substrates as one of the active layers, and these devices mainly worked in photodiode mode and showed better performance than ours at reverse biases. This result is not a surprise since silicon-only diodes can be used as good photodetectors due to their thickness and high quantum efficiency[370, 371], while photoresponses from our devices mainly come from the WSe_2 layer alone. The solid squares represent Ohmic contacted devices fabricated in a lateral structure, and these devices can only be operated in photoconductor mode due to the lack of built-in potential. Our device working as a photoconductor (positive bias) gives the highest R_{ph} to be about 1.5 A W^{-1} at 1 V. The only R_{ph} which is close to our result at 1 V is shown in the solid triangle. It refers to a vertically structured and Ohmic contacted device that WSe_2 layer was sandwiched between two metal electrodes made from carbon nanotubes. The large R_{ph} probably comes from much reduced channel length in a vertical structure compared with that in a lateral one.

To explore the operating mechanism of the obtained device, *F*-dependent *J-V* curves were fitted by modifying equation 1 to include a photoinduced current density J_{ph}.[202] When the device is not biased, J_{ph} is equivalent to J_{sc}.

$$J = J_{ph} - J_s\left[\exp(\frac{q(V - JR_sA)}{nkT}) - 1\right] \tag{7.7}$$

This equation fits the data very well as shown in **Figure 7.11A**, with the extracted parameters plotted versus *F* in **Figure 7.11B**. Both *n* and J_s remain almost constant at $F \leq$ ~100 W m^{-2}, but increase significantly when *F* exceeds this critical value. Above ~100 W m^{-2}, thermal effects increase J_s by roughly 4 orders of

magnitude. Incidentally, this leads to even poorer photovoltaic performances as shown in **Figure 7.9B**. The series resistance, R_s, decreases with F, consistent with a positive photoconductivity σ_{ph} of the device. Assuming the photoconductivity is associated with the WSe_2 layer, σ_{ph} is calculated using $\sigma_{ph}(F) = (t_{film} / A)[R_s^{-1}(F) - R_s^{-1}(F = 0)]$. The resultant photoconductivity is plotted versus F in **Figure 7.11C**. The lowest observed photoconductivity value was ~4×10^{-7} S m^{-1} at 15 W m^{-2}. In comparison, the σ_{ph} of ITO/ZnO/Al, an Ohmic-contacted device to evaluate its photoconductivity, was measured to be 3.46×10^{-8} S m^{-1} at 1000 W m^{-2} and a bias of 1 V, which is significantly lower than that for the whole device. Therefore, σ_{ph} mainly comes from WSe_2 layer. σ_{ph} increases as a power law with F ($\sigma_{ph} \propto F^{\beta}$), showing two regimes separated at F ~100 W m^{-2}. At relatively low F, σ_{ph} exhibits superlinear dependence with β to be 1.39. β varies to 0.88 while F is above 100 W m^{-2}, corresponding to a slightly sublinear dependence.

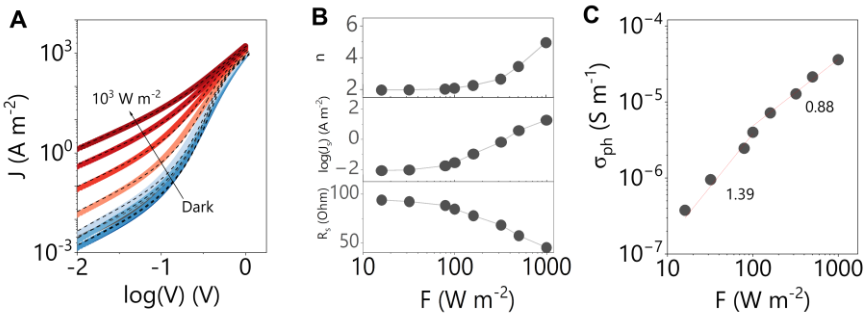

Figure 7.11 Fitting results for the full stack heterojunction under illumination. (A) Fitting curves of the heterojunction device (dash line). (B) The extracted parameters n, J_s and R_s are plotted versus F. (C) Photoconductivity σ_{ph} is plotted against F.

Sublinear dependence of σ_{ph} on F was often observed in solution-processed semiconducting nanosheet networks owing to the presence of trap states which increase the recombination.[223, 372] Since thermal effects are usually more obvious at higher F, this phenomenon is consistent with previous reports. On the other

hand, superlinear dependence is infrequently observed[373, 374] and it arises from an increase of majority carrier lifetime with *F*. In other words, the device becomes more photo-sensitive with increasing *F*, which can be contrasted with decreased carrier lifetime from sublinear dependence (less sensitive with *F*). Superliner behavior has been ascribed to two types of recombination centers with different capture cross sections for electrons and holes. One could act as sensitizer centers that prolong the carrier lifetime while the other one could induce recombination.[375, 376] Increasing *F* results in a shift of recombination center from one to the other, therefore showing different dependence behaviors. However, our measurement is inadequate to distinguish the pure photo-effect from a photothermal one. The complexity of the nanosheet composition and network morphology could also contribute to the phenomena, and more measurements and characterisations are required.

7.4 Conclusion

In this study, we have successfully fabricated solution-processed heterojunctions based on LPE WSe_2 nanosheet networks where their active layers are all solution-processed. The obtained devices show a high rectification ratio up to ~10^4 at ±1 V. It can be used as a self-powered photodetector that can be operated in both photodiode mode and photoconductor mode. R_{ph} in photoconductor mode is the highest for LPE WSe_2 based photodetectors and is around 1.5 A W^{-1} at 1 V. However, R_{ph} obtained in photodiode mode is still lower than that from silicon-based heterojunctions.

Progress is made by trial and failure.
The failures are generally a hundred
times more numerous than the successes,
yet they are usually left unchronicled.
William Ramsay

Chapter 8 Manipulating Heterojunction Interfaces

8.1 Introduction

The solution-processed heterojunctions based on LPE WSe_2 can be used as self-powered photodetectors owing to the built-in potential realized at the WSe_2/ZnO interface. It indicates that they can also be used as photovoltaic devices, however, the performance of these heterojunctions obtained from the last chapter is still lower than those based on LPE TMDs/doped-Si heterojunctions. It is believed that the heterojunction interfaces are important and the device performance could be further optimized if the interfacial properties could be manipulated. As demonstrated in the last chapter, PEDOT:PSS with a deep work function could greatly lower the potential barrier height at the ITO/WSe_2 interface. However, PEDOT:PSS itself can only provide a sole function of facilitating hole transport for WSe_2 at least. There are other types of transport layer materials available that can be solution-processed into thin films. Especially, they could not only provide the carrier transport properties but can allow only specific types of carriers to be transported (carrier-selectivity), depending on their energy band structures.

The device structure will determine its performance. The light penetrates into thin films and its intensity will decay exponentially along the light incident direction. Therefore, for any devices working based on the heterojunctions, it is preferably to place the main rectifying interface on the front to allows more photons to be

absorbed in the depletion region, as only photocarriers generated in the depletion region will contribute to the photocurrent at zero and reverse bias conditions. To test this, devices were fabricated with both normal and inverted structures and more details will be given in the following sections.

Another factor will be addressed in this chapter is the LPE TMDs and their networks. Few-layered WSe_2 that may bring energy band variations in the network that could trap the photocarriers. Therefore, the size-selection step is adjusted to yield the multi-layered nanosheets that would exhibit bulk-like properties. The photovoltaic performance of the devices under illumination will be investigated.

8.2 Experimental

8.2.1 Material preparation

The liquid exfoliation was performed in nitrogen environment following the protocols described in the last chapter. However, the size-selection was adjusted to 0.5-2 krpm, 2 h for each speed. The collected sediment was re-dispersed in IPA and washed for 3 rounds by centrifugation.

The transport layer materials are summarized in the below table.

Table 8.1 Materials and ink formulation

Material	Function	No.	Supplier	Ink formulation
PEDOT:PSS	HTL	Al4083	Ossila	1.3-1.7 wt% in aqueous solution
m-PEDOT:PSS	HTL	Al4083	Ossila	Al4083 diluted in IPA with a volume ratio of 1:1
ZnO NPs	ETL	N-11	Avantama	Partical size~12 nm, 2.5 wt% in IPA
NiO NPs	HTL	P-21	Avantama	Partical size~7 nm, 2.5 wt% in ethanol
WO_3 NPs	HTL	P-10	Avantama	Partical size~16 nm, 2.5 wt% in IPA
75 wt% TAA in IPA	ETL	17927-72-9	Sigma-Aldrich	Diluted in anhydrous IPA with a volume ratio of 1:9

Note: TAA refers to titanium diisopropoxide bis(acetylacetonate), which is used to fabricate compact TiO_2 film.

8.2.2 Device fabrication

Device structure

The device structure and energy band diagram are illustrated in **Figure 8.1**. There are two types of device structures: normal and inverted. For the normal structure, HTL is fabricated on top of the cathode, i.e., ITO, and ETL is beneath the anode (Al). The inverted structure changes the stacking sequence of the active layers, and it allows more air-stable metals such as Au to be used as the top electrode, which could improve the stability of the device. Moreover, as some of the transport layers used in this project are semiconductors, the device is either a p-i-n or n-i-p structure, where p, i and n refers to the p-type, intrinsic and n-type semiconductors, respectively. Here, WSe_2 is referred as the intrinsic semiconductor to distinguish it from the transport layers, despite that it may be un-intentionally doped by the surfactant which was used for exfoliation. There will be two heterojunctions separately formed at HTL/WSe_2 and ETL/WSe_2 interfaces, corresponding to p-i and n-i types of heterojunctions. Having two interfaces is more desirable for spatial separation of photocarriers as the depletion regions will be formed at both interfaces and extend within the WSe_2 layer. The photocarriers can be driven towards to both electrodes by two built-in potentials. As shown in the last chapter, the short circuit current is limited by the narrow depletion width and a short photocarrier diffusion length. Two heterojunction interfaces could widen the depletion width at least, if the energy bands of adjacent materials are well-matched.

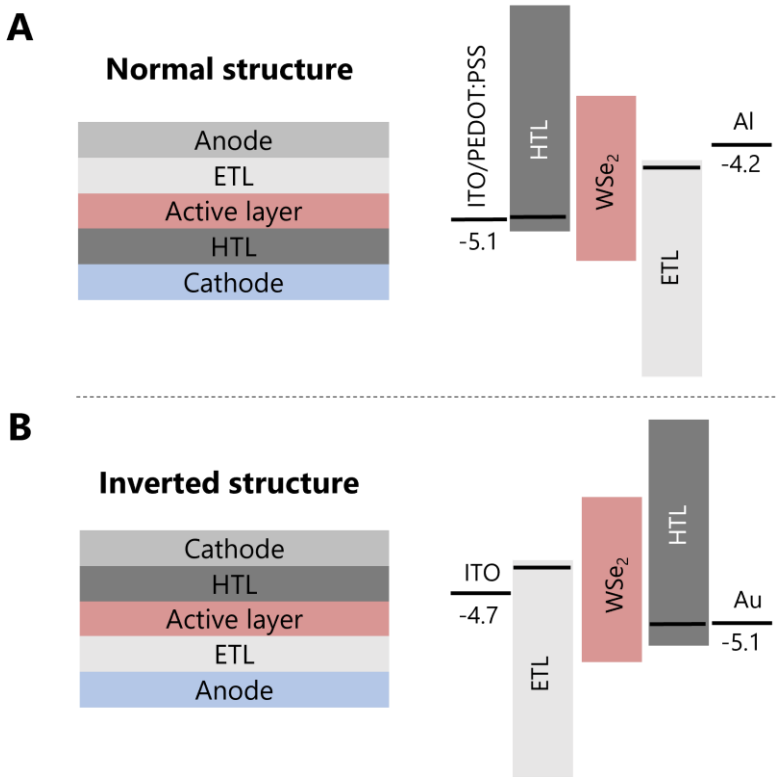

Figure 8.1 Device structures and energy band diagrams. (A) Normal structure and its energy band diagram. (B) Inverted structure and its energy band diagram.

Fabrication processes

ITO glasses from Ossila are used as the bottom transparent and conductive substrate. The etching and cleaning protocols including the oxygen plasma treatment were identical to the method presented in the last chapter. All the active layers were processed by a spin coater (model: WS-650). Here, the devices are consisted of two different types of transport layers and a layer of WSe_2 in-between as the light absorbing material. Appropriate metals will be chosen to fabricate top electrodes to form Ohmic contacts with the transport layers that are on top of the WSe_2 layer. The fabrication protocols for each type of layers are kept the same unless stated otherwise.

For the WSe_2 layer, WSe_2 nanosheet IPA dispersion was adjusted to ~3 mg mL^{-1}. The spin coating parameter was set to 1 krpm and 20 s, and 50 µL dispersion was

dynamically dispensed onto the substrate for each coating. The coating cycle was performed consecutively for 15 times. The obtained WSe_2 film was annealed in glovebox at 80 °C for 10 min. The film thickness is 75±23 nm measured by profilometry.

For the PEDOT:PSS layer, PEDOT:PSS on ITO follows the same spin coating protocols as in the last chapter. However, PEDOT:PSS is in an aqueous solution, which is difficult to be coated onto hydrophobic nanosheet film surface. The as-received PEDOT:PSS solution was diluted in IPA with a volume ratio of 1:1 and stirred overnight, which yielded modified PEDOT:PSS (m-PEDOT:PSS). m-PEDOT:PSS showed improved wettability on the nanosheet networks. The solution was also filtered by PTFE 0.45 μm filters. The coating was performed twice to maximize the coverage as it was coated on top of the nanosheet network. The spin coating parameters was set to 1 krpm and 40 s, and a static dispense process was used to make sure the entire nanosheet network is covered with the m-PEDOT:PSS solution. A 5 min-annealing at 80 °C was used before performing the second coating. A 10 min-annealing at 100 °C was adopted after two coating cycles in the air. The annealing should be performed quickly after each coating cycle to avoid the PEDOT:PSS solution from diffusing into the nanosheet network. The thickness of the m-PEDOT:PSS film was measured by profilometer and is 155±17 nm.

TiO_2 compact film was fabricated by spin-coating the TAA precursor solution on ITO substrates twice. The spin coating is set to 3 krpm and 40 s. The film after the first coating was annealed at 200 °C for 10 min and cooled down to room temperature naturally. The substrate was coated again with the precursor solution with the same coating parameters and annealed in air at 500 °C for 30 min. The substrate was naturally cooled down to room temperature and was stored in glovebox before use.

Nanoparticle (ZnO, NiO and WO_3) films were coated onto substrates twice using a coating parameter of 2 krpm and 40 s. For consistency, the static dispense was used for nanoparticle coatings. A short 5 min annealing was performed at 80 °C after the first coating. The annealing was performed again after the second coating cycle. 120 °C for 10 min was used for ZnO and WO_3, and 80 °C for 10 min was used for NiO. The annealing was conducted in ambient conditions. The thicknesses for nanoparticle based thin films are around 75 nm with standard deviations less than 10 nm.

The top electrodes were made by e-beam evaporation. Al (100 nm) was chosen as the low work function metal to make Ohmic contacts with ZnO. Ag (50 nm) and Au (100 nm) were used to make Ohmic contact with semiconductors with deep work functions, such as NiO and WO_3. After evaporating the top electrodes, the devices were further annealed in glovebox at 80 °C for 30 min before electrical measurements.

8.3 Results and discussion

8.3.1 Microscopy characterisations

The liquid exfoliated WSe_2 nanosheets were characterised by TEM and a typical image is shown in **Figure 8.2A**. The nanosheets have a lateral size of ~1.2 μm (the longest). As the aspect ratio (L_{NS}/t_{NS}) of LPE nanosheets is usually ~30,[122, 123] the corresponding nanosheet thickness will be around 40 nm, which is clearly multi-layered nanosheet, confirming the susseceful size-selection of nanosheets. The nanosheet is spin-coated onto glass substrates with identical coating parameters used for device fabrications. The nanosheet network morphology is imaged by SEM, which is shown in **Figure 8.2B**. Unfortunately, micron-sized pinholes are visible. The area of pinhole can be obtained by loading the image into Image J and converting it into a binary image. The density of pinhole is found to

be ~50%. The poor coverage of nanosheets may originate from the morphology of the nanosheet. Such large and rigid objects (100s of nanometers to a few microns) with a relatively large aspect ratio can be easily be taken away from the substrates by the liquid due to the centrifugal force. Further optimization will be required to maximize the nanosheet coverage. The morphology of the nanosheet network may lower the performance of the device as there will be contacts between transport layers. However, there will be no metal/semiconductor contacts as confirmed by SEM when nanoparticles were coated on top of the WSe_2 film (**Figure 8.2C-D**). Nanoparticles form seamless films without any pinholes and will allow ideal top-electrode depostion.

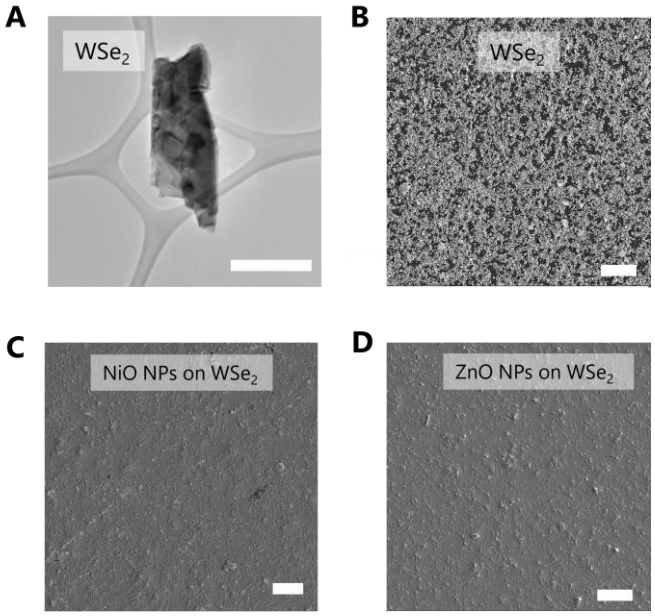

Figure 8.2 Microscopy characterisations. (A) TEM image of a typical WSe_2 nanosheet. SEM images of spin coated WSe_2 nanosheet networks (B), NiO NPs on the WSe_2 film (C), and ZnO NPs on the WSe_2 film (D). The scale bar in (A) is 500 nm and the scale bars in (B-D) are 10 μm.

A pinhole-free light absorbing layer is surely desirable for photovoltaics, which is true for all high performance solar cells. However, in some cases, as an example, Barrows[377] showed that poor coverage perovsike-based solar cells with a p-i-n structure will only exhibit around 1 order of magnitude lower efficiency than the

cells with a good perovskite coverage. Similar phenomena were also observed in other solution-processed solar cells.[378] The reduction in the short circuit current density J_{sc} is likely due to reduced number of photons absorbed in a poorly coverered light absorbing layer. However, if the number of the absorbed photons is similar for either fully or poorly covered light absorbing layer (comparable film thicknesses), J_{sc} is expected to be similar. It is believed that the reason lies in that the light absorbing layer is sandwiched between two layers of semiconductors. The photocarriers generated from the WSe_2 layer will still experience the internal built electrical field formed at the interface due to Fermi level alignment and are spatially seperated towards both electrodes. The contact between ETL and HTL through pinholes on the light absorbing layer may affect the open circuit voltage V_{oc}, but it doesn't nessarily mean that V_{oc} will be greatly reduced if approporiate transport layer combinations are chosen.[378] Overall, although further optimization for the film formation would be required, the heterojunctions could still provide insights into the properties of the interfaces.

8.3.2 Device structure and energy bands

The transport layer could change the carrier transport behaviors across the interface at metal/light absorbing layer. It is generally pursued that the transport layer can form a heterojunction interface with the light absorbing layer, preferably a type-2 staggered one for photovoltaic applications. Due to the relatively high carrier density of the highly doped transport layer (e.g., holes), the carrier with the opposite polarity (i.e., electrons) in the less-doped light absorbing layer (a relatively lower carrier density), will be attracted and diffused towards the transport layer. A region where the electrons are depleted is formed in the light absorbing layer near the heterojunction interface with a width that can be calculated by equation 7.3 or 7.4. Due to the large absorption coefficients and small bandgaps of the light absorbing layer, it is expected that the number of the

photocarriers generated in this layer is significantly higher those generated in the transport layers with small absorption coefficients and large bandgaps. It is worth noting that only photocarriers that generated in the depletion region can be driven by the built-in potential formed at the heterojunction interface and be spatially separated and collected by the electrodes, which is the origin of the photocurrent. In short, it is crucial to enlarger the depletion width in the semiconducting layer to increase the number of photocarriers. To realize this, we can choose transport layers with a higher doping density compared with that of the light absorbing layer. Moreover, the transport layer can also realize carrier selectivity functions if they have a relatively large bandgap and a suitable energy band. After Fermi level alignment, the band offset can block the transport of the majority carrier to prevent them from recombining with the minority carriers, which is the photogenerated carriers in the case of heterojunction type devices. The recombination current can be reduced which will later be shown experimentally in the followings that can increase the open circuit voltage. Those transport layers with larger bandgaps could form a larger band offset that can greatly reduce the recombination. Further, the energy band positions of the transport layer will also be able to change the energy band offsets formed with the light absorbing layer after Fermi level alignment.

The energy bands of materials are illustrated in **Figure 8.3**. TiO_2 is a widely used ETL for solar cells due to its high transmittance in the visible regime and the excellent electron mobility. It exhibits several crystal phases, such as anatase, rutile, and brookite, which will show slightly different energy bands.[379] The CBM for TiO_2 is around -4.1 eV and the VBM will be -7.5 eV, taking a bandgap of 3.4 eV.[378] The CBM for ZnO is found to be -4.5 eV from a Schottky device (ITO/PEDOT:PSS/ZnO/Al), and its VBM will be around -7.6 eV, taking a bandgap of 3.1 eV. The positions of Fermi level for both ZnO and TiO_2 are

assumed to be ~0.1 eV below CBM.[380, 381] The indirect energy band gap for bulk-like WSe_2 is 1.2 eV.[382] WF is taken the value obtained for few-layered WSe_2, which is -5.1 eV from the last chapter. For NiO, its VBM is taken to be -5.4 eV[247] and its CBM will be -1.8 eV taking a bandgap of 3.6 eV. Its work function is -5.2 eV provided by supplier. For WO_3, it is actually a n-type semiconductor but with a deep work function of -5.5 eV by supplier. The CBM and VBM for WO_3 are reported to be -5.3 eV and -8.3 eV.[383] It can be found that NiO and WO_3 as HTLs exhibit very different energy band structures. It is expected that NiO with a large bandgap could be able to block the electron from recombining with holes at the WSe_2/NiO, which can enhance V_{oc} eventually owign to the reduced recombination events. For WO_3, its energy band structure highly depends on its stoichiometry. The gap states will be present in the energy band due to the oxygen deficiency. As a result, its deep WF will attract holes to transport through these gap states to realize carrier selectivity.[383]

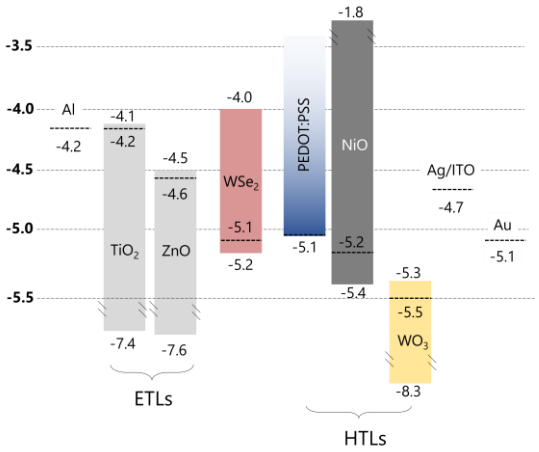

Figure 8.3 Energy bands of materials. Unit: eV.

Having all these materials, we can fabricate various types of devices which are summarized in **Table 8.2**. First, the influence of the HTLs is investigated, corresponding to device A-C. The ITO/PEDOT:PSS used here is regarded as an electrode with an equivalent work function as gold (-5.1 eV) but remains transparent. The ETL is kept to ZnO with Al top electrodes to make Ohmic

contacts. Then, with better HTLs obtained from device A-C after comparing the performance, we move onto the inverted structured devices D-F. Both the role of ETLs (ZnO and TiO_2) and HTLs (m-PEDOT:PSS and NiO) will be investigated. The top electrodes are either Ag or Au, which are used for contacting m-PEDOT:PSS and NiO, respectively.

Table 8.2 Summarization of device types and structures.

No.	Type	Device
A	Normal: i-n	ITO/PEDOT:PSS/WSe_2/ZnO/Al
B	Normal: p-i-n	ITO/PEDOT:PSS/NiO/WSe_2/ZnO/Al
C	Normal: p-i-n	ITO/PEDOT:PSS/WO_3/WSe_2/ZnO/Al
D	Inverted: n-i-p	ITO/ZnO/WSe_2/m-PEDOT:PSS/Ag
E	Inverted: n-i-p	ITO/ZnO/WSe_2/NiO/Au
F	Inverted: n-i-p	ITO/TiO_2/WSe_2/NiO/Au

8.3.3 Electrical measurements

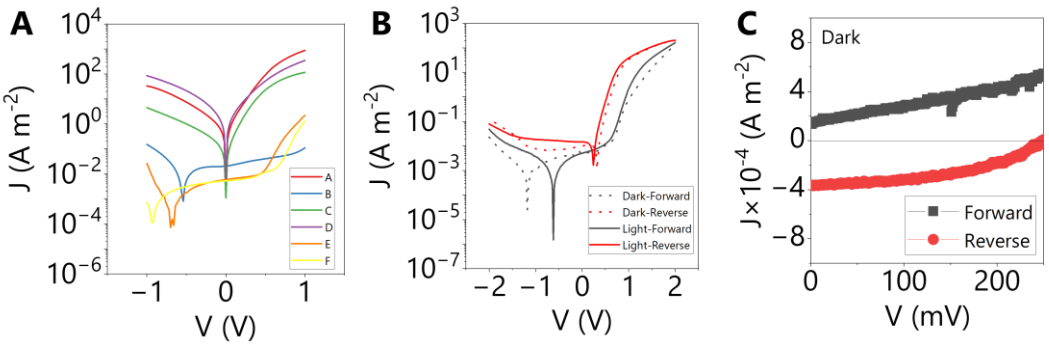

Figure 8.4 Electrical characteristics of heterojunctions. (A) Typical *J-V* curves for device A-F in the dark at -1 to 1 V. (B) *J-V* curves for device with NiO measured using forward and reverse sweeps under dark or illumination conditions. (C) The device with NiO measured using small voltage ranges and steps in the dark.

The *J-V* characteristics of the obtained devices were collected in the dark. The measurement was conducted in the range of -1 V to 1 V with 20 mV voltage steps

and a step interval of 50 ms. The anode of the device was always connected with the reference electrode to the external Keithley station to allow the forward current to display at the first quadrant. For example, for the normal structured devices, the reference electrode is connected to the Al top electrode, while it will be connected with the bottom ITO electrode for the inverted structured devices. The representative curves for each type of devices are shown in **Figure 8.4A**. These devices exhibit different rectifying behaviors, while the ones with NiO transport layers show the lowest reverse current density at negative biases but the forward current is also lower than the rest devices. Offset voltages (the voltage for the minimum *J*) can be observed at the reverse bias, rather than at the zero bias. Therefore, devices with NiO were further measured both forward (from -2 V to 2 V) and reverse (from 2 V to -2 V), separately. One typical curve is shown in **Figure 8.4B** for ITO/ZnO/WSe_2/NiO/Au. The *J-V* curves for both forward and reverse sweeps in the dark exhibit obvious hysteresis effects. The hysteresis also exists when the device is measured under 1000 W m^{-2} illumination. Such hysteresis behavior is likely associated with NiO. It has been reported that NiOOH or Ni_2O_3 species could form on the surface of solution processed NiO films upon exposure to air[384, 385], inducing changes in the energy band structure including bandgap and the position of Fermi level, which will depend on the relative ratio of these species to NiO.[384] Similar phenomena were also observed by Girolamo et al.[386] and Cheng et al.[387], when NiO was used as HTL for perovskite solar cells. Briefly, the presence of oxide impurities will induce a large surface dipole that will introduce considerable amounts of defect densities ~10^{17} cm^{-3}.[387] The defects on the surface will be gradually filled or emptied depending on the applied voltages and sweeping directions, causing an offset voltage.[386]

To further test if the hysteresis will affect the electrical behavior around origin, as it is where the photovoltaic parameters to be extracted. The device was tested in

the dark for both forward and reverse but with a small voltage step 1 mV and a narrowed voltage range (-0.05 V - 0.25 V), which is shown in **Figure 8.4C**. The forward sweep yields a curve at the first quadrant while the curve for the reverse sweep is at the fourth quadrant. For the current measurement, the photovoltaic behaviors are expected at the fourth quadrant. Therefore, for these NiO based devices, the photovoltaic measurements should be conducted only by the forward sweep to minimize the hysteresis effects. For consistency, all devices will be tested by the same method.

The photovoltaic performances of devices were evaluated under AM 1.5D illumination with a light intensity of 1000 W m^{-2}. The collected forward *J-V* curves for devices in the range of -0.05 to 0.25 V are shown in **Figure 8.5**. To make it clear, *I-V* curves of 8 identical devices fabricated on each substrate were collected and were further used to extract electrical parameters to find their statistical results. The power density *P* of the device is plotted by $P=JV$ in the corresponding insets, where the maximum power density P_{max} can be found at certain voltages. All devices show measurable photovoltaic responses with J_{sc} at V=0 V and V_{oc} at J=0 A m^{-2}. The highest J_{sc} ~2.50 A m^{-2} is observed in device A and the lowest is found from device F, which is only 1.32 mA m^{-2}. The highest V_{oc} 242 mV is obtained from device F, while the lowest one is only 4 mV for device D. Overall, these devices exhibit obvious different electrical behaviors under illumination.

The electrical parameters are extracted from **Figure 8.5**, including J_{sc}, V_{oc}, *FF* and P_{max}. The efficiency η of the solar cells are obtained by $\eta=P_{max}/F$. All these parameters are plotted in **Figure 8.6A-D**. Starting from device A-C, these devices are designed to compare the HTLs, where ZnO is used for ETL. Device A (ITO/PEDOT:PSS/WSe_2/ZnO/Al) using PEDOT:PSS as the HTL exhibits the

highest $\langle J_{sc} \rangle$~1.47 A m^{-2} and the device B (ITO/PEDOT:PSS/NiO/WSe_2/ZnO/Al) using NiO as the HTL showed the highest $\langle V_{oc} \rangle$~100 mV. An around 5% reduction in $\langle FF \rangle$ is observed for device B compared with the other two, which are both ~25%. As a result, the highest η is obtained for device A ~1.1×10^{-3} %. The comparison between device A-C indicates that PEDOT:PSS would provide the best hole-extraction capability and yield higher J_{sc}, while NiO could reduce the carrier recombination at the interface and enhance V_{oc}. For device C (ITO/PEDOT:PSS/WO_3/WSe_2/ZnO/Al) using WO_3 as the HTL, it performs moderately in both J_{sc} and V_{oc}.

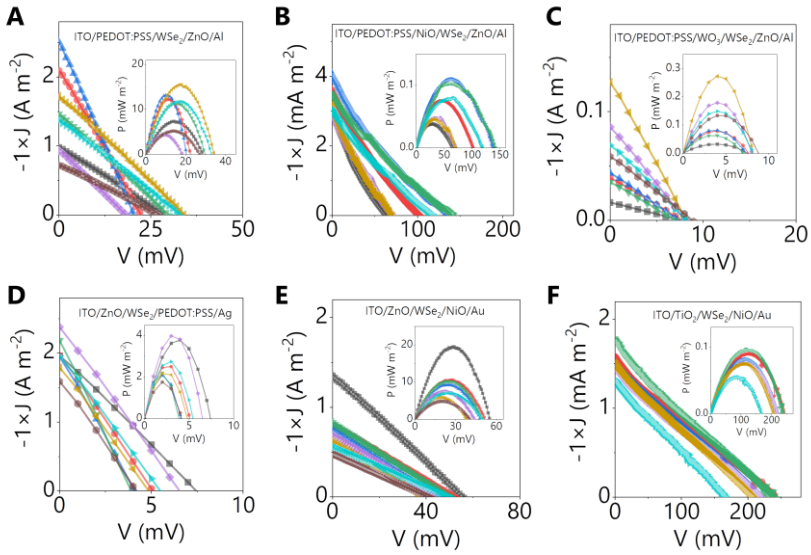

Figure 8.5 Electrical characterisation of heterojunctions under illumination. (A-F) *J-V* curves for devices with various transport layers. The insets are power density *P* versus voltage *V* curves.

To understand these behaviors, energy band diagrams at the HTL/WSe_2 interface after contacting are depicted in **Figure 8.6E** (top). PEDOT:PSS can form an Ohmic contact with WSe_2, as a result, there is virtually not potential barrier or built-in potential formed at this interface and holes can transport through this interface. There is also no depletion region formed at this interface on the WSe_2 side. Therefore, the separation of photocarriers is only realized at WSe_2/ZnO

interfaces. For NiO/WSe_2 interfaces, the relatively deeper WF of NiO (-5.2 eV) would induce a small band offset (~0.1 eV) on the WSe_2 side which prevent electrons from diffusing from WSe_2 into NiO. The low CBM of NiO will further block electrons diffusion. Therefore, the photocarrier recombination at the interface can be significantly reduced. However, the deep VBM of NiO (-5.4 eV) and a band offset formed at NiO after Fermi level aligning will together act as a potential barrier that would partially block the hole transport. Therefore, a high V_{oc} but low J_{sc} is obtained for the device with NiO as the HTL. For WO_3/WSe_2 interfaces, the ultra-deep VBM will not assist the hole transport but the holes will transport through the gap states within WO_3, providing the carrier-selectivity function.[341, 383] However, from the result, WO_3 based devices show a reduced V_{oc} comparing with that from PEDOT:PSS based devices, implying that there is still significant recombination at this interface, possibly due to the WO_3 layer is too thick. J_{sc} also shows a few times reduction. Therefore, PEDOT:PSS and NiO are both picked to fabricate the inverted devices.

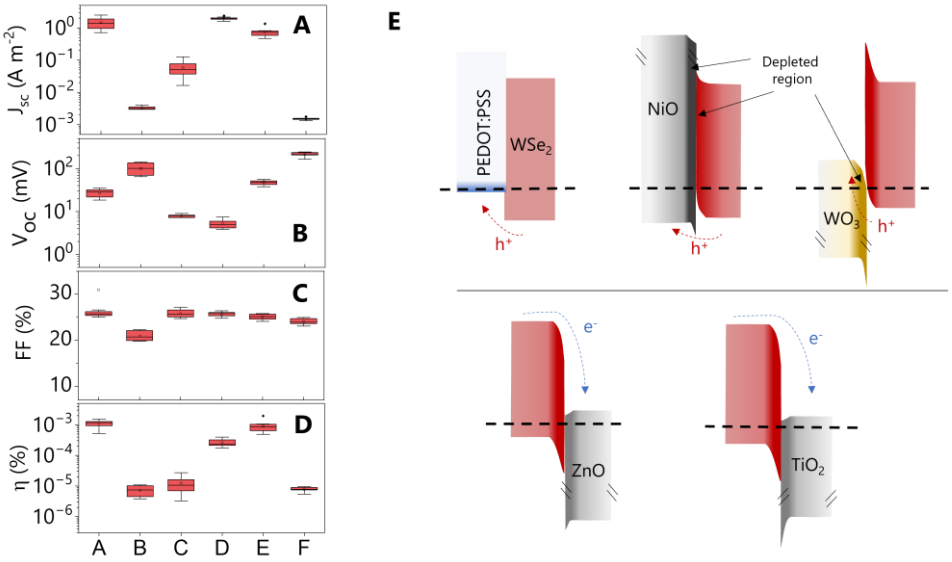

Figure 8.6 Photovoltaic performances and energy band diagrams. (A-D) Extracted electrical parameters from *J-V* curves. (E) Energy band diagrams of WSe_2 with transport layers after contact. The darker region corresponds to the depleted region in the heterojunction. A-F are devices types in table 8.2.

For the device D: ITO/ZnO/WSe_2/PEDOT:PSS/Ag, it is an inverted structure to device A with PEDOT:PSS and ZnO. For this type of device, there is mainly one heterojunction at WSe_2/ZnO interfaces. By inverting the device structure, the heterojunction interface will experience the illumination first, given that the light intensity decays exponentially into the WSe_2 layer (~75 nm), it will improve the number of photons absorbed in the depletion region near this interface and allows a greater number of photocarriers to be generated. Therefore, a slight increase of $\langle J_{sc} \rangle$ ~1.97 A m^2 is observed for this inverted structure. However, $\langle V_{oc} \rangle$ decreases to only ~5.2 mV. The poor coverage of WSe_2 will introduce extra PEDOT:PSS/WSe_2 interfaces as PEDOT:PSS will diffuse into the network. As this interface is an Ohmic contact in nature and cannot provide any additional hole blocking function, the recombination at this interface will be enhanced compared with device A, that the PEDOT:PSS/WSe_2 interface is a planar one, and therefore limit V_{oc}. The *FF* of the inverted device is comparable with that with the normal structure.

The effect of ETLs is investigated in device E and F, and both devices use NiO as HTLs. Device E (ITO/ZnO/WSe_2/NiO/Au) is an inverted device structure compared with the device B that both use NiO and ZnO as transport layers. Changing the device structure to an inverted one, the obtained $\langle V_{oc} \rangle$ is about half of that from the normal structured device. However, device E shows significant higher J_{sc} than that from device B, which can be partially attributed to the WSe_2/ZnO interface that experience a higher light intensity illumination in an inverted structure. Keeping the NiO layer as the HTL, the ZnO ETL is replaced with a TiO_2 compact layer, which is the device F: ITO/TiO_2/WSe_2/NiO/Au. In this device, the highest $\langle V_{oc} \rangle$~219 mV is obtained among all the others, but the $\langle J_{sc} \rangle$ is only ~1.52 mA m^{-2}. As depicted in **Figure 8.6E** (bottom), upon contact between

ETL and WSe_2, both types of ETLs will form energy band offsets that would block the holes diffusing into ETL and prevent recombination, while electrons can transport. As TiO_2 exhibits a shallower work function, it will result in a relatively larger energy offsets (compared with ZnO) that will be more effectively block the hole diffusion, which is believed to be the reason for the high $\langle V_{oc} \rangle$. Devices with NiO transport layers (B/E/F) show lower $\langle J_{sc} \rangle$ compared with devices with PEDOT:PSS (A/D). Therefore, another possible reason could be the surface traps may act as additional barriers for the photocarriers. However, devices with NiO but different ETLs (ZnO for device E and TiO_2 for device F) show a significant difference in J_{sc}. The underlying reason may come from the ITO/TiO_2 interface. For the current proposed energy band diagram, ITO (WF=-4.7 eV) may induce a potential barrier with TiO_2 (WF=-4.2 eV) for electrons, while the WF of ZnO =-4.7 eV would be close to that of ITO that can yield Ohmic contact. However, TiO_2 is widely used on top of ITO according to previous reports.[388-390] Therefore, it is doubtful that if this can be applied here given that the fabrication process and chemicals may not be identical.

Overall, we have compared performance from devices with various transport layers as well as the device structures. The results indicate that the carrier blocking property (i.e., hole-blocking for ETL or electron-blocking for HTL) is crucial to improve V_{oc}. The inverted device structures that allow the main heterojunction interface (WSe_2/ETL) to experience the illumination will improve J_{sc} due to increased numbers of absorbed photons. However, the mismatched energy bands between transport layers and WSe_2 (such as NiO/WSe_2) will result in an undesired photocarrier blocking that will lead to a lowered J_{sc}.

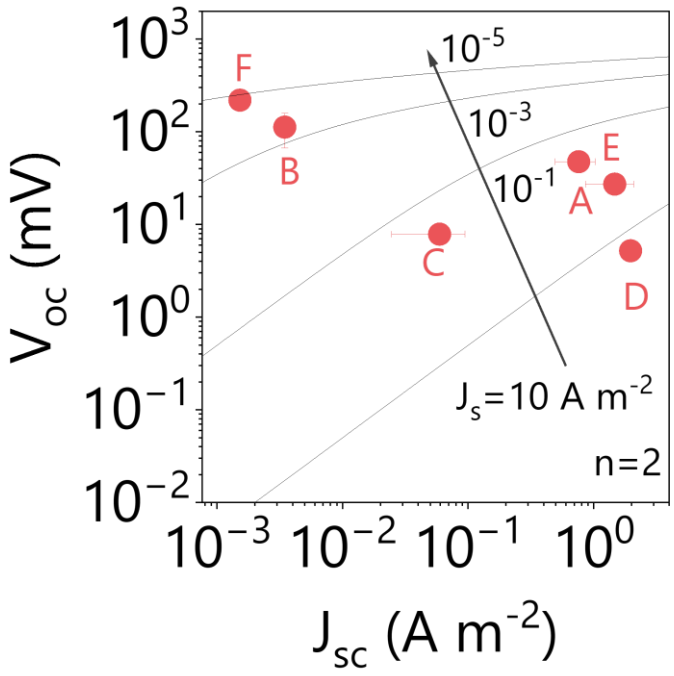

Figure 8.7 The saturation current density. The obtained V_{oc} is plotted versus J_{sc}. The grey line is simulated with equation 7.2 with various J_s values and using n=2. A-F refer to device types in table 8.2.

The extracted V_{oc} and J_{sc} are plotted against each other in **Figure 8.7**. V_{oc} depends on the J_{sc} and J_s, and simulated curves with different J_s values using equation 7.2 and n=2 are plotted in the figure. First of all, the thermal effect is likely involved already and the increased light intensity will induce a higher J_s that lowers V_{oc}. Despite of the thermal effect, large differences can be observed in the figure. Generally, good performance solar cells would be on the top right corner, corresponding to both high values of V_{oc} and J_{sc}. However, the extracted values are mainly scattered around the top left or the bottom right, which are either limited by the low J_{sc} or the high J_s, respectively. It can be found that J_{sc} varies over around 3 orders of magnitude and J_s varies over at least 6 orders of magnitude, leading to an around 45-folds variation in V_{oc}. Nevertheless, the performance of the solar cell is mainly limited by J_{sc} due to its large variation, which can be observed in **Figure 8.6A** and **D** that J_{sc} and η follow very a similar

trend. The results indicates that the interface between the nanosheet network and the transport layer plays a vital role in the performance of the solar cell. It is possible to use transport layers to manipulate the interface properties and improving J_{sc} is critical, which will lead to an increase in both V_{oc} and η.

The recombination events could affect the saturation current density, that eventually results in a change in V_{oc}. In this study, it is believed that these devices are mainly dominated by the non-radiative recombination as the bulky WSe_2 nanosheets are indirect semiconductors and the radiative band-to-ban recombination is unlikely to happen. The recombination could happen either at the surface of the nanosheet network or within the network, which can be referred as surface recombination or bulk recombination, respectively.[1] In both cases, the recombination rate U will be proportional to the excess carrier densities due to photo-generation (Δn for electrons or Δp for holes).[1] It is shown from the above that when suitable transport layers are used adjacent to WSe_2, the saturation current could vary significantly, indicating that they can effectively reduce the recombination between photo-generated minority carriers and intrinsic majority carriers at the surface. There could also be recombination within the network. For perfect semiconductors, the recombination is realized by band-to-band recombination events, that electrons in the conduction band jump into the valence band and recombines with holes (release photons with an energy corresponding to the bandgap energy for direct bandgap semiconductors). However, these liquid-exfoliated nanosheets could have some defects, such as interstitials, vacancies and impurities, that could introduce permitted energy levels within the bandgap. These permitted energy levels require energies less than the energy of the bandgap, so the transitions of electrons and holes between these levels are more likely to happen than those through the band-to-band transitions.[1] Such behavior is referred as the Shockley-Read-Hall (SRH) recombination events. The SRH recombination

rate can be described by[1]

$$U_{SRH} = \frac{pn - n_i^2}{\tau_0 \left[p + n + \cosh(\frac{E_t - E_i}{kT}) \right]} \tag{8.1}$$

where n_i is the intrinsic carrier density, E_t and E_i correspond to trap energy level and intrinsic energy level, respectively. τ_0 can be found by $\tau_0 = \frac{1}{N_t v_{th} \sigma_0}$, where v_{th} is the thermal velocity of electrons, N_t is the density of the recombination centers, σ_0 is the carrier capture cross section. However, the trap energy level should be experimentally determined to find the recombination rate, which should be further explored.

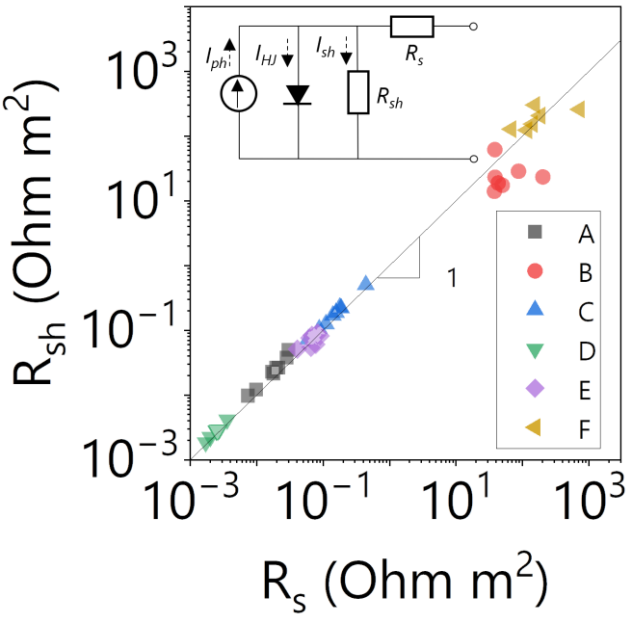

Figure 8.8 The resistive effect of the heterojunctions. The extracted R_{sh} is plotted versus R_s. The inset is the equivalent circuit of solar cells. The letters correspond to above-mentioned device types.

FF remains low ~25% across all devices. This factor is used to evaluate the squareness of the *J-V* characteristic curve. *FF*=1 means that there is no photocarrier loss and all photocarriers in the depletion region can be spatially separated by the built-in potential and collected by the electrode. However, this is

impossible to realize as the *J-V* curves follows exponential functions rather than step functions. In reality, *FF* can be affected by the series resistance R_s and the shunt resistance R_{sh}.[391] The classic equivalent circuit for the solar cell is illustrated in the inset of **Figure 8.8**. It consists of a diode and a shunt resistor R_{sh} in parallel, and a series resistor R_s is in series connection with this parallel component.[390] The series resistance could arise from the resistivity of materials in the heterojunction and the potential barrier effect due to the energy band alignment. The shunt resistance describes the leakage current across the junctions and could come from the contact between ETL and HTL due to the coverage issue of WSe_2.[325] A high *FF* can be achieved by increasing R_{sh}, decreasing R_s and reducing *n* to unity. The currents pass through the diode and the shunt resistor are termed as I_{HJ} and I_{sh}, respectively. In the dark, the total current of the heterojunction I_{total} is the sum of I_{HJ} and I_{sh}. Under illumination, the heterojunction will generate a photocurrent I_{ph} that take an opposite sign, and the total current is reduced by the amount of I_{ph}. The total current can be described by[392]

$$I = I_{ph} - I_s\left[\exp(\frac{q(V-IR_s)}{nkT})-1\right]-\frac{V-IR_s}{R_{sh}} \tag{8.2}$$

The current terms in the above equation can be converted into current density by dividing them by *A*. However, this equation contains several unknown variables and cannot be directly used for fitting in Origin. Alternatively, R_{sh} and R_s (both in the unit of Ohm m^2) can be extracted using the *J-V* curves in **Figure 8.5** by $\left(dJ/dV\right)^{-1}$ at V= 0 V and V=V_{oc}, respectively.[393] Under zero external bias condition, the heterojunction will operate based on its internal built-in potential, that shunt resistance is proportional to the photocurrent. When the heterojunction is supplied with a voltage that is equivalent to V_{oc}, the photocurrent and diode current will be cancelled and the current will be solely depending on the series

resistance. The extracted R_{sh} and R_s in the unit of Ohm m^2 are plotted in **Figure 8.8**. Ideally, R_{sh} should be maximized to reduce the leakage current and R_s should be minimized to improve the fill factor. A linear dependence of these two resistances is observed with an exponent close to unity.

Several reasons may be responsible for the obtained results. Firstly, due to pinholes on the WSe_2 layer, there is a non-negligible contact area between ETLs and HTLs. The contact between TLs/WSe_2 compared with ETL/HTLs regarding the energy band alignment and bending will be different. These undesirable contacts between transport layers will affect V_{oc} values. It can be found that some combinations of transport layer materials (e.g., a combination of NiO and TiO_2) can significantly reduce the recombination current at the interface due to their better carrier-selectivity properties. Secondly, these transport layers were fabricated without optimizations regarding the film thickness, as the main goal was to achieve good coverage on the nanosheet network. The obtained oxides type transport layers are around 75 nm thick. Some of them may induce high series resistance due to their low electrical conductivity (around 10^{-5} S m^{-1} for NiO[394], 10^{-7} - 10 S m^{-1} for ZnO[395, 396], 10^{-11} - 10^{-6} S m^{-1} for TiO_2[397, 398], 10^{-2} for WO_3[399]). As a result, these transport layers may introduce a large series resistance, which will decrease J_{sc} as the photocarriers cannot diffuse to the electrode through a thick and resistive transport layer. A thickness-dependent study would be required to find the suitable thickness for each type of transport layers to achieve a high R_{sh} but introduce a low R_s to the device. Thirdly, for transport layer such as NiO, although it provides good electron-blocking properties due to its low CBM but also induce a small energy offset that block the hole transport due to a slight energy band mismatch to VBM. It will be desirable to use another type of p-type HTL to form a better energy alignment with WSe_2. Moreover, the voltage dependent defect states on the NiO surface will be inevitably involved in the

photocarrier transport process, which may hinder their transport to the electrode.

8.4 Conclusion

In this chapter, using multi-layered WSe_2 nanosheets as light absorbing material, the electrical properties of heterojunctions are studied by using different types of transport layers. The photovoltaic performances of devices are investigated under AM1.5D 1000 W m^2 illumination. The obtained J_{sc} varies from around 1.32 mA m^{-2} to 2.50 A m^{-2}, and V_{oc} varies from around 4 mV to 242 mV. The best efficiency is around 1.95×10^{-3} % with an inverted device structure ITO/ZnO/WSe_2/NiO/Au. The low J_{sc} is identified to be the main reason for the low efficiency. Overall, this study proves that it is feasible to tune the carrier transport behaviors at the transport layer/nanosheets interface by using suitable transport layers.

The best way to predict the future is to invent it.

Alan Kay

Chapter 9 Solution-Processed van der Waals Heterojunction

9.1 Introduction

Solution processed semiconducting nanosheet networks are promising for electronic and optoelectronic applications. We have demonstrated in the previous chapters that the interfacial properties of the nanosheet network can significantly affect the optoelectronic performances of heterojunctions. However, the morphology of the nanosheet network should also be focused. The morphological and electrical properties of the networks will be affected by the nanosheets themselves and their arrangement, which will depend on both the nanosheet morphology and the deposition methods. For example, LPE TMDs nanosheets usually display a relatively small length-to-thickness aspect ratio 10~30[122, 123, 168] and tend to be rigid. As a result, nanosheets will form an edge-to-plane arrangements in the network (**Figure 9.1A**), that the junctions between adjacent nanosheets are point-like, yielding a small nanosheet-to-nanosheet contacting area and a high network porosity ~50%.[168, 199] It was found that the electrical properties of such networks, such as conductivity and mobility, are mostly hampered by carriers transporting across these junctions, which could be orders of magnitude inferior to that of the individual nanosheet.[189, 199] In contrast, electrochemically exfoliated (EE) nanosheets display a high degree of mechanical flexibility owing their large aspect ratios,[189] which could approach ~300 according to the result produced in our lab.[219] Conformal nanosheet arrangements in the network can be realized using this type of nanosheets, forming plane-to-plane nanosheet

arrangements with a high contacting area and an ultra-small porosity.[219] Such alignment is schematically demonstrated in **Figure 9.1B**. The electrical performance of such network was proven to be only a few times lower than that of the individual nanosheet.[189, 231, 234, 400, 401]

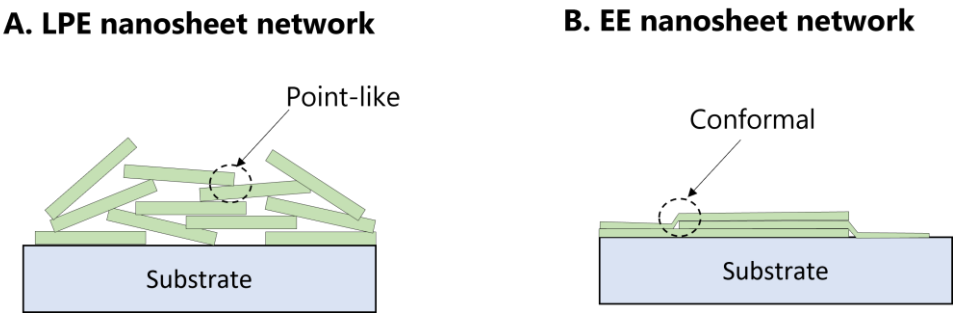

Figure 9.1 Nanosheet networks. Schematic illustration of networks formed by LPE nanosheets (A) and EE nanosheets (B).

Further, dangling bonds-free surfaces of 2D TMDs can greatly minimize the interfacial states which could limit the carrier transport.[218] The carrier transport at such atomic-level clean interfaces is expected to be superior to the interfaces formed with materials showing rich surface dangling bonds, represented by 0D quantum dots.[218] Hence, for EE nanosheet based networks, their surfaces can be utilized to construct vdW heterojunctions if two types of EE nanosheets are used. This novel structure has been proved to be feasible using single flake,[402-405] however, is not achieved yet using solution-processable nanosheets.

In this project, TMDs nanosheets will be exfoliated by the EE method, which will yield ultra-thin nanosheets with large lateral sizes. These nanosheets will be used to construct the vdW heterojunctions and their electrical properties will be investigated.

9.2 Experimental

9.2.1 Electrochemical exfoliation

The electrochemical exfoliation of bulk crystals was performed by Dr. Tian Carey.

The bulk crystals of WS_2 and niobium doped WSe_2 (Nb:WSe_2) are provided by Prof. Zdenek Sofer from University of Chemistry and Technology Prague.

The crystal was cut into thin pieces and was used as the cathode, and a platinum foil (Alfa Aesar) was used as the anode. For the electrolyte, tetrapropylammonium (TPA) bromide (Sigma-Aldrich, 5 mg mL^{-1}) was added to ~50 mL propylene carbonate (Sigma-Aldrich, HPLC grade). A voltage of 8 V was applied for 30 min between the electrodes to intercalate the 2D crystal with TPA^+ cations. After intercalation, the 2D crystal is emersed in IPA (Sigma-Aldrich, HPLC grade) overnight to dissolve and remove any residual bromide ions (Br^-) on the crystal.

The 2D crystal was then bath-sonicated in 1 mg mL^{-1} poly(vinylpyrrolidone) (PVP, molecular weight ~40000 from Sigma-Aldrich) in dimethylformamide (DMF, HPLC grade from Sigma-Aldrich) for 5 min followed by centrifugation at 0.5 krpm for 20 min to remove unexfoliated crystals. The dispersion was size-selected by centrifuging the supernatant at 1 krpm for 1 h and collecting the sediment. The sediment was diluted with 2 mL of DMF and centrifuged at 10 krpm for 1 h to remove PVP. The process was repeated twice, and the sediment was collected each time. A third washing step was used to remove residual DMF, which involved diluting the sediment in IPA (0.5 mL) and subsequently centrifuging at 10 krpm and collecting the sediment. The sediment was redispersed in ~0.5 mL IPA.

9.2.2 Device fabrication

The device structure is a normal one as ITO/PEDOT:PSS/2D/ZnO/Al. The device fabrication process follows a similar procedure described in Chapter 7. ITO glasses were etched and cleaned by solvents and an oxygen plasma treatment before use. PEDOT:PSS solution (Ossila, AI 4083) was filtered before use and the spin coating was performed by a spinner WS-400A-8NPP/LITE. The coating

parameter was set to 3 krpm for 40 s. The obtained PEDOT:PSS film was annealed at 140 °C for 20 min. Around 100-150 μL nanosheet dispersion from the concentrated one after centrifugation was diluted in 20 mL IPA. The diluted dispersion was shaken and briefly sonicated. The nanosheet dispersion was sprayed onto ITO/PEDOT:PSS without heating. The obtained ITO/PEDOT:PSS/2D films are annealed in glovebox at 120 °C for 30 min and are allowed to cool down naturally. ZnO nanoparticle dispersion (N-10, ~12 nm, IPA) received from Avantama was directly used to fabricate the electron transport layer. The spin coating was performed by the static dispense method with a speed of 2 krpm for 40 s twice. Annealing processes were performed in air at 80 °C for 5 min and 100 °C for 10 min after the first and the second coatings, respectively. The top electrode Al with a thickness of 100 nm was evaporated through the shadow mask at a rate of 2 Å s^{-1}. The final device was annealed in glovebox for 30 min and was deliberately aged in air overnight to stabilise the electrical behavior.

9.2.3 Optical characterisation

An optical microscope (Olympus DSX1000 digital microscope) was used to image deposited nanosheet networks in bright field mode.

9.3 Result and discussion

9.3.1 Basic characterisations

The bulk crystals of WS_2 and Nb:WSe_2 were exfoliated into nanosheets by electrochemical exfoliation. After size-selection and removing residual intercalants, the obtained WS_2 and Nb:WSe_2 nanosheet IPA dispersions are characterised by the UV-Vis spectroscopy, where the absorption spectra are shown in **Figure 9.2**. The absorption excitonic peaks A and B for WS_2 and Nb:WSe_2 can be found at 628 and 520 nm, and 759 and 558 nm, respectively. The position of A peak is closely related to the number of layers for TMDs and the observed A peak

positions for both materials are consistent with previous reports for few-layered nanosheets.[49, 120, 394, 395].[52, 123, 406, 407] The resultant nanosheets from EE are usually few-layered and display a high aspect ratio (AR) up to ~300.[219] The high aspect ratio is expected to be desired for making conformal nanosheet junctions (AR>~40[189]).

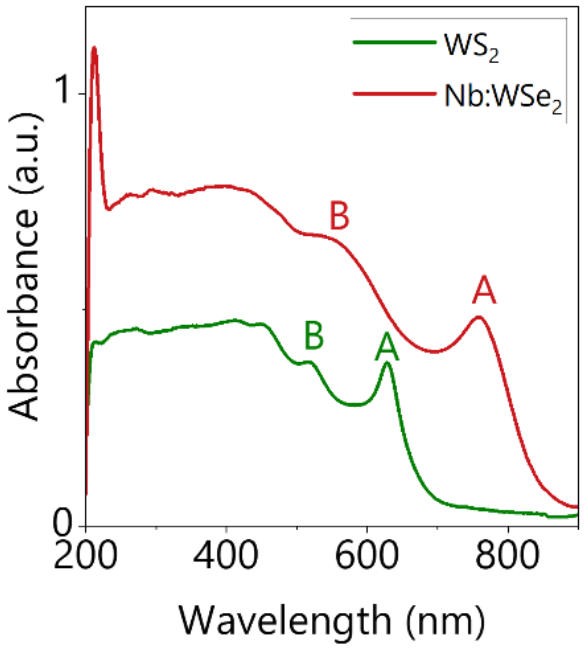

Figure 9.2 UV-Vis spectra of EE nanosheet dispersions. The absorption spectra of WS_2 (A) and Nb:WSe_2 (B) IPA dispersions.

Due to the low yield of EE nanosheets, there was only a limited volume of the dispersion for device fabrication. Therefore, around 100-150 µL concentrated nanosheet dispersion (~2.5 mg mL^{-1}) was diluted in 20 mL IPA. The nanosheet networks were formed by separately spraying the diluted dispersion onto ITO/PEDOT:PSS substrates and their thicknesses are both 24±13 nm by profilometry. The morphology of the networks was characterised by an optical microscopy, and the optical images under low magnifications are shown in **Figure 9.3A-B**. The networks made from both types of materials show a good uniformity over a large area. For high-magnification images in **Figure 9.3C-D**, nanosheets

with sizes as large as ~10 μm can be observed. However, pinholes are visible due to the limited mass of nanosheets.

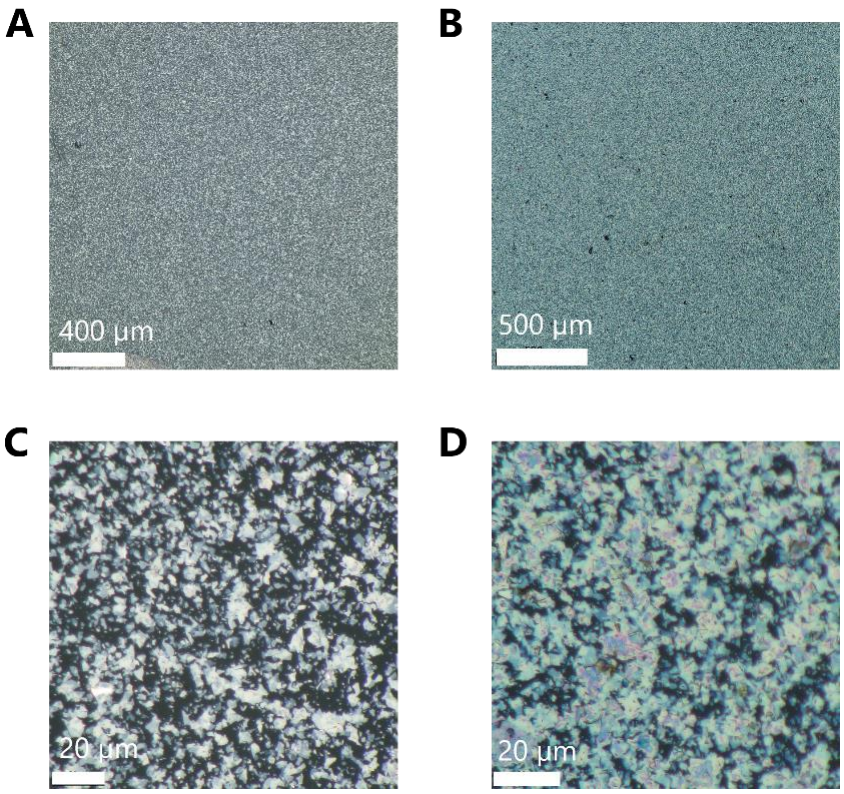

Figure 9.3 Optical microscopy characterisation of sprayed networks. Low-magnification optical images of sprayed Nb:WSe_2 (A) and WS_2 (B) thin films and higher-magnification images are shown in (C) and (D), respectively.

The energy bands of used materials are shown in **Figure 9.4**. Due to the employed electrochemical exfoliation method, the obtained EE nanosheets will exhibit considerable differences compared with LPE nanosheets. First, liquid cascade centrifugation (LCC) method applied for EE nanosheets usually yields mono- to few-layered nanosheets, and the refinement of the dispersion to narrow down the size and thickness distribution or sorting out thicker species is difficult through this method. This is likely due to the large aspect ratio of EE nanosheets will enhance the vdW interactions between nanosheets that modifies rheological behaviors of the dispersion. As a result, the obtained EE nanosheets will be expected to exhibit larger bandgaps E_g than those from LPE nanosheets obtained

at relatively low centrifugation speed (large and thick species). The bandgap for 2D semiconductors can be approximated by the sum of the A excitonic energy E_A obtained from the absorption spectrum and exciton binding energies E_b. Synnatschke et al.[52] systematically studied the evolution of the E_A with LPE TMDs nanosheets. For monolayer enriched dispersions, E_A for WS_2 and WSe_2 are around 2 and 1.7 eV, respectively. E_b could be as high as 0.5-0.6 eV for a free-standing nanosheet but may be reduced in other dielectric environments (liquids or films). In short, the actual bandgap for the EE nanosheet obtained in this study could be larger than E_A but requires additional techniques to determine the value of E_b. Moreover, energy band variation across EE nanosheet networks due to mono- and few-layer species seems inevitable, which implies that these networks are not suitable for solar cell applications, where energy band variation across the network should be minimized. Second, during intercalation, the used intercalant will introduce an inevitable doping effect to the nanosheets. Carey et al.[219] found that most of the obtained EE TMDs nanosheets exhibited n-type electrical behaviors regardless of the material types. The result is clearly different with another study done by Kelly et al.[199] that TMDs nanosheets after ultra-sonication in N-Methyl-2-pyrrolidone could maintain their intrinsic electrical properties depending on the transition metal. Therefore, EE WS_2 used in this study is n-doped by the intercalant and the position of E_f is ~0.2 eV under the conduction band minimum (CBM, 3.8 eV for monolayer WS_2[304, 400]) according to the report adopting similar exfoliation protocols.[401] To fabricate the vdW heterojunction, it would be better to have another p-type semiconductor to form a p-n junction. To this end, niobium doped WSe_2 is used to achieve p-type electrical behaviors and nanosheets remain as a semiconductor, which is confirmed by Dr. Tian Carey with an electrolyte-gated transistor (not shown). The energy band for few-layered Nb:WSe_2 is not reported yet. However, Nb doping to the bulk WSe_2 could shift

the E_f to 0.05 eV above VBM.[408] The molar ratio of Nb in Nb:WSe_2 is around 3% and a significant shift of E_f to VBM is expected.[409] Moreover, a change in both CBM and VBM of WSe_2 after doping could happen however it should not result in a significant difference compared with the undoped one in the case of a small doping amount.[410] Therefore, the position of E_f for Nb:WSe_2 is estimated to be 0.05 eV above VBM (~5.3 eV for undoped EE WSe_2[400]). The CBM for ZnO is obtained to be ~4.6 eV by electrical characterisations on a Schottky diode formed with PEDOT:PSS and its Fermi level is 0.1 eV below CBM.

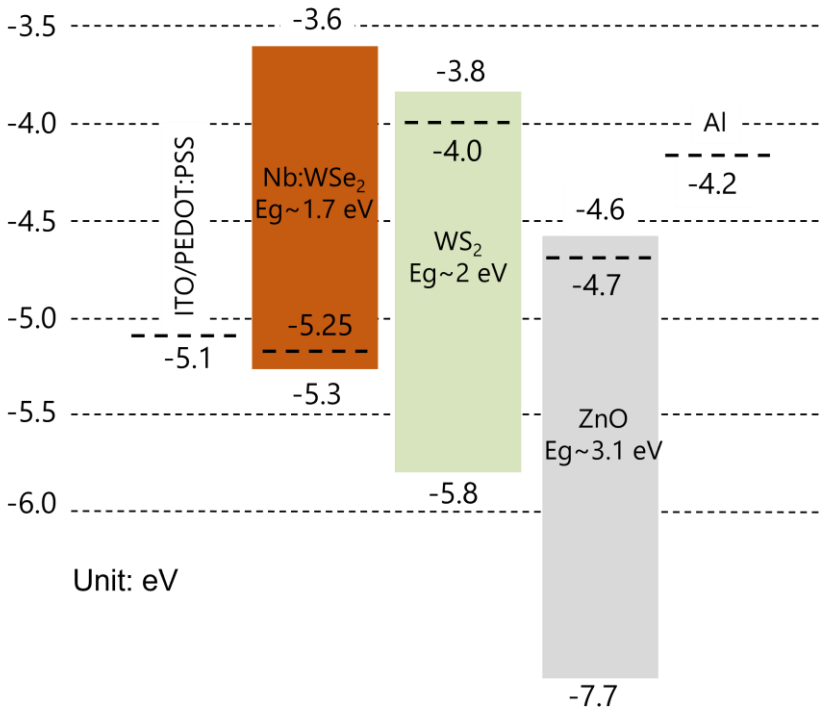

Figure 9.4 Energy bands of materials. Unit: eV.

9.3.2 Electrical measurements

Before examining the electrical properties of vdW heterojunction, heterojunctions were firstly fabricated with a single type of EE nanosheets and a device structure ITO/PEDOT:PSS/2D/ZnO/Al, where ZnO nanoparticles are spin coated on top of the EE nanosheet networks followed by the evaporation of the top electrode Al. The *J-V* characteristics were collected both in the dark and under AM1.5D 1000

W m^{-2} illumination (1 sun) and are shown in **Figure 9.5**. The heterojunctions display rectifying behaviors in the dark with rectification ratios (RR) of ~3.6 and ~3.8 for WS_2 and Nb:WSe_2 based devices at ±1 V ($RR=J_{+1V}/J_{-1V}$), respectively. The obtained rectification ratios for EE nanosheets are significant smaller than LPE WSe_2 based heterojunctions. The origin of RR lies in two aspects: the series resistance of materials, which determines the current density at 1 V assuming the device reach to the Ohmic conduction regime; and the energy band offsets that could block the majority carriers and determine the current density at -1 V. The current densities at 1 V and the fittings that will be introduced later imply that the series resistance from the device is comparable with those obtained from LPE WSe_2 based heterojunctions in the previous chapter. The main factor that causes the low RRs is due to the large reverse current density at -1 V. For the proposed device structure, the majority carrier blocking should arise from the energy band offsets formed at heterojunction interfaces.

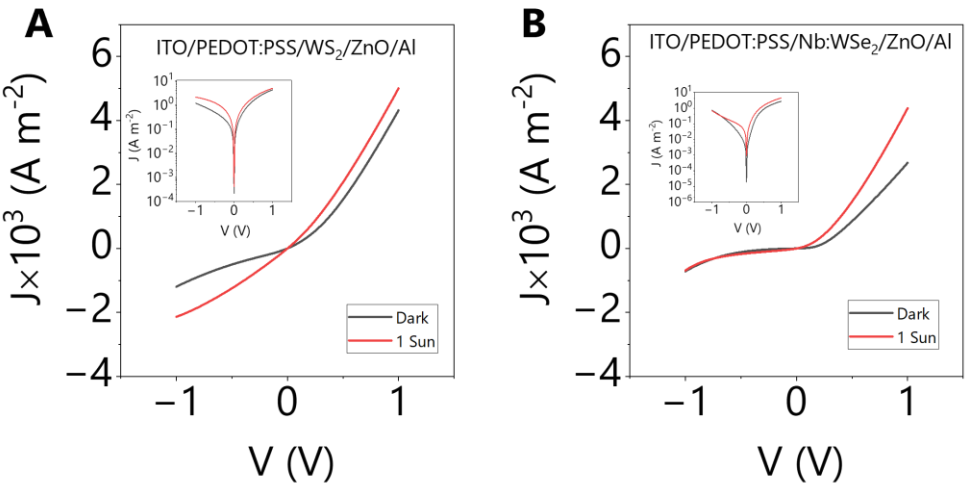

Figure 9.5 Electrical characterisation of heterojunctions using EE nanosheets. *J-V* curves of ITO/PEDOT:PSS/WS_2/ZnO/Al and ITO/PEDOT:PSS/Nb:WSe_2/ZnO/Al in the dark and under AM 1.5D illumination with a light intensity of 1000 W m^{-2}. The insets are corresponding semi-log *J-V* curves.

To understand the carrier transport process, the energy band diagram upon contacting is illustrated in **Figure 9.6**. For the EE WS_2 based device, it is actually

a Schottky junction (PEDOT:PSS/WS_2) and a n-n junction (WS_2/ZnO) in series, while it will mainly be a p-n type heterojunction for the Nb:WSe_2/ZnO interface with a type-II band alignment, although a small potential barrier for the hole transport may be present at the PEDOT:PSS/Nb:WSe_2 interface. A key feature here is the large bandgap and the shallow E_f of WS_2 will reduce the valence band offset ΔVBM at the WS_2/ZnO interface to ~1.1 eV, which is apparently lower than that from the LPE WSe_2/ZnO interface ~2.4 eV. The reduced band offset will hinder the hole-blocking ability of ZnO and hence increase the number of hole transport from WSe_2 to ZnO that induces a high reverse current density. However, for the EE Nb:WSe_2 based device, the rectification ratio is still low even the offset ΔVBM could be up to ~2.85 eV. There could be other factors that increase the reverse current density, which will be discussed below.

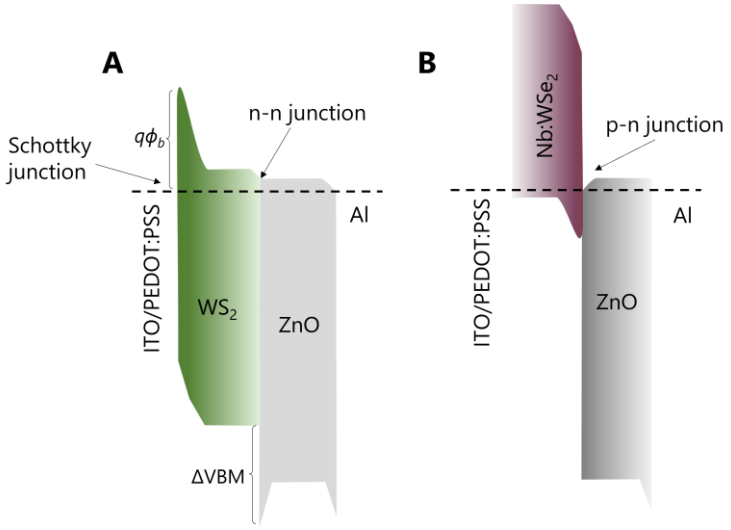

Figure 9.6 Energy band diagram of materials after contact.

The obtained heterojunctions respond to the AM1.5D illumination differently. The semi-log *J-V* curves are shown in **Figure 9.5** insets for a better visualization. For EE WS_2 based heterojunction, the photoresponse can be observed at both positive and negative voltages. The photoresponsivity R_{ph} at 1 and -1 V can be calculated and are 0.69 and 0.94 A W^{-1}, respectively. For the Nb:WSe_2 based heterojunction,

it exhibits positive photoresponses from -0.74 V to 1 V and R_{ph} at 1 V reaches to 1.71 A W^{-1}. However, negative photoresponses are found from -0.74 to -1 V and the R_{ph} at -1 V is -2.82×10^{-2} A W^{-1}. The negative photoresponse was previously observed in $WSe_2/SnSe_2$ heterojunctions, where $SnSe_2$ is degenerately n-doped and WSe_2 is p-type.[411] This heterojunction forms a type-III energy band diagram with a broken gap under certain gate and source-drain voltages, which could lead to a band-to-band tunneling (B2BT) of electrons from CBM of $SnSe_2$ to the VBM of WSe_2. The B2BT process refers to the case, for example, the electron in CBM of the n-type semiconductor could tunnel across the potential barrier and reach to the VBM of the p-type semiconductor. Moreover, under illumination, a substantial generation of photocarriers would shift the E_f of WSe_2 towards its midgap. The change of WSe_2 E_f will modify the degree of band overlap for electron tunneling from WSe_2 VBM to $SnSe_2$ CBM, that eventually reduces the number of the tunneling electrons.

It is believed that it could be a similar case for the Nb:WSe_2/ZnO heterojunction, that it remains as type-II heterojunction under illumination at relatively smaller reverse voltages (-0.74-0 V) and becomes a type-III type when the reverse voltage is larger than -0.74 V. The possible energy band under reverse voltages is illustrated in **Figure 9.7**. The generation of the photocarriers and the applied reverse voltage will both affect the E_f position and also the relative energy band position of Nb:WSe_2 and ZnO. The result also demonstrates that Nb doping indeed introduce considerable holes that brings the E_f of Nb:WSe_2 very close to its VBM. Moreover, the B2BT will also increase the reverse current density in the dark, which will reduce its rectification ratio. At last, there is no photovoltaic effect observed in both type of heterojunctions, which is expected due to the energy band variation in such network consisted of few-layered nanosheets that act as traps for photocarriers. The photodetection or photovoltaic performance

could be further improved if the energy band variation could be minimized by using a more uniformly distributed thickness nanosheet network.

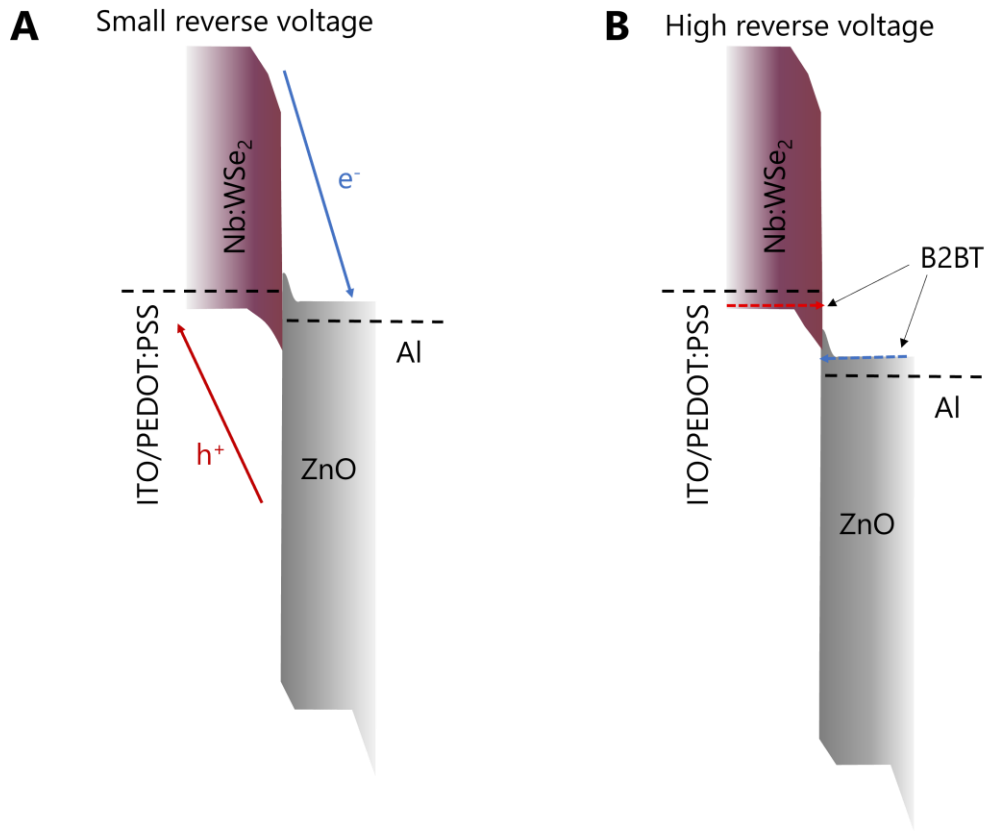

Figure 9.7 Band to band tunneling current. Schematic band diagrams of ITO/PEDOT:PSS/Nb:WSe_2/ZnO/Al at small reverse voltage (A) and at high reverse voltage (B).

The *J-V* curves are further fitted through equation 7.1 and the fitting results are given in **Figure 9.8**. For the WS_2 based heterojunction, the extracted ideality factor *n* is much larger than ideal values 1-2, which could be the influence of the Schottky junction and n-n junction that complicate the interfacial electrical properties. The obtained saturation current density J_s is also considerably large which is around 324.23 A m^{-2} and even increases around 3 times under illumination, indicating a high recombination current in the heterojunction. The extracted series resistance R_s is 17.54 Ohm but shows a slight increase to 17.85 Ohm under illumination. For the Nb:WSe_2 based heterojunction, the extracted *n* in

the dark is 2.21, which is reasonably ideal that can be ascribed to the single rectifying interface formed in this device. The obtained J_s in the dark is 3.72 A m^{-2}, which is significantly lower than that from the WS_2 heterojunction, and it increases ~16 times under illumination, which can be ascribed to increased carrier recombination due to photo-generated carriers. R_s decreases from 36.46 Ohm in the dark to 22.15 Ohm under illumination, corresponding to a positive photoconductivity. The good fitting results using Shockley equation imply that the heterojunctions remain as the type-2 energy band alignment and are absent of the tunneling effect at positive voltages.

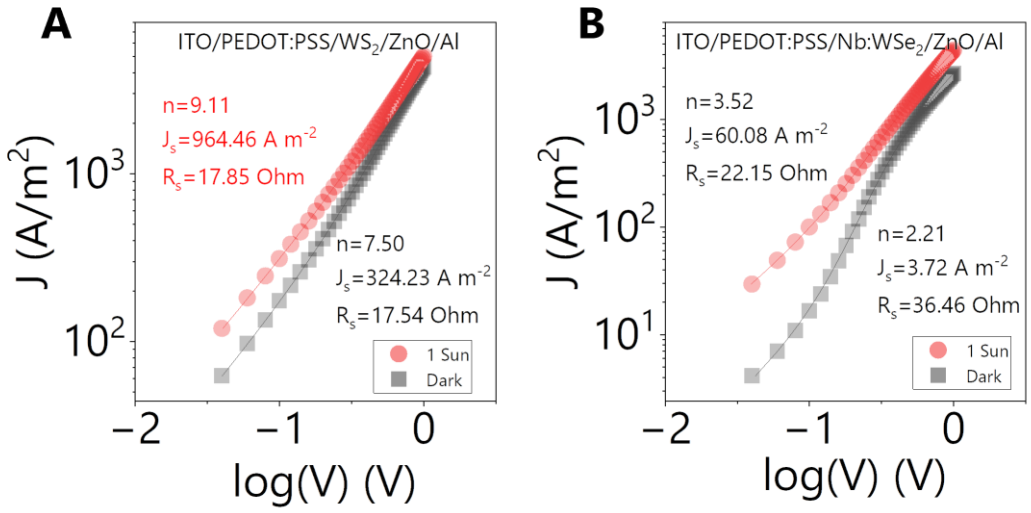

Figure 9.8 Fittings of *J-V* curves. The fitting results of *J-V* curves for heterojunction in the dark and under illumination. The extracted electrical parameters are given in each figure.

vdW heterojunctions

Having the heterojunctions with a single type of EE nanosheets, we could move on to fabricate the vdW heterojunction that consist of two types of EE nanosheets and importantly, form the interface that could rectify the current. To realize this structure, the Nb:WSe_2 dispersion was sprayed onto a PEDOT:PSS coated ITO glass substrate, forming a film with a mean thickness of 166±24 nm. Nb:WSe_2 will form an Ohmic contacted interface with PEDOT:PSS. Then, the n-type WS_2

thin film was subsequently sprayed on top of ITO/PEDOT:PSS/Nb:WSe_2 with a mean thickness of 89±30 nm, and ZnO nanoparticle film was spin-coated on the WS_2 surface. The device is completed by evaporation of 100 nm Al to form Ohmic contact with ZnO. ZnO is kept in this device to be consistent with the heterojunctions in the last section so we can compare the electrical performances. The final device structure is ITO/PEDOT:PSS/Nb:WSe_2/WS_2/ZnO/Al. Although the whole device structure is complicated having 6 layers of materials, it is expected that the governing heterojunction is formed at the Nb:WSe_2/WS_2 interface, despite that WS_2/ZnO may also contribute to the overall electrical behavior with a n-n junction.

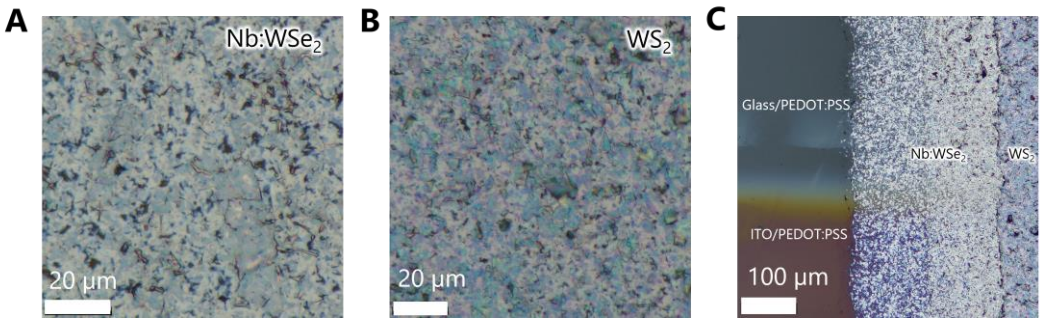

Figure 9.9 Optical microscopy characterisations of vdW heterojunctions. Optical images of the sprayed Nb:WSe_2 (A) and WS_2 (B) films. (C) The optical image of the spray-coated vdW heterojunction.

The morphology of the sprayed nanosheet network is characterised by an optical microscope. Due to increased film thickness, both Nb:WSe_2 film and the subsequently sprayed WS_2 on its top show much improved surface coverage (**Figure 9.9A-B**). Some pinholes can be found on Nb:WSe_2 but it is much improved due to more sprayed dispersion volumes. It is expected that these pinholes on the Nb:WSe_2 film may not result in a significant contact between the WS_2 nanosheets and PEDOT:PSS. This is due to the large aspect ratio and large sizes of the EE nanosheets could bridge these pinholes on the top but needs to be further confirmed by other characterisation techniques. An optical image at the

edge of the sprayed film is shown in **Figure 9.9C**. Due to the difference in their optical properties, ITO/PEDOT:PSS can be found with a reddish color at the bottom left. A distinctive edge for the Nb:WSe_2 and WS_2 films which is caused by the Kapton tape can be found, confirming the successful construction of the vdW heterojunction.

The *J-V* curves for the vdW heterojunction was collected in the dark and under illumination (**Figure 9.10A**). However, the heterojunction barely rectifies and shows a weak photoresponse, that the obtained R_{ph} are 0.13 and 0.14 A W^{-1} at -1 and 1 V, respectively. Ideally, this vdW heterojunction should exhibit a large built-in potential of ~1.25 eV (the E_f difference between WS_2 and Nb:WSe_2). The energy band diagram with no applied voltage is depicted in **Figure 9.10B**. The induced band offsets due to this large built-in potential will act as potential barriers and prohibit electrons from transporting towards the ITO electrode, or holes from transporting towards Al electrode. As a result, the reverse current density should be minimized, but is not observed here. The high reverse current implies that the energy bands under the reverse voltage conditions will not be able to block the carrier transport. It is worth mentioning that the possible contacts between any of the layers that are not adjacent should still yield rectifying behaviors. For examples, if WS_2 is in contact with PEDOT:PSS through some pinholes on the Nb:WSe_2 layer, it will yield a Schottky contact and make the device behave as Schottky diodes, which will reduce the reverse current density. In another case that if ZnO is in contact with Nb:WSe_2, it will result in a type-II heterojunction as observed in the last section. Therefore, we can rule out the possibility that the high reverse current is induced by the device structural reasons. The *J-V* curves were further fitted through equation 7.1 and the results are shown in **Figure 9.10C**. Giant ideality factors are obtained, which implies that the device will not follow the Shockley equation and other conduction

mechanisms may be involved. Another possibility could be the B2BT current due to the highly doped nature of both Nb:WSe_2 and WS_2. Under reverse voltages, the energy band alignment becomes type-III one and induces a large B2BT current. However, it has to be noted that there is a n-n junction at the WS_2/ZnO which may complicate the overall electrical behaviors. The tunneling current should be further verified by performing a temperature dependent electrical measurement on a device with a structure ITO/PEDOT:PSS/Nb:WSe_2/WS_2/Al.

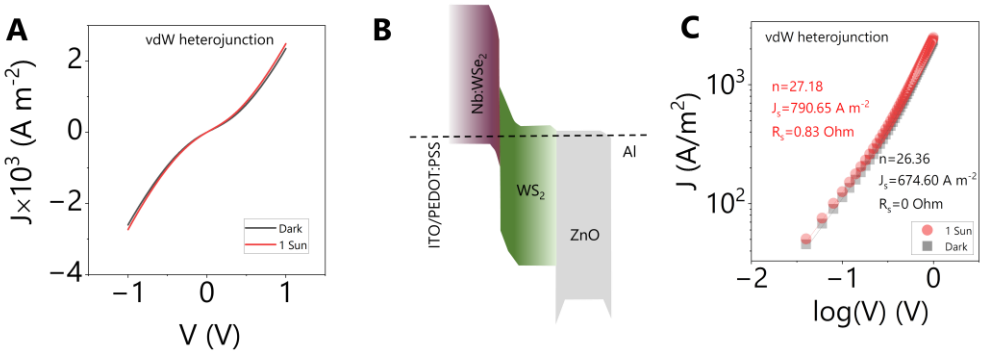

Figure 9.10 vdW heterojunction. (A) *J-V* curves of the vdW heterojunction measured in the dark and under illumination, (B) Schematic illustration of the energy band diagram after contacting without an external voltage, (C) Fitting results of *J-V* curves in (A).

9.4 Conclusion

In this study, electrochemically exfoliated semiconducting WS_2 and Nb:WSe_2 nanosheets were used to construct heterojunction type devices. The electrical measurements were performed in the dark and under 1000 W m^{-2} AM 1.5D illumination. For heterojunctions incorporating only one type of nanosheet, the devices exhibited relatively low rectification ratios due to the large bandgap for these nanosheets and the B2BT current. Negative photoresponse was observed for the Nb:WSe_2/ZnO based heterojunction. The vdW heterojunction was successfully fabricated with WS_2 and Nb:WSe_2, however, its reverse current is significantly large possibly due to the B2BT current and results in a low rectification ratio ~1 at ±1 V.

Conclusion & Outlook

Two-dimensional TMDs nanosheets are promising materials towards optoelectronic applications. However, it is still challenging to integrate networks formed with these nanosheets into realistic devices in a solution-processing way. The aim of this thesis is to address the current challenges regarding the device fabrication and performance improvements.

Vertically structured devices can significantly reduce the channel resistance, which allows the metal-semiconductor interfacial electrical properties to be observed. Vertical MSM devices were fabricated using ITO as the bottom electrode, liquid exfoliated WS_2 nanosheet networks as the semiconducting layer and SWNTs as the top electrode. The 1D high aspect-ratio nanomaterials enable such devices to be short-free, even when the WS_2 layer is down to ~0.5 μm thick. It is expected that this strategy can also be applied to the other porous semiconducting thin films to build vertical heterostructures. By performing electrical measurements, bulk-limited behaviors such as Ohmic and space charge limited conductions, were observed when SWNTs were dispersed in isopropanol. It was found that the extracted conductivity and mobility along the out-of-plane directions of the networks were around 1.63×10^{-4} S m^{-1} and 5.36×10^{-3} cm^2 V^{-1} s^{-1}, respectively, which were both around one order of magnitude lower than their in-plane values. Further, electrode-limited behaviors, i.e., Schottky contact, were observed when SWNTs were dispersed in surfactant aqueous solutions. The Schottky devices displayed electrical rectifying behaviors with relatively low rectification ratios (<10 at ±1 V). By performing a WS_2 film thickness study, a transition from electrode- to bulk-limited behaviors was observed, which is characterised by a critical film thickness ~2.6 μm.

Heterojunctions are widely adopted device types for optoelectronic applications.

Semiconducting n-type ZnO nanoparticles were coated on top of the liquid exfoliated p-type WSe_2 nanosheet network to form a p-n type heterojunction at the WSe_2/ZnO interface. Meanwhile, these nanoparticles could fill in the porous nanosheet network to avoid metal diffusing problems. Further, PEDOT:PSS was used to lower the potential barrier at the ITO/WSe_2 interface, which eventually leads to a high rectification ratio ~10^4 at ±1 V. When the heterojunction was measured under illumination, they can be used as self-powered photodetectors in both photoconductor and photodiode modes, giving a photoresponsivity of ~1.5 A W^{-1} at 1 V.

The optoelectronic response of the heterojunction is largely affected by the carrier transport process through the nanosheet network interface. To manipulate the interfacial properties, various types of carrier transport layer were introduced between the metal and liquid exfoliated WSe_2 nanosheet networks to construct p-i-n type heterojunctions. Their photovoltaic performances were investigated under AM 1.5D 1000 W m^{-2} illumination. These devices showed distinctive electrical behaviors with short-circuit current densities ranging from 1.32×10^{-3} to 2.50 A m^{-2}, open circuit voltages from 4 to 242 mV, and a rather low fill factor around 20-27%. The obtained highest efficiency was 1.95×10^{-3} % when ZnO and NiO were used as electron and hole transport layers, respectively.

Electrochemically exfoliated nanosheets can form tiled nanosheet networks with an ultra-low porosity. n-type WS_2 and p-type Nb:WSe_2 were used to construct the p-n type vdW heterojunction, where dangling bond-free surfaces can be utilized. The vdW heterojunction showed a rectification ratio approaching to unity owing to the high reverse current, which may be ascribed to the band-to-band tunneling conduction when both materials are highly doped. The heterojunction was further measured under 1000 W m^{-2} AM 1.5D illumination, and photoresponsivity of 0.13 and 0.14 A W^{-1} were obtained at -1 V and 1 V, respectively.

To answer the question proposed in the introduction, vertical stacking of active materials should be the feasible route towards fabricating vdW heterostructures based on semiconducting nanosheet networks. Their electrical behaviors can be tuned by manipulating the interfacial properties or the nanosheet network morphologies.

However, there are some limitations encountered in this thesis and should be solved in the future.

1. The energy bands of materials should be considered when making heterostructures. The energy bands referred throughout the thesis are mostly taken from literatures, while some of them were extracted from electrical measurements, such as ZnO based Schottky diodes. It is possible that the proposed energy bands in this thesis still show some deviations due to different sources of materials and processing methods. It will be convenient once the energy bands can be obtained in the future using techniques such as ultraviolet photoelectron spectroscopy, X-ray photoelectron spectroscopy and Kelvin probe force microscopy.
2. The doping of nanosheets should be investigated and be more controllable. In this thesis, it was found that the Fermi levels of nanosheets were affected by the surfactants or intercalants used for exfoliation. The doping is important as it governs several electrical properties, including conductivity, mobility and carrier density. The position of Fermi level will also shift depending on the doping type and density. When forming a diode device, the depletion width and diffusion length will both change when the doping density change, which will eventually affect the optoelectronic responses. Therefore, it would be necessary to controllably dope these materials, e.g., elemental doping or organic ligand functionalization, to boost the device performance in the future.
3. It may be too early to say that EE nanosheets are superior to LPE nanosheets

in all aspects. Despite of advantages of EE nanosheets regarding its good morphology, these nanosheets still exhibit some limitations: 1) the obtained nanosheets are mostly monolayer to few-layers. This will lead to energy band variations across the networks trapping the photocarriers, which is not desirable for most optoelectronic devices. A more effective size selection method is required to solve this problem. 2) the yield of EE nanosheet is extremely low, which will limit the available inks for thin film formations.

Appendix

A1 Electrode resistance calculation and subtraction

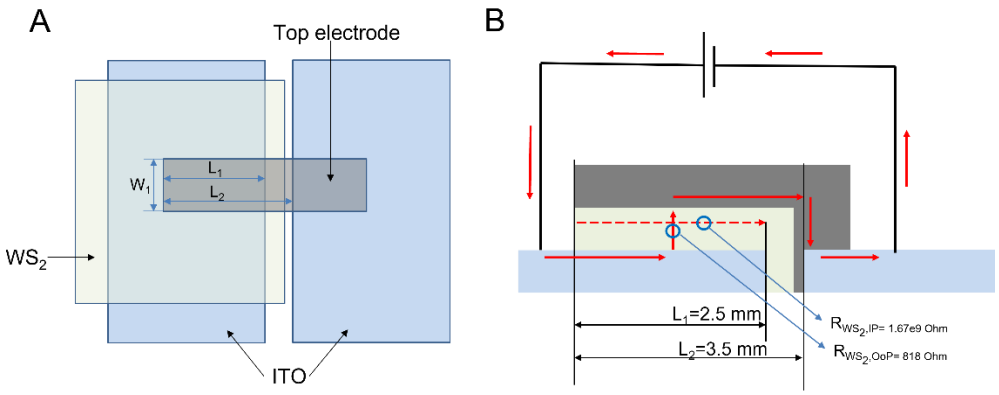

Figure A1 An illustration of device dimensions. (A) top view and (C) cross-section view and the red arrows represent the current flow direction.

The electrode resistance will depend on its conductivity σ_e and dimensions (length, width, and thickness). First, σ_e was obtained by a two-probe measurement with identical electrode films sprayed on glass slides as on devices. Then, dimensions of these films such as length L, width W, and thickness t_{film} were measured. The σ_e can be obtained by $\sigma_e = \frac{L}{R_e W t_e}$, where the subscript e refers to electrode. The obtained conductivity for electrodes are 1.8×10^3 S m^{-1} for 80 nm I-SWNTs, 6.8×10^3 S m^{-1} for 650 nm S-SWNTs, 4.8×10^5 S m^{-1} for 260 nm I-SWNTs/AgNWs and 4.8×10^5 S m^{-1} for 100 nm ITO (quoted value). We can find the first two electrodes are much less conductive than the latter two. It is important to find out how much influence of these electrodes' resistance can impose on the total device resistance R_{total}, which is given by $R_{total} = R_c + R_{WS_2} + R_e$, where R_c is the contact resistance, R_{WS_2} is the WS_2 resistance, and R_e is the electrode resistance. The device area A is defined as $A = L_1 W_1$.

Next, we find the actual electrode dimensions by comparing the OoP and IP resistance from WS_2 and finding the charge/current transporting route. A schematic demonstration of the top view of the device dimensions is shown in **Figure A1-A** as well as its cross-sectional schematic showing the current flow indicated by red arrows (**Figure A2-B**). Using the mean conductivity $<\sigma_{OoP}>\sim 1.63\times10^{-4}$ S m^{-1} and $<\sigma_{IP}>\sim 2\times10^{-3}$ S m^{-1} of WS_2 given in the manuscript, and device dimensions (L_1=2.5 mm and W_1=1.5 mm), we can find the OoP and IP resistance ($R_{WS_2, OoP}$ and $R_{WS_2, IP}$) for WS_2 will be 818 Ohm and 1.67×10^9 Ohm, respectively, for a 500 nm thick WS_2 film. This large OoP and IP resistance difference indicates the charge will preferably flow from ITO along the OoP direction of WS_2 to the top SWNTs electrode and is not likely to flow horizontally along WS_2 layer. Then, the charge will flow laterally along the top electrode to the other ITO. The longest distance current can flow through the electrode is L_2 (all the way from the end) while the shortest distance is L_2-L_1 (only from the nearest edge of the active area of the device). Assuming the OoP current through the WS_2 flows through the entire device area, then the average distance current flows through the top electrodes is L_2-$L_1/2$. Then we can estimate R_e using

$$R_e = \frac{L_2 - L_1/2}{\sigma_e W_1 t_e} \tag{A1}$$

Using the above conductivities for each type of electrodes and an electrode dimension L_2-$L_1/2$=2.25 mm and W_1=1.5 mm, we can obtain R_e for I-SWNTs, S-SWNTs, I-SWNTs/AgNWs, and ITO electrodes can be calculated to be 1×10^4, 340, 12.2, and 29.8 Ohm, respectively. Comparing with $R_{WS_2, OoP}$~818 Ohm, one can easily see that I-SWNTs/AgNWs and ITO electrodes would impose a small influence on the resistance of the whole device and its influence could be ignored. However, R_e from I-SWNTs is much too large to be useable. In addition, R_e from

S-SWNTs (340 Ohm), although smaller than R_{WS_2} at all WS_2 thickness (minimum value 818 Ohm) cannot be ignored if we want to obtain accurate results. Although R_e could always be reduced by increasing electrode thickness, we deliberately avoided to spray much solvent on top of nanosheet network in case the network may be damaged by the compressed nitrogen flow or the re-dispersing problem in case the solvent dried slowly.

Because of the discussion above, we did not use I-SWNTs as electrodes, instead using I-SWNTs/AgNWs (assuming R_e for I-SWNTs/AgNWs based devices could be neglected). In the case of S-SWNTs based devices, we find R_e for S-SWNTs using the equation above and then subtracted this from the total device resistance to find the correct WS_2 resistance.

The current flow behavior in such system is further justified by Prof. Jonathan Coleman as follows. In our systems, especially the devices with I-SWNTs top electrodes, the top electrode resistance is relatively high compared to an evaporated/sputtered metal electrode. Then there is a concern that the current density through the WS_2 might be larger on the side where the top electrode first meets the WS_2, with the vertical current density falling off further into the film. Such a spatial variation in vertical current density would be driven by the predilection of the current to take the path of least resistance. This scenario is illustrated in **Figure A2**. If the current density was to decay rapidly with distance into the film (from right to left) then the majority of current flow would be on the extreme right-hand side of the WS_2 film. In that case it would be inappropriate to use the area of electrode overlap as the active area of the WS_2. Alternatively, if the current density were to decay very slowly with distance into the film, one could approximate the current flow as uniform throughout the active area of the WS_2. Although such behavior could be analyzed using a transmission line model, we

take a simpler approach to demonstrate that transmission line analysis is not necessary.

To do this, we model a simplified scenario of current flow we divide the active area of WS_2 into two regions, one on the right where there is a uniform current flow, and one on the left where no current flows. We labeled the depth of the region where corn flows as a comma as shown in **Figure A2-A&B**. For example, if the current density decayed exponentially with distance into the film, then a would be equivalent to the decay length.

Under these circumstances the resistance of the system is there's some of the horizontal resistance associated with top electrode and vertical resistance associated with the region through which current flows (neglecting the very low resistance associated with the bottom electrode). This means:

$$R_{total} = R_{WS_2} + R_e \tag{A2}$$

$$R_{total} = \frac{t_{WS_2}}{\sigma_{OoP,WS_2} W_1 a} + \frac{L_2 - L_1 + a/2}{\sigma_e W_1 t_e} \tag{A3}$$

where t_{WS_2} is the WS_2 film thicknesses. This equation shows that increasing a (so the current occupies more of the active area) increases the resistance associated with the current flowing through the top electrode. Decreasing a increases the resistance associated with the current flowing through the WS_2.

We propose that the extent of the active WS_2 area through which current flows, represented by the parameter a, can be found by minimizing R_{total}, i.e., when $dR_{total} / da = 0$.

Differentiating yields

$$\frac{dR_{total}}{da} = -\frac{t_{WS_2}}{\sigma_{OoP,WS_2} W_1 a^2} + \frac{1}{2\sigma_e W_1 t_e} \tag{A4}$$

When this derivative is zero defines the value of a consistent with the minimal resistance, a_{min}:

$$a_{\min} = \sqrt{\frac{2\sigma_e t_e t_{WS_2}}{\sigma_{OoP,WS_2}}} \tag{A5}$$

Taking σ_{OoP,WS_2} and σ_e given above allows us to calculate a_{min} versus t_{WS_2}=500 nm for the two top electrode types used. These graphs are plotted in **Figure A3-C**. In all cases, we fine that a_{min} is larger than the length of the active device area, L_1 (2.5 mm). This means that the resistance is minimized by the current flowing through the entire active area of the device. This justifies our initial assumption.

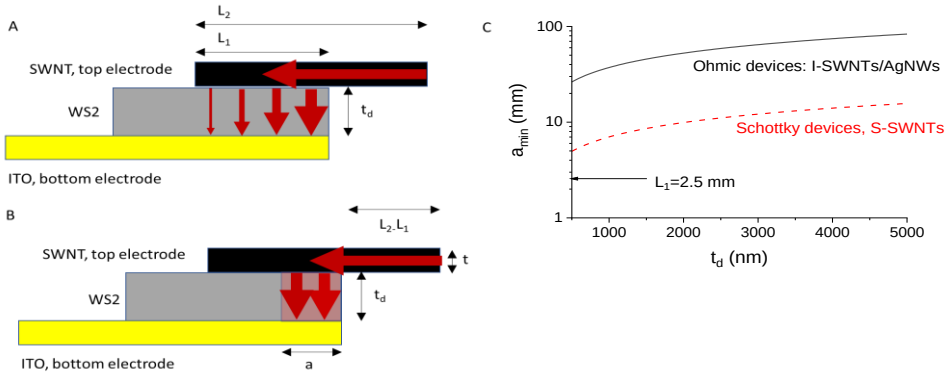

Figure A2 Current flow behaviors. (A,B) schematics showing current density decaying across the device (A) and a simplified approximation showing constant current flowing through a localized region of the device of depth a. C) Calculated values of a which minimize the device resistance as a function of WS_2 thickness.

A2 Heterojunction performance comparisons

Table A1 Rectification ratios at various biases from the reported planar heterojunctions using liquid exfoliated TMD nanosheets.

No.	Material	Method	Structure	Rectification ratio	Ref.
1	MoS_2	Spray coat	In/n-Si/MoS_2/Au	*3.7e4 at ±1 V	[269]
2	WSe_2	Drop cast	Ag/WSe_2/n-Si/Ag	84.06 at ±1 V	[270]
3	WS_2	Drop cast	Al/ZnO:WS_2/p-Si	155 at ±1.5 V	[240]
4	MoS_2	Spin coat	Au/MoS_2/p-Si/Al	1e5 at ±3 V	[238]
5	MoS_2	Drop cast	Graphite/ZnO:MoS_2/p-Si/Graphite	*1 at ±1 V	[412]
6	$MoSe_2$	Spin coat	Au/$MoSe_2$/p-Si/Al	1e5 at ±5 V	[241]
7	WSe_2	Drop cast	Ag/WSe_2/p-Si/Ag	69 at ±1 V	[244]
8	WS_2	Drop cast	Ag/Ni:WS_2/p-Si/Ag	23 at ±2 V	[271]
9	SnS_2	Drop cast	Ag/SnS_2/p-Si/Ag	*1.62 at ±4 V	[413]
10	MoS_2	Spin coat	ITO/n-MoS_2/p-MoS_2/Ag	*1 at ±1 V	[272]
11	EE MoS_2	Spin coat	Graphene/s-CNTs/MoS_2/HfO_2/Graphene	200 at ±1 V	[234]
12	NiO	Spin coat	Ni/NiO/p-Si/InGa	16827 at ±3 V	[414]
13	SnS	Drop-cast	Ag/SnS/n-Si/Ag	171 at ±2 V	[242]
14	SnS	Dip coat	Pt/SnS/TiO_2/FTO	7.65 at ±0.5 V	[415]
15	WSe_2	Spray coat	ITO/PEDOT:PSS/WSe_2/ZnO/Al	13699 at ±1 V	Our work

Note: “Method” refers to the film formation method for LPE materials. “n-” and “p-” refer to n-type and p-type doping, respectively. “Gra” refers to graphite. “FTO” refers to Fluoride-doped tin oxide glasses**.** “EE” refers to electrochemically exfoliated. The symbol “*” refers to estimated values.

Table A2 Comparison of photo-responsivity from photodetectors based on LPE WSe_2

Device				Performance		Ref.
No.	Type	Structure	Method	Light source	R_{ph} (A W^{-1})	
1	PHJ	Ag/WSe_2/p-Si/Ag	Drop cast	670 nm	1.15 at -1.5 V	[244]
2		Ag/WSe_2/n-Si/Ag	Drop cast	LED	8.61e-2 at 0 V	[245]
3		Ag/WSe_2/p-Si/Ag	Electrophoresis	520 nm	*8.4e-2 at -2 V	[239]
4		ITO/PEDOT:PSS/WSe_2/ZnO/Al	Spray coat	AM1.5D	6.08e-3 at -1 V 6.53e-5 at 0 V 1.5 at 1 V	Our work
5	IP	Ag/WSe_2/Ag	Dip coat	590 nm	1.78e-2 at 5 V	[416]
6	IP	Ag/WSe_2/Ag	Dip coat	670 nm	*6e-3 at 5 V	[417]
7	OoP	CNT/WSe_2/CNT	Aerosol-jet	660 nm	1 at 1 V	[229]
8	IP	Gra/WSe_2/Gra	Drop cast	670 nm	6.66e-3 at 1 V	[418]
9	IP	ITO/WSe_2/ITO	Drop cast	Visible light	3.65e-6 at 1 V	[228]
10	IP	ITO/Cu:WSe_2/ITO	Drop cast	670 nm	9.31e-5 at 0 V	[419]
11	IP	Ag/WSe_2:PVC/Ag	-	470 nm	3.31e-4 at 20 V	[420]

Note: Device type: “PHJ”, “IP” and “OoP” refer to planar heterojunction, in-plane and out-of-plane Ohmic-contacted devices, respectively. The symbol “*” refers to estimated values.

A3 Symbols and acronyms

Symbol	
h	Planck's constant
E_f	Fermi level energy
ΔG_{mix}	Gibb's free energy
ΔH_{mix}	Enthalpy of mixing
T	Temperature
ΔS_{mix}	Entropy of mixing
V	Volume
t_{NS}	Thickness of nanosheets
δ_{Gra}	Surface tension of graphene
δ_{Sol}	Surface tension of the solvent
ϕ_{Gra}	Volume fraction of graphene in the solvent
δ_T	Hildebrand solubility parameter
U	Potential energy
A_{NS}	Nanosheet area
ε_0	Dielectric constants in vacuum
ε_r	Dielectric constants of material
r_p	Particle radius
k	Boltzmann constant
ζ	Zeta potential of the dispersion
κ^{-1}	Debye screening length
D	Inter-nanosheet distance
ρ_{NS}	Number of atoms per unit area in nanosheets
m	Mass of the nanosheet
ρ_{Sol}	Density of the solvent
v	Volume of nanoparticle occupied per mass unit
f	Frictional coefficient
γ	Interfacial tension
t_{film}	Film thickness

ω	Angular velocity
R_e	Electrode resistance
R_c	Contact resistance
R_s	Series resistance
L	Channel length
W	Channel width
σ_{IP}	In-plane conductivity
σ_{OoP}	Out-of-plane conductivity
$\alpha(\lambda)$	Absorption coefficient
F	Light intensity
G	Electron-hole pairs generation rate
ϕ_m	Work function of the metal
ϕ_s	Work function of the semiconductor
χ_s	Electron affinity of the semiconductor
E_g	Bandgap energy
E_v	Valence band energy
Ec	Conduction band energy
μ	Mobility
σ_{ph}	Photoconductivity
σ_L	Conductivity under illumination
σ_D	Conductivity in the dark
q	Elementary charge
n_0	Intrinsic electron density in the semiconductor
p_0	Intrinsic hole density in the semiconductor
Δn	Photogenerated electron density
Δp	Photogenerated hole density
W_n	Depletion width in the n-type semiconductor
W_p	Depletion width in the p-type semiconductor
n_{p0}	Equilibrium electron concentration in the p-type semiconductor
p_{n0}	Equilibrium hole concentration in the n-type semiconductor,
N_m	Carrier density of the metal

ϕ_b	Potential barrier height
R^*	Richardson constant
m_e	Effective carrier mass
n	Ideality factor
I_s	Saturation current
ΔE_v	Valence band energy offset
ΔE_c	Conduction band energy offset
Φ_b	Built-in potential
N_a	Acceptor concentration in p-type semiconductors
N_d	Donor concentration in n-type semiconductors
D	Diffusion coefficient
n_0	Equilibrium carrier concentration
L	Diffusion length
J	Current density
R_{ph}	Photoresponsivity
A	Device area
D^*	Detectivity
Δf	Bandwidth
NEP	Noise equivalent power
S_n	Noise spectral density
G_{ph}	Photogain
τ_{life}	carrier lifetime
τ_{trans}	transition time
I_{sc}	Short circuit current
V_{oc}	Open circuit voltage
η	Conversion efficiency
RCF	Relative centrifugal force
r	Rotor radius
A_{opt}	Optical absorbance
$T(\lambda)$	Transmittance
C_{NMs}	Nanomaterial concentration

l_{light}	Light path length
$\Delta\nu$	Frequency shift
λ_i	Incident light wavelength
λ_s	Scattered light wavelength
$\langle L_{NS} \rangle$	Mean nanosheet length
$\langle N_{NS} \rangle$	Mean nanosheet number of layer
$\langle L_{NT} \rangle$	Mean nanotube length
$\langle D_{NT} \rangle$	Mean nanotube diameter
$\langle t_{film} \rangle$	Mean film thickness
$\langle R_a \rangle$	Mean film average roughness
E	Electric field
τ	Photocarrier lifetime
U_{SRH}	Shockley-Read-Hall recombination rate
n_i	Intrinsic carrier density
E_t	Trap energy level
E_i	Intrinsic energy level
v_{th}	Thermal velocity of electrons
N_t	Density of the recombination centers
σ_0	Carrier capture cross section
R_{sh}	Shunt resistance
I_{sh}	Shunt current
I_{HJ}	Diode current

Acronym	
0D	Zero-dimensional
1D	One-dimensional
2D	Two-dimensional
AFM	Atomic force microscopy
AgNWs	Silver nanowires
AR	Aspect ratio
B2B	Back-to-back
B2BT	Band-to-band tunneling
CBM	Conduction band minimum
CHP	Cyclohexyl-pyrrolidinone
CMC	Critical micelle concentration
CNTs	Carbon nanotubes
DFT	Density functional theory
DGU	Density gradient based ultracentrifugation
DMF	Dimethylformamide
DOS	Density of states
EDL	Electrical double layer
EE	Electrochemical exfoliation
EQE	External quantum efficiency
ETL	Electron transport layer
FF	Fill factor
FIB	Focused ion beam
h-BN	Hexagonal boron nitride
HTL	Hole transport layer
IGZO	In-Ga-Zn oxide
IP	In-plane
IPA	Isopropanol
ITO	Indium tin oxide
LCC	Liquid cascade centrifugation
LDMs	Low-dimensional materials

LPE	Liquid-phase exfoliation
MOs	Metal oxides
MSM	Metal-semiconductor-metal
MWNTs	Multi-walled carbon nanotubes
NMP	N-Methyl-2-pyrrolidone
NVP	N-vinyl-Pyrrolidinone
OoP	Out-of-plane
PEDOT:PSS	Poly(3,4-ethylenedioxythiophene) polystyrene sulfonate
PVP	Polyvinylpyrrolidone
RBM	Radial breathing mode
RPM	Revolutions per minute
RR	Rectification ratio
SCLC	Space-charge-limited conduction
SDBS	Sodium dodecyl benzene sulfonate
SEM	Scanning electron microscopy
SEs	Secondary electrons
SRH	Shockley-Read-Hall
SWNTs	Single-walled carbon nanotubes
TAA	Titanium diisopropoxide bis(acetylacetonate)
TCEs	Transparent conductive electrodes
TE	Thermionic emission
TEM	Transmission electron microscopy
TMDs	Transition metal chalcogenides
TMOs	Transition metal oxides
TPA	Tetrapropylammonium
UV-Vis-NIR	Ultraviolet-visible-near Infrared
VBM	Valance band maximum
vdW	van der Waals

Bibliography

[1] J.-P. Colinge and C. A. Colinge, *Physics of semiconductor devices*, Springer Science & Business Media, 2005.

[2] B. C. Brodie, "XIII. On the atomic weight of graphite," *Philosophical Transactions of the Royal Society of London*, vol. 149, no. 0, pp. 249-259, 1859.

[3] P. R. Wallace, "The band theory of graphite," *Physical Review*, vol. 71, no. 9, pp. 622-634, 1947.

[4] H. P. Boehm, Clauss, A., Fischer, G., & Hofmann, U., presented in part at the Proceedings of the fifth conference on carbon, New York, USA, 1962.

[5] J. A. Venables, G. D. T. Spiller and M. Hanbucken, "Nucleation and growth of thin films," *Reports on Progress in Physics*, vol. 47, no. 4, pp. 399-459, 1984.

[6] K. S. Novoselov, A. K. Geim, S. V. Morozov, D. Jiang, Y. Zhang, S. V. Dubonos, I. V. Grigorieva and A. A. Firsov, "Electric field effect in atomically thin carbon films," *Science*, vol. 306, no. 5696, pp. 666-669, 2004.

[7] J. C. Meyer, A. K. Geim, M. I. Katsnelson, K. S. Novoselov, T. J. Booth and S. Roth, "The structure of suspended graphene sheets," *Nature*, vol. 446, no. 7131, pp. 60-63, 2007.

[8] A. Fasolino, J. H. Los and M. I. Katsnelson, "Intrinsic ripples in graphene," *Nature Materials*, vol. 6, no. 11, pp. 858-861, 2007.

[9] A. H. Castro Neto, F. Guinea, N. M. R. Peres, K. S. Novoselov and A. K. Geim, "The electronic properties of graphene," *Reviews of Modern Physics*, vol. 81, no. 1, pp. 109-162, 2009.

[10] T. Enoki, M. Endo and M. Suzuki, *Graphite intercalation compounds and applications*, Oxford University Press, 2003.

[11] A. K. Geim and K. S. Novoselov, "The rise of graphene," *Nature Materials*,

vol. 6, no. 3, pp. 183-191, 2007.

[12] Y. Zhang, Y.-W. Tan, H. L. Stormer and P. Kim, "Experimental observation of the quantum Hall effect and Berry's phase in graphene," *Nature*, vol. 438, no. 7065, pp. 201-204, 2005.

[13] K. S. Novoselov, A. K. Geim, S. V. Morozov, D. Jiang, M. I. Katsnelson, I. V. Grigorieva, S. V. Dubonos and A. A. Firsov, "Two-dimensional gas of massless Dirac fermions in graphene," *Nature*, vol. 438, no. 7065, pp. 197-200, 2005.

[14] M. Dresselhaus and G. Dresselhaus, "Intercalation compounds of graphite," *Advances in Physics*, vol. 30, no. 2, pp. 139-326, 1981.

[15] R. R. Nair, P. Blake, A. N. Grigorenko, K. S. Novoselov, T. J. Booth, T. Stauber, N. M. Peres and A. K. Geim, "Fine structure constant defines visual transparency of graphene," *Science*, vol. 320, no. 5881, pp. 1308-1308, 2008.

[16] Q. Li, J. Lu, P. Gupta and M. Qiu, "Engineering optical absorption in graphene and other 2D Materials: Advances and applications," *Advanced Optical Materials*, vol. 7, no. 20, pp. 1900595, 2019.

[17] C. Lee, X. Wei, J. W. Kysar and J. Hone, "Measurement of the elastic properties and intrinsic strength of monolayer graphene," *Science*, vol. 321, no. 5887, pp. 385-388, 2008.

[18] A. A. Balandin, S. Ghosh, W. Bao, I. Calizo, D. Teweldebrhan, F. Miao and C. N. Lau, "Superior thermal conductivity of single-layer graphene," *Nano Letters*, vol. 8, no. 3, pp. 902-907, 2008.

[19] B. Partoens and F. M. Peeters, "From graphene to graphite: Electronic structure around the K point," *Physical Review B*, vol. 74, no. 7, pp., 2006.

[20] S. V. Morozov, K. S. Novoselov, F. Schedin, D. Jiang, A. A. Firsov and A. K. Geim, "Two-dimensional electron and hole gases at the surface of graphite," *Physical Review B*, vol. 72, no. 20, pp., 2005.

[21] R. P. Feynman, “Plenty of room at the bottom,” *APS annual meeting*, Massachusetts, USA, 1959.

[22] R. Frisenda, Y. Niu, P. Gant, M. Muñoz and A. Castellanos-Gomez, "Naturally occurring van der Waals materials," *npj 2D Materials and Applications*, vol. 4, no. 1, pp. 38, 2020.

[23] X. Ren, G. Liao, Z. Li, H. Qiao, Y. Zhang, X. Yu, B. Wang, H. Tan, L. Shi, X. Qi and H. Zhang, "Two-dimensional MOF and COF nanosheets for next-generation optoelectronic applications," *Coordination Chemistry Reviews*, vol. 435, no. pp., 2021.

[24] F. Yang, S. Cheng, X. Zhang, X. Ren, R. Li, H. Dong and W. Hu, "2D organic materials for optoelectronic applications," *Advanced Materials*, vol. 30, no. 2, pp. 1702415, 2018.

[25] K. A. Lozovoy, Izhnin, II, A. P. Kokhanenko, V. V. Dirko, V. P. Vinarskiy, A. V. Voitsekhovskii, O. I. Fitsych and N. Y. Akimenko, "Single-element 2D materials beyond graphene: Methods of epitaxial synthesis," *Nanomaterials*, vol. 12, no. 13, pp., 2022.

[26] T. Wang, H. Wang, Z. Kou, W. Liang, X. Luo, F. Verpoort, Y. J. Zeng and H. Zhang, "Xenes as an Emerging 2D Monoelemental Family: Fundamental Electrochemistry and Energy Applications," *Advanced Functional Materials*, vol. 30, no. 36, pp. 2002885, 2020.

[27] B. Wang, S. Zhong, Y. Ge, H. Wang, X. Luo and H. Zhang, "Present advances and perspectives of broadband photo-detectors based on emerging 2D-Xenes beyond graphene," *Nano Research*, vol. 13, no. 4, pp. 891-918, 2020.

[28] K. S. Novoselov, D. Jiang, F. Schedin, T. J. Booth, V. V. Khotkevich, S. V. Morozov and A. K. Geim, "Two-dimensional atomic crystals," *Proceedings of the National Academy of Sciences*, vol. 102, no. 30, pp. 10451-10453, 2005.

[29] H. Wang, Y. Zhao, Y. Xie, X. Ma and X. Zhang, "Recent progress in synthesis

of two-dimensional hexagonal boron nitride," *Journal of Semiconductors*, vol. 38, no. 3, pp. 031003, 2017.

[30] K. Zhang, Y. Feng, F. Wang, Z. Yang and J. Wang, "Two dimensional hexagonal boron nitride (2D-hBN): synthesis, properties and applications," *Journal of Materials Chemistry C*, vol. 5, no. 46, pp. 11992-12022, 2017.

[31] J. Zhu, J. Kang, J. Kang, D. Jariwala, J. D. Wood, J. W. Seo, K. S. Chen, T. J. Marks and M. C. Hersam, "Solution-processed dielectrics based on thickness-sorted two-dimensional hexagonal boron nitride nanosheets," *Nano Letters*, vol. 15, no. 10, pp. 7029-7036, 2015.

[32] T. Carey, S. Cacovich, G. Divitini, J. Ren, A. Mansouri, J. M. Kim, C. Wang, C. Ducati, R. Sordan and F. Torrisi, "Fully inkjet-printed two-dimensional material field-effect heterojunctions for wearable and textile electronics," *Nature Communications*, vol. 8, no. 1, pp. 1202, 2017.

[33] B. Gupta and H. S. S. R. Matte, "Solution-processed layered hexagonal boron nitride dielectrics: a route toward fabrication of high performance flexible devices," *ACS Applied Electronic Materials*, vol. 1, no. 10, pp. 2130-2139, 2019.

[34] S. Das Sarma, S. Adam, E. H. Hwang and E. Rossi, "Electronic transport in two-dimensional graphene," *Reviews of Modern Physics*, vol. 83, no. 2, pp. 407-470, 2011.

[35] V. K. Sangwan and M. C. Hersam, "Electronic transport in two-dimensional materials," *Annual Review of Physical Chemistry*, vol. 69, pp. 299-325, 2018.

[36] F. Xia, H. Wang, D. Xiao, M. Dubey and A. Ramasubramaniam, "Two-dimensional material nanophotonics," *Nature Photonics*, vol. 8, no. 12, pp. 899-907, 2014.

[37] M. Naguib, M. W. Barsoum and Y. Gogotsi, "Ten years of progress in the synthesis and development of MXenes," *Advanced Materials*, vol. 33, no. 39,

pp. 2103393, 2021.

[38] C. Lan, Z. Zhou, R. Wei and J. C. Ho, "Two-dimensional perovskite materials: From synthesis to energy-related applications," *Materials Today Energy*, vol. 11, no. pp. 61-82, 2019.

[39] L. M. Xie, "Two-dimensional transition metal dichalcogenide alloys: preparation, characterization and applications," *Nanoscale*, vol. 7, no. 44, pp. 18392-18401, 2015.

[40] M. Zhang, J. Wu, Y. Zhu, D. O. Dumcenco, J. Hong, N. Mao, S. Deng, Y. Chen, Y. Yang, C. Jin, S. H. Chaki, Y. S. Huang, J. Zhang and L. Xie, "Two-dimensional molybdenum tungsten diselenide alloys: photoluminescence, Raman scattering, and electrical transport," *ACS Nano*, vol. 8, no. 7, pp. 7130-7137, 2014.

[41] A. H. Davis and W. Zheng, "Discrete composition control of two-dimensional morphologic all-inorganic metal halide perovskite nanocrystals," *Journal of Energy Chemistry*, vol. 59, pp. 257-275, 2021.

[42] F. He, Y. Zhou, Z. Ye, S.-H. Cho, J. Jeong, X. Meng and Y. Wang, "Moiré patterns in 2D materials: A review," *ACS Nano*, vol. 15, no. 4, pp. 5944-5958, 2021.

[43] M. Chhowalla, H. S. Shin, G. Eda, L. J. Li, K. P. Loh and H. Zhang, "The chemistry of two-dimensional layered transition metal dichalcogenide nanosheets," *Nature Chemistry*, vol. 5, no. 4, pp. 263-275, 2013.

[44] R. G. Dickinson and L. Pauling, "The crystal structure of molybdenite," *Journal of the American Chemical Society*, vol. 45, no. 6, pp. 1466-1471, 1923.

[45] R. F. Frindt, "Single crystals of MoS_2 several molecular layers thick," *Journal of Applied Physics*, vol. 37, no. 4, pp. 1928-1929, 1966.

[46] P. Joensen, R. F. Frindt and S. R. Morrison, "Single-layer MoS_2," *Materials*

Research Bulletin, vol. 21, no. 4, pp. 457-461, 1986.

[47] Q. H. Wang, K. Kalantarzadeh, A. Kis, J. N. Coleman and M. S. Strano, "Electronics and optoelectronics of two-dimensional transition metal dichalcogenides," *Nature Nanotechnology*, vol. 7, no. 11, pp. 699-712, 2012.

[48] J. A. Wilson and A. D. Yoffe, "The transition metal dichalcogenides discussion and interpretation of the observed optical, electrical and structural properties," *Advances in Physics*, vol. 18, no. 73, pp. 193-335, 1969.

[49] M. A. Py and R. R. Haering, "Structural destabilization induced by lithium intercalation in MoS2 and related compounds," *Canadian Journal of Physics*, vol. 61, no. 1, pp. 76-84, 1983.

[50] A. Splendiani, L. Sun, Y. Zhang, T. Li, J. Kim, C. Y. Chim, G. Galli and F. Wang, "Emerging photoluminescence in monolayer MoS_2," *Nano Letters*, vol. 10, no. 4, pp. 1271-1275, 2010.

[51] K. F. Mak, C. Lee, J. Hone, J. Shan and T. F. Heinz, "Atomically thin MoS_2: A new direct-gap semiconductor," *Physical Review Letters*, vol. 105, no. 13, pp., 2010.

[52] K. Synnatschke, P. A. Cieslik, A. Harvey, A. Castellanos-Gomez, T. Tian, C.-J. Shih, A. Chernikov, E. J. G. Santos, J. N. Coleman and C. Backes, "Length- and thickness-dependent optical response of liquid-exfoliated transition metal dichalcogenides," *Chemistry of Materials*, vol. 31, no. 24, pp. 10049-10062, 2019.

[53] K. F. Mak and J. Shan, "Photonics and optoelectronics of 2D semiconductor transition metal dichalcogenides," *Nature Photonics*, vol. 10, no. 4, pp. 216-226, 2016.

[54] Q. H. Wang, K. Kalantar-Zadeh, A. Kis, J. N. Coleman and M. S. Strano, "Electronics and optoelectronics of two-dimensional transition metal dichalcogenides," *Nature Nanotechnology*, vol. 7, no. 11, pp. 699-712, 2012.

[55] D. W. Latzke, W. Zhang, A. Suslu, T.-R. Chang, H. Lin, H.-T. Jeng, S. Tongay, J. Wu, A. Bansil and A. Lanzara, "Electronic structure, spin-orbit coupling, and interlayer interaction in bulk MoS_2 and WS_2," *Physical Review B*, vol. 91, no. 23, pp., 2015.

[56] G. Wang, A. Chernikov, M. M. Glazov, T. F. Heinz, X. Marie, T. Amand and B. Urbaszek, "Colloquium: Excitons in atomically thin transition metal dichalcogenides," *Reviews of Modern Physics*, vol. 90, no. 2, pp. 021001, 2018.

[57] M. Florian, M. Hartmann, A. Steinhoff, J. Klein, A. W. Holleitner, J. J. Finley, T. O. Wehling, M. Kaniber and C. Gies, "The dielectric impact of layer distances on exciton and trion binding energies in van der Waals heterostructures," *Nano Letters*, vol. 18, no. 4, pp. 2725-2732, 2018.

[58] M. Bernardi, M. Palummo and J. C. Grossman, "Extraordinary sunlight absorption and one nanometer thick photovoltaics using two-dimensional monolayer materials," *Nano Letters*, vol. 13, no. 8, pp. 3664-3670, 2013.

[59] S. Bertolazzi, J. Brivio and A. Kis, "Stretching and breaking of ultrathin MoS_2," *ACS Nano*, vol. 5, no. 12, pp. 9703-9709, 2011.

[60] X. Yu, T. J. Marks and A. Facchetti, "Metal oxides for optoelectronic applications," *Nature Materials*, vol. 15, no. 4, pp. 383-396, 2016.

[61] H. A. Klasens and H. Koelmans, "A tin oxide field-effect transistor," *Solid-State Electronics*, vol. 7, no. 9, pp. 701-702, 1964.

[62] K. Nomura, H. Ohta, A. Takagi, T. Kamiya, M. Hirano and H. Hosono, "Room-temperature fabrication of transparent flexible thin-film transistors using amorphous oxide semiconductors," *Nature*, vol. 432, no. 7016, pp. 488-492, 2004.

[63] S. R. Thomas, P. Pattanasattayavong and T. D. Anthopoulos, "Solution-processable metal oxide semiconductors for thin-film transistor applications,"

Chemical Society Reviews, vol. 42, no. 16, pp. 6910-6923, 2013.

[64] W. C. Choy and D. Zhang, "Solution-processed metal oxides as efficient carrier transport layers for organic photovoltaics," *Small*, vol. 12, no. 4, pp. 416-431, 2016.

[65] A. I. Hofmann, E. Cloutet and G. Hadziioannou, "Materials for transparent electrodes: from metal oxides to organic alternatives," *Advanced Electronic Materials*, vol. 4, no. 10, pp. 1700412, 2018.

[66] E. Fortunato, P. Barquinha and R. Martins, "Oxide semiconductor thin-film transistors: A review of recent advances," *Advanced Materials*, vol. 24, no. 22, pp. 2945-2986, 2012.

[67] Z. Wang, P. K. Nayak, J. A. Caraveo-Frescas and H. N. Alshareef, " Recent developments in p-type oxide semiconductor materials and devices," *Advanced Materials*, vol. 28, no. 20, pp. 3831-3892, 2016.

[68] X. Liang, S. Bai, X. Wang, X. Dai, F. Gao, B. Sun, Z. Ning, Z. Ye and Y. Jin, "Colloidal metal oxide nanocrystals as charge transporting layers for solution-processed light-emitting diodes and solar cells," *Chemical Society Reviews*, vol. 46, no. 6, pp. 1730-1759, 2017.

[69] S. S. Shin, S. J. Lee and S. I. Seok, "Metal oxide charge transport layers for efficient and stable perovskite solar cells," *Advanced Functional Materials*, vol. 29, no. 47, pp. 1900455, 2019.

[70] M. Gardon and J. M. Guilemany, "A review on fabrication, sensing mechanisms and performance of metal oxide gas sensors," *Journal of Materials Science: Materials in Electronics*, vol. 24, no. 5, pp. 1410-1421, 2013.

[71] P. Barquinha, L. Pereira, G. GonçAlves, R. Martins and E. Fortunato, "Toward high-performance amorphous GIZO TFTs," *Journal of The Electrochemical Society*, vol. 156, no. 3, pp. H161, 2009.

[72] W. H. Lee, S. J. Lee, J. A. Lim and J. H. Cho, "Printed In-Ga-Zn-O drop-based thin-film transistors sintered using intensely pulsed white light," *RSC Advances*, vol. 5, no. 96, pp. 78655-78659, 2015.

[73] J. J. Jasieniak, N. D. Treat, C. R. McNeill, B. J. de Villers, E. Della Gaspera and M. L. Chabinyc, "Interfacial characteristics of efficient bulk heterojunction solar cells fabricated on MoO_x anode interlayers," *Advanced Materials*, vol. 28, no. 20, pp. 3944-3951, 2016.

[74] M. E. Franke, T. J. Koplin and U. Simon, "Metal and metal oxide nanoparticles in chemiresistors: does the nanoscale matter?," *Small*, vol. 2, no. 1, pp. 36-50, 2006.

[75] A. Rothschild and Y. Komem, "The effect of grain size on the sensitivity of nanocrystalline metal-oxide gas sensors," *Journal of Applied Physics*, vol. 95, no. 11, pp. 6374-6380, 2004.

[76] M.-A. Neouze and U. Schubert, "Surface modification and functionalization of metal and metal oxide nanoparticles by organic ligands," *Monatshefte für Chemie - Chemical Monthly*, vol. 139, no. 3, pp. 183-195, 2008.

[77] S. Iijima, "Helical microtubules of graphitic carbon," *Nature*, vol. 354, no. 6348, pp. 56-58, 1991.

[78] S. Iijima and T. Ichihashi, "Single-shell carbon nanotubes of 1-nm diameter," *Nature*, vol. 363, no. 6430, pp. 603-605, 1993.

[79] D. S. Bethune, C. H. Kiang, M. S. de Vries, G. Gorman, R. Savoy, J. Vazquez and R. Beyers, "Cobalt-catalysed growth of carbon nanotubes with single-atomic-layer walls," *Nature*, vol. 363, no. 6430, pp. 605-607, 1993.

[80] S. Rathinavel, K. Priyadharshini and D. Panda, "A review on carbon nanotube: An overview of synthesis, properties, functionalization, characterization, and the application," *Materials Science and Engineering: B*, vol. 268, no. pp., 2021.

[81] S. Reich, C. Thomsen and J. Maultzsch, *Carbon nanotubes: basic concepts and physical properties*, John Wiley & Sons, 2008.

[82] P. G. Collins and P. Avouris, "The electronic properties of carbon nanotubes," *Contemporary Concepts of Condensed Matter Science*, vol. 3, pp. 49-81, 2008.

[83] M. V. Kharlamova, "Advances in tailoring the electronic properties of single-walled carbon nanotubes," *Progress in Materials Science*, vol. 77, pp. 125-211, 2016.

[84] T. W. Odom, J.-L. Huang, P. Kim and C. M. Lieber, "Structure and electronic properties of carbon nanotubes," *The Journal of Physical Chemistry B*, vol. 104, no. 13, pp. 2794-2809, 2000.

[85] Y. Wang and G. Weng, in *Micromechanics Nanomechanics of Composite Solids*, 2018, pp. 123-156.

[86] T. Dürkop, S. A. Getty, E. Cobas and M. S. Fuhrer, "Extraordinary mobility in semiconducting carbon nanotubes," *Nano Letters*, vol. 4, no. 1, pp. 35-39, 2004.

[87] J. Fang, W. G. Vandenberghe and M. V. Fischetti, "Transistors performance in the sub-1 nm technology node based on one-dimensional nanomaterials," *International Conference on Simulation of Semiconductor Processes and Devices (SISPAD)*, pp. 84-87, Washington, DC, USA, 2015.

[88] M. F. Yu, O. Lourie, M. J. Dyer, K. Moloni, T. F. Kelly and R. S. Ruoff, "Strength and breaking mechanism of multiwalled carbon nanotubes under tensile load," *Science*, vol. 287, no. 5453, pp. 637-640, 2000.

[89] C. Chen, Y. Zhang, C. Chen and Y. Zhang, "Synthesis and purification of carbon nanotubes," *Nanowelded Carbon Nanotubes: From Field-Effect Transistors to Solar Microcells*, Springer Science & Business Media, 2009.

[90] D. S. Hecht, D. Thomas, L. Hu, C. Ladous, T. Lam, Y. Park, G. Irvin and P.

Drzaic, "Carbon‐nanotube film on plastic as transparent electrode for resistive touch screens," *Journal of the Society for information Display*, vol. 17, no. 11, pp. 941-946, 2009.

[91] S.-H. Park, P. J. King, R. Tian, C. S. Boland, J. Coelho, C. Zhang, P. McBean, N. McEvoy, M. P. Kremer and D. Daly, "High areal capacity battery electrodes enabled by segregated nanotube networks," *Nature Energy*, vol. 4, no. 7, pp. 560-567, 2019.

[92] M. H. Al-Saleh and U. Sundararaj, "Electromagnetic interference shielding mechanisms of CNT/polymer composites," *Carbon*, vol. 47, no. 7, pp. 1738-1746, 2009.

[93] D. Langley, G. Giusti, C. Mayousse, C. Celle, D. Bellet and J. P. Simonato, "Flexible transparent conductive materials based on silver nanowire networks: a review," *Nanotechnology*, vol. 24, no. 45, pp. 452001, 2013.

[94] J. H. Lee, P. Lee, D. Lee, S. S. Lee, S. H. Ko and design, "Large-scale synthesis and characterization of very long silver nanowires via successive multistep growth," *Crystal growth*, vol. 12, no. 11, pp. 5598-5605, 2012.

[95] S. Sorel, P. E. Lyons, S. De, J. C. Dickerson and J. N. Coleman, "The dependence of the optoelectrical properties of silver nanowire networks on nanowire length and diameter," *Nanotechnology*, vol. 23, no. 18, pp. 185201, 2012.

[96] T. Wang, K. Lu, Z. Xu, Z. Lin, H. Ning, T. Qiu, Z. Yang, H. Zheng, R. Yao and J. Peng, "Recent developments in flexible transparent electrode," *Crystals*, vol. 11, no. 5, pp. 511, 2021.

[97] S. B. Yang, B.-S. Kong, D.-H. Jung, Y.-K. Baek, C.-S. Han, S.-K. Oh and H.-T. Jung, "Recent advances in hybrids of carbon nanotube network films and nanomaterials for their potential applications as transparent conducting films," *Nanoscale*, vol. 3, no. 4, pp. 1361-1373, 2011.

[98] S. De, T. M. Higgins, P. E. Lyons, E. M. Doherty, P. N. Nirmalraj, W. J. Blau, J. J. Boland and J. N. Coleman, "Silver nanowire networks as flexible, transparent, conducting films: extremely high DC to optical conductivity ratios," *ACS Nano*, vol. 3, no. 7, pp. 1767-1774, 2009.

[99] S. De and J. N. Coleman, "The effects of percolation in nanostructured transparent conductors," *MRS Bulletin*, vol. 36, no. 10, pp. 774-781, 2011.

[100] M. R. Azani, A. Hassanpour and T. Torres, "Benefits, problems, and solutions of silver nanowire transparent conductive electrodes in indium tin oxide (ITO) ‐ free flexible solar cells," *Advanced Energy Materials*, vol. 10, no. 48, pp. 2002536, 2020.

[101] D. Tan, C. Jiang, Q. Li, S. Bi and J. Song, "Silver nanowire networks with preparations and applications: a review," *Journal of Materials Science: Materials in Electronics*, vol. 31, no. 18, pp. 15669-15696, 2020.

[102] Z. Cai, B. Liu, X. Zou and H.-M. Cheng, "Chemical vapor deposition growth and applications of two-dimensional materials and their heterostructures," *Chemical Reviews*, vol. 118, no. 13, pp. 6091-6133, 2018.

[103] S. Vishwanath, P. Dang and H. G. Xing, "Challenges and opportunities in molecular beam epitaxy growth of 2D crystals: An overview," *Molecular Beam Epitaxy (Second Edition)*, Elsevier, 2018.

[104] J. Chen, Q. Ma, X.-J. Wu, L. Li, J. Liu and H. Zhang, "Wet-chemical synthesis and applications of semiconductor nanomaterial-based epitaxial heterostructures," *Nano-Micro Letters*, vol. 11, no. pp. 1-28, 2019.

[105] M. A. Islam, P. Serles, B. Kumral, P. G. Demingos, T. Qureshi, A. Meiyazhagan, A. B. Puthirath, M. S. B. Abdullah, S. R. Faysal, P. M. Ajayan, D. Panesar, C. V. Singh and T. Filleter, "Exfoliation mechanisms of 2D materials and their applications," *Applied Physics Reviews*, vol. 9, no. 4, pp., 2022.

[106] Y. Hernandez, V. Nicolosi, M. Lotya, F. M. Blighe, Z. Sun, S. De, I. T. McGovern, B. Holland, M. Byrne, Y. K. Gun'Ko, J. J. Boland, P. Niraj, G. Duesberg, S. Krishnamurthy, R. Goodhue, J. Hutchison, V. Scardaci, A. C. Ferrari and J. N. Coleman, "High-yield production of graphene by liquid-phase exfoliation of graphite," *Nature Nanotechnology*, vol. 3, no. 9, pp. 563-568, 2008.

[107] Y. Yang, H. Hou, G. Zou, W. Shi, H. Shuai, J. Li and X. Ji, "Electrochemical exfoliation of graphene-like two-dimensional nanomaterials," *Nanoscale*, vol. 11, no. 1, pp. 16-33, 2018.

[108] J. N. Coleman, M. Lotya, A. O'Neill, S. D. Bergin, P. J. King, U. Khan, K. Young, A. Gaucher, S. De, R. J. Smith, I. V. Shvets, S. K. Arora, G. Stanton, H. Y. Kim, K. Lee, G. T. Kim, G. S. Duesberg, T. Hallam, J. J. Boland, J. J. Wang, J. F. Donegan, J. C. Grunlan, G. Moriarty, A. Shmeliov, R. J. Nicholls, J. M. Perkins, E. M. Grieveson, K. Theuwissen, D. W. McComb, P. D. Nellist and V. Nicolosi, "Two-dimensional nanosheets produced by liquid exfoliation of layered materials," *Science*, vol. 331, no. 6017, pp. 568-571, 2011.

[109] K. R. Paton, E. Varrla, C. Backes, R. J. Smith, U. Khan, A. O'Neill, C. Boland, M. Lotya, O. M. Istrate, P. King, T. Higgins, S. Barwich, P. May, P. Puczkarski, I. Ahmed, M. Moebius, H. Pettersson, E. Long, J. Coelho, S. E. O'Brien, E. K. McGuire, B. M. Sanchez, G. S. Duesberg, N. McEvoy, T. J. Pennycook, C. Downing, A. Crossley, V. Nicolosi and J. N. Coleman, "Scalable production of large quantities of defect-free few-layer graphene by shear exfoliation in liquids," *Nature Materials*, vol. 13, no. 6, pp. 624-630, 2014.

[110] S. A. Paniagua, P. J. Hotchkiss, S. C. Jones, S. R. Marder, A. Mudalige, F. S. Marrikar, J. E. Pemberton and N. R. Armstrong, "Phosphonic acid modification of indium− tin oxide electrodes: Combined XPS/UPS/contact

angle studies," *The Journal of Physical Chemistry C*, vol. 112, no. 21, pp. 7809-7817, 2008.

[111] I. A. Gilca, V. I. Popa and C. Crestini, "Obtaining lignin nanoparticles by sonication," *Ultrasonics sonochemistry*, vol. 23, pp. 369-375, 2015.

[112] L. Dumée, K. Sears, J. Schütz, N. Finn, M. Duke and S. Gray, "Influence of the sonication temperature on the debundling kinetics of carbon nanotubes in propan-2-ol," *Nanomaterials*, vol. 3, no. 1, pp. 70-85, 2013.

[113] J. A. Gallego-Juárez, K. F. Graff and M. Lucas, *Power ultrasonics: applications of high-intensity ultrasound*, Woodhead Publishing, 2023.

[114] Z. Li, R. J. Young, C. Backes, W. Zhao, X. Zhang, A. A. Zhukov, E. Tillotson, A. P. Conlan, F. Ding, S. J. Haigh, K. S. Novoselov and J. N. Coleman, "Mechanisms of liquid-phase exfoliation for the production of graphene," *ACS Nano*, vol. 14, no. 9, pp. 10976-10985, 2020.

[115] S. Biccai, S. Barwich, D. Boland, A. Harvey, D. Hanlon, N. McEvoy and J. N. Coleman, "Exfoliation of 2D materials by high shear mixing," *2D Materials*, vol. 6, no. 1, pp. 015008, 2018.

[116] J. B. Boland, Doctoral Dissertation, Trinity College Dublin, 2021.

[117] K. Synnatschke, J. van Dinter, A. Müller, D. Tiede, L. Spillecke, S. Shao, D. Kelly, J. Konecny, B. Konkena and M. McCrystall, "Exfoliablity, magnetism, energy storage and stability of metal thiophosphate nanosheets made in liquid medium," *2D Materials*, vol. 10, no. 2, pp. 024003, 2023.

[118] J. Kang, S. A. Wells, V. K. Sangwan, D. Lam, X. Liu, J. Luxa, Z. Sofer and M. C. Hersam, "Solution‐based processing of optoelectronically active indium selenide," *Advanced Materials*, vol. 30, no. 38, pp. 1802990, 2018.

[119] T. Carey, A. Alhourani, R. Tian, S. Seyedin, A. Arbab, J. Maughan, L. Šiller, D. Horvath, A. Kelly and H. Kaur, "Cyclic production of biocompatible few-layer graphene ink with in-line shear-mixing for inkjet-printed electrodes and

Li-ion energy storage," *npj 2D Materials Applications*, vol. 6, no. 1, pp. 3, 2022.

[120] G. Cunningham, M. Lotya, C. S. Cucinotta, S. Sanvito, S. D. Bergin, R. Menzel, M. S. Shaffer and J. N. Coleman, "Solvent exfoliation of transition metal dichalcogenides: dispersibility of exfoliated nanosheets varies only weakly between compounds," *ACS Nano*, vol. 6, no. 4, pp. 3468-3480, 2012.

[121] D. Hanlon, C. Backes, E. Doherty, C. S. Cucinotta, N. C. Berner, C. Boland, K. Lee, A. Harvey, P. Lynch, Z. Gholamvand, S. Zhang, K. Wang, G. Moynihan, A. Pokle, Q. M. Ramasse, N. McEvoy, W. J. Blau, J. Wang, G. Abellan, F. Hauke, A. Hirsch, S. Sanvito, D. D. O'Regan, G. S. Duesberg, V. Nicolosi and J. N. Coleman, "Liquid exfoliation of solvent-stabilized few-layer black phosphorus for applications beyond electronics," *Nature Communications*, vol. 6, no. pp. 8563, 2015.

[122] C. Backes, R. J. Smith, N. McEvoy, N. C. Berner, D. McCloskey, H. C. Nerl, A. O'Neill, P. J. King, T. Higgins, D. Hanlon, N. Scheuschner, J. Maultzsch, L. Houben, G. S. Duesberg, J. F. Donegan, V. Nicolosi and J. N. Coleman, "Edge and confinement effects allow in situ measurement of size and thickness of liquid-exfoliated nanosheets," *Nature Communications*, vol. 5, no. pp. 4576, 2014.

[123] C. Backes, B. M. Szydlowska, A. Harvey, S. Yuan, V. Vega-Mayoral, B. R. Davies, P. L. Zhao, D. Hanlon, E. J. Santos, M. I. Katsnelson, W. J. Blau, C. Gadermaier and J. N. Coleman, "Production of highly monolayer enriched dispersions of liquid-exfoliated nanosheets by liquid cascade centrifugation," *ACS Nano*, vol. 10, no. 1, pp. 1589-1601, 2016.

[124] C. Backes, D. Campi, B. M. Szydlowska, K. Synnatschke, E. Ojala, F. Rashvand, A. Harvey, A. Griffin, Z. Sofer, N. Marzari, J. N. Coleman and D. D. O'Regan, "Equipartition of energy defines the size-thickness relationship

in liquid-exfoliated nanosheets," *ACS Nano*, vol. 13, no. 6, pp. 7050-7061, 2019.

[125] G. Walker and W. Garrett, "Chemical exfoliation of vermiculite and the production of colloidal dispersions," *Science*, vol. 156, no. 3773, pp. 385-387, 1967.

[126] D. W. Murphy and G. W. Hull Jr, "Monodispersed tantalum disulfide and adsorption complexes with cations," *The Journal of Chemical Physics*, vol. 62, no. 3, pp. 973-978, 1975.

[127] C. Liu, O. Singh, P. Joensen, A. E. Curzon and R. F. Frindt, "X-ray and electron microscopy studies of single-layer TaS_2 and NbS_2," *Thin Solid Films*, vol. 113, no. 2, pp. 165-172, 1984.

[128] C. Vallés, C. Drummond, H. Saadaoui, C. A. Furtado, M. He, O. Roubeau, L. Ortolani, M. Monthioux and A. Pénicaud, "Solutions of negatively charged graphene sheets and ribbons," *Journal of the American Chemical Society*, vol. 130, no. 47, pp. 15802-15804, 2008.

[129] J. Zhou, Z. Lin, H. Ren, X. Duan, I. Shakir, Y. Huang and X. Duan, "Layered intercalation materials," *Advanced Materials*, vol. 33, no. 25, pp. e2004557, 2021.

[130] R. Yang, Y. Fan, L. Mei, H. S. Shin, D. Voiry, Q. Lu, J. Li and Z. Zeng, "Synthesis of atomically thin sheets by the intercalation-based exfoliation of layered materials," *Nature Synthesis*, vol. 2, no. 2, pp. 101-118, 2023.

[131] Y. Jung, Y. Zhou and J. J. Cha, "Intercalation in two-dimensional transition metal chalcogenides," *Inorganic Chemistry Frontiers*, vol. 3, no. 4, pp. 452-463, 2016.

[132] T. E. Weller, M. Ellerby, S. S. Saxena, R. P. Smith and N. T. Skipper, "Superconductivity in the intercalated graphite compounds C6Yb and C6Ca," *Nature Physics*, vol. 1, no. 1, pp. 39-41, 2005.

[133] C. Wang, Q. He, U. Halim, Y. Liu, E. Zhu, Z. Lin, H. Xiao, X. Duan, Z. Feng, R. Cheng, N. O. Weiss, G. Ye, Y. C. Huang, H. Wu, H. C. Cheng, I. Shakir, L. Liao, X. Chen, W. A. Goddard, III, Y. Huang and X. Duan, "Monolayer atomic crystal molecular superlattices," *Nature*, vol. 555, no. 7695, pp. 231-236, 2018.

[134] Z. Lin, Y. Liu, U. Halim, M. Ding, Y. Liu, Y. Wang, C. Jia, P. Chen, X. Duan, C. Wang, F. Song, M. Li, C. Wan, Y. Huang and X. Duan, "Solution-processable 2D semiconductors for high-performance large-area electronics," *Nature*, vol. 562, no. 7726, pp. 254-258, 2018.

[135] R. A. Wells, M. Zhang, T.-H. Chen, V. Boureau, M. Caretti, Y. Liu, J.-H. Yum, H. Johnson, S. Kinge, A. Radenovic and K. Sivula, "High performance semiconducting nanosheets via a scalable powder-based electrochemical exfoliation technique," *ACS Nano*, vol. 16, no. 4, pp. 5719-5730, 2022.

[136] P. Joensen, R. Frindt and S. R. J. M. r. b. Morrison, "Single-layer MoS_2," vol. 21, no. 4, pp. 457-461, 1986.

[137] H.-L. Tsai, J. Heising, J. L. Schindler, C. R. Kannewurf and M. G. Kanatzidis, "Exfoliated−restacked phase of WS_2," *Chemistry of Materials*, vol. 9, no. 4, pp. 879-882, 1997.

[138] J. Zheng, H. Zhang, S. Dong, Y. Liu, C. Tai Nai, H. Suk Shin, H. Young Jeong, B. Liu and K. Ping Loh, "High yield exfoliation of two-dimensional chalcogenides using sodium naphthalenide," *Nature Communications*, vol. 5, no. 1, pp. 2995, 2014.

[139] G. Eda, T. Fujita, H. Yamaguchi, D. Voiry, M. Chen and M. Chhowalla, "Coherent atomic and electronic heterostructures of single-layer MoS_2," *ACS Nano*, vol. 6, no. 8, pp. 7311-7317, 2012.

[140] W. Li, X. Qian and J. Li, "Phase transitions in 2D materials," *Nature Reviews Materials*, vol. 6, no. 9, pp. 829-846, 2021.

[141] J. S. Kang, M. Ke and Y. Hu, "Ionic intercalation in two-dimensional van der Waals materials: in situ characterization and electrochemical control of the anisotropic thermal conductivity of black phosphorus," *Nano Letters*, vol. 17, no. 3, pp. 1431-1438, 2017.

[142] F. Liu, C. Wang, X. Sui, M. A. Riaz, M. Xu, L. Wei and Y. Chen, "Synthesis of graphene materials by electrochemical exfoliation: Recent progress and future potential," *Carbon Energy*, vol. 1, no. 2, pp. 173-199, 2019.

[143] J. Peng, Y. Liu, H. Lv, Y. Li, Y. Lin, Y. Su, J. Wu, H. Liu, Y. Guo and Z. Zhuo, "Stoichiometric two-dimensional non-van der Waals $AgCrS_2$ with superionic behavior at room temperature," *Nature Chemistry*, vol. 13, no. 12, pp. 1235-1240, 2021.

[144] J. Peng, Y. Liu, X. Luo, J. Wu, Y. Lin, Y. Guo, J. Zhao, X. Wu, C. Wu and Y. Xie, "High phase purity of large‐sized 1T′‐MoS2 monolayers with 2D superconductivity," *Advanced Materials*, vol. 31, no. 19, pp. 1900568, 2019.

[145] J. Peng, J. Wu, X. Li, Y. Zhou, Z. Yu, Y. Guo, J. Wu, Y. Lin, Z. Li and X. Wu, "Very large-sized transition metal dichalcogenides monolayers from fast exfoliation by manual shaking," *Journal of the American Chemical Society*, vol. 139, no. 26, pp. 9019-9025, 2017.

[146] G. Eda, H. Yamaguchi, D. Voiry, T. Fujita, M. Chen and M. Chhowalla, "Photoluminescence from chemically exfoliated MoS_2," *Nano Letters*, vol. 11, no. 12, pp. 5111-5116, 2011.

[147] H. Bayhan and M. Bayhan, "A simple approach to determine the solar cell diode ideality factor under illumination," *Solar Energy*, vol. 85, no. 5, pp. 769-775, 2011.

[148] X. Zhang, J. Liu, E. Zhang, R. Pan, Y. Li, X. Wan, H. Wang and J. Zhang, "Atomically thin PdSeO(3) nanosheets: a promising 2D photocatalyst produced by quaternary ammonium intercalation and exfoliation," *Chemical*

Communications, vol. 56, no. 41, pp. 5504-5507, 2020.

[149] J. Li, P. Song, J. Zhao, K. Vaklinova, X. Zhao, Z. Li, Z. Qiu, Z. Wang, L. Lin, M. Zhao, T. S. Herng, Y. Zuo, W. Jonhson, W. Yu, X. Hai, P. Lyu, H. Xu, H. Yang, C. Chen, S. J. Pennycook, J. Ding, J. Teng, A. H. Castro Neto, K. S. Novoselov and J. Lu, "Printable two-dimensional superconducting monolayers," *Nature Materials*, vol. 20, no. 2, pp. 181-187, 2021.

[150] J. Li, C. Chen, S. Liu, J. Lu, W. P. Goh, H. Fang, Z. Qiu, B. Tian, Z. Chen and C. Yao, "Ultrafast electrochemical expansion of black phosphorus toward high-yield synthesis of few-layer phosphorene," *Chemistry of Materials*, vol. 30, no. 8, pp. 2742-2749, 2018.

[151] Z. Huang, H. Hou, Y. Zhang, C. Wang, X. Qiu and X. Ji, "Layer‐tunable phosphorene modulated by the cation insertion rate as a sodium-storage anode," *Advanced Materials*, vol. 29, no. 34, pp. 1702372, 2017.

[152] J. N. Coleman, "Liquid-phase exfoliation of nanotubes and graphene," *Advanced Functional Materials*, vol. 19, no. 23, pp. 3680-3695, 2009.

[153] C. M. Hansen, *Hansen solubility parameters: a user's handbook*, CRC press, 2007.

[154] S. P. Ogilvie, M. J. Large, G. Fratta, M. Meloni, R. Canton-Vitoria, N. Tagmatarchis, F. Massuyeau, C. P. Ewels, A. A. King and A. B. Dalton, "Considerations for spectroscopy of liquid-exfoliated 2D materials: emerging photoluminescence of N-methyl-2-pyrrolidone," *Scientific Reports*, vol. 7, no. 1, pp. 16706, 2017.

[155] F. I. Alzakia, W. Jonhson, J. Ding and S. C. Tan, "Ultrafast exfoliation of 2D materials by solvent activation and one-step fabrication of all-2D-material photodetectors by electrohydrodynamic printing," *ACS Applied Materials & Interfaces*, vol. 12, no. 25, pp. 28840-28851, 2020.

[156] A. Griffin, K. Nisi, J. Pepper, A. Harvey, B. M. Szydłowska, J. N. Coleman

and C. Backes, "Effect of surfactant choice and concentration on the dimensions and yield of liquid-phase-exfoliated nanosheets," *Chemistry of Materials*, vol. 32, no. 7, pp. 2852-2862, 2020.

[157] B. Derjaguin and L. Landau, "Theory of the stability of strongly charged lyophobic sols and of the adhesion of strongly charged particles in solutions of electrolytes," *Progress in Surface Science*, vol. 43, no. 1-4, pp. 30-59, 1993.

[158] E. J. W. Verwey, "Theory of the stability of lyophobic colloids," *The Journal of Physical Chemistry B*, vol. 51, no. 3, pp. 631-636, 1947.

[159] R. J. Smith, M. Lotya and J. N. Coleman, "The importance of repulsive potential barriers for the dispersion of graphene using surfactants," *New Journal of Physics*, vol. 12, no. 12, pp. 125008, 2010.

[160] A. Griffin, Trinity College Dublin. School of Physics. Discipline of Physics, 2021.

[161] J. N. Israelachvili, *Intermolecular and surface forces*, Academic press, 2011.

[162] R. Nagarajan and E. Ruckenstein, "Critical micelle concentration: a transition point for micellar size distribution: a statistical thermodynamical approach," *Journal of Colloid Interface Science*, vol. 60, no. 2, pp. 221-231, 1977.

[163] F. Bonaccorso, A. Bartolotta, J. N. Coleman and C. Backes, "2D-crystal-based functional inks," *Advanced Materials*, vol. 28, no. 29, pp. 6136-6166, 2016.

[164] J. Kang, J.-W. T. Seo, D. Alducin, A. Ponce, M. J. Yacaman and M. C. Hersam, "Thickness sorting of two-dimensional transition metal dichalcogenides via copolymer-assisted density gradient ultracentrifugation," *Nature Communications*, vol. 5, no. 1, pp. 5478, 2014.

[165] T. Sato and R. Ruch, *Stabilization of colloidal dispersions by polymer adsorption*, Dekker, 1980.

[166] D. Nuvoli, L. Valentini, V. Alzari, S. Scognamillo, S. B. Bon, M. Piccinini, J. Illescas and A. Mariani, "High concentration few-layer graphene sheets obtained by liquid phase exfoliation of graphite in ionic liquid," *Journal of Materials Chemistry*, vol. 21, no. 10, pp. 3428-3431, 2011.

[167] A. Pattammattel and C. V. Kumar, "Kitchen chemistry 101: multigram production of high quality biographene in a blender with edible proteins," *Advanced Functional Materials*, vol. 25, no. 45, pp. 7088-7098, 2015.

[168] S. Liu, E. X. Ding, A. G. Kelly, L. Doolan, C. Gabbett, H. Kaur, J. Munuera, T. Carey, J. Garcia and J. N. Coleman, "Solution processed, vertically stacked hetero-structured diodes based on liquid-exfoliated WS_2 nanosheets: from electrode-limited to bulk-limited behavior," *Nanoscale*, vol. 14, no. 42, pp. 15679-15690, 2022.

[169] S. Biccai, C. S. Boland, D. P. O'Driscoll, A. Harvey, C. Gabbett, D. R. O'Suilleabhain, A. J. Griffin, Z. Li, R. J. Young and J. N. Coleman, "Negative gauge factor piezoresistive composites based on polymers filled with MoS_2 nanosheets," *ACS Nano*, vol. 13, no. 6, pp. 6845-6855, 2019.

[170] G. Hu, J. Kang, L. W. T. Ng, X. Zhu, R. C. T. Howe, C. G. Jones, M. C. Hersam and T. Hasan, "Functional inks and printing of two-dimensional materials," *Chem Soc Rev*, vol. 47, no. 9, pp. 3265-3300, 2018.

[171] J. Kang, V. K. Sangwan, J. D. Wood and M. C. Hersam, "Solution-based processing of monodisperse two-dimensional nanomaterials," *Accounts of Chemical Research*, vol. 50, no. 4, pp. 943-951, 2017.

[172] M. K. Brakke, "Zonal separations by density-gradient centrifugation," *Archives of biochemistry and biophysics*, vol. 45, no. 2, pp. 275-290, 1953.

[173] G. Hu, J. Kang, L. W. T. Ng, X. Zhu, R. C. T. Howe, C. G. Jones, M. C. Hersam and T. Hasan, "Functional inks and printing of two-dimensional materials," *Chemical Society Reviews*, vol. 47, no. 9, pp. 3265-3300, 2018.

[174] F. Bonaccorso, T. Hasan, P. Tan, C. Sciascia, G. Privitera, G. Di Marco, P. Gucciardi and A. Ferrari, "Density gradient ultracentrifugation of nanotubes: Interplay of bundling and surfactants encapsulation," *The Journal of Physical Chemistry C*, vol. 114, no. 41, pp. 17267-17285, 2010.

[175] J. B. Ifft and J. Vinograd, "The buoyant behavior of bovine serum mercaptalbumin in salt solutions at equilibrium in the ultracentrifuge. II. net hydration, ion binding, and solvated molecular weight in various salt solutions1a, b," *The Journal of Physical Chemistry*, vol. 70, no. 9, pp. 2814-2822, 1966.

[176] A. A. Green and M. C. Hersam, "Solution phase production of graphene with controlled thickness via density differentiation," *Nano Letters*, vol. 9, no. 12, pp. 4031-4036, 2009.

[177] F. I. Alzakia, W. Sun, S. J. Pennycook and S. C. Tan, "Introducing normalized centrifugation for a more accurate thermodynamic analysis of molybdenum disulfide dispersions: A study on mixed solvents of alcohols and amines with water," *ACS applied materials interfaces*, vol. 12, no. 2, pp. 3096-3103, 2019.

[178] T. Svedberg and K. O. Pedersen, *The Ultracentrifuge*, Oxford: Clarendon Press, 1940.

[179] C. Backes, K. R. Paton, D. Hanlon, S. Yuan, M. I. Katsnelson, J. Houston, R. J. Smith, D. Mccloskey, J. F. Donegan and J. N. Coleman, "Spectroscopic metrics allow in situ measurement of mean size and thickness of liquid-exfoliated few-layer graphene nanosheets," *Nanoscale*, vol. 8, no. 7, pp. 4311-4323, 2016.

[180] J. Li, M. M. Naiini, S. Vaziri, M. C. Lemme and M. Östling, "Inkjet Printing of MoS_2," *Advanced Functional Materials*, vol. 24, no. 41, pp. 6524-6531, 2014.

[181] F. Torrisi, T. Hasan, W. Wu, Z. Sun, A. Lombardo, T. S. Kulmala, G. W. Hsieh, S. Jung, F. Bonaccorso, P. J. Paul, D. Chu and A. C. Ferrari, "Inkjet-printed graphene electronics," *ACS Nano*, vol. 6, no. 4, pp. 2992-3006, 2012.

[182] A. Capasso, A. E. Del Rio Castillo, H. Sun, A. Ansaldo, V. Pellegrini and F. Bonaccorso, "Ink-jet printing of graphene for flexible electronics: An environmentally-friendly approach," *Solid State Communications*, vol. 224, pp. 53-63, 2015.

[183] U. Bröckel, W. Meier and G. Wagner, *Product design and engineering: formulation of gels and pastes*, John Wiley & Sons, 2013.

[184] D. Kumar and S. N. Srivastava, "Wettability and surface energies of polymer substrates," *Surface Phenomena and Fine Particles in Water-Based Coatings and Printing Technology*, pp. 299-307, 1991.

[185] R. Good, "Contact angle, wetting, and adhesion: a critical review," *Journal of adhesion science technology*, vol. 6, no. 12, pp. 1269-1302, 1992.

[186] B. D. Chernomordik, A. R. Marshall, G. F. Pach, J. M. Luther and M. C. Beard, "Quantum dot solar cell fabrication protocols," *Chemistry of Materials*, vol. 29, no. 1, pp. 189-198, 2016.

[187] L. Li, X. Yu, Z. Lin, Z. Cai, Y. Cao, W. Kong, Z. Xiang, Z. Gu, X. Xing, X. Duan and Y. Song, "Interface capture effect printing atomic-thick two-dimensional semiconductor thin film," *Advanced Materials*, vol. 34, no. 49, pp. 2207392, 2022.

[188] G. Hu, T. Albrow-Owen, X. Jin, A. Ali, Y. Hu, R. C. T. Howe, K. Shehzad, Z. Yang, X. Zhu, R. I. Woodward, T. C. Wu, H. Jussila, J. B. Wu, P. Peng, P. H. Tan, Z. Sun, E. J. R. Kelleher, M. Zhang, Y. Xu and T. Hasan, "Black phosphorus ink formulation for inkjet printing of optoelectronics and photonics," *Nature Communications*, vol. 8, no. 1, pp. 278, 2017.

[189] A. G. Kelly, D. O'Suilleabhain, C. Gabbett and J. N. Coleman, "The

electrical conductivity of solution-processed nanosheet networks," *Nature Reviews Materials*, vol. 7, no. 3, pp. 217-234, 2021.

[190] K. Norrman, A. Ghanbari-Siahkali and N. B. Larsen, "6 Studies of spin-coated polymer films," *Annual Reports Section" C"(Physical Chemistry)*, vol. 101, no. pp. 174-201, 2005.

[191] D. Meyerhofer, "Characteristics of resist films produced by spinning," *Journal of Applied Physics*, vol. 49, no. 7, pp. 3993-3997, 1978.

[192] S. Y. Jeong, S. H. Kim, J. T. Han, H. J. Jeong, S. Y. Jeong and G.-W. Lee, "Highly concentrated and conductive reduced graphene oxide nanosheets by monovalent cation-π interaction: Toward printed electronics," *Advanced Functional Materials*, vol. 22, no. 15, pp. 3307-3314, 2012.

[193] A. C. M. Moraes, W. J. Hyun, J. W. T. Seo, J. R. Downing, J. M. Lim and M. C. Hersam, "Ion-conductive, viscosity-tunable hexagonal boron nitride nanosheet inks," *Advanced Functional Materials*, vol. 29, no. 39, pp., 2019.

[194] J. Huang, S. E, J. Li, F. Jia, Q. Ma, L. Hua and Z. Lu, "Ball-milling exfoliation of hexagonal boron nitride in viscous hydroxyethyl cellulose for producing nanosheet films as thermal interface materials," *ACS Applied Nano Materials*, vol. 4, no. 12, pp. 13167-13175, 2021.

[195] K. Matsuba, C. Wang, K. Saruwatari, Y. Uesusuki, K. Akatsuka, M. Osada, Y. Ebina, R. Ma and T. Sasaki, "Neat monolayer tiling of molecularly thin two-dimensional materials in 1 min," *Science Advances*, vol. 3, no. 6, pp. e1700414, 2017.

[196] H. Yano, N. Sakai, Y. Ebina, R. Ma, M. Osada, K. Fujimoto and T. Sasaki, "Construction of multilayer films and superlattice-and mosaic-like heterostructures of 2D metal oxide nanosheets via a facile spin-coating process," *ACS Applied material Interfaces*, vol. 13, no. 36, pp. 43258-43265, 2021.

[197] W. Deng, X. Zhang, L. Wang, J. Wang, Q. Shang, X. Zhang, L. Huang and J. Jie, "Wafer-scale precise patterning of organic single-crystal nanowire arrays via a photolithography-assisted spin-coating method," *Advanced Material*, vol. 27, no. 45, pp. 7305-7312, 2015.

[198] F. Aziz and A. F. Ismail, "Spray coating methods for polymer solar cells fabrication: A review," *Materials Science in Semiconductor Processing*, vol. 39, pp. 416-425, 2015.

[199] A. G. Kelly, T. Hallam, C. Backes, A. Harvey, A. S. Esmaeily, I. Godwin, J. Coelho, V. Nicolosi, J. Lauth, A. Kulkarni, S. Kinge, L. D. Siebbeles, G. S. Duesberg and J. N. Coleman, "All-printed thin-film transistors from networks of liquid-exfoliated nanosheets," *Science*, vol. 356, no. 6333, pp. 69-73, 2017.

[200] T. Carey, C. Jones, F. Le Moal, D. Deganello and F. Torrisi, "Spray-coating thin films on three-dimensional surfaces for a semitransparent capacitive-touch device," *ACS Applied Materials & Interfaces*, vol. 10, no. 23, pp. 19948-19956, 2018.

[201] H. Klauk, G. Schmid, W. Radlik, W. Weber, L. Zhou, C. D. Sheraw, J. A. Nichols and T. N. Jackson, "Contact resistance in organic thin film transistors," *Solid-State Electronics*, vol. 47, no. 2, pp. 297-301, 2003.

[202] J. Singh, *Semiconductor devices: basic principles*, John Wiley & Sons, 2007.

[203] S. Akhavan, A. Ruocco, G. Soavi, A. T. Najafabadi, S. Mignuzzi, S. Doukas, A. Cadore, Y. Samad, L. Lombardi and K. Dimos, "Graphene-black phosphorus printed photodetectors," *2D Materials*, vol. 10, no. 3, pp. 035015, 2023.

[204] F. Staub, I. Anusca, D. C. Lupascu, U. Rau and T. Kirchartz, "Effect of reabsorption and photon recycling on photoluminescence spectra and transients in lead-halide perovskite crystals," *Journal of Physics: Materials*,

vol. 3, no. 2, pp., 2020.

[205] F.-C. Chiu, "A review on conduction mechanisms in dielectric films," *Advances in Materials Science and Engineering*, vol. 2014, pp. 1-18, 2014.

[206] J. A. Rohr, D. Moia, S. A. Haque, T. Kirchartz and J. Nelson, "Exploring the validity and limitations of the Mott-Gurney law for charge-carrier mobility determination of semiconducting thin-films," *Journal of Physics: Condensed Matter*, vol. 30, no. 10, pp. 105901, 2018.

[207] A. Rose, "Space-charge-limited currents in solids," *Physical Review*, vol. 97, no. 6, pp. 1538-1544, 1955.

[208] S. M. Sze, Y. Li and K. K. Ng, *Physics of semiconductor devices*, John wiley & sons., 2021.

[209] G. Konstantatos, M. Badioli, L. Gaudreau, J. Osmond, M. Bernechea, F. P. G. de Arquer, F. Gatti and F. H. L. Koppens, "Hybrid graphene–quantum dot phototransistors with ultrahigh gain," *Nature Nanotechnology*, vol. 7, no. 6, pp. 363-368, 2012.

[210] F. I. Alzakia, B. Tang, S. J. Pennycook and S. C. Tan, "Engineering the photoresponse of liquid-exfoliated 2D materials by size selection and controlled mixing for an ultrasensitive and ultraresponsive photodetector," *Materials Horizons*, vol. 7, no. 12, pp. 3325-3338, 2020.

[211] A. Grillo and A. Di Bartolomeo, "A current–voltage model for double Schottky barrier devices," *Advanced Electronic Materials*, vol. 7, no. 2, pp. 2000979, 2020.

[212] Z. Wang, W. Zang, Y. Shi, X. Zhu, G. Rao, Y. Wang, J. Chu, C. Gong, X. Gao, H. Sun, S. Huanglong, D. Yang and P. Wangyang, "Extraction and analysis of the characteristic parameters in back-to-back bonnected asymmetric Schottky diode," *physica status solidi (a)*, vol. 217, no. 8, pp. 1901018, 2020.

[213] J. K. Hite, T. J. Anderson, M. A. Mastro, L. E. Luna, J. C. Gallagher, R. L. Myers-Ward, K. D. Hobart and C. R. Eddy, "Effect of surface morphology on diode performance in vertical GaN Schottky diodes," *ECS Journal of Solid State Science Technology*, vol. 6, no. 11, pp. S3103, 2017.

[214] Z. Zheng, X. Zu, Y. Zhang and W. Zhou, "Rational design of type-II nano-heterojunctions for nanoscale optoelectronics," *Materials Today Physics*, vol. 15, no. pp. 100262, 2020.

[215] Z. Sun and H. Chang, "Graphene and graphene-like two-dimensional materials in photodetection: mechanisms and methodology," *ACS Nano*, vol. 8, no. 5, pp. 4133-4156, 2014.

[216] F. H. L. Koppens, T. Mueller, P. Avouris, A. C. Ferrari, M. S. Vitiello and M. Polini, "Photodetectors based on graphene, other two-dimensional materials and hybrid systems," *Nature Nanotechnology*, vol. 9, no. 10, pp. 780-793, 2014.

[217] F. I. Alzakia and S. C. Tan, "Liquid-exfoliated 2D materials for optoelectronic applications," *Advanced Science*, vol. 8, no. 11, pp. 2003864, 2021.

[218] Z. Lin, Y. Huang and X. Duan, "Van der Waals thin-film electronics," *Nature Electronics*, vol. 2, no. 9, pp. 378-388, 2019.

[219] T. Carey, O. Cassidy, K. Synnatschke, E. Caffrey, J. Garcia, S. Liu, H. Kaur, A. G. Kelly, J. Munuera, C. Gabbett, D. O'Suilleabhain and J. N. Coleman, "High-mobility flexible transistors with low-temperature solution-processed tungsten dichalcogenides," *ACS Nano*, vol. 17, no. 3, pp. 2912-2922, 2023.

[220] C. P. Gabbett, Trinity College Dublin. School of Physics. Discipline of Physics, 2021.

[221] C. Gabbett, C. S. Boland, A. Harvey, V. Vega-Mayoral, R. J. Young and J. N. Coleman, "The effect of network formation on the mechanical properties of

1D: 2D nano: nano composites," *Chemistry of Materials*, vol. 30, no. 15, pp. 5245-5255, 2018.

[222] G. Cunningham, U. Khan, C. Backes, D. Hanlon, D. McCloskey, J. F. Donegan and J. N. Coleman, "Photoconductivity of solution-processed MoS_2 films," *Journal of Materials Chemistry C*, vol. 1, no. 41, pp. 6899, 2013.

[223] G. Cunningham, D. Hanlon, N. McEvoy, G. S. Duesberg and J. N. Coleman, "Large variations in both dark- and photoconductivity in nanosheet networks as nanomaterial is varied from MoS_2 to WTe_2," *Nanoscale*, vol. 7, no. 1, pp. 198-208, 2015.

[224] D. J. Finn, M. Lotya, G. Cunningham, R. J. Smith, D. McCloskey, J. F. Donegan and J. N. Coleman, "Inkjet deposition of liquid-exfoliated graphene and MoS2 nanosheets for printed device applications," *Journal of Materials Chemistry C*, vol. 2, no. 5, pp. 925-932, 2014.

[225] D. McManus, S. Vranic, F. Withers, V. Sanchez-Romaguera, M. Macucci, H. Yang, R. Sorrentino, K. Parvez, S. K. Son, G. Iannaccone, K. Kostarelos, G. Fiori and C. Casiraghi, "Water-based and biocompatible 2D crystal inks for all-inkjet-printed heterostructures," *Nature Nanotechnology*, vol. 12, no. 4, pp. 343-350, 2017.

[226] D. McManus, A. Dal Santo, P. B. Selvasundaram, R. Krupke, A. Libassi and C. Casiraghi, "Photocurrent study of all-printed photodetectors on paper made of different transition metal dichalcogenide nanosheets," *Flexible and Printed Electronics*, vol. 3, no. 3, pp. 034005, 2018.

[227] H. Lee, M. Koo, C. Park, M. Patel, H. Han, T. H. Park, P. Kumar, W.-G. Koh and C. Park, "Zwitterion-assisted transition metal dichalcogenide nanosheets for scalable and biocompatible inkjet printing," *Nano Research*, vol. 13, no. 10, pp. 2726-2734, 2020.

[228] B. L. Chauhan, S. A. Bhakhar, P. M. Pataniya, S. U. Gupta, G. K. Solanki, V.

M. Pathak and V. Patel, "Liquid-phase exfoliation of WSe_2 nanosheets for ITO/WSe_2 photodetector," *Journal of Materials Science: Materials in Electronics*, vol. 33, no. 13, pp. 10314-10322, 2022.

[229] Y. Li, X. Feng, M. Sivan, J. F. Leong, B. Tang, X. Wang, J. N. Tey, J. Wei, K. W. Ang and A. V. Y. Thean, "Aerosol jet printed WSe_2 crossbar architecture device on kapton with dual functionality as resistive memory and photosensor for flexible system integration," *IEEE Sensors Journal*, vol. 20, no. 9, pp. 4653-4659, 2020.

[230] D. B. Velusamy, R. H. Kim, S. Cha, J. Huh, R. Khazaeinezhad, S. H. Kassani, G. Song, S. M. Cho, S. H. Cho, I. Hwang, J. Lee, K. Oh, H. Choi and C. Park, "Flexible transition metal dichalcogenide nanosheets for band-selective photodetection," *Nature Communications*, vol. 6, no. 1, pp. 8063, 2015.

[231] O. Song, D. Rhee, J. Kim, Y. Jeon, V. Mazánek, A. Söll, Y. A. Kwon, J. H. Cho, Y.-H. Kim, Z. Sofer and J. Kang, "All inkjet-printed electronics based on electrochemically exfoliated two-dimensional metal, semiconductor, and dielectric," *npj 2D Materials and Applications*, vol. 6, no. 1, pp., 2022.

[232] D. Rhee, B. Han, M. Jung, J. Kim, O. Song and J. Kang, "Hierarchical nanoscale structuring of solution-processed 2D van der Waals networks for wafer-scale, stretchable electronics," *ACS Applied Materials & Interfaces*, vol. 14, no. 51, pp. 57153-57164, 2022.

[233] L. Kuo, V. K. Sangwan, S. V. Rangnekar, T. C. Chu, D. Lam, Z. Zhu, L. J. Richter, R. Li, B. M. Szydlowska, J. R. Downing, B. J. Luijten, L. J. Lauhon and M. C. Hersam, "All-printed ultrahigh-responsivity MoS_2 nanosheet photodetectors enabled by megasonic exfoliation," *Advanced Materials*, vol. 34, no. 34, pp. 2203772, 2022.

[234] J. Kim, D. Rhee, O. Song, M. Kim, Y. H. Kwon, D. U. Lim, I. S. Kim, V.

Mazánek, L. Valdman, Z. Sofer, J. H. Cho and J. Kang, "All-solution-processed van der Waals heterostructures for wafer-scale electronics," *Advanced Materials*, vol. 34, no. 12, pp. 2106110, 2022.

[235] M. Farbod, R. Taheri and A. Kosarian, "High performance photoresponsivity and high frequency of phosphorene/metal heterojunction as Schottky photodiode rectifier," *Applied Materials Today*, vol. 24, pp., 2021.

[236] R. K. Chowdhury, R. Maiti, A. Ghorai, A. Midya and S. K. Ray, "Novel silicon compatible p-WS_2 2D/3D heterojunction devices exhibiting broadband photoresponse and superior detectivity," *Nanoscale*, vol. 8, no. 27, pp. 13429-13436, 2016.

[237] X. Geng, Y. Yu, X. Zhou, C. Wang, K. Xu, Y. Zhang, C. Wu, L. Wang, Y. Jiang and Q. Yang, "Design and construction of ultra-thin $MoSe_2$ nanosheet-based heterojunction for high-speed and low-noise photodetection," *Nano Research*, vol. 9, no. 9, pp. 2641-2651, 2016.

[238] S. Mukherjee, S. Biswas, S. Das and S. K. Ray, "Solution-processed, hybrid 2D/3D MoS_2/Si heterostructures with superior junction characteristics," *Nanotechnology*, vol. 28, no. 13, pp. 135203, 2017.

[239] A. B. Patel, P. Chauhan, K. Patel, C. K. Sumesh, S. Narayan, K. D. Patel, G. K. Solanki, V. M. Pathak, P. K. Jha and V. Patel, "Solution-processed uniform $MoSe_2$–WSe_2 heterojunction thin film on silicon substrate for superior and tunable photodetection," *ACS Sustainable Chemistry & Engineering*, vol. 8, no. 12, pp. 4809-4817, 2020.

[240] M. Patel, P. M. Pataniya, V. Patel, C. K. Sumesh and D. J. Late, "Large area, broadband and highly sensitive photodetector based on ZnO-WS_2/Si heterojunction," *Solar Energy*, vol. 206, pp. 974-982, 2020.

[241] S. Jana, S. Ray and S. Mukherjee, "Colloidal molybdenum diselenide nanocrystals for tunable, broadband, and mixed-dimensional photodetectors,"

ACS Applied Nano Materials, vol. 4, no. 2, pp. 1877-1885, 2021.

[242] K. H. Modi, P. M. Pataniya, V. Patel and C. K. Sumesh, "Microwave assisted synthesis of SnS nanosheets for fabrication of large area SnS/Si heterojunction," *Solar Energy*, vol. 221, pp. 412-417, 2021.

[243] M. Patel, P. M. Pataniya, D. J. Late and C. K. Sumesh, "Plasmon-enhanced photoresponse in Ag-WS_2/Si heterojunction," *Applied Surface Science*, vol. 538, pp. 148121, 2021.

[244] S. Kapatel and C. K. Sumesh, "Atomically thin WSe_2 nanosheets for fabrication of high-performance p-Si/WSe_2 heterostructure," *Optical Materials*, vol. 129, pp. 112537, 2022.

[245] P. M. Pataniya, C. K. Zankat, M. Tannarana, A. Patel, S. Narayan, G. K. Solanki, K. D. Patel, P. K. Jha and V. M. Pathak, "Photovoltaic activity of WSe_2/Si hetero junction," *Materials Research Bulletin*, vol. 120, pp. 110602, 2019.

[246] C. Z. Li, C. Y. Chang, Y. Zang, H. X. Ju, C. C. Chueh, P. W. Liang, N. Cho, D. S. Ginger and A. K. Y. Jen, "Suppressed charge recombination in inverted organic photovoltaics via enhanced charge extraction by using a conductive fullerene electron transport layer," *Advanced Materials*, vol. 26, no. 36, pp. 6262-6267, 2014.

[247] K. Wang, C. Liu, T. Meng, C. Yi and X. Gong, "Inverted organic photovoltaic cells," *Chemical Society Reviews*, vol. 45, no. 10, pp. 2937-2975, 2016.

[248] R. Schmechel and H. Von Seggern, "Electronic traps in organic transport layers," *physica status solidi (a)*, vol. 201, no. 6, pp. 1215-1235, 2004.

[249] S. Lattante, "Electron and hole transport layers: their use in inverted bulk heterojunction polymer solar cells," *Electronics*, vol. 3, no. 1, pp. 132-164, 2014.

[250] C. Liu, C. Xiao and W. Li, "Zinc oxide nanoparticles as electron transporting

interlayer in organic solar cells," *Journal of Materials Chemistry C*, vol. 9, no. 40, pp. 14093-14114, 2021.

[251] T. Zhang, Q. He, J. Yu, A. Chen, Z. Zhang and J. Pan, "Recent progress in improving strategies of inorganic electron transport layers for perovskite solar cells," *Nano Energy*, vol. 104, pp. 107918, 2022.

[252] S. Bellani, A. Bartolotta, A. Agresti, G. Calogero, G. Grancini, A. Di Carlo, E. Kymakis and F. Bonaccorso, "Solution-processed two-dimensional materials for next-generation photovoltaics," *Chemical Society Reviews*, vol. 50, no. 21, pp. 11870-11965, 2021.

[253] N. Balis, E. Stratakis and E. Kymakis, "Graphene and transition metal dichalcogenide nanosheets as charge transport layers for solution processed solar cells," *Materials Today*, vol. 19, no. 10, pp. 580-594, 2016.

[254] Q. V. Le, J. Y. Choi and S. Y. Kim, "Recent advances in the application of two-dimensional materials as charge transport layers in organic and perovskite solar cells," *Flatchem*, vol. 2, pp. 54-66, 2017.

[255] B. Adilbekova, Y. Lin, E. Yengel, H. Faber, G. Harrison, Y. Firdaus, A. El-Labban, D. H. Anjum, V. Tung and T. D. Anthopoulos, "Liquid phase exfoliation of MoS_2 and WS_2 in aqueous ammonia and their application in highly efficient organic solar cells," *Journal of Materials Chemistry C*, vol. 8, no. 15, pp. 5259-5264, 2020.

[256] D. Jariwala, A. R. Davoyan, J. Wong and H. A. Atwater, "Van der Waals materials for atomically-thin photovoltaics: Promise and outlook," *ACS Photonics*, vol. 4, no. 12, pp. 2962-2970, 2017.

[257] N. Tabet, F. El-Mellouhi, F. H. Alharbi and M. I. Hossain, "Design optimization of solar cell with molybdenum sulfide as light absorber," *Journal of Photonics for Energy*, vol. 8, no. 02, pp. 1, 2018.

[258] B. Ozdemir and V. Barone, "Thickness dependence of solar cell efficiency in

transition metal dichalcogenides MX_2 (M: Mo, W; X: S, Se, Te)," *Solar Energy Materials and Solar Cells*, vol. 212, pp. 110557, 2020.

[259] R. Austin, Y. R. Farah, T. Sayer, B. M. Luther, A. Montoya-Castillo, A. T. Krummel and J. B. Sambur, "Hot carrier extraction from 2D semiconductor photoelectrodes," *Proceedings of the National Academy of Sciences*, vol. 120, no. 15, pp. e2220333120, 2023.

[260] F. Barati, M. Grossnickle, S. Su, R. K. Lake, V. Aji and N. M. Gabor, "Hot carrier-enhanced interlayer electron-hole pair multiplication in 2D semiconductor heterostructure photocells," *Nature Nanotechnology*, vol. 12, no. 12, pp. 1134-1139, 2017.

[261] K. K. Paul, J.-H. Kim and Y. H. Lee, "Hot carrier photovoltaics in van der Waals heterostructures," *Nature Reviews Physics*, vol. 3, no. 3, pp. 178-192, 2021.

[262] S. Das, D. Pandey, J. Thomas and T. Roy, "The role of graphene and other 2D materials in solar photovoltaics," *Advanced Materials*, vol. 31, no. 1, pp. 1802722, 2019.

[263] T. Kirchartz and U. Rau, "What makes a good solar cell?," *Advanced Energy Materials*, vol. 8, no. 28, pp. 1703385, 2018.

[264] E. Fortin and W. M. Sears, "Photovoltaic effect and optical absorption in MoS2," *Journal of Physics Chemistry of Solids*, vol. 43, no. 9, pp. 881-884, 1982.

[265] A. Jäger-Waldau, M. C. Lux-Steiner and E. Bucher, "MoS_2, $MoSe_2$, WS_2 and WSe_2 thin films for photovoltaics," *Solid State Phenomena*, vol. 37, no. pp. 479-484, 1994.

[266] Y. Zhao, L. Yu and M. Sun, "Recent progress in emerging 2D layered materials for organic solar cells," *Solar Energy*, vol. 218, pp. 621-638, 2021.

[267] G. Kakavelakis, A. E. Del Rio Castillo, V. Pellegrini, A. Ansaldo, P.

Tzourmpakis, R. Brescia, M. Prato, E. Stratakis, E. Kymakis and F. Bonaccorso, "Size-tuning of WSe_2 flakes for high efficiency inverted organic solar cells," *ACS Nano*, vol. 11, no. 4, pp. 3517-3531, 2017.

[268] R. Ahmad, R. Srivastava, S. Yadav, S. Chand and S. Sapra, "Functionalized 2D-MoS2-incorporated polymer ternary solar cells: Role of nanosheet-induced long-range ordering of polymer chains on charge transport," *ACS applied materials interfaces*, vol. 9, no. 39, pp. 34111-34121, 2017.

[269] S. K. Lee, D. Chu, D. Y. Song, S. W. Pak and E. K. Kim, "Electrical and photovoltaic properties of residue-free MoS_2 thin films by liquid exfoliation method," *Nanotechnology*, vol. 28, no. 19, pp. 195703, 2017.

[270] S. K. Lee, D. Chu, J. Yoo and E. K. Kim, "Formation of transition metal dichalcogenides thin films with liquid phase exfoliation technique and photovoltaic applications," *Solar Energy Materials and Solar Cells*, vol. 184, no. pp. 9-14, 2018.

[271] M. Patel, P. M. Pataniya and C. K. Sumesh, "Enhanced photoresponse by plasmon resonance in Ni-WS_2/Si photodiode," *Materials Research Bulletin*, vol. 145, no. pp., 2022.

[272] J. Ye, X. Li, J. Zhao, X. Mei and Q. Li, "A facile way to fabricate high-performance solution-processed n-MoS_2/p-MoS_2 bilayer photodetectors," *Nanoscale Research Letters*, vol. 10, no. 1, pp. 454, 2015.

[273] S. Barwich, U. Khan and J. N. Coleman, "A technique to pretreat graphite which allows the rapid dispersion of defect-free graphene in solvents at high concentration," *The Journal of Physical Chemistry C*, vol. 117, no. 37, pp. 19212-19218, 2013.

[274] L. Ueberricke, J. N. Coleman and C. Backes, "Robustness of size selection and spectroscopic size, thickness and monolayer metrics of liquid-exfoliated WS_2," *Physica Status Solidi (b)*, vol. 254, no. 11, pp. 1700443, 2017.

[275] C. Backes, T. M. Higgins, A. Kelly, C. Boland, A. Harvey, D. Hanlon and J. N. Coleman, "Guidelines for exfoliation, characterization and processing of layered materials produced by liquid exfoliation," *Chemistry of Materials*, vol. 29, no. 1, pp. 243-255, 2016.

[276] B. M. Tissue, "Ultraviolet and visible absorption spectroscopy," *Characterization of Materials*, John Wiley & Sons, 2002.

[277] D. F. Swinehart, "The Beer-Lambert law," *Journal of Chemical Education*, vol. 39, no. 7, pp. 333, 1962.

[278] C. V. Raman, "A new radiation," *Indian Journal of physics*, vol. 2, no. pp. 387-398, 1928.

[279] K. J. Ember, M. A. Hoeve, S. L. McAughtrie, M. S. Bergholt, B. J. Dwyer, M. M. Stevens, K. Faulds, S. J. Forbes and C. Campbell, "Raman spectroscopy and regenerative medicine: A review," *NPJ Regenerative medicine*, vol. 2, no. 1, pp. 12, 2017.

[280] R. S. Das and Y. K. Agrawal, "Raman spectroscopy: Recent advancements, techniques and applications," *Vibrational Spectroscopy*, vol. 57, no. 2, pp. 163-176, 2011.

[281] X. L. Li, W. P. Han, J. B. Wu, X. F. Qiao, J. Zhang and P. H. Tan, "Layer‐number dependent optical properties of 2D materials and their application for thickness determination," *Advanced Functional Materials*, vol. 27, no. 19, pp. 1604468, 2017.

[282] M. W. Iqbal, K. Shahzad, R. Akbar and G. Hussain, "A review on Raman finger prints of doping and strain effect in TMDCs," *Microelectronic Engineering*, vol. 219, no. pp. 111152, 2020.

[283] X. Cong, X.-L. Liu, M.-L. Lin and P.-H. Tan, "Application of Raman spectroscopy to probe fundamental properties of two-dimensional materials," *npj 2D Materials pplications*, vol. 4, no. 1, pp. 13, 2020.

[284] G. Binnig, C. F. Quate and C. Gerber, "Atomic force microscope," *Physical Review Letters*, vol. 56, no. 9, pp. 930, 1986.

[285] Y. Seo and W. Jhe, "Atomic force microscopy and spectroscopy," *Reports on Progress in Physics*, vol. 71, no. 1, pp., 2008.

[286] M. S. Dresselhaus, "Intercalation in layered materials," *MRS Bulletin*, vol. 12, no. 3, pp. 24-28, 2013.

[287] Y. Zhao and G. Ouyang, "Thickness-dependent photoelectric properties of MoS2/Si heterostructure solar cells," *Scientific Reports*, vol. 9, no. 1, pp. 17381, 2019.

[288] C. Backes, K. R. Paton, D. Hanlon, S. Yuan, M. I. Katsnelson, J. Houston, R. J. Smith, D. McCloskey, J. F. Donegan and J. N. Coleman, "Spectroscopic metrics allow in situ measurement of mean size and thickness of liquid-exfoliated few-layer graphene nanosheets," *Nanoscale*, vol. 8, no. 7, pp. 4311-4323, 2016.

[289] A. Harvey, C. Backes, Z. Gholamvand, D. Hanlon, D. McAteer, H. C. Nerl, E. McGuire, A. Seral-Ascaso, Q. M. Ramasse and N. McEvoy, "Preparation of gallium sulfide nanosheets by liquid exfoliation and their application as hydrogen evolution catalysts," *Chemistry of Materials*, vol. 27, no. 9, pp. 3483-3493, 2015.

[290] F. J. Giessibl, "Advances in atomic force microscopy," *Reviews of Modern Physics*, vol. 75, no. 3, pp. 949, 2003.

[291] B. J. Inkson, in *Materials characterization using nondestructive evaluation (NDE) methods*, Elsevier, 2016.

[292] P. J. Goodhew, J. Humphreys and R. Beanland, *Electron microscopy and analysis*, CRC press, 2000.

[293] J. C. Spence, *High-resolution electron microscopy*, OUP Oxford, 2013.

[294] J. Melngailis, "Focused ion beam technology and applications," *Journal of*

Vacuum Science & Technology B: Microelectronics Processing and Phenomena, vol. 5, no. 2, pp. 469-495, 1987.

[295] S. Reyntjens and R. Puers, "A review of focused ion beam applications in microsystem technology," *Journal of Micromechanics Microengineering*, vol. 11, no. 4, pp. 287, 2001.

[296] B. Geffroy, P. Le Roy and C. Prat, "Organic light‐emitting diode (OLED) technology: materials, devices and display technologies," *Polymer International*, vol. 55, no. 6, pp. 572-582, 2006.

[297] V. Wood and V. Bulović, "Colloidal quantum dot light-emitting devices," *Nano reviews*, vol. 1, no. 1, pp. 5202, 2010.

[298] L. Etgar, P. Gao, Z. Xue, Q. Peng, A. K. Chandiran, B. Liu, M. K. Nazeeruddin and M. Gratzel, "Mesoscopic $CH_3NH_3PbI_3/TiO_2$ heterojunction solar cells," *Journal of the American Chemical Society*, vol. 134, no. 42, pp. 17396-17399, 2012.

[299] A. G. Kelly, D. Finn, A. Harvey, T. Hallam and J. N. Coleman, "All-Printed Capacitors from Graphene-BN-Graphene Nanosheet Heterostructures," *Applied Physics Letters*, vol. 109, no. 2, pp. 023107, 2016.

[300] Y. Nalawade, J. Pepper, A. Harvey, A. Griffin, D. Caffrey, A. G. Kelly and J. N. Coleman, "All-printed dielectric capacitors from high-permittivity, liquid-exfoliated BiOCl nanosheets," *ACS Applied Electronic Materials*, vol. 2, no. 10, pp. 3233-3241, 2020.

[301] A. A. Bessonov, M. N. Kirikova, D. I. Petukhov, M. Allen, T. Ryhänen and M. J. A. Bailey, "Layered memristive and memcapacitive switches for printable electronics," *Nature Materials*, vol. 14, no. 2, pp. 199-204, 2015.

[302] X. Yu, M. S. Prévot and K. Sivula, "Multiflake thin film electronic devices of solution processed 2D MoS_2 Enabled by sonopolymer assisted exfoliation and surface modification," *Chemistry of Materials*, vol. 26, no. 20, pp. 5892-

5899, 2014.

[303] W. Zhao, Z. Ghorannevis, L. Chu, M. Toh, C. Kloc, P.-H. Tan and G. Eda, "Evolution of electronic structure in atomically thin sheets of WS_2 and WSe_2," *ACS Nano*, vol. 7, no. 1, pp. 791-797, 2013.

[304] J. Kang, S. Tongay, J. Zhou, J. Li and J. Wu, "Band offsets and heterostructures of two-dimensional semiconductors," *Applied Physics Letters*, vol. 102, no. 1, pp. 012111, 2013.

[305] C. Backes, R. J. Smith, N. McEvoy, N. C. Berner, D. McCloskey, H. C. Nerl, A. O'Neill, P. J. King, T. Higgins, D. Hanlon, N. Scheuschner, J. Maultzsch, L. Houben, G. S. Duesberg, J. F. Donegan, V. Nicolosi and J. N. Coleman, "Edge and confinement effects allow in situ measurement of size and thickness of liquid-exfoliated nanosheets," *Nat. Commun.*, vol. 5, no. pp. 1-10, 2014.

[306] M. L. Guaragno, R. Gottardi, M. V. Fedorchak, A. Roy, P. N. Kumta and S. R. Little, "One-step synthesis of fluorescently labelled, single-walled carbon nanotubes," *Chemical Communications*, vol. 51, no. 97, pp. 17233-17236, 2015.

[307] E.-X. Ding, Q. Zhang, N. Wei, A. T. Khan and E. I. Kauppinen, "High-performance single-walled carbon nanotube transparent conducting film fabricated by using low feeding rate of ethanol solution," *Royal Society Open Science*, vol. 5, no. 6, pp. 180392, 2018.

[308] W. Zhang, Q. Zhao, C. Munuera, M. Lee, E. Flores, J. E. F. Rodrigues, J. R. Ares, C. Sanchez, J. Gainza, H. S. J. van der Zant, J. A. Alonso, I. J. Ferrer, T. Wang, R. Frisenda and A. Castellanos-Gomez, "Integrating van der Waals materials on paper substrates for electrical and optical applications," *Applied Materials Today*, vol. 23, no. pp. 101012, 2021.

[309] S. Kim, J. Yim, X. Wang, D. D. C. Bradley, S. Lee and J. C. deMello, "Spin-

and spray-deposited single-walled carbon-nanotube electrodes for organic solar cells," *Advanced Functional Materials*, vol. 20, no. 14, pp. 2310-2316, 2010.

[310] P. Liu, Q. Sun, F. Zhu, K. Liu, K. Jiang, L. Liu, Q. Li and S. Fan, "Measuring the work function of carbon nanotubes with thermionic method," *Nano Letters*, vol. 8, no. 2, pp. 647-651, 2008.

[311] J. A. Rohr, D. Moia, S. A. Haque, T. Kirchartz and J. Nelson, "Exploring the validity and limitations of the Mott-Gurney law for charge-carrier mobility determination of semiconducting thin-films," *J. Phys. Condens. Matter.*, vol. 30, no. 10, pp. 105901, 2018.

[312] V. M. Le Corre, E. A. Duijnstee, O. El Tambouli, J. M. Ball, H. J. Snaith, J. Lim and L. J. A. Koster, "Revealing charge carrier mobility and defect densities in metal halide perovskites via space-charge-limited current measurements," *ACS Energy Letters*, vol. 6, no. 3, pp. 1087-1094, 2021.

[313] W. P. Dumke, "On the additivity of ohmic and space charge limited currents," *Solid-State Electronics*, vol. 25, no. 2, pp. 101-103, 1982.

[314] A. Laturia, M. L. Van de Put and W. G. Vandenberghe, "Dielectric properties of hexagonal boron nitride and transition metal dichalcogenides: from monolayer to bulk," *npj 2D Materials and Applications*, vol. 2, no. 1, pp. 1-7, 2018.

[315] S. Barwich, J. Medeiros de Araújo, A. Rafferty, C. Gomes da Rocha, M. S. Ferreira and J. N. Coleman, "On the relationship between morphology and conductivity in nanosheet networks," *Carbon*, vol. 171, no. pp. 306-319, 2021.

[316] T. M. Higgins, S. Finn, M. Matthiesen, S. Grieger, K. Synnatschke, M. Brohmann, M. Rother, C. Backes and J. Zaumseil, "Electrolyte-gated n-type transistors produced from aqueous inks of WS_2 nanosheets," *Advanced*

Functional Materials, vol. 29, no. 4, pp. 1804387, 2019.

[317] D. O'Suilleabhain, V. Vega-Mayoral, A. G. Kelly, A. Harvey and J. N. Coleman, "Percolation effects in electrolytically gated WS_2/graphene nano:nano composites," *ACS Applied Materials & Interfaces*, vol. 11, no. 8, pp. 8545-8555, 2019.

[318] J. H. Kim, S. Yu, S. W. Lee, S.-Y. Lee, K. S. Kim, Y. A. Kim and C.-M. Yang, "Enhanced thermoelectric properties of WS_2/single-walled carbon nanohorn nanocomposites," *Crystals*, vol. 10, no. 2, pp. 140, 2020.

[319] A. Matthäus, A. Ennaoui, S. Fiechter, S. Tiefenbacher, T. Kiesewetter, K. Diesner, I. Sieber, W. Jaegermann, T. Tsirlina and R. Tenne, "Highly textured films of layered metal disulfide 2H-WS_2: Preparation and optoelectronic properties," *Journal of The Electrochemical Society*, vol. 144, no. 3, pp. 1013-1019, 1997.

[320] V. Ulianova, Y. Didenko, S. Bolat, G. T. Sevilla, D. Tatarchuk, I. Shorubalko, E. Gilshtein and Y. E. Romanyuk, "Effect of post-deposition treatment on electrical properties of solution-processed a-IGZO Schottky diodes," *AIP Advances*, vol. 10, no. 7, pp. 075104, 2020.

[321] J. Lee, M. J. Kim, B. G. Jeong, C. Kwon, Y. Cha, S. H. Choi, K. K. Kim and M. S. Jeong, "Electrical role of sulfur vacancies in MoS_2: Transient current approach," *Applied Surface Science*, vol. 613, pp.155900, 2023.

[322] C. Shih, G. Paulus, Q. Wang, Z. Jin, D. Blankschtein, M. Strano, "Understanding surfactant/graphene interactions using a graphene field effect transistor: Relating molecular structure to hysteresis and carrier mobility," *Langmuir*, vol.28, pp. 8579-8586, 2012.

[323] C. Lan, X. Kang, Y. Meng, R. Wei, X. Bu, S. Yip and J. C. Ho, "The origin of gate bias stress instability and hysteresis in monolayer WS_2 transistors," *Nano Research*, vol. 13, no. 12, pp. 3278-3285, 2020.

[324] M. Farbod, R. Taheri and A. Kosarian, "High performance photoresponsivity and high frequency of phosphorene/metal heterojunction as Schottky photodiode rectifier," *Applied Materials Today*, vol. 24, pp. 101092, 2021.

[325] S. Dongaonkar, J. D. Servaites, G. M. Ford, S. Loser, J. Moore, R. M. Gelfand, H. Mohseni, H. W. Hillhouse, R. Agrawal, M. A. Ratner, T. J. Marks, M. S. Lundstrom and M. A. Alam, "Universality of non-Ohmic shunt leakage in thin-film solar cells," *Journal of Applied Physics*, vol. 108, no. 12, pp. 124509, 2010.

[326] C. D. Lien, F. C. T. So and M. A. Nicolet, "An improved forward I-V method for nonideal Schottky diodes with high series resistance," *IEEE Transactions on Electron Devices*, vol. 31, no. 10, pp. 1502-1503, 1984.

[327] M. C. Newton, S. Firth and P. A. Warburton, "ZnO tetrapod Schottky photodiodes," *Applied Physics Letters*, vol. 89, no. 7, pp. 072104, 2006.

[328] S. K. Cheung and N. W. Cheung, "Extraction of Schottky diode parameters from forward current-voltage characteristics," *Applied Physics Letters*, vol. 49, no. 2, pp. 85-87, 1986.

[329] J. C. Tinoco, M. Estrada, B. Iñiguez and A. Cerdeira, "Conduction mechanisms of silicon oxide/titanium oxide MOS stack structures," *Microelectronics Reliability*, vol. 48, no. 3, pp. 370-381, 2008.

[330] H. Schmidt, F. Giustiniano and G. Eda, "Electronic transport properties of transition metal dichalcogenide field-effect devices: surface and interface effects," *Chemical Society Reviews*, vol. 44, no. 21, pp. 7715-7736, 2015.

[331] Q. Liang, J. Gou, Arramel, Q. Zhang, W. Zhang and A. T. S. Wee, "Oxygen-induced controllable p-type doping in 2D semiconductor transition metal dichalcogenides," *Nano Research*, vol. 13, no. 12, pp. 3439-3444, 2020.

[332] P. Han, E. R. Adler, Y. Liu, L. St Marie, A. El Fatimy, S. Melis, E. Van Keuren and P. Barbara, "Ambient effects on photogating in MoS_2

photodetectors," *Nanotechnology*, vol. 30, no. 28, pp. 284004, 2019.

[333] A. G. Martinez-Lopez, W. Y. Padron-Hernandez, D. Pourjafari, G. Oskam, G. Rodriguez-Gattorno, M. Estrada and J. C. Tinoco, "Electrical characterization of Schottky diodes based on inkjet-printed TiO_2 films," *IEEE Electron Device Letters*, vol. 39, no. 12, pp. 1940-1943, 2018.

[334] K.-Y. Chan, Z.-N. Ng, B. W.-C. Au and D. Knipp, "Visibly transparent metal oxide diodes prepared by solution processing," *Optical Materials*, vol. 75, no. pp. 595-600, 2018.

[335] D. Drdlik, Z. Chlup, H. Hadraba and K. Drdlikova, "Surface roughness improvement of near net shaped alumina by EPD," *Journal of the Australian Ceramic Society*, vol. 56, no. 2, pp. 721-727, 2019.

[336] L. Karger, K. Synnatschke, S. Settele, Y. J. Hofstetter, T. Nowack, J. Zaumseil, Y. Vaynzof and C. Backes, "The role of additives in suppressing the degradation of liquid-exfoliated WS_2 monolayers," *Advanced Materials*, vol. 33, no. 42, pp. 2102883, 2021.

[337] I. Tanabe, M. Gomez, W. C. Coley, D. Le, E. M. Echeverria, G. Stecklein, V. Kandyba, S. K. Balijepalli, V. Klee, A. E. Nguyen, E. Preciado, I. H. Lu, S. Bobek, D. Barroso, D. Martinez-Ta, A. Barinov, T. S. Rahman, P. A. Dowben, P. A. Crowell and L. Bartels, "Band structure characterization of WS_2 grown by chemical vapor deposition," *Applied Physics Letters*, vol. 108, no. 25, pp. 252103, 2016.

[338] S. M. Sze, *Semiconductor devices*, John Wiley and Sons, 1985.

[339] W. J. Beek, M. M. Wienk, M. Kemerink, X. Yang and R. A. Janssen, "Hybrid zinc oxide conjugated polymer bulk heterojunction solar cells," *The Journal of Physical Chemistry B*, vol. 109, no. 19, pp. 9505-9516, 2005.

[340] M. S. Chavali and M. P. Nikolova, "Metal oxide nanoparticles and their applications in nanotechnology," *SN Applied Sciences*, vol. 1, no. 6, pp.,

2019.

[341] S. Chen, J. R. Manders, S.-W. Tsang and F. So, "Metal oxides for interface engineering in polymer solar cells," *Journal of Materials Chemistry*, vol. 22, no. 46, pp. 24202-24212, 2012.

[342] T. Kida, S. Fujiyama, K. Suematsu, M. Yuasa and K. Shimanoe, "Pore and particle size control of gas sensing films using SnO_2 nanoparticles synthesized by seed-mediated growth: Design of highly sensitive gas sensors," *The Journal of Physical Chemistry C*, vol. 117, no. 34, pp. 17574-17582, 2013.

[343] J. H. Prosser, T. Brugarolas, S. Lee, A. J. Nolte and D. Lee, "Avoiding cracks in nanoparticle films," *Nano Letters*, vol. 12, no. 10, pp. 5287-5291, 2012.

[344] A. Alexandrov, M. Zvaigzne, D. Lypenko, I. Nabiev and P. Samokhvalov, "Al-, Ga-, Mg-, or Li-doped zinc oxide nanoparticles as electron transport layers for quantum dot light-emitting diodes," *Scientific Reports*, vol. 10, no. 1, pp. 7496, 2020.

[345] J. B. Coulter and D. P. Birnie, "Assessing Tauc plot slope quantification: ZnO thin films as a model system," *Physica Status Solidi (b)*, vol. 255, no. 3, pp., 2018.

[346] A. Srivastava, N. Kumar and S. Khare, "Enhancement in UV emission and band gap by Fe doping in ZnO thin films," *Opto-Electronics Review*, vol. 22, pp. 68-76, 2014.

[347] M. Rasheed and R. Barillé, "Room temperature deposition of ZnO and Al:ZnO ultrathin films on glass and PET substrates by DC sputtering technique," *Optical and Quantum Electronics*, vol. 49, no. 5, pp., 2017.

[348] Y. Zhang, Y.-H. Wen, J.-C. Zheng and Z.-Z. Zhu, "Direct to indirect band gap transition in ultrathin ZnO nanowires under uniaxial compression," *Applied Physics Letters*, vol. 94, no. 11, pp., 2009.

[349] W. R. Saleh, N. M. Saeed, W. A. Twej and M. Alwan, "Synthesis sol-gel derived highly transparent ZnO thin films for optoelectronic applications," *Advances in Materials Physics and Chemistry*, vol. 02, no. 01, pp. 11-16, 2012.

[350] W. Zhao, Z. Ghorannevis, K. K. Amara, J. R. Pang, M. Toh, X. Zhang, C. Kloc, P. H. Tan and G. Eda, "Lattice dynamics in mono- and few-layer sheets of WS2 and WSe2," *Nanoscale*, vol. 5, no. 20, pp. 9677-9683, 2013.

[351] T. Yang, M. Wang, C. Duan, X. Hu, L. Huang, J. Peng, F. Huang and X. Gong, "Inverted polymer solar cells with 8.4% efficiency by conjugated polyelectrolyte," *Energy Environmental Science*, vol. 5, no. 8, pp. 8208-8214, 2012.

[352] Y. Xia and S. Dai, "Review on applications of PEDOTs and PEDOT:PSS in perovskite solar cells," *Journal of Materials Science: Materials in Electronics*, vol. 32, pp. 12746-12757, 2021.

[353] J. Huang, Z. Yin and Q. Zheng, "Applications of ZnO in organic and hybrid solar cells," *Energy Environmental Science*, vol. 4, no. 10, pp. 3861-3877, 2011.

[354] W. Han, G. Ren, J. Liu, Z. Li, H. Bao, C. Liu and W. Guo, "Recent progress of inverted perovskite solar cells with a modified PEDOT:PSS hole transport layer," *ACS Applied Materials & Interfaces*, vol. 12, no. 44, pp. 49297-49322, 2020.

[355] X. Deng, R. Nie, A. Li, H. Wei, S. Zheng, W. Huang, Y. Mo, Y. Su, Q. Wang, Y. Li, J. Tang, J. Xu and K.-y. Wong, "Ultra-low work function transparent electrodes achieved by naturally occurring biomaterials for organic optoelectronic devices," *Advanced Material Interfaces*, vol. 1, no. 7, pp., 2014.

[356] O. Bubnova, Z. U. Khan, H. Wang, S. Braun, D. R. Evans, M. Fabretto, P.

Hojati-Talemi, D. Dagnelund, J.-B. Arlin, Y. H. Geerts, S. Desbief, D. W. Breiby, J. W. Andreasen, R. Lazzaroni, W. M. Chen, I. Zozoulenko, M. Fahlman, P. J. Murphy, M. Berggren and X. Crispin, "Semi-metallic polymers," *Nature Materials*, vol. 13, no. 2, pp. 190-194, 2014.

[357] M. Sun, Q. Fang, D. Xie, Y. Sun, L. Qian, J. Xu, P. Xiao, C. Teng, W. Li, T. Ren and Y. Zhang, "Heterostructured graphene quantum dot/WSe_2/Si photodetector with suppressed dark current and improved detectivity," *Nano Research*, vol. 11, no. 6, pp. 3233-3243, 2018.

[358] H. Sahin, S. Tongay, S. Horzum, W. Fan, J. Zhou, J. Li, J. Wu and F. M. Peeters, "Anomalous Raman spectra and thickness-dependent electronic properties of WSe_2," *Physical Review B*, vol. 87, no. 16, pp. 165409, 2013.

[359] K. B. Sundaram and A. Khan, "Work function determination of zinc oxide films," *J. Vac. Sci. Technol.*, vol. 15, no. 2, pp. 428-430, 1997.

[360] A. G. Kelly, J. O'Reilly, C. Gabbett, B. Szydłowska, D. O'Suilleabhain, U. Khan, J. Maughan, T. Carey, S. Sheil, P. Stamenov and J. N. Coleman, "Highly conductive networks of silver nanosheets," *Small*, vol. 18, no. 14, pp. 2105996, 2022.

[361] J. H. Lee, S. Cho, A. Roy, H.-T. Jung and A. J. Heeger, "Enhanced diode characteristics of organic solar cells using titanium suboxide electron transport layer," *Applied Physics Letters*, vol. 96, no. 16, pp., 2010.

[362] K. Lu, Y. Wang, J. Yuan, Z. Cui, G. Shi, S. Shi, L. Han, S. Chen, Y. Zhang, X. Ling, Z. Liu, L. Chi, J. Fan and W. Ma, "Efficient PbS quantum dot solar cells employing a conventional structure," *Journal of Materials Chemistry A*, vol. 5, no. 45, pp. 23960-23966, 2017.

[363] C. Li, Z. Song, D. Zhao, C. Xiao, B. Subedi, N. Shrestha, M. M. Junda, C. Wang, C. S. Jiang, M. Al-Jassim, R. J. Ellingson, N. J. Podraza, K. Zhu and Y. Yan, "Reducing saturation-current density to realize high‐efficiency

low‐bandgap mixed tin‐lead halide perovskite solar cells," *Advanced Energy Materials*, vol. 9, no. 3, pp., 2018.

[364] X. Yu, M. S. Prevot, N. Guijarro and K. Sivula, "Self-assembled 2D WSe_2 thin films for photoelectrochemical hydrogen production," *Nature Communications*, vol. 6, no. pp. 7596, 2015.

[365] S. Chander, A. Purohit, A. Sharma, Arvind, S. P. Nehra and M. S. Dhaka, "A study on photovoltaic parameters of mono-crystalline silicon solar cell with cell temperature," *Energy Reports*, vol. 1, no. 1, pp. 104-109, 2015.

[366] X. Cai, S. Zeng, X. Li, J. Zhang, S. Lin, A. Lin and B. Zhang, presented in part at the 2011 International Conference on Electrical and Control Engineering, 2011.

[367] S. Fonash, *Solar cell device physics*, Elsevier, 2012.

[368] A. Laturia, M. L. Van de Put and W. G. Vandenberghe, "Dielectric properties of hexagonal boron nitride and transition metal dichalcogenides: from monolayer to bulk," *npj 2D Materials and Applications*, vol. 2, no. 1, pp., 2018.

[369] W. C. Shen, R. S. Chen and Y. S. Huang, "Photoconductivities in MoS2 Nanoflake Photoconductors," *Nanoscale Research Letters*, vol. 11, no. 1, pp. 124, 2016.

[370] X. Kong, L. Zhang, B. Liu, H. Gao, Y. Zhang, H. Yan and X. Song, "Graphene/Si Schottky solar cells: a review of recent advances and prospects," *RSC Advances*, vol. 9, no. 2, pp. 863-877, 2019.

[371] X. Li, H. Zhu, K. Wang, A. Cao, J. Wei, C. Li, Y. Jia, Z. Li, X. Li and D. Wu, "Graphene-on-silicon Schottky junction solar cells," *Advanced Materials*, vol. 22, no. 25, pp. 2743-2748, 2010.

[372] S. Ghosh, M. Wasala, N. R. Pradhan, D. Rhodes, P. D. Patil, M. Fralaide, Y. Xin, S. A. McGill, L. Balicas and S. Talapatra, "Low temperature

photoconductivity of few layer p-type tungsten diselenide (WSe_2) field-effect transistors (FETs)," *Nanotechnology*, vol. 29, no. 48, pp. 484002, 2018.

[373] V. Klee, E. Preciado, D. Barroso, A. E. Nguyen, C. Lee, K. J. Erickson, M. Triplett, B. Davis, I. H. Lu, S. Bobek, J. McKinley, J. P. Martinez, J. Mann, A. A. Talin, L. Bartels and F. Leonard, "Superlinear composition-dependent photocurrent in CVD-grown monolayer $MoS_{2(1-x)}Se_{2x}$ alloy devices," *Nano Letters*, vol. 15, no. 4, pp. 2612-2619, 2015.

[374] J. Kang, V. K. Sangwan, H.-S. Lee, X. Liu and M. C. Hersam, "Solution-processed layered gallium telluride thin-film photodetectors," *ACS Photonics*, vol. 5, no. 10, pp. 3996-4002, 2018.

[375] R. H. Bube, "A new mechanism for superlinear photoconductivity with relevance to amorphous silicon," *Journal of Applied Physics*, vol. 74, no. 8, pp. 5138-5143, 1993.

[376] R. H. Bube, "Analysis of photoconductivity applied to cadmium-sulfide-type photoconductors," *Journal of Physics and Chemistry of Solids*, vol. 1, no. 4, pp. 234-248, 1957.

[377] A. T. Barrows, Doctoral dissertation, University of Sheffield, 2015.

[378] P. Kaienburg, P. Hartnagel, B. E. Pieters, J. Yu, D. Grabowski, Z. Liu, J. Haddad, U. Rau and T. Kirchartz, "How contact layers control shunting losses from pinholes in thin-film solar cells," *The Journal of Physical Chemistry C*, vol. 122, no. 48, pp. 27263-27272, 2018.

[379] D. S. Che Halin, A. W. Azhari, M. A. A. Mohd Salleh, N. I. Muhammad Nadzri, P. Vizureanu, M. M. A. B. Abdullah, J. A. Wahab and A. V. Sandu, "Metal-doped TiO2 thin film as an electron transfer layer for perovskite solar cells: A review," *Coatings*, vol. 13, no. 1, pp., 2022.

[380] M. Zlamalova, V. Mansfeldova, H. Tarabkova, H. Krysova and L. Kavan, "Variable work function of semiconducting thin-film oxide electrodes: a case

study of SnO_2 and TiO_2," *Journal of Solid State Electrochemistry*, vol. 27, no. 7, pp. 1935-1943, 2022.

[381] A. G. Pattantyus-Abraham, I. J. Kramer, A. R. Barkhouse, X. Wang, G. Konstantatos, R. Debnath, L. Levina, I. Raabe, M. K. Nazeeruddin, M. Gratzel and E. H. Sargent, "Depleted-heterojunction colloidal quantum dot solar cells," *ACS Nano*, vol. 4, no. 6, pp. 3374-3380, 2010.

[382] H. Zhou, C. Wang, J. C. Shaw, R. Cheng, Y. Chen, X. Huang, Y. Liu, N. O. Weiss, Z. Lin, Y. Huang and X. Duan, "Large area growth and electrical properties of p-type WSe2 atomic layers," *Nano Letters*, vol. 15, no. 1, pp. 709-713, 2015.

[383] C. C. Chen, W. H. Chang, K. Yoshimura, K. Ohya, J. You, J. Gao, Z. Hong and Y. Yang, "An efficient triple‐junction polymer solar cell having a power conversion efficiency exceeding 11%," *Advanced Materials*, vol. 26, no. 32, pp. 5670-5677, 2014.

[384] E. L. Ratcliff, J. Meyer, K. X. Steirer, A. Garcia, J. J. Berry, D. S. Ginley, D. C. Olson, A. Kahn and N. R. Armstrong, "Evidence for near-surface NiOOH species in solution-processed NiOx selective interlayer materials: Impact on energetics and the performance of polymer bulk heterojunction photovoltaics," *Chemistry of Materials*, vol. 23, no. 22, pp. 4988-5000, 2011.

[385] H. Bode, K. Dehmelt and J. J. E. A. Witte, "Zur kenntnis der nickelhydroxidelektrode—I. Über das nickel (II)-hydroxidhydrat," *Electrochimica Acta*, vol. 11, no. 8, pp. 1079-1087, 1966.

[386] D. Di Girolamo, F. Matteocci, F. U. Kosasih, G. Chistiakova, W. Zuo, G. Divitini, L. Korte, C. Ducati, A. Di Carlo, D. Dini and A. Abate, "Stability and dark hysteresis correlate in NiO-based perovskite solar cells," *Advanced Energy Materials*, vol. 9, no. 31, pp. 1901642, 2019.

[387] Y. Cheng, M. Li, X. Liu, S. H. Cheung, H. T. Chandran, H.-W. Li, X. Xu, Y.-

M. Xie, S. K. So, H.-L. Yip and S.-W. Tsang, "Impact of surface dipole in NiO_x on the crystallization and photovoltaic performance of organometal halide perovskite solar cells," *Nano Energy*, vol. 61, no. pp. 496-504, 2019.

[388] H. Wang, C. Oey, A. Djurišić, M. Xie, Y. Leung, K. Man, W. Chan, A. Pandey, J.-M. Nunzi and P. Chui, "Titania bicontinuous network structures for solar cell applications," *Applied Physics Letters*, vol. 87, no. 2, pp., 2005.

[389] A. J. Bett, P. S. Schulze, K. Winkler, J. Gasparetto, P. F. Ndione, M. Bivour, A. Hinsch, M. Kohlstädt, S. Lee and S. Mastroianni, "Low temperature perovskite solar cells with an evaporated TiO_2 compact layer for perovskite silicon tandem solar cells," *Energy Procedia*, vol. 124, no. pp. 567-576, 2017.

[390] K. O. Ukoba, F. L. Inambao and A. C. Eloka-Eboka, "Fabrication of affordable and sustainable solar cells using NiO/TiO_2 PN heterojunction," *International Journal of Photoenergy*, vol. 2018, no. pp., 2018.

[391] M.-H. Jao, H.-C. Liao and W.-F. Su, "Achieving a high fill factor for organic solar cells," *Journal of Materials Chemistry A*, vol. 4, no. 16, pp. 5784-5801, 2016.

[392] M. Rawa, M. Calasan, A. Abusorrah, A. A. Alhussainy, Y. Al-Turki, Z. M. Ali, H. Sindi, S. Mekhilef, S. Aleem and H. Bassi, "Single diode solar cells-improved model and exact current-voltage analytical solution based on Lambert's W function," *Sensors (Basel)*, vol. 22, no. 11, pp., 2022.

[393] M. Diantoro, T. Suprayogi, A. Hidayat, A. Taufiq, A. Fuad and R. Suryana, "Shockley's equation fit analyses for solar cell parameters from *I-V* curves," *International Journal of Photoenergy*, vol. 2018, pp. 1-7, 2018.

[394] J. Zheng, L. Hu, J. S. Yun, M. Zhang, C. F. J. Lau, J. Bing, X. Deng, Q. Ma, Y. Cho, W. Fu, C. Chen, M. A. Green, S. Huang and A. W. Y. Ho-Baillie, "Solution-processed, silver-doped NiO_x as hole transporting layer for high-efficiency inverted perovskite solar cells," *ACS Applied Energy Materials*,

vol. 1, no. 2, pp. 561-570, 2018.

[395] K. Bang, G.-C. Son, M. Son, J.-H. Jun, H. An, K. H. Baik, J.-M. Myoung and M.-H. Ham, "Effects of Li doping on the structural and electrical properties of solution-processed ZnO films for high-performance thin-film transistors," *Journal of Alloys and Compounds*, vol. 739, no. pp. 41-46, 2018.

[396] M. Caglar, S. Ilican, Y. Caglar and F. Yakuphanoglu, "Electrical conductivity and optical properties of ZnO nanostructured thin film," *Applied Surface Science*, vol. 255, no. 8, pp. 4491-4496, 2009.

[397] Y. Katsuta, R. Akahane and K. Yahagi, "Electrical properties of rutile TiO_2 thin film," *Japanese Journal of Applied Physics*, vol. 10, no. 8, pp., 1971.

[398] K. Pomoni, A. Vomvas and C. Trapalis, "Electrical conductivity and photoconductivity studies of TiO_2 sol–gel thin films and the effect of N-doping," *Journal of Non-Crystalline Solids*, vol. 354, no. 35-39, pp. 4448-4457, 2008.

[399] M. Gillet, K. Aguir, C. Lemire, E. Gillet and K. Schierbaum, "The structure and electrical conductivity of vacuum-annealed WO_3 thin films," *Thin Solid Films*, vol. 467, no. 1-2, pp. 239-246, 2004.

[400] Y. Jeon, D. Rhee, B. Wu, V. Mazanek, I. S. Kim, D. Son, Z. Sofer and J. Kang, "Electrochemically exfoliated phosphorene nanosheet thin films for wafer-scale near-infrared phototransistor array," *npj 2D Materials and Applications*, vol. 6, no. 1, pp., 2022.

[401] T. Zou, H. J. Kim, S. Kim, A. Liu, M. Y. Choi, H. Jung, H. Zhu, I. You, Y. Reo, W. J. Lee, Y. S. Kim, C. J. Kim and Y. Y. Noh, "High-performance solution-processed 2D P-type WSe_2 transistors and circuits through molecular doping," *Advanced Materials*, vol. 35, no. 7, pp. e2208934, 2022.

[402] Y. Deng, Z. Luo, N. J. Conrad, H. Liu, Y. Gong, S. Najmaei, P. M. Ajayan, J. Lou, X. Xu and P. D. Ye, "Black phosphorus-monolayer MoS_2 van der Waals

heterojunction p-n diode," *ACS Nano*, vol. 8, no. 8, pp. 8292-8299, 2014.

[403] M. M. Furchi, F. Höller, L. Dobusch, D. K. Polyushkin, S. Schuler and T. Mueller, "Device physics of van der Waals heterojunction solar cells," *npj 2D Materials and Applications*, vol. 2, no. 1, pp. 3, 2018.

[404] W. Xia, L. Dai, P. Yu, X. Tong, W. Song, G. Zhang and Z. Wang, "Recent progress in van der Waals heterojunctions," *Nanoscale*, vol. 9, no. 13, pp. 4324-4365, 2017.

[405] C. Li, Q. Cao, F. Wang, Y. Xiao, Y. Li, J. J. Delaunay and H. Zhu, "Engineering graphene and TMDs based van der Waals heterostructures for photovoltaic and photoelectrochemical solar energy conversion," *Chemical Society Reviews*, vol. 47, no. 13, pp. 4981-5037, 2018.

[406] W. Zhao, Z. Ghorannevis, L. Chu, M. Toh, C. Kloc, P. H. Tan and G. Eda, "Evolution of electronic structure in atomically thin sheets of WS_2 and WSe_2," *ACS Nano*, vol. 7, no. 1, pp. 791-797, 2013.

[407] H. P. Hsu, D. Y. Lin, J. J. Jheng, P. C. Lin and T. S. Ko, "High optical response of niobium-doped WSe_2-layered crystals," *Materials*, vol. 12, no. 7, pp. 1161, 2019.

[408] D. Chu and E. K. Kim, "Hole conduction of tungsten diselenide crystalline transistors by niobium dopant," *Advanced Electronic Materials*, vol. 5, no. 2, pp., 2019.

[409] F. Lévy, P. Schmid and H. Berger, "Electrical properties of layered $MoSe_2$ single crystals doped with Nb and Re," *Philosophical Magazine*, vol. 34, no. 6, pp. 1129-1139, 2006.

[410] T. Nishimura, K. Nakaji, J. Chantana, A. Mavlonov, Y. Kawano, T. Negami and T. Minemoto, "P-type Nb-doped MoS_2 layer for solar cell application," *physica status solidi (RRL)-Rapid Research Letters*, vol. 17, no. 2, pp. 2200236, 2022.

[411] S. Ghosh, A. Varghese, H. Jawa, Y. Yin, N. V. Medhekar and S. Lodha, "Polarity-tunable photocurrent through band alignment engineering in a high-speed $WSe_2/SnSe_2$ diode with large negative responsivity," *ACS Nano*, vol. 16, no. 3, pp. 4578-4587, 2022.

[412] M. Patel, P. Pataniya, H. Vala and C. K. Sumesh, "One-dimensional/two-dimensional/three-dimensional dual heterostructure based on MoS_2-modified ZnO-heterojunction diode with silicon," *The Journal of Physical Chemistry C*, vol. 123, no. 36, pp. 21941-21949, 2019.

[413] D. Thangaraju, R. Marnadu, V. Santhana, A. Durairajan, P. Kathirvel, J. Chandrasekaran, S. Jayakumar, M. Valente and D. C. Greenidge, "Solvent influenced synthesis of single-phase SnS_2 nanosheets for solution-processed photodiode fabrication," *CrystEngComm*, vol. 22, no. 3, pp. 525-533, 2020.

[414] B. Parida, S. Kim, M. Oh, S. Jung, M. Baek, J.-H. Ryou and H. Kim, "Nanostructured-NiO/Si heterojunction photodetector," *Materials Science in Semiconductor Processing*, vol. 71, no. pp. 29-34, 2017.

[415] A. Umar, M. S. Akhtar, R. I. Badran, M. Abaker, S. H. Kim, A. Al-Hajry and S. Baskoutas, "Electrical properties of solution processed p-SnS nanosheets/n-TiO_2 heterojunction assembly," *Applied Physics Letters*, vol. 103, no. 10, pp., 2013.

[416] P. Pataniya, C. K. Zankat, M. Tannarana, C. K. Sumesh, S. Narayan, G. K. Solanki, K. D. Patel, V. M. Pathak and P. K. Jha, "Paper-based flexible photodetector functionalized by WSe_2 nanodots," *ACS Applied Nano Materials*, vol. 2, no. 5, pp. 2758-2766, 2019.

[417] D. Kannichankandy, P. M. Pataniya, C. K. Zankat, M. Tannarana, V. M. Pathak, G. K. Solanki and K. D. Patel, "Paper based organic–inorganic hybrid photodetector for visible light detection," *Applied Surface Science*, vol. 524, pp. 146589, 2020.

[418] P. M. Pataniya and C. K. Sumesh, "Low cost and flexible photodetector based on WSe2 Nanosheets/Graphite heterostructure," *Synthetic Metals*, vol. 265, pp. 116400, 2020.

[419] B. L. Chauhan, S. A. Bhakhar, P. M. Pataniya, G. K. Solanki and V. M. Pathak, "Self-powered photodetector based on liquid phase exfoliated Cu–WSe_2 nanosheets," *Optical Materials*, vol. 133, no. pp., 2022.

[420] D. Kannichankandy, P. M. Pataniya, V. Dhamecha, V. M. Pathak and G. K. Solanki, "Self-standing polyvinyl chloride film as flexible substrate for WSe_2 based photodetector," *Current Applied Physics*, vol. 39, no. pp. 140-146, 2022.